Modeling of Compression Ignition Engines for Advanced Engine Operation and Alternative Fuels by the Second Law of Thermodynamics

BY

Jonathan Michael Stearns Mattson

Submitted to the graduate degree program in the Department of Mechanical Engineering and the Graduate Faculty of the University of Kansas in fulfillment of the requirements for the Degree of Doctor of Philosophy.

_____

Chair: Dr. Christopher Depcik
Dept. of Mechanical Engineering

_____

Dr. Lin Liu
Dept. of Mechanical Engineering

_____

Dr. Xianglin Li
Dept. of Mechanical Engineering

_____

Dr. Edward Peltier
Dept. of Civil, Environmental, and Architectural Engineering

_____

Dr. Susan Stagg-Williams
Dept. of Chemical and Petroleum Engineering

Defended: September 9th, 2019

The Dissertation Committee for Jonathan Mattson certifies that this is the approved version of the following dissertation:

Modeling of Compression Ignition Engines for Advanced Engine Operation and Alternative Fuels by the Second Law of Thermodynamics

BY

Jonathan Michael Stearns Mattson

_____

Chair: Dr. Christopher Depcik
Dept. of Mechanical Engineering

Approved: September 10th, 2019

Abstract

With the advent of modern engine control strategies, and particularly electronic common-rail injection, the scope and scale of what is achievable and controllable in compression-ignition engines has exploded quite rapidly in recent years. The potential marriage of electronically-controlled and multi-point fuel injection, dual fuel combustion, variable exhaust gas recirculation, exhaust waste heat recovery, low-temperature combustion, and the immense variety of potential liquid and gaseous fuels available means that the older understanding of compression ignition engine combustion is incomplete and inadequate to explain, predict, control, and optimize more novel engine combustion and operational regimes. This mandates that new models, both diagnostic and theoretical, be developed to explore engine combustion and pick apart the various phenomena that result, and includes revisiting models that previously have been sidelined for a lack of usefulness.

To that end, this work details the construction, validation, and usage of a diagnostic heat release model focused on the application of the 2nd Law of Thermodynamics and the phenomena associated with entropy generation and availability destruction from the accumulated test data of numerous fuels and engine operational modes. A critical aspect of this research includes the marriage of this model with a suite of emissions analysis technologies, allowing for a complete characterization of engine-out regulated and unregulated emissions species, as well as a thoroughly instrumented and highly modified single-cylinder compression-ignition engine. This combined test apparatus for novel fuels and engine operational modes, in combination with the models described herein, serve as a means to collect and dissect engine performance, in-cylinder pressure, engine knock and noise, emissions, heat release, and availability release and consumption, and the interrelationships between these characteristics

The experimental results of this work showcase both the direct usage of the 2nd Law Analysis (both alongside and separate from the more traditional 1st Law Heat Release Analysis), and also the potential usage of this model for the exploration of engine operational modes. In particular, the 2nd Law analysis appears to be of immense importance to the exploration of low temperature combustion regimes, as well as the usage of exhaust waste heat recovery systems.

Acknowledgements

The work within this dissertation would not have been possible if not for the contributions, support, advice, and aid of numerous individuals, organizations, and entities. The University of Kansas, the KU Mechanical Engineering Department, the Transportation Research Institute, and the Kansas Soybean Commission must all be noted for their integral financial support and knowledgebase. Special thanks is also owed to Charles Gabel, Ash Shadrick, Kate Maisch, Ansel Armstrong, Will Vincent, Josie Nixon, and Al Syvongsay for their help and support over the years from within the Department.

In particular, Dr. Christopher Depcik provided the opportunity to work on numerous projects, both those described within, and those described in the other papers and projects I have had the privilege to work on. In addition, Dr. Depcik has provided invaluable guidance, support, and feedback towards the completion of this work. Additional help, support, and technical guidance from Dr. Susan Stagg-Williams and Dr. Edward Peltier has been very much appreciated, particularly with respect to the manufacture, material testing, and analysis of the various fuels used over the course of this work.

Thanks is also owed to all of the past and present members of the lab. In particular, this work would have been impossible without Michael Magnus and Chenaniah Langness, who were integral in the creation and initial bench-testing of all of the instruments that this work is built upon, and also for the teaching and training I received both from and alongside them. Finally, this long journey would not have been completed without the love, understanding, and patience of my parents, Michael J. Mattson and Ruth E. Stearns.

Publications

The following peer-reviewed Journal and Conference publications provide the basis for this dissertation.

J. Mattson, C. Langness, C. Depcik. "Modified Heat Release Analysis for CNG-Assisted Diesel Combustion." SAE 2015 World Congress & Exhibition, SAE Technical Paper 2015-01-1744.

This work established necessary changes to the First Law Heat Release Model, in order to allow it to correctly analyze data from dual-fuel combustion with moderate amounts of Compressed Natural Gas. My contributions comprise all of the analytical and modeling work, as well as experimentation to collect the data utilized in the publication. I was assisted by another graduate student (Chenaniah Langness), who oversaw experimentation, and who also used the data to analyze combustion from a more conventional perspective for his Master's Thesis efforts.

J. Mattson, C. Langness, B. Niles, C. Depcik. "Usage of Gylcerin-Derived, Hydrogen-Rich Syngas Augmented by Soybean Biodiesel to Power a Biodiesel Production Facility," International Journal of Hydrogen Energy (2016), vol. 41(38), pp. 17132-17144.

This work investigated the usage of an artificial synthesis gas mixture in a single-cylinder engine alongside Soybean Biodiesel in a Dual-Fuel Combustion regime, from a First Law Heat Release perspective. My contributions comprise overseeing the experimentation to collect the data utilized in the publication, and analysis of that data. I was assisted in designing and running the experiment by a fellow graduate student (Chenaniah Langness) who was responsible for the design and construction of the dual-fueling system on the single-cylinder test cell, and who also gave input during the analysis of the publication. In addition, we both oversaw an undergraduate student researcher (Brendan Niles), who aided us with performing the experiments.

J. Mattson, E Reznicek, C. Depcik. "*Second Law Heat Release Modeling of a Compression Ignition Engine Fueled with Blends of Palm Biodiesel," ASME Journal of Engineering for Gas Turbines and Power (2016), vol. 138(9), 091502.*

This work established the fundamentals of the Second Law Heat Release Model, and explored the usage of the model through the usage of a relatively straightforward fuel blending study with ULSD and Palm

Biodiesel. My contributions comprise all of the analytical and modeling work, as well as experimentation to collect the data utilized in the publication, and analysis of that data. I was assisted in writing the initial MATLAB codes that would be installed in my main Heat Release program by an undergraduate student researcher (Even Reznicek).

J. Mattson, C. Depcik. "First and Second Law Heat Release Analysis in a Single Cylinder Engine," SAE International Journal of Engines (2016), SAE Technical Paper 2016-01-0559.

This work further established the Second Law Heat Release Model, and offered a more thorough comparison against the preexisting and already established First Law Heat Release Model. My contributions comprise all of the analytical and modeling work, as well as experimentation to collect the data utilized in the publication, and analysis of that data.

J. Mattson, C. Langness, and C. Depcik. "Exergy Analysis of Dual-Fuel Operation with Diesel and Moderate Amounts of Compressed Natural Gas in a Single-Cylinder Engine," Combustion Science and Technology (2018), vol. 190(3), pp. 471-489.

This work examined the usage of the Second Law Heat Release Model on Dual-Fuel operation with Compressed Natural Gas through low-to-moderate Energy Substitution Ratios. My contributions comprise the experimentation to collect the data utilized in the publication, and the analysis of that data from a Second Law perspective. The data was initially collected in partnership with another graduate student (Chenaniah Langness), who oversaw experimentation, and who also used the data to analyze combustion from a more conventional perspective for his Master's Thesis efforts.

J. Mattson, C. Depcik. "Comparison of Injection Systems with Respect to Compression Ignition Engine Knock," SAE 2018 World Congress & Exposition, SAE Technical Paper 2018-01-0219.

This work established and examined the use of a pair of engine knock and noise analysis techniques for use on the Yanmar L100v Single Cylinder engine. My contributions comprise the examination and analysis of previously-collected engine data using these techniques.

J. Mattson, C. Langness, and C. Depcik. "An Analysis of Dual-Fuel Combustion of Diesel with Compressed Natural Gas in a Single-Cylinder Engine," SAE 2018 World Congress & Exposition, SAE Technical Paper 2018-01-0248.

This work was a comprehensive First-Law Analysis of dual-fuel combustion on the Single Cylinder Engine, using low, moderate, and high amounts of Compressed Natural Gas. My contributions comprise the experimentation to collect the data utilized in the publication, and the analysis of that data. The data was initially collected in partnership with another graduate student (Chenaniah Langness), who oversaw experimentation, and who also used some of the data (particularly the lower Energy Substitution Ratios) to analyze combustion from a more conventional perspective for his Master's Thesis efforts.

J. Mattson, N. V. Burnete, C. Depcik, D. Moldovanu, N. Burnete. "Second Law Analysis of Waste Cooking Oil Biodiesel versus ULSD during Operation of a CI Engine," Fuel (2019) (in press).

This work was a collaborative effort with researchers at the Technical University of Cluj-Napoca, Romania, and examined the usage of the Second Law Heat Release Model with conventional fuels in a relatively lower compression-ratio engine. My contributions comprise the analysis of the data from the experiments. The data itself was collected in experiments by Nicholae Vlad Burnete, Dan Moldovanu, and Nicolae Burnete. Nicolae Vlad Burnete also aided in analysis of the data, particularly with respect to engine emissions.

In all of the above works, Christopher Depcik provided invaluable mentorship and guidance as my advisor and PI, as well as guiding the analyses and helping craft experimental methodologies.

Table of Contents

Table of Figures

Note: Unless otherwise specified as being measured, all figures provided **modeled** results.

Table of Tables

Nomenclature

A	area [m^2], first Arrhenius coefficient [ms], availability [J], exergy [J]
A_n	injector nozzle area [m^2]
A_s	surface area within cylinder [m^2]
a	coefficient for gas emissivity correlation [- , Pa^{-1} m^{-1}, Pa^{-2} m^{-2}, Pa^{-3} m^{-3}], lipid carbon number
b	engine bore [m], second value of lipid number
$BSFC_g$	gross brake specific fuel consumption [g kW^{-1} h^{-1}]
C_d	coefficient of discharge
c	connecting rod length [m], constant value
c_f	liquid fuel specific heat [J kg^{-1}]
c_p	constant pressure specific heat [J kg^{-1}]
$\bar{c}_p$	constant pressure molar heat [J $mole^{-1}$]
c_v	constant volume specific heat [J kg^{-1}]
d	correlation coefficient used for CHEMKIN-III correlations [- , K^{-1}, K^{-2}, K^{-3}, K^{-4}, K]
E_a	activation energy [kJ $mole^{-1}$]
ESR	energy substitution ratio
e_c	fuel chemical exergy content [kJ kg^{-1}]
e_{RMS}	RMS error in internal energy [J]
f	residual fraction (mass basis)
g	global reaction coefficients, dependant variable in Newton-Raphson and secant methods
g'	derivative of dependant variable in Newton-Raphson and secant methods
H	enthalpy [J]
h	specific enthalpy [J kg^{-1}]
$\bar{h}$	molar enthalpy [J $mole^{-1}$]
h_c	conductive heat transfer coefficient [W m^{-2} K^{-1}]

$IMEP_g$	gross indicated mean effective pressure [bar]
K	fuel combustion rate coefficient [$m^3\ kg^{-1}\ sec^{-1}$]
L_b	mean beam length [m]
l	local combustion formula coefficient
m	mass [kg], number of spatial dimensions
m_f	total mass of fuel used per cycle [kg $cycle^{-1}$], mass of the fuel zone [kg]
$m_{f,con}$	total mass of fuel consumed by combustion [kg]
$m_{f,rem}$	mass of fuel remaining after combustion [kg]
$\dot{m}_a$	mass flow rate of air [kg s^{-1}]
$\dot{m}_f$	mass flow rate of fuel [kg s^{-1}]
$\dot{m}_{f,inj}$	mass flow rate of fuel by injection [kg s^{-1}]
N	average engine speed [rev min^{-1}]
n	moles of material [mole], total number of zones, counter for iterations
n'	second Arrhenius coefficient
n_h	number of holes on a single fuel injector
n_{inj}	number of fuel injectors within a cylinder
n_R	number of revolutions per engine cycle [rev $cycle^{-1}$]
P_g	gross power [kW]
p	pressure [Pa]
p_0	ambient pressure [Pa]
p_g	partial pressure of bulk CO_2 and H_2O[Pa]
p_{net}	net pressure [Pa]
Q_{hr}	heat release [J]
Q_{ht}	heat transfer [J]
Q_{LHV}	fuel lower heating value [kJ kg^{-1}]

R	gas constant [J kg^{-1} K^{-1}]
R_{univ}	universal gas constant [J mole^{-1} K^{-1}]
r	crank length [m], ratio of fuel exergy to energy [J_A/J_E]
r_c	compression ratio
S	entropy [J K^{-1}]
s	specific entropy [J kg^{-1} K^{-1}]
$\bar{s}$	specific molar entropy [J mol^{-1} K^{-1}]
Sk	Stark number ratio of convective to radiative heat transfer
T	temperature [K]
T_f	temperature of the flame [K]
T_{inj}	injection temperature [K]
T_0	ambient temperature [K]
T_s	temperature, single-zone approximation [K]
T_{vap}	fuel vaporization temperature [K]
T_w	cylinder wall temperature [K]
t	time [s]
t_{step}	time step [s]
U	internal energy [J]
$\forall$	volume [m^3]
$\forall_{bowl}$	piston bowl volume [m^3]
$\forall_{clear}$	clearance volume [m^3]
$\forall_d$	displacement volume [m^3]
W	work [J], molecular weight [kg mole^{-1}]
$\dot{W}$	work energy per unit time [J s^{-1}], power [W]
x	mole fraction, independent variable in Newton-Raphson and secant methods

Y_{mb} fraction of mass burned

y mass fraction

α_w wall absorptivity

γ ratio of specific heats

Δ_θ heat transfer term for thermodynamic loss angle calculation [Pa]

δ molar amount of intake air [moles]

ε fraction of intake air that is composed of residual gases (molar basis)

ε_{fl} emissivity of the luminous flame

ε_g emissivity of the bulk gas

ϵ fraction of intake air that is composed of recycled exhaust gases (molar basis)

η exponent controlling heat transfer in calculations for thermodynamic loss angle

η_c combustion efficiency

η_f fuel conversion efficiency

η_q gross energy accountability

η_t thermal efficiency

θ crank angle [degree]

θ_0 crank angle offset [degree]

θ_{TDC} crank angle for top dead center [degree]

$\hat{\theta}_{TDC}$ guessed crank angle for top dead center [degree]

ξ molar amount of injected fuel [moles]

ρ density [kg m^{-3}]

τ ignition delay [s]

ϕ equivalence ratio

Subscripts

a air

avg	average
b	burned zone, burned
c	combustion
cv	control volume, bulk gas
CNG	compressed natural gas
e	entrained, exhaust, exergy, 2nd Law
ef	exergetic fuel conversion
EGR	exhaust gas recirculation
f	fuel zone, fuel
fa	fuel added
fb	fuel burned
g	bulk gas
h	injector nozzle hole, cylinder head
ht	heat transfer
i	index for zones, inlet
ig	time of ignition
ig,c	correlated time of ignition
ig,ex	expected time of ignition
$igend$	time of end of ignition
inj	injected, time of injection, injectors
$injend$	time of end of injection
ir	irreversibility
IVC	time of intake value closing
j	index for species
k	index for data points

mix	fuel-air mix
p	produced, piston face
res	residual
u	unburned zone
w	carbon atoms in fuel molecule, wall, work
x	hydrogen atoms in fuel molecule
y	oxygen atoms in fuel molecule
z	nitrogen atoms in fuel molecule

Chapter I: Engine Research at the University of Kansas

Some material published as "Availability Analysis of Alternative Fuels for Compression Ignition Engine Combustion," Fourth International Congress of Automotive and Transport Engineering, Accepted June 22nd, 2018

1.1 Introduction

The internal combustion engine has been an important and reliable means of power production for well over a century, particularly due to successive advances in increasing power and efficiency, as well as the gradual reduction of harmful emissions, within that same time period [1, 2]. However, these advances have been largely superficial to the underlying processes of engine operation, such that spark ignition (SI) and compression ignition (CI) engines have each remained largely unchanged since the birth of these technologies by the close of the 19th century [1].

In this time, the CI (or diesel) engine has been at the forefront of efficient power production, particularly in stationary or steady-state power generation, all while remaining true to Rudolf Diesel's initial design of compressing a working fluid and adding fuel late in the engine's compression stroke [1]. This injected fuel is then prepared through a combination of both physical and chemical processes over a short time period (known as ignition delay), before finally igniting due to the combined high pressure and temperature within the cylinder. Because the fuel is added relatively late in the engine cycle, particularly in comparison to SI engines, improper early ignition of the fuel is largely avoided. As a result, engines running through a CI process are able to increase their compression ratios to very high levels, and thus raise the peak cylinder pressure [1]. This higher variation in pressure between the in-cylinder environment and the ambient leads to a higher change in temperature of the working fluid within the cylinder itself, and thus increases the thermal efficiency of the engine. Therefore, the high compression ratios needed to promote autoignition of fuel contribute to the higher efficiency of CI engines. With that in mind, the primary challenge in engine operation is the timing of combustion, which is brought about through precise timing and duration of the fuel injection event itself [1].

The fuel injection event, and the means by which this event is controlled, has been the central interest of CI engine research for the past century, since the introduction of the mechanical injection pump in 1921 that injected fuel into a prechamber at low pressures (relative to modern systems) [1]. As time has passed, advances in technology have increased the efficacy of fuel injection while steadily moving to higher pressures. This has reduced the time required to promote complete mixing of the fuel, allowing the injection event to move from a prechamber to directly injecting into the cylinder itself. In the past few decades, these advance often led (or were in response) to increasing emissions requirements by various government agencies worldwide, or by increased demand for higher engine efficiency in the face of more volatile petroleum prices [3].

Of particular note is the modern common rail electronic injection system. In this system, all fuel injectors on the engine draw from a single pressurized fuel distribution system (the "common rail"), rather than injection pumps responsible for individual injectors, often with pressures exceeding 100 MPa. In addition, instead of each individual injector system requiring a pulse to propagate through the fuel line in order to move the injector needle and initiate injection, each individual injector is now triggered directly by electric signals sent from an Engine Control Unit (ECU). As a result, the ECU can perform highly precise and on-the-fly adjustments to engine operation, ensuring high-efficiency operation at nearly any engine speed or load (and thus, any required power output). Because of this reliance on a functionally instantaneous electronic signal, rather than a much slower mechanical pulse, fuel injection can be triggered multiple times per engine cycle, resulting in engine manufacturers adding multiple early injection events (typically to smooth the ignition event, reducing engine noise) or late injection events (providing additional hydrocarbons to aid in catalytic aftertreatment), in addition to the main injection event itself [1, 4].

These more advanced injection technologies have also opened the door to repurposing a given CI engine to a different fuel with relative ease. As the ignition delay of a given fuel is dependent on its physical and chemical characteristics (most notably, viscosity and energy density), changing a fuel will result in changing the ignition delay the engine experiences, in turn changing how efficiently and cleanly

the engine operates if not recalibrated. As a result, while alternative drop-in fuels to standard ultra-low sulfur diesel (ULSD) functioned adequately in most CI engines utilizing older mechanical injection systems, these fuels would be doomed to operate in less-than-optimal conditions, as the process needed to change the mechanical injection timing often involved partially disassembling the engine in order to access the timing mechanisms. Modern electronic injection systems, however, allow for a researcher to more easily explore the performance limits of a given fuel, resulting in a level playing field when comparing ULSD to alternative fuels (most significantly, biodiesels) [5].

Finally, changing the nature of fuel injection control has also opened up CI engines to newer engine cycles or fueling mechanisms that would have been too difficult to control without dynamic and fluid control on the process of injection. One prominent example is dual-fuel combustion, where a gaseous fuel (such as methane or natural gas) is added to the intake of the CI engine, and a small pilot charge of liquid fuel is injected in order to ignite the entire mixture [6]. Utilizing dual-fuel combustion requires changes in the injection event in order to keep combustion behaving optimally, but this recalibration is conceptually identical to the process for recalibrating an engine for biodiesels [7]. Similarly, CI engines can be repurposed to attempt premixed-charge compression ignition (PCCI) combustion, where fuel is injected extremely early in the intake and/or compression strokes, and in low quantities, achieving optimal fuel atomization and vaporization, allowing for near-constant volume combustion, which can result in extremely high engine thermal efficiency (potentially exceeding 50%) [8]. While this mode of engine combustion is more temperamental and only functions properly (if at all) in a very small and temperature-dependant operational window, on paper it is still just a matter of proper engine calibration, and which is only possible thanks to the relatively immense levels of control allowed by modern electronic injection systems [9, 10].

The advent of precision control over injection timing and duration has also necessitated more advanced modeling of internal combustion engine processes. Thanks to the wide variety of fuels, engine operational modes, and operating conditions controllable by the ECU, it is now necessary to take a deeper look at the actual thermodynamic processes that the engines operate on, in order to see how changing

between these modes of combustion may change the nature of engine operation. This is possible either through complex 3-D modeling of combustion processes, or through simpler thermodynamic modeling fed by experimental results and test data, particularly through the measurement of the in-cylinder pressure [11, 12]. Of these two options, the first is more necessary for investigating specific processes within a given engine, while the second is much more useful in comparing and contrasting various operating modes (or, potentially, various engines) in a time-efficient manner [13].

1.2 The First and Second Laws of Thermodynamics

In the study and modeling of internal combustion engines, few individual physical laws are as important as the 1st Law of Thermodynamics, or the concept that the total energy within a system must be conserved and accounted for [1, 14]. The result of this is that one may evaluate the various means by which energy is added to the cylinder environment in the form of fuel chemical potential energy, liberated and converted to thermal energy by combustion, and then either utilized as work, lost as heat transfer, or retained within the working fluid as hot gas and lost to the environment at the exhaust blowdown event at the close of the cycle. The interrelationships between work output, heat transfer losses, and thermal retention of the gas is a relatively well-understood set of phenomenon, often expressed more informally as the "Rule of Thirds," in that roughly one-third of chemical potential added to the cylinder will go towards each of these three main modes of energy transfer out of the cylinder, with lesser amounts of thermal energy lost through mass transfer into or out of the cylinder (notably, injection and cylinder blow-by).

By comparison, the 2nd Law of Thermodynamics is not as heavily relied upon in engine modeling [12]. While numerous versions of the 2nd Law have been penned and used, inevitably depending on the precise context in which the 2nd Law is being utilized, perhaps the most simple and useful for engine operation modeling is the Entropy Statement of the 2nd Law, which states that it is impossible for an isolated system to operate in such a way that entropy is destroyed [14].

With respect to engines, the 2nd Law implies the inevitability of the generation of entropy throughout the engine cycle, and thus the inevitability that a significant portion of the energy liberated by

combustion will not be accessible for extraction as useful work. Within engine modeling, the processes by which an understanding of entropy generation can be utilized are closely related to the inefficiencies and processes by which the potential to use fuel thermal energy for work are diminished, particularly because the system is striving to come into thermal equilibrium with the surrounding heat reservoir (i.e. the ambient environment itself). This potential work is known classically as availability, and as exergy in more modern contexts [14, 15]. In this way, availability represents the total amount of thermal energy within the heated working fluid that is still potentially useful in whatever process is being studied. This availability is decreased over time, partly as it is converted to actual work or leaves the cylinder through heat and mass transfer. However, a portion of the availability is permitted to be destroyed. This destroyed availability (sometimes called anergy) increases with time, and is directly related to the generation of entropy by the 2nd Law [15]. Specifically, generated entropy is associated with a portion of the total energy in the cylinder, such that this energy is no longer available, and is thus referred to as destroyed availability.

Following the 1st Law, the sum total of exergy and anergy must remain constant, as the total amount of availability added by combustion must be equal to the total amount of available exergy and unavailable anergy at any given moment after combustion has occurred. Due to the 2nd Law, though, it is ensured that unavailability may only increase, and the 1st Law thus ensures that this unavailability can only come at the expense of availability.

The source of this availability addition is the chemical potential availability of the unburned fuel and oxidizer, given that the fuel exists in a relatively low-entropy state [15]. That fuel is injected and consumed by combustion, and thus has its chemical energy transformed into thermal energy, heating the cylinder, raising the pressure, and eventually (and ideally) exiting the cylinder as work by driving the piston downward. From a 2nd Law perspective, chemical potential availability is converted to thermal availability by combustion, with some of that availability being converted to useful work as it exits the cylinder through the "intended" manner. At the same time, much of that thermal availability degrades and becomes unavailable, even within the cylinder environment, and this internal unavailability grows as the

difference in energy content (or, functionally, the difference in temperature) between the cylinder interior and the surrounding environment decreases, and the two sides approach thermal equilibrium. Simultaneously, as this same temperature difference decreases, the amount of heat transfer through the cylinder walls to the environment decreases, and exergy destruction external to the control volume of the cylinder falls as well. Finally, whatever availability is not destroyed, extracted as work, or lost through heat transfer is inevitably retained by the working fluid, and is released to the atmosphere by the exhaust event at the end of the engine cycle.

1.3 Diagnostic Rate of Heat Release Modeling

An important outlet for both the 1st and 2nd Law heat release analyses is in the diagnostic modeling of engine processes from experimental data, typically an in-cylinder pressure trace. 1st Law models are quite common, and have been a mainstay of internal combustion engine research for decades [1]. By summing the rate of change of the energy within the cylinder, and how this energy is entering or leaving the cylinder, these models calculate the total rate of heat release (RHR) as a function of the thermodynamic properties of the working fluids within the control volume, and the amount of energy present (available from the measured flowrate of fuel entering the cylinder). This overall RHR is typically characterized by two separate phases of combustion (see Figure 1) [13]. The first phase is a spike in the heat release rate immediately following ignition, as relatively high amounts of fuel are injected, vaporize, chemically prepare, and finally combust all at once. The magnitude of the spike is directly related to the amount of fuel that can be prepared for combustion prior to ignition, and is known as the premixed combustion phase [1]. Usually following this is a phase of heat release that is lower in magnitude, but longer in duration. In this second phase, late-injected fuel that was unable to prepare prior to the onset of combustion finally ignites in the high temperature environment after it fully atomizes, vaporizes, and diffuses throughout the cylinder. This phase is controlled by diffusion and other mixing effects, and is known as the diffusion-dominated or mixing-controlled phase [1].

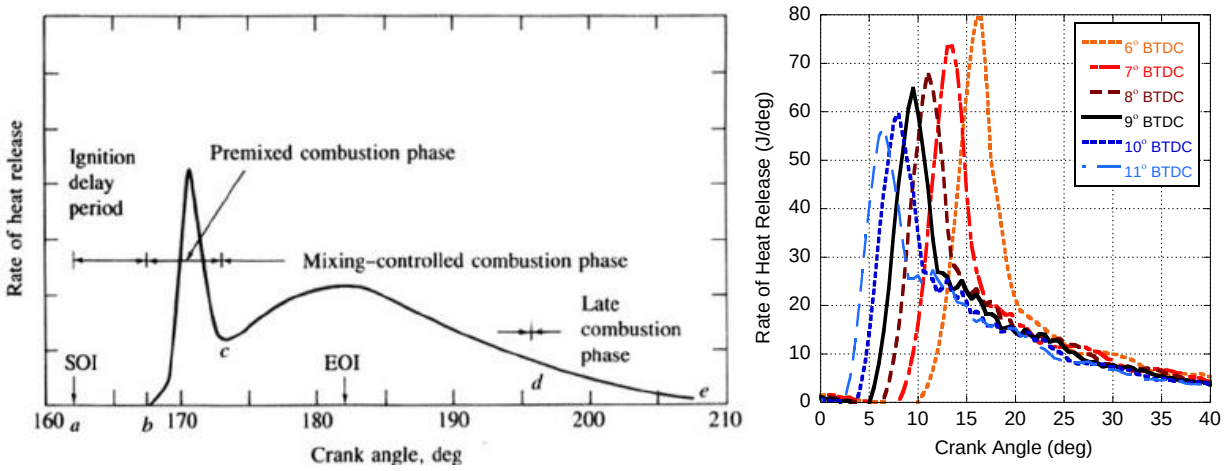

Figure 1. Examples of idealized and experimental engine-out RHR, displaying the premixed and diffusion-dominated combustion phases [1, 16].

From an efficiency-standpoint, the premixed phase is significantly more advantageous. The premixing of fuel leads to a high amount of heat release in a relatively short time frame, approaching the theoretical limit of constant volume heat addition. In addition, the timing of this heat addition is typically controlled (by adjusting the fuel injection timing) in order to allow for heat addition when the piston-cylinder has a combination of high in-cylinder pressure (which decreases as the piston moves further from Top Dead Center - TDC) and reasonable mechanical advantage between the crank and rocker arm (that increases as the piston moves further from TDC). Thus, adding as much energy to the premixed spike as possible leads to the most efficient CI combustion process, particularly if this spike occurs at the point of optimum combined thermodynamic and mechanical advantage known as the maximum brake torque (MBT) timing [1, 16]. However, heat addition in this manner leads to higher in-cylinder pressures and temperatures, straining the cylinder structure and requiring sturdier (and heavier) materials. In addition, the high temperature environment caused by this premixed spike, combined with the fact that a CI engine will almost always operated with significant excess oxygen, will lead to the formation of pollutants in the form of oxides of nitrogen (collectively, NO_x). Finally, CI engine knock (or ringing combustion) is generally tied to the amount of premixed combustion in the engine, and is characterized by high-frequency oscillation within the pressure trace caused by detonations of small pockets of fuel and air. This

may damage the piston or cylinder and is often one of the more undesirable facets of CI combustion perceived by a consumer.

By comparison, combustion in the diffusion-dominated phase is significantly less efficient. The prolonged heat addition in this phase does not serve to significantly raise cylinder pressures. In addition, this heat addition is late in the cycle, after the MBT point, and is often prolonged well into the expansion stroke of the engine [16]. As a result, while positive energy output from the engine is achieved, the net efficiency of the energy released in this phase is significantly lower than in the premixed phase. However, this carries some advantages. Given that this phase features lower pressures and temperatures, strain on the engine is significantly lessened, and these same lower temperatures also do not contribute to as much NO_x formation as the premixed phase. The diffusion phase also does not greatly contribute to the amount of ringing combustion, and may also serve to stifle CI knock from the premixed phase as the pressure oscillations caused by detonation of some of the fuel are swallowed up in the pressure waves generated by the more chaotic combustion of the diffusion phase.

Ultimately, diffusion dominated combustion is also largely unavoidable, particularly at high engine loads where the fuel injectors cannot physically deliver fuel fast enough for it all to prepare prior and combust in the premixed phase [1]. As a result, when increasing engine loads from idle, the in-cylinder pressure trace and calculated RHR will tend to indicate that the engine will gradually increase the amount of premixed combustion only. At a certain load, the amount of fuel combusted in the premixed spike will plateau, and all fuel added beyond this point will be combusted in the diffusion phase. Finally, as load increases further, the rising in-cylinder temperatures will lower the fuel ignition delay period, meaning the amount of fuel that the engine is able to prepare for the premixed phase will begin to decrease, leading to a decrease in the magnitude of the premixed phase as the diffusion phase grows further.

All of these individual aspects of engine combustion are visible through the 1st Law Model, and as a result it is possible to use the RHR to visualize and compare the thermodynamic performance differences across multiple operational modes, multiple fuels or fuel combinations, or even potentially

between engines. The 1st Law model shows what the engine was able to achieve during testing, and how much of the fuel's raw energy content was left unutilized. However, this paints a rather bleak picture, particularly given that the Rule of Thirds dictates that only 30-40% of fuel energy is generally utilized for work. For a clearer picture, it is necessary to include a sense of context into how much of that fuel energy can be realistically used, and how much of that unused energy is actually not available to be extracted as work, as an inevitable consequence of the type of power cycle being utilized. Given that the availability or unavailability of energy is within the sphere of the 2nd Law of Thermodynamics and the process of entropy generation, it is clear that a 2nd Law Analysis is required in order to provide this context.

With respect to engine diagnostics, the 2nd Law model is often passed over in favor of the simpler 1st Law RHR analysis. In compression ignition (CI) engines, this is at least partly due to the relative consistency of engine combustion, and the degree to which conventional diesel combustion is understood. However, different fuels will often result in changing engine performance, due to shifts in fuel properties [17, 18]. The most common example of this is in exchanging standard ultra-low sulfur diesel (ULSD) for biodiesel. The increased viscosity of biodiesel fuels generally inhibit fuel vaporization and atomization, while the higher cetane numbers and increased oxygen content result in a shortened ignition delay for biodiesel fuels [13, 19]. This, in turn, requires reoptimization of the engine's injection strategy in order to maintain peak efficiency [16]. While this reoptimization was difficult to achieve with older mechanical injection systems, the advent of electronic injection systems has made switching fuels without sacrificing efficiency a much more feasible prospect, as the engine can easily and quickly reprogrammed by flashing a new set of operational specifications to the engine control unit (ECU) [20].

This also opens up exploration of fuels with more divergent properties than biodiesel; so long as the operating characteristics for a given fuel are known, the engine can be quickly reoptimized. Included in this are alternative renewable or recycled fuels. For instance, the pyrolysis of waste plastic products can be used to create a liquid hydrocarbon fuel similar to petroleum diesel, due to the plastics being sourced from petroleum products [21-24]. This emphasis on renewability of fuels is not reserved for synthetic diesel fuels. For example, while biodiesel itself cannot generally be used in aircraft turbine engines, the

feedstock oils that are used to create biodiesel can alternatively be run through a hydrotreating process to produce a renewable analogue to jet fuel [7, 25-29].

Finally, electronic injection has opened up enough control over CI engine combustion to allow for advanced usage of gaseous fuels [6, 18, 30]. Normally, methane-rich fuels (such as compressed natural gas, or CNG) cannot be utilized directly in a CI engine alone without preheating the engine intake or raising the compression ratio, and which also poses a significant hazard from preignition and misfire [6, 31]. As an alternative, gaseous fuels can be used in a relatively unmodified CI engine through dual-fuel combustion, whereby fuel is added to the intake and ignited by a liquid fuel added through direct injection. While this generally comes at the cost of efficiency, the decreased cost of gaseous fuel means that the costs of fueling the engine are substantially reduced [6].

Dual-fuel combustion also presents the ability to reutilize waste products. For example, one byproduct of biodiesel manufacturing is glycerin, a hydrocarbon substance that (in its pure form) cannot be injected conventionally in an engine, due to its exceedingly high viscosity [32, 33]. Worse, the rise in biodiesel manufacturing has led to a glut of glycerin, and the need to store and dispose of this product is a significant impediment to the viability of biodiesel [33, 34]. However, glycerin may be partially oxidized in the presence of a catalyst to form a hydrogen-rich synthesis gas (syngas), which can then be utilized as fuel through dual-fuel combustion, turning a problematic waste product into a potential source of energy to feed the biodiesel production process [32].

However, all of these alternative fuels are subject to significant variation. Fuels derived from vegetable oils generally see high amounts of variation depending on the precise feedstock utilized [19, 25]. Similarly, waste plastic derived diesel is prone to variation based on the precise mixture of plastics used in the pyrolysis reaction, as well as the temperature and pressure of the reaction itself [21]. Syngas and biogas will be subject to both feedstock and production variances [32]. Even established products such as compressed natural gas will often vary between regions [6]. These inconsistencies in fuel constituencies and properties lead to difficulty in fuel studies, as engine researchers must utilize a model that is receptive to these changes.

To that end, this work explores the development and usage of a diagnostic 2nd Law model with respect to these various fueling modes. This demonstrates both the various effects of fuel properties on engine combustion, and showcases how the 2nd Law model is able to identify the phenomena associated with these properties. In particular, variations in fuel density, viscosity, cetane number, and energy content, and their effect on engine performance, are all observable through the lens of the 2nd Law model and in a way that goes beyond what is achievable with the 1st Law analysis alone.

1.4 Single-Cylinder Engine Instrumentation and Prior Work

Currently, research in CI engine combustion at the University of Kansas has been centered on the usage of a single-cylinder Yanmar L100V CI engine capable of 8.3 hp (6.2 kW) under continuous operation. This engine was formerly used in its originally packaged format, including an internal port for exhaust gas recirculation (EGR). Most importantly, this engine featured a cam-actuated mechanical fuel injection system, capable of injection at a constant (and uncontrolled) pressure of 19.8 MPa, and utilized a speed governor to maintain operation at 3600 revolutions per minute (RPM). This engine was eventually coupled with a Dyne Systems Alternating Current (AC) dynamometer, used to adjust the torque demand on the engine. This original setup was extremely restrictive in terms of how few facets of engine operation the researchers could actually alter, but was nonetheless instrumental in preliminary research into internal combustion engine operation at the University of Kansas.

Previous work was done to increase the amount of control over the Yanmar engine. To that end, the engine's speed governor and mechanical fuel injection system were removed entirely, in favor of a modern electronic high-pressure fuel system controlled by a Bosch MS15.1 ECU [35]. This allowed researchers to utilize the engine dynamometer to maintain engine speed, as opposed to torque, meaning independent adjustment of both the engine's speed (by varying the dynamometer speed setting) and engine torque (by varying the fuel flow rate at each injection event) was now possible, opening up the full operational range of the engine for experimentation. In addition, further upgrades and changes to this system included a blocking of the build-in EGR port in favor of an external system capable of providing

cooled EGR, and the addition of a separate system to allow for adding gaseous fuels to the engine intake. The test cell also features a full suite of emissions equipment in the form of an AVL Fourier Transform Infrared (FTIR) spectroscopy system, allowing for the monitoring of the lion's share of regulated emissions, as well as many unregulated emissions compounds, and an AVL Smoke Metering system for the capture and analysis of particulate matter (PM) emitted by the engine.

Of note, the Yanmar L100v is able to achieve reasonable repeatability between tests with the control fuel of ultra low-sulfur diesel (see Figure 2), particularly since 2014 when the in-cylinder pressure trace resolution was improved from 0.5 degrees of crank angle to 0.2 degrees. However, the engine is still subject to some uncontrollable phenomena that can affect repeatability of experiments. First and foremost are the test cell ambient conditions, particularly pressure, temperature, and humidity. As the test cell does not have active climate control systems, the engine is subject to large variance in seasonal weather conditions (in specific, summers with warmer and more humid air, and winters with colder and drier air). In addition, testing is generally abandoned in the event of heavy rain at any point in the year, entirely due to a significant divergence from the normal conditions of that season due to climbing humidity and lowered barometric pressures. In addition, the system is subject to variation in performance due to injector wear and tear, sometimes necessitating a swap of injectors (typically triggered by the injection system pressure diverging significantly from the normal 45-48 MPa operational range). Despite this, the KU single-cylinder test cell is able to achieve reasonable repeatability, with variation on the order of 1 bar or less in the measured pressure trace during the compression, ignition, and at the approximate end of combustion.

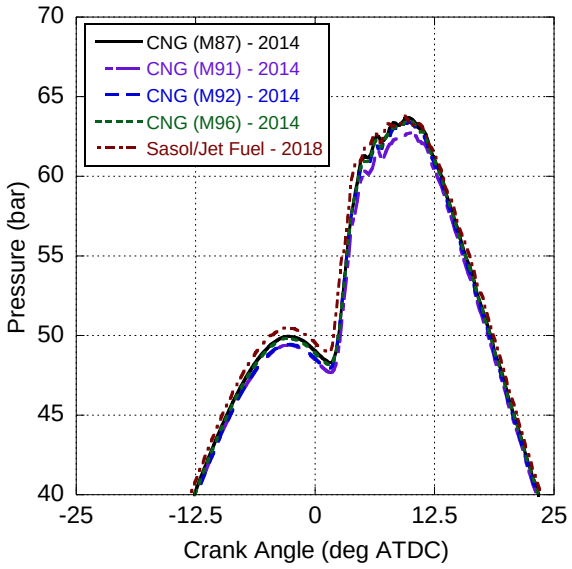

Figure 2. Measured pressure traces with ULSD control at 18.0 N-m over various tests on the Yanmar L100v Single-Cylinder Engine.

1.5 Motivation and Scope of Work

The primary scope of this research effort is to create a 2nd Law RHR model to calculate the net rate of change in availability liberated from fuel by combustion, and to utilize that model to study the changes in availability generation and destruction under a variety of engine operation modes. The creation of the model serves to revive and utilize a relatively unused aspect of engine thermodynamic modeling in a modern engine control environment [36, 37]. While the 2nd Law analysis for engine combustion diagnostics has existed for quite some time, the advantages of such an analysis were relatively low for traditional CI engine combustion. The far older 1st Law analysis, combined with the relatively static nature of CI engine operation, the extreme limitations of engine control systems, and less strict emissions control legislation, all resulted in traditional CI engine combustion being treated somewhat as a "solved problem."

In a modern context, however, engine combustion is no longer a simple affair. Current emission standards have mandated more thorough control over engine control systems, and the widespread adoption of these more advanced systems (most prominently, electronically-controlled high pressure

injection systems) has resulted in more control being given to the engineer and the ECU to provide on-the-fly adjustments to engine operation. Simultaneously, the rising interest in renewable/recycled fuels and dual-fuel operation, as well as the changes in combustion due to the different properties of these fuels, has further opened up the amount of variation a given ECU may encounter. Finally, CI engines have the potential to operate under more novel and unusual engine cycles, namely low temperature combustion (LTC) combustion regimes, and the relatively intense degrees of control needed to harness these novel cycles necessitates a thorough understanding of the underlying thermodynamics. As a result, avoiding usage of the 2nd Law model is no longer advisable, particularly when the "one size fits all" approach to calibrating engine operation from a single fuel in a single set of operational modes is no longer a realistic representation of what the engine will experience.

To that end, this document covers the development and usage of a 2nd Law model used to provide diagnostic modeling of in-cylinder engine processes. First, a number of updates and changes to the previously-constructed 1st Law model to allow for more novel fueling modes are discussed (particularly, dual fuel combustion) [11]. This document also details the usage of a pair of ancillary models used together to evaluate the intensity of combustion ringing and noise from the pressure trace, which form a useful supplement to the 1st and 2nd Law analyses. Next, the 2nd Law model is developed explicitly, and its immediate effects and usages on various fueling modes is explored. Finally, an overview of the unique strengths of the 2nd Law model are given, along with an algorithm utilizing the usage of the 2nd Law model for the identification of potential low-temperature combustion (LTC) regimes. Of note, the figures displayed within this document are the results of thermodynamic modeling, and are not raw experimental data unless otherwise specified.

Chapter II: Updated First Law Heat Release Analysis

Some material published as "Modified Heat Release Analysis for Diesel-Assisted CNG Combustion," SAE International, Technical Paper 2015-01-1744, April 14th, 2015

Some material published as "An Analysis of Dual-Fuel Combustion of Diesel with Compressed Natural Gas in a Single-Cylinder Engine," SAE International, Technical Paper 2018-01-0248, April 10th, 2018

2.1 Abstract

The growth of hydraulic fracking has resulted in a dramatic cost reduction of Compressed Natural Gas (CNG), a low carbon fuel. CNG cannot be used as singular fuel in conventional Compression Ignition (CI) engines because of the difficulties associated with controlling its auto-ignition characteristics. However, CNG-assisted diesel combustion represents a means to shift the energy consumption of CI engines away from liquid fossil fuels. Calculation of the rate of heat release is vital for understanding and optimizing this mode of engine operation. A previously constructed three-zone equilibrium heat release model that is calibrated to engine exhaust hydrocarbon measurements was augmented in order to allow for the addition of CNG in the engine intake. The model was also adapted to permit reuse of unburned CNG gas with other exhaust species via exhaust gas recirculation. This is because experiments demonstrated a potentially dramatic increase in methane emissions under high CNG flow rates. Specifically, the CNG mixture is modeled as a single lumped chemical species, and is held apart from the intake air within the model. Representative results are given for a high compression ratio single-cylinder CI engine with variable amounts of CNG addition, and the effects of engine phenomena on heat release modeling are discussed.

In addition, this work examines the differing engine emissions profiles with varying energy substitution ratios (*ESR*s), highlighting the potential for CNG usage to lower Particulate Matter (PM) emissions, while alternatively increasing or decreasing NO_x production through changes to in-cylinder temperatures and heat release rates. Dual-fuel combustion is noted for significant decreases in combustion efficiency, and a rise in emissions of methane and non-methane hydrocarbons, showcasing an increasing

likelihood of flame quenching from cooler in-cylinder temperatures. This lowered combustion efficiency also affects brake-specific engine efficiency, requiring slightly more fuel energy to be expended as *ESR* increases in comparison to operation with neat ULSD. However, this may be offset from an operational perspective due to the lowered costs of CNG as a fuel. Finally, there may exist the potential to achieve high thermal efficiencies just below peak engine operation for relatively large substitution rates of CNG without potentially increasing NO_x emissions over operation with neat ULSD.

2.2 Introduction

Vehicle energy consumption comprises a vital part of the economy of the United States (U.S.), particularly in over-the-road movement of heavy freight [38]. While petroleum-free alternatives have surfaced for other automotive power plants (e.g., vehicle electrification), this particular segment of the U.S. automotive fleet has proven more resistant to these potential solutions due to the need for an on-board power plant that contains a combination of high energy density, long range, and a high power output. Hence, this fleet is largely reliant on the compression ignition (CI) engine [1, 39]. However, through the recent boom in hydraulic fracturing within the North American energy industry, a potential alternative fuel source has arisen for CI engines in the form of methane-rich compressed natural gas (CNG), which can achieve parity in operation with ultra-low sulfur diesel (ULSD) in many aspects, in addition to being relatively economical [40].

At the same time, CNG presents a significant hurdle to operation in CI engines [31, 41, 42]. Methane is particularly resistant to autoignition, requiring CI engines fueled solely on CNG to undergo extensive modifications in order to combust the fuel, including higher compression ratios or heating of the engine intake [31]. In addition, utilizing CNG alone in a CI engine can present a significant hazard due to misfire or preignition of the methane fuel. In place of this, a more straightforward means to utilize CNG in a CI engine is through dual-fuel combustion. In this scenario, CNG (or any gaseous fuel) is added to the intake of a largely unmodified CI engine, and is subsequently ignited by the injection of a small amount of diesel as a pilot fuel that additionally serves as a means to add fuel energy to the cylinder [6].

Dual-fuel operation allows for a significant reduction in fuel costs, due to the plentiful nature of natural gas, and also provides for operation over a wide array of operating points that determine the relative ratio of diesel to CNG in the engine [6].

Fueling in a dual-fuel CI engine is commonly governed by the mass-based gas substitution rate. This ranges from lower amounts of CNG addition, where the diesel fuel shoulders most of the thermodynamic burden, to high substitution rates where CNG is supplying the lion's share of the energy and ULSD is primarily used to initiate combustion [6, 43]. Operation at these various substitution rates carries numerous potential benefits and drawbacks, with lower substitution rates being useful for achieving dual-fuel combustion without a costly engine retuning; whereas, higher CNG usage may be preferred to lower fuel costs as much as possible by utilizing as little ULSD as required. However, the latter option may require significant engine functional modifications to meet operational and emissions standards [6].

Prior work in dual-fuel combustion has shown that CNG usage will generally decrease in-cylinder temperatures and pressures [6, 9, 43-45]. In addition, utilization of CNG displaces air in the intake, leading to lowered volumetric efficiencies [6]. By achieving a relatively homogeneous fuel-air mixture, dual-fuel CNG combustion can be flame-front driven [46, 47]. However, given its relatively lean operation and cooler in-cylinder temperatures, CNG combustion has been shown to result in flame quenching, causing increased emission of partial combustion products while additionally lowering combustion and fuel conversion efficiencies [18, 30, 48]. Moreover, the combination of reduced temperatures and enhanced fuel-air mixing has been demonstrated to raise or lower the peak heat release rate, depending on the engine load and the amount of CNG utilized [6, 9, 49-52]. Furthermore, CNG combustion has been linked to alternatively lower or higher emissions of oxides of nitrogen (NO_x), depending on the relative degrees of cool combustion (decreasing NO_x) versus premixed combustion (increasing NO_x) [6, 43, 48, 53, 54]. In addition, particulate matter (PM) emissions nearly universally trend downwards with CNG usage, due to the fact that dual-fuel operation deliberately lowers the amount of liquid fuel entering the cylinder [48, 53].

With respect to high substitution ratios, usage of CNG has generally demonstrated the same overall trends at lower substitution rates; namely, an increase in unburned products of combustion, worsening fuel consumption, and decreasing PM emissions [55]. However, high substitution rates of CNG can reduce NO_x emissions in some situations [56-58]. This reaction occurs in spite of increasing exhaust gas temperatures that would normally be associated with higher amounts of NO_x emissions [56]. In particular, advancing diesel fuel injection timings lead to a shorter ignition delay period, resulting in less fuel being able to prepare prior to the onset of combustion. This then lowers the initial premixed rate of heat release, in turn reducing local temperatures around the fuel spray subsequently inhibiting the formation of NO_x emissions [30].

In order to understand the combustion processes of diesel-assisted CNG, the rate of heat release (RHR) from fuel combustion must be ascertained, either through predictive or diagnostic modeling [59]. In the case of diagnostic heat release (HR), equilibrium models are often used to calculate the total energy released by the combustion of fuel based on the measurement of in-cylinder characteristics (most notably pressure), with all modes of heat release serving to balance the 1st Law of Thermodynamics [11, 60]:

1st Law Rate of Heat Release	$\frac{dQ_{hr}}{d\theta} = \frac{dU_{cv}}{d\theta} + \frac{dW_{cv}}{d\theta} + \frac{dQ_{ht}}{d\theta} + \sum h \frac{dm_{cv}}{d\theta}$	(1)

where the engine output heat release (Q_{hr}) is given as a function of internal energy retained by the working fluid (U_{cv}), output work done by the engine (W_{cv}), heat transfer through the cylinder walls (Q_{ht}), and other means of mass transfer ($dm_{cv}/d\theta$) into or out of the cylinder (e.g., crevice flow, fuel injection, etc.). This understanding of fuel heat release is vital, particularly when linked to changes in engine operation and exhaust emissions, and as a means for characterizing the behavior and efficacy of combustion when using alternative fuels or combustion modes (see Figure 3) [61, 62].

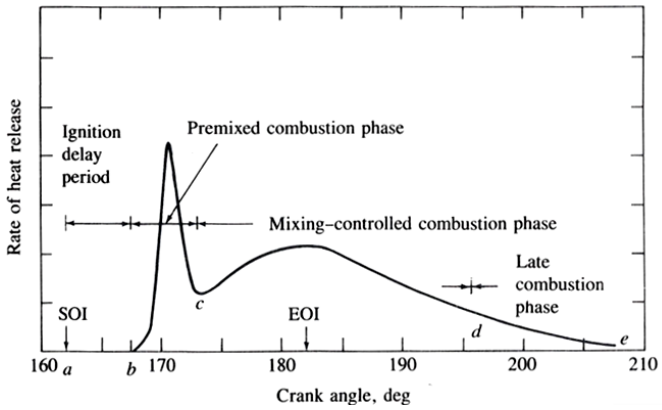

Figure 3: Example of Rate of Heat Release and combustion phases found in a Compression Ignition engine, from Heywood [60].

The HR model on which this work is based contains filtering necessary for removing combustion noise, and also allows the rate of combustion (and, therefore, the RHR) to be indirectly controlled by the measured changes in the pressure trace. Hence, no changes are necessary to account for these particular phenomena [11]. However, these same effects can present a challenge to HR modeling, and so their presence (or absence) within the experimental results is discussed later in this work. To that end, this work provides an update to a previously constructed HR model in order to illustrate how to adapt heat release models for intake CNG in dual-fuel engine operation [11]. This model utilizes a 1st Law of Thermodynamics analysis, and separates the engine cylinder into three zones; an unburned zone for intake air and EGR, a fuel zone for unburned CNG and vaporized fuel, and a burned zone for the products of combustion. The model employs the measured in-cylinder pressure trace to form the basis of its analysis, and is calibrated to the amount of unburned fuel exiting the engine as determined during experimentation.

Selected data is presented in this effort, along with a discussion of the efficacy of the model, dealing in the usage of CNG species of varying constituency (ranging from 87-96% methane content [6]). Of importance, this work includes testing at numerous CNG substitution rates, comprising low (0-18%), moderate (40-60%), and high (75-85%) *ESR*s, in order to achieve a comprehensive investigation on the various phenomena observed in each operational regime. Measured in-cylinder pressure, as well as the

calculated engine-out heat release rate, cylinder temperatures, brake performance parameters, and engine emissions are considered within this analysis [9, 13].

2.3 Model Updates

The general architecture of the original HR model was preserved within the new CNG-HR model [11]. This, in turn, shifted the majority of the changes needed for the updated model to the calculation of the governing chemical combustion reaction, as well as the subroutines responsible for mass transfer between the zones during combustion. For brevity, this work only dictates the necessary changes for dual-fuel operation, and does not detail the portions of the original model where changes are unneeded.

2.3.1 Fuel Chemistry and Evaluation

In the unmodified program, a lumped "global" chemical model is used to evaluate the process as a single chemical reaction, which is then used to populate the cylinder contents at the crank angle when the intake valve has closed (IVC). The original global chemical formula is as follows [11]:

Original Model Global Chemical Combustion Formula	$\xi(\mathrm{C}_w\mathrm{H}_x\mathrm{O}_y\mathrm{N}_z) + \delta(g_1\mathrm{O}_2 + g_2\mathrm{N}_2) + \varepsilon(g_3\mathrm{O}_2 + g_4\mathrm{CO}_2 + g_5\mathrm{H}_2\mathrm{O} + g_6\mathrm{N}_2) \rightarrow \lambda(g_3\mathrm{O}_2 + g_4\mathrm{CO}_2 + g_5\mathrm{H}_2\mathrm{O} + g_6\mathrm{N}_2) + \zeta\mathrm{C}_\mathrm{w}\mathrm{H}_\mathrm{x}\mathrm{O}_\mathrm{y}\mathrm{N}_\mathrm{z}$	(2)

where ξ and δ are the average amount (in moles) of fuel and air (respectively) present in each engine cycle, and ε is the percentage of the recycled gases from both residual and EGR species (respectively). Among the products, λ represents the moles of species either remaining after or produced from combustion, and ζ is the moles of hydrocarbon species remaining after combustion, expressed as a function of the measured amount of fuel used:

Moles of Hydrocarbon Species Surviving Combustion	$\zeta = (1 - \eta_c)\ \xi$	(3)

where η_c is the combustion efficiency of the combustion process, and which is measured experimentally. The coefficients g_1 and g_2 hold the percentages of molecular oxygen and nitrogen present in the intake air, while the coefficients g_3, g_4, g_5, and g_6 are molar amounts of each of the considered emissions species per

mole of emissions gases produced, and are used on both the left- and right-hand sides (for recycled and exhaust gases, respectively). Here, the liquid fuel is given on a carbon, hydrogen, oxygen, and nitrogen (CHON) basis, which *w*, *x*, *y*, and *z* representing the number of average number of each element within the liquid fuel molecules.

Note that Equation 2 only considers oxygen and nitrogen as being present in the intake, and uses the products of complete combustion in place of partial combustion species (such as carbon monoxide) or other species typically seen in the exhaust (i.e., nitrogen oxides or NO_x). Finally, the program treats emitted hydrocarbons as unburned fuel, rather than evaluating dissociated fuel atoms.

In the updated model, a number of changes are made to the overall function of the global model. First, the species of the CNG are represented by a second CHON-style formula (*a*, *b*, *c*, and *d*), held separate from the liquid fuel while being evaluated in much the same manner. Because of the possibility of unburned methane surviving combustion and remaining within the cylinder (or being forcibly reused through EGR), the coefficient used to specify the number of moles of gaseous fuel at the beginning of the cycle is made up of two separate terms. One term is for the total amount of CNG added through the intake, and a second is for additional gas added through EGR.

Updated Model Global Chemical Combustion Formula	$\xi_p\left(\mathrm{C_wH_xO_yN_z}\right)_p + (\xi_g + \zeta_g\varepsilon)(\mathrm{C_aH_bO_cN_d})_g$ $+\delta(g_1\mathrm{O_2} + g_2\mathrm{N_2} + g_3\mathrm{Ar})$ $+ \varepsilon(g_3\mathrm{Ar} + g_4\mathrm{O_2} + g_5\mathrm{CO_2} + g_6\mathrm{H_2O} + g_7\mathrm{N_2}) \rightarrow$ $\lambda(g_3\mathrm{Ar} + g_4\mathrm{O_2} + g_5\mathrm{CO_2} + g_6\mathrm{H_2O} + g_7\mathrm{N_2})$ $+\zeta_p\left(\mathrm{C_wH_xO_yN_z}\right)_p + \zeta_g(\mathrm{C_aH_bO_cN_d})_g$	(4)

where the fuel used is separated chemically into two species; the liquid pilot fuel (subscript p) used to initiate combustion, and the gaseous CNG (subscript g) used to provide a portion of the required engine load. The hydrocarbon species surviving combustion are likewise represented by the coefficients ζ_p (for the pilot) and ζ_g (for the CNG), and are both calculated in the same manner as Equation 2. The molar amount of CNG entering the cycle is composed of two terms: a term to account for the flow of fresh CNG entering the engine (ξ_g), and a term to allow for the reuse of CNG through EGR ($\zeta_g\varepsilon$). This second term

may be extended to reuse of vaporized fuel by EGR as well, but is assumed to be negligible and so is not included. Finally, an additional gaseous term is added in order to account for atmospheric argon (on the order of approximately 1% of intake air speciation) in order to increase the general accuracy of the underlying model.

For simplicity, it is assumed that the unburned CNG is identical to CNG added to the intake, in the same manner as liquid diesel fuel, and does not suffer from dissociation or partial combustion during the previous combustion cycle. In addition, the CNG is given a single "lumped" chemical formula (again in the CHON format) for simplicity, and so the model calculates the average number of each atom present per fuel molecule within the greater mixture.

In addition to the global combustion formula, a local formula exists to provide for the transformation of air and fuel to exhaust species through combustion. In the original model, this process was expressed as the following [11]:

Original Model Local Chemical Combustion Formula	$C_wH_xO_yN_z + l_1O_2 \rightarrow l_2CO_2 + l_3H_2O + l_4N_2$	(5)

where the coefficients l_1 through l_4 represent the moles of oxygen used, and moles of CO_2, H_2O, and N_2 produced (respectively), per mole of fuel burned. Using these coefficients, it is then possible to provide for mass transformation between zones as a function of the rate of fuel consumed at any given time. To expand this equation for the use of CNG, a second CHON term is added:

Updated Model Local Chemical Combustion Formula	$n_p(C_wH_xO_yN_z)_p + n_g(C_aH_bO_cN_d)_g + l_1O_2 \rightarrow$ $l_2CO_2 + l_3H_2O + l_4N_2$	(6)

where n_p and n_g are the molar percentages of the liquid pilot fuel and gaseous CNG (respectively) out of the total fuel used in the cycle, both measured through experimentation by the ratio flow rates of CNG and liquid fuel into the engine.

Of importance; the new model for dual-fuel combustion is used for all combustion models, even those that do not incorporate the usage of gaseous fuels. To reflect this, in the event that no gaseous fuel is

added to the cylinder, the gaseous fuel flow rate is simply set to zero within the model, and the global and local models are both simplified to their original form, albeit incorporating argon in the case of the global formula. While not tested, this same algorithm will work for gaseous-only fuel usage; simply setting the pilot fuel to zero will result in only gaseous fuel being used. However, for gaseous-fuel only usage it is suggested that the original model's ignition delay algorithms (which are calibrated for liquid fuels) not be utilized; instead, the model should rely on the 2nd derivative of the pressure trace to identify the start of combustion [1, 13].

The process of accounting for the effects of these differing species within the mixture is left to the portion of the model concerned with calculation of thermodynamic variables. The original program utilizes CHEMIKIN-III style coefficients for evaluation of the change in internal energy and enthalpy of the three zones, which are in turn used to iterate the model based on a 1st Law approach. This is done in addition to calculating other values, such as the adiabatic flame temperature. The equations that utilize the CHEMKIN-III coefficients are as follows [63]:

CHEMKIN-III Equation for Constant Pressure Molar Specific Heating Value	$\frac{\bar{c_p}}{R_{univ}} = a_1 + a_2T + a_3T^2 + a_4T^3 + a_5T^4$	(7)
CHEMKIN-III Equation for Molar Enthalpy	$\frac{\bar{h}}{TR_{univ}} = a_1 + \frac{a_2T}{2} + \frac{a_3T^2}{3} + \frac{a_4T^3}{4} + \frac{a_5T^4}{5} + \frac{a_6}{T}$	(8)
CHEMKIN-III Equation for Molar Entropy	$\frac{\bar{s}}{R_{univ}} = a_1\, ln\, T + a_2T + \frac{a_3T^2}{2} + \frac{a_4T^3}{3} + \frac{a_5T^4}{4} + a_7$	(9)

where $\bar{c}_p$, $\bar{h}$, and $\bar{s}$ are the molar constant pressure heating value, molar enthalpy, and molar entropy, R_{univ} is the universal gas constant, T is the temperature, and a_1 through a_7 are pre-determined coefficients unique to each gas. If all of the components of the CNG are assumed to be at the same temperature, the molar enthalpy, entropy, and heating values can be evaluated relatively easily. Using enthalpy as an example:

Gas Mixture Molar Enthalpy	$\frac{\bar{h}_{gas}}{TR_{univ}} = \frac{1}{TR_{univ}} \sum b_i \bar{h}_i$	(10)

where b_i is the fraction of a given species of the entire mixture, and $\bar{h}_i$ is the molar enthalpy of that given species. As a result, each of the coefficients on the right-hand side of Equation 10 can be broken up according to composition in order to attain a correct fit for the gas mixture:

Lumped Gas Coefficient	$a_j = \sum b_i \, a_i$	(11)

where a_i is any of the coefficients used for a given gas, and a_j is the resulting coefficient used for the CNG mixture. With these equations, the model can solve for the specific heating values of the CNG mixture, and by extension can evaluate the change in temperatures as a function of the change in speciation and pressure.

2.3.2 Combustion Cycle Evaluation

In the original HR model, the combustion cycle was solved through the evaluation of the components of the chosen equation of state. When assuming Ideal Gas behavior, the state equation is given as follows:

Ideal Gas State Equation	$pV = mRT = nR_{univ}T$	(12)

where p is the measured cylinder pressure, V is the volume, T is the temperature, and R and R_{univ} are the specific and universal gas constants for use on a mass (m) or molar (n) basis, respectively. At each step (corresponding to a fraction of crank angle degree), the components of the state equation are solved, both within the individual zones (where mass transfer is allowed to occur during combustion only), and on a cylinder-wide scale (where mass transfer is not permitted, except through injection of liquid fuel).

The solution procedure for each step is the same. First, pressure is known through the measured pressure trace taken during experimentation. Next, mass flux and change in speciation by combustion are solved, yielding the mass, moles, and gas constants. Finally, temperature is solved iteratively through a 1st Law balance, and the volumes of the individual zones are solved directly through the state equation. This process continues throughout the entire close portion of the engine cycle (i.e., IVC to Exhaust Valve Opening), and at the close of the cycle, the modeled mass fraction burned is compared to the experimental

mass fraction burned obtained through emissions analysis. The entire engine cycle is then iterated to convergence of the modeled and experimental mass fraction burned values.

Mass within each of the three zones was assumed to be constant, with two exceptions. The first was during the injection process, where fuel mass was simply added to the fuel zone at a rate defined by the following equation:

Rate of Liquid Fuel Mass Addition by Injection	$\frac{dm_{fa}}{d\theta} = C_d A_n n_h n_{inj} (2 \cdot \rho_f \cdot \Delta p)^{1/2}$	(13)

where A_n is the area of the nozzle holes, n_h is the number of holes per injector, n_{inj} is the number of injectors per cylinder, ρ_f is the density of the injected fuel, Δp is the pressure differential across the injector, and C_d is a coefficient of discharge for the nozzle (nominally set to 0.39). Upon injection, fuel is assumed to be vaporized instantly in order to simplify the zonal analysis.

The second exception to the constant mass assumption is during the combustion process. While mass on a cylinder-wide scale is held constant, the masses of each of the three zones experience entrainment as fuel and unburned air are brought together, combust, and are then moved to the burned zone. The rate of this mass flux is set by the coefficients of the local combustion formula (see Equation 6) and by the rate of fuel mass combusted as given by an Arrhenius-style formula [64, 65]:

Rate of Combustion of Fuel	$\frac{dm_{fb}}{d\theta} \approx K \cdot \rho_{cv}^2 \cdot y_f \cdot y_{O_2}^5 \cdot V_{cv} \cdot e^{-E_a/(R_{univ} \cdot T_{cv})}$	(14)

where the rate of fuel mass burned ($\underline{m_{fb}}$) is expressed as a function of the mass fractions of fuel (y_f) and oxygen (y_{O_2}) present within the cylinder, the volume (V_{cv}), temperature (T_{cv}), and density (ρ_{cv}) of the control volume, the Universal Gas Constant, and the bulk activation energy of fuel. In addition, the formula is calibrated during operation using the dimensionless value *K*. Of note, while the reaction rate equation can change for separate fuels, the overall reaction is both calibrated to engine emissions (discussed later), and is generally consistent between fuels even before recalibration is considered.

In the previous model, the ignition delay (τ) was calculated using a second Arrhenius expression [64, 66]:

Fuel Ignition Delay	$\tau = A \cdot 10^{-3} \left(\frac{p}{10^5}\right)^{-n_a} \cdot e^{E_a/(R_{univ} \cdot T_{cv})}$	(15)

where p is the pressure (in Pascals). This equation also utilizes a number of coefficients (A, n_a, and the activation energy E_a), which have been tabulated by other authors [65-71]. The model then may predict the onset of combustion by checking to establish that the following argument is true at a given timestep:

Fuel Ignition Delay Check	$\int_0^{\theta} \frac{1}{\tau} d\theta \geq 1$	(16)

Functionally, the program uses this expression at each data point to find when the ignition delay is reduced to a time period less than the time between successive data points, at which point the program begins combustion at the next timestep within the provided experimental data. Alternatively, the model can also find the onset of combustion by finding the peak value of the second derivative of the pressure trace with respect to time [72]. In either case, once combustion is begun (based on the 2nd derivative of the pressure trace), the rate and duration of combustion is left entirely to Equation 14, and becomes largely a function of the amount of fuel and unburned oxygen left in the cylinder, as well as the change in pressure as given by the experimental pressure trace (expressed through the terms for temperature, density, and volume).

The CNG-assisted diesel combustion mode of the model progresses in the same overall manner, with the following adjustments made to simulate the presence of the CNG. During normal operation, the fuel zone is held empty through the majority of the compression process (with the only addition being liquid fuel injected towards the end). Under the dual fuel operation, this zone is filled with CNG, which must then be compressed along with the other intake air gases. For the HR model, the CNG is added to the fuel zone, with the assumption that mass and constituency are held constant, and that proper mixing is achieved before the intake process, such that the temperatures of the CNG, intake air, and EGR are identical. At IVC, the temperature is given through measurement of the intake charge, and after IVC, the temperature is evaluated through the chosen equation of state.

At injection, the liquid fuel is added to the fuel zone. In addition to increasing the overall mass of the fuel zone, this causes a change in the constituency, requiring the model to re-evaluate the bulk molecular weight (W_f) and gas constant (R_f) of the mass contained within the fuel zone:

Bulk Fuel Molecular Weight	$\frac{1}{W_f} = \left[\frac{m_g}{W_g} + \frac{1}{W_p}\left(\frac{dm_{fa}}{d\theta} + m_p\right)\right] / m_f$	(17)
Bulk Fuel Gas Constant	$\frac{1}{R_f} = \left[\frac{m_g}{R_g} + \frac{1}{R_p}\left(\frac{dm_{fa}}{d\theta} + m_p\right)\right] / m_f$	(18)

where W is the molecular weight, R is the species' gas constant, and m_f is the total mass contained within the fuel zone at a given time. Note that the subscripts for the CNG and vaporized pilot fuel are g and p (respectively), and the portion of the equations concerned with the qualities of the pilot fuel include both the current mass of vaporized fuel and the change in mass due to injection.

As the Arrhenius-based correlations used by the model for ignition delay are based on empirical relationships for diesel operation only, they are not suitable as-is for CNG-assisted combustion. As a result, the CNG-assisted model disregards the ignition delay correlations, in favor of using the pressure trace-indicated onset of combustion.

After ignition, the mixture of CNG and fuel is burned at the rate set by Equations 13 and 14. Other than through additional fuel injection after ignition has already begun, the ratio of CNG to vaporized fuel is held constant, causing the molecular weight and specific heating value of the fuel zone to remain constant despite the overall loss in mass to the burned zone. As the combustion equation advances further and the total amount of fuel and oxygen is depleted, the equation slows dramatically. While further combustion reactions are not prohibited, the amount of mass flux and heat release by combustion in this late stage are functionally negligible (assuming no late-stage injection occurs).

2.3.3 Fuel Injection Artifact

Initially, the core heat release model (see Equation 1) incorporated five separate terms of heat release-related phenomena, representing the rates of fuel energy released by combustion, transferred as work, lost by heat transfer, retained by the working fluids, or changed due to mass transfer across the boundary. During the otherwise-closed portion of the engine cycle, there is one major source of mass

transfer across the boundary; fuel injection. This effect manifests as a positive amount of heat release in the form of energy being added to the in-cylinder environment prior to combustion (see Figure 4).

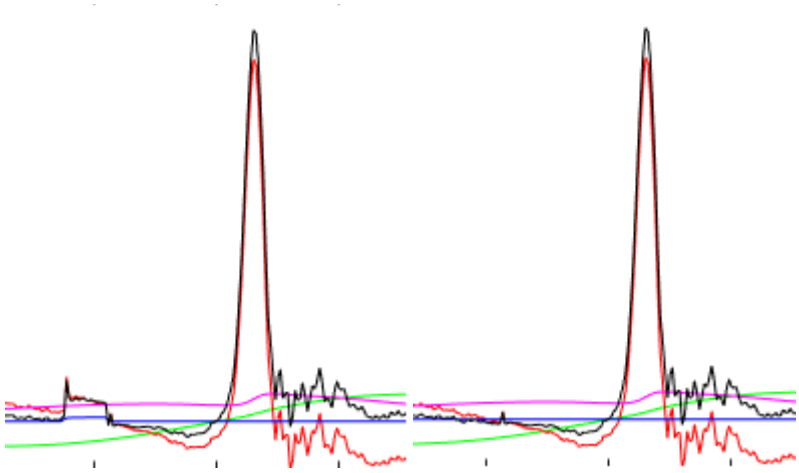

Figure 4: Example of Rate of Heat Release both with (left) and without (right) the injection artifact.

This artifact presents useful diagnostic information, particularly with respect to visually showing the onset and duration of the injection event. However, it comes with two net negatives. First, the artifact obscures the net decrease in in-cylinder energy content (when fuel mass is excluded) due to energy being transferred into the fuel in order to atomize and vaporize the fuel. Second, for very long injection events (more typical of low injection pressures, high engine loads, or high speeds) the injection event is lengthy enough to blend into the combustion event, obscuring the point of ignition normally visible within the rate of heat release.

As a result, it is useful to allow for the removal of the injection artifact from the rest of the heat release rate displayed by the heat release program. To facilitate this, the program's primary UI contains an option (see Figure 5) to communicate to the program whether or not the injection event should be ignored in the calculated heat release rate. When toggled on, the injection artifact is calculated normally. When toggled off, the injection artifact is deliberately removed from the heat release rate; the temperature and thermodynamic properties of the injected fuel is still calculated, but the thermal energy associated with injection and vaporization is not included in the final heat release rate, resulting in the artifact being removed altogether.

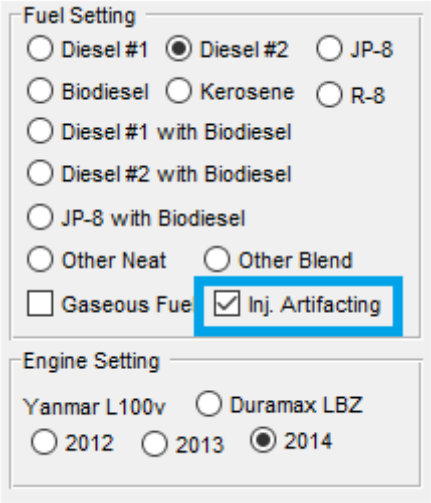

Figure 5: Heat Release UI Fuel Settings, highlighting the Injection Artifact toggle, currently set in the 'On' position to allow for the artifact to remain in the Heat Release Rate.

Note that the heat release model defaults the Injection Artifacting control set in the 'On' position. This is more useful to calibrate and test the stability of the heat release model prior to utilizing it to collect data, particularly to ensure that the model is correctly allowing for liquid fuel injection. Only after initial testing has been done should the Injection Artifacting control be turned off and the heat release data post-processed. The maximum net error associated with toggling the Injection Artifact 'Off" is on the order of 1% change in thermal efficiency, and only for minimal engine loads, and is decreased substantially for higher engine loads.

2.4 First Law Analysis of Dual Fuel Operation

Dual-fuel testing was performed using a Yanmar L100v single cylinder CI engine (see Table 1). For brevity, only information relevant to the dual-fuel experimentation is presented here, with a much more thorough documentation of the experimental setup available from previous work [73]. Most notably, the Yanmar's stock mechanical fuel injection system has been replaced with a modern high-pressure electronically controlled direct-injection system, controlled via a Bosch MS15.1 Diesel Electronic Control Unit (ECU) and Bosch ModasSport [73]. This system allows for variable injection timings at a resolution of 0.02 degrees of crank angle, used here to standardize combustion timing against typical operation with ULSD. Of note, this fuel system is pressurized by an externally powered fuel pump (Bosch CP3.2),

isolating the system from the engine's measured power output. Engine loading is monitored and controlled using an alternating current regenerative dynamometer by Dyne Systems, Inc. (with specifications shown in Table 2). Engine torque is measured with a FUTEK transducer (Model #TRS-705) installed between the output and input shafts of the engine and dynamometer, respectively. Finally, it is important to note that the Yanmar's stock exhaust gas recirculation system has been blocked in favor of a separate external system (not utilized here).

Table 1. Yanmar L100V Engine Specifications.

Displacement [cc]	435
Valve Number/Type	1 Intake, 1 Exhaust
Bore [mm]	86
Stroke [mm]	75
Connecting Rod Length [mm]	118
Crank Radius [mm]	38
Compression Ratio	21.2
Injection Timing	Variable
Injection Pressure	Variable, Maximum 200 MPa
Continuous Rated Output [kw]	3.4
Rated Speed [RPM]	3600
ULSD Heating Value [kJ/g]	42.8
ULSD Cetane Number	40
IVC [° ATDC]	-122
EVO [° ATDC]	144

Table 2. Dynamometer Specifications.

Model	Dymond Series 12
Rated Torque [N-m]	28.6
Rated Power [hp]	8.95
Speed Range [RPM]	0-7500
Voltage [V]	480
Phase	Three-Phase
Frequency [Hz]	60
Controller	DyneSystems Inter-Loc V OCS

The mass flow rate of the ULSD used is monitored by a Micro-Motion Coriolis flow meter (Model #CFM010M), and the mass flow rate of intake air (prior to the introduction of the gaseous fuel) are measured using a Merriam laminar flow element (Model #50MW20-2) and an Omega differential pressure transducer (Model #PX277-30D5V). The in-cylinder pressure trace is captured using a Kistler

pressure transducer (Model #6052C), alongside a Kistler encoder (Model #2614B) to link the pressure signals to corresponding crank angles [73]. The CNG used to achieve dual-fuel combustion is stored in gas cylinders and fed at 50 psig into a Brooks thermal mass flow controller (model #SLA5850), which both controls and monitors the flow rate of gaseous fuel. This fuel is fed into the engine intake through a mixing box, where the air-fuel mixture has sufficient time to become relatively homogeneous before entering the engine itself [6, 74]. Engine emissions are characterized using an AVL SESAM FTIR emission analyzer, including a Magnos 106 oxygen sensor. Soot emissions are monitored using a separate AVL Variable Sampling Smoke Meter (Model #415S), with soot measurements serving as a stand-in for PM.

The characteristics of the four CNG mixtures chosen for testing are shown in Table 3 [6]. Each of the four mixtures is dominated by methane gas at 87% (M87), 91.67% (M91), 92% (M92), and 96% (M96) of the total composition. Each mixture was selected in order to ensure a common volumetric energy density of 37.3 MJ/m3, and the range of methane composition was chosen in order to represent the common composition of typical CNG [6, 43]. Engine operation is monitored and categorized by the relative flow rates of the CNG mixtures with ULSD, based on an energy-basis equivalent of the more common gas substation rate, called the energy substitution rate, or *ESR* [6]:

Energy Substitution Ratio	$ESR = \frac{\dot{m}_g Q_{LHV_g}}{\dot{m}_g Q_{LHV_g} + \dot{m}_p Q_{LHV_p}}$	(19)

where ṁ is the mass flow rate, and QLHV is the lower heating value. The nominal *ESR* values for testing were 0%, 7.5%, 18%, and 40%, with the actual *ESR* values varying slightly during experimentation. Both *ESR* and gas flowrate were monitored and controlled through LabVIEW [75, 76]. The nominal setpoints for each of the tests were 0% (ULSD only), 7%, 18%, 40%, 50%, 60%, 75%, and 85%, with some variation in the actual setpoints for each of the mixtures. Normalization of combustion timing when needed (typically at or above 40% *ESR*) was accomplished by changing the injection timing of the ULSD pilot, in order to align the fired pressure trace of any given test with CNG to that of operation with ULSD

only. The ULSD injection setpoints were found previously in order to maximize engine efficiency during standard operation [16].

Table 3: CNG mixture specifications employed in a dual fuel manner [75].

Constituent/Property	ULSD	M87	M91	M92	M96
Methane	-	87.00%	91.67%	92.00%	96.00%
Ethane	-	5.10%	4.08%	3.50%	1.80%
Propane	-	1.50%	0.71%	0.80%	0.20%
Isobutane	-	0.29%	0.01%	0.15%	0.30%
Nitrogen	-	5.60%	1.00%	2.85%	1.30%
Carbon Dioxide	-	0.51%	2.53%	0.70%	0.40%
Density @ 20˚ C [kg/m^3]	837.58	0.755	0.725	0.723	0.698
Lower Heating Value [MJ/kg]	45.60	49.50	51.48	51.62	53.50
Constant Pressure Specific Heat [kJ/kg-K]	-	37.07	36.75	36.62	36.29
Ratio of Specific Heats	-	1.297	1.295	1.297	1.298
Cetane Number	40.0	-	-	-	-
Octane Number	-	73.1	85.0	85.1	96.1
Methane Number	-	49.5	49.6	49.8	50.0

Testing was accomplished at steady-state, defined when engine oil and exhaust temperatures changed by less than one percent over a 60 second period with a consistent room temperature of approximately 27 ℃ [6, 73]. In-cylinder pressure data are recorded over 60 consecutive thermodynamic cycles at a resolution of 0.2 degrees of crank angle. Engine performance data, particularly the flow rates of both gaseous and liquid fuels, are collected over a course of 120 seconds at a sampling rate of 20 Hz. Emissions readings were collected and catalogued at a rate of 1 Hz over 600 seconds, while multiple sets of soot emissions (at least two) were collected, with the sampling time adjusted as needed to ensure a smoke blackening number of approximately four, indicating a measurement in the ideal range of the smoke meter's measuring capabilities [73]. Engine operation was maintained at 1800 RPM for all tests, chosen to ensure the presence of both premixed and diffusion-dominated combustion phases at varying engine loads, based on prior observation with ULSD [16, 35]. Testing occurred at increments of 4.5 N-m (or 25% of the rated load of the Yanmar L100v) to a maximum of 18.0 N-m, in addition to operation at 0.5 N-m to provide an analogue for engine idling. For each set of tests, the engine was brought up to the desired load using ULSD only, at which point engine operation was catalogued. After this, dual-fuel

operation began by utilizing enough CNG to meet the desired *ESR*, and data were taken again. After achieving operation with all of the desired *ESR*s, the CNG flow rate was cut, the engine was loaded to the next desired output torque with ULSD only, and the process was repeated. After testing, the emissions, performance, and in-cylinder data were analyzed via MATLAB in order to calculate time-averaged test results and standard deviations. These values were then used to calibrate a single-zone heat release model to calculate the rate of heat release (RHR) and in-cylinder temperature, in addition to calculating ignition delays and equivalence ratios [13].

For brevity, the pressure traces, RHR figures, and temperature plots shown here are only taken from testing with the M92 CNG mixture as it is reasonably representative of the "average" of the four mixtures. The remaining data from the other three mixtures can be found in Appendix A. Furthermore, previous analysis has shown a lack of differentiation between the four mixtures inasmuch as can be seen from the pressure, temperature, and RHR behavior of the engine [43].

Figure 6 (Appendix A1-A5) shows the pressure traces for various *ESR*s using the M92 mixture at 0% (a), 25% (b), 50% (c), 75% (d), and 100% (e) of rated engine load, in addition to the maximum pressure rise rates (MPRR, f) for all fuels and *ESR*s. For lower engine loads, the addition of low to moderate amounts of CNG results in a relatively minor change in the in-cylinder pressure profile, with the most significant differences being in the lowering of pressure at top-dead center (TDC). This reduction in pressure is largely due to the effects of the changing constituency on the thermodynamic properties of the working fluid. Specifically, the increasing usage of CNG leads to a decrease in the ratio of specific heats away from air (1.4) and towards methane (see Table 3). However, at and above 40% *ESR*, the addition of CNG serves to also lower the peak combustion pressure, indicating the engine begins to struggle to combust high amounts of methane. This is also reflected in the MPRR for high *ESR*s and low loads.

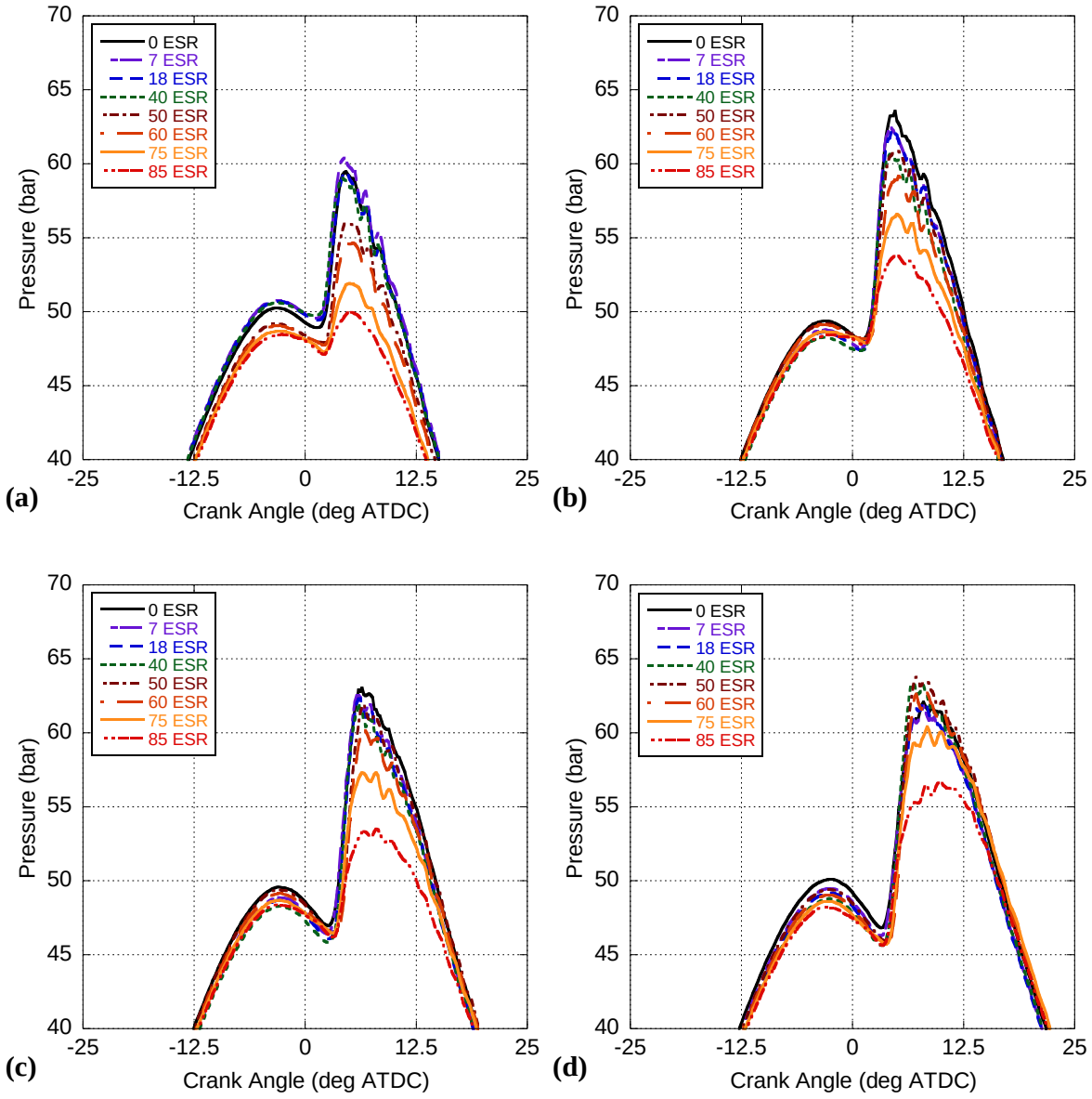
0 ESR
7 ESR
18 ESR
40 ESR
50 ESR
60 ESR
75 ESR
85 ESR
Pressure (bar)
Crank Angle (deg ATDC)
70
65
60
55
50
45
40
-25
-12.5
0
12.5
25
(a)
(b)
(c)
(d)

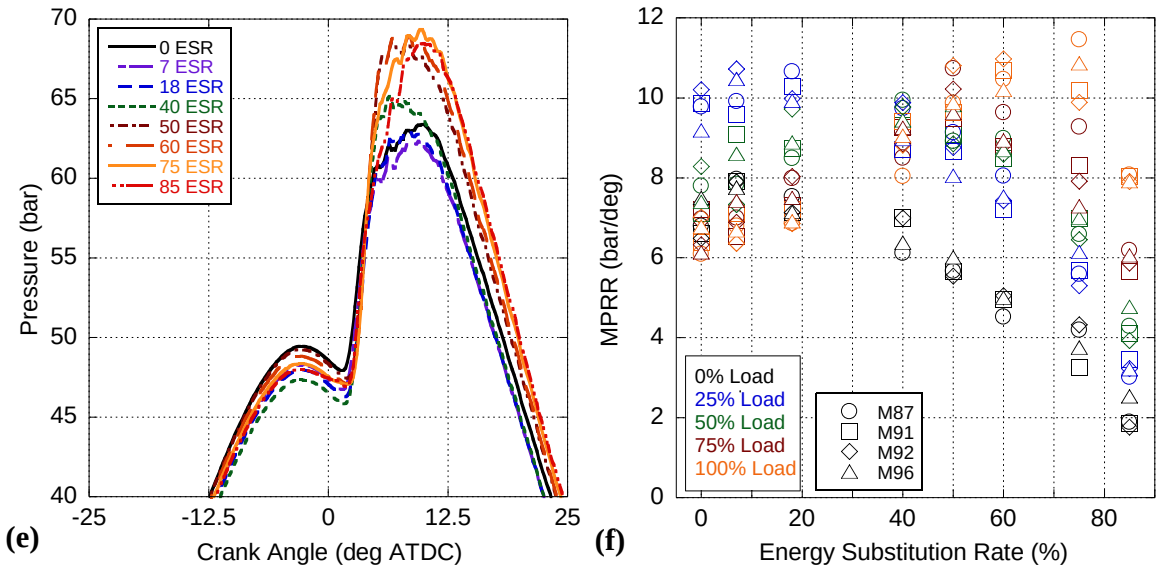

Figure 6. Average of measured in-cylinder pressure traces for M92 gas mixture at varying *ESR*s at 0% (a), 25% (b), 50% (c), 75% (d), and 100% (e) of rated engine load, as well as the MPRR for all fuels, *ESR*s, and loads (f).

At higher engine loads, the addition of low to moderate amounts of CNG again demonstrates a relatively small change in overall operation. However, as the *ESR* grows past 18%, the magnitude of peak pressure begins to climb significantly, and the timing of this peak pressure begins to approach TDC, with the more rapid pressure rise (see Figure 6c) revealing greater degrees of premixed combustion. This shifting in the pressure trace continues until 50% *ESR*, past which point the magnitude of peak cylinder pressure ceases to rise any further. Moreover, the timing of peak pressure begins to delay itself closer to the original timing found with ULSD, indicating a return to a combination of premixed and diffusion flame combustion, more similar to regular operation with ULSD, except at a relatively enhanced pressure. This slight growth in diffusion-based combustion for high *ESR*s is unexpected, given the relatively low amount of injected ULSD fuel that must be prepared prior to combustion (which is the usual source of diffusion-dominated combustion). This indicates a difficulty of the engine to combust high fractions of CNG across multiple engine loading conditions, and is further evidenced by the fact that, for maximum *ESR*, engine MPRR falls at 18.0 N-m, after previously rising steadily with increasing usage of CNG.

To understand this impediment in the engine's ability to combust high-*ESR* mixtures, the equivalence ratios for all fuels and engine loads are shown in Figure 7, showcasing the universal rise in equivalence ratio with added CNG usage. Across all loads, this growth in equivalence ratio is expected and is primarily linked to the CNG displacing air in the intake charge. However, for engine loads below 9.0 N-m, the equivalence ratio for operation with 75-85% *ESR*s often exceeds, or at least is roughly equivalent to, the equivalence ratio of the engine operating on ULSD at the next highest engine load tested. Furthermore, the change in engine equivalence ratio from 0% to 85% *ESR* is relatively large for lower engine loads, and this growth in equivalence ratio falls with added load.

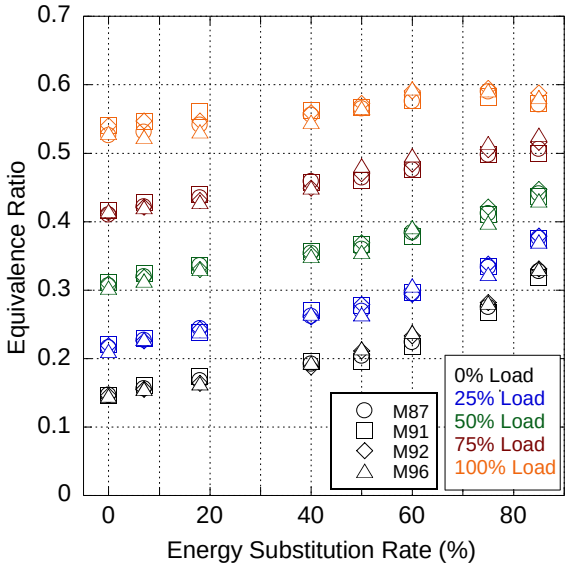

Figure 7. Engine equivalence ratios for all loads, *ESR*s, and CNG mixtures tested [6].

Above 9.0 N-m, the rise in equivalence ratio is substantially more subdued, although it still increases. This behavior suggests that the engine is having more difficulty in completely combusting the fuel mixtures as the engine leans more heavily on CNG in place of ULSD. In turn, this means that more CNG and ULSD must be added in order to make up for this inefficiency; hence, this raises the equivalence ratio even higher and further promotes inefficient combustion. However, there is still sufficient oxygen available within the cylinder at all loads. Therefore, the degradation in combustion seen at lower engine loads and high *ESR*s (Figure 1(a)) is not due to a lack of oxidant. Altogether, this signals that as *ESR* rises, the conditions in the cylinder make it more difficult for the ULSD pilot to ignite

completely the CNG-air mixture. Furthermore, this may illustrate that the mixture struggles to remain ignited and may quench away from the ULSD pilot. In addition, while this phenomenon becomes more subdued at greater engine loads, where enhanced temperatures counter the possibility of flame quenching, it remains problematic as indicated by the delaying of peak pressure timing.

The various timings for start of injection (SOI), as well as the calculated ignition delays (calculated with using the 2nd derivative of the pressure trace), are shown in Figure 8 [1]. Ignition delay generally shortens with rising engine load, due to a growth of in-cylinder temperatures. Usage of CNG has been shown to generally lengthen ignition delay, related to the high octane number of the various mixtures and the resistance of CNG to autoignition [6, 56]. As a result, raising the *ESR* serves to lengthen the ignition delay of the injected fuel, subsequently requiring the injection timing of the fuel pilot to be advanced for higher *ESR*s in order to ensure combustion occurs at the optimum time. Of note, CNG substitution at or below 18% *ESR* leads to essentially no change in ignition delay (and no need to change injection timing), and even moderate substitution up to 50-60% *ESR* leads to relatively small changes in ignition delay. However, for CNG substitution above 60% *ESR*, the injection timing necessary for optimum operation diverges significantly from that of standard operation with ULSD; hence, operation with higher *ESR*s necessitates retuning of the engine, and a gradual shift in SOI towards earlier injection.

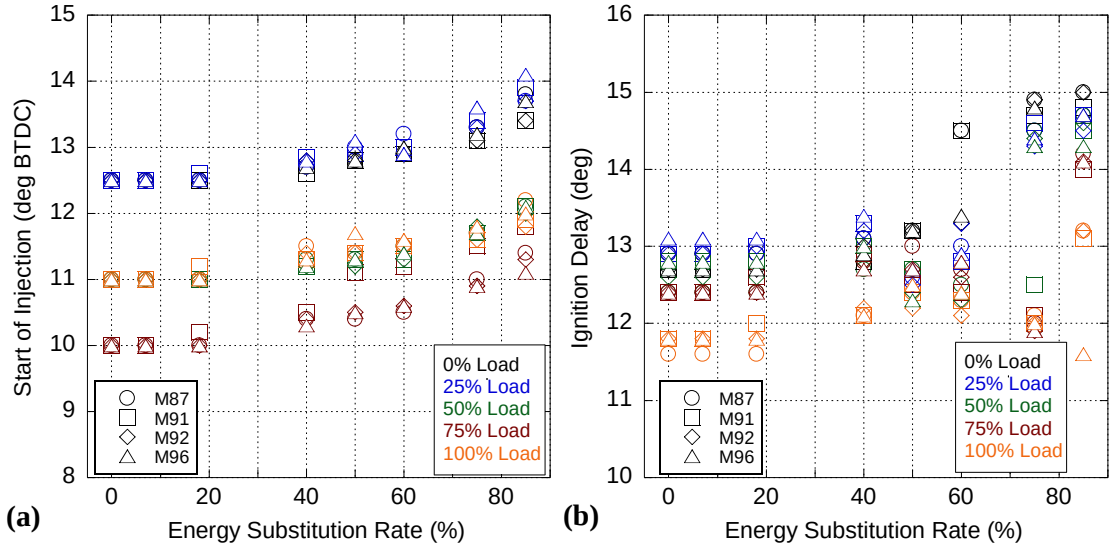

Figure 8. Engine measured injection timing (a) and ignition delay (b) (in crank angle degrees) for all loads, *ESR*s, and CNG mixtures tested.

The RHR for various *ESR*s are given in Figure 9 (Appendix A6-A10) for operation at 0% (a), 25% (b), 50% (c), 75% (d), and 100% (e) of rated load, along with the timings of CA50 for all fuels, *ESR*s, and loads (c). For lower engine loads, the same trends seen in the pressure trace are broadly repeated here. In specific, CNG usage brings about a consistent growth of premixed combustion up to 50% *ESR*, with peak RHR found for mixtures of around 40% *ESR*. Prior research has found that this engine achieves largely premixed combustion with ULSD up through 9.0 N-m. As a result, the small rise in the premixed spike relative to ULSD is not surprising. In particular, the engine is already operating in a relatively thermally efficient manner and the addition of CNG does not significantly affect this outcome.

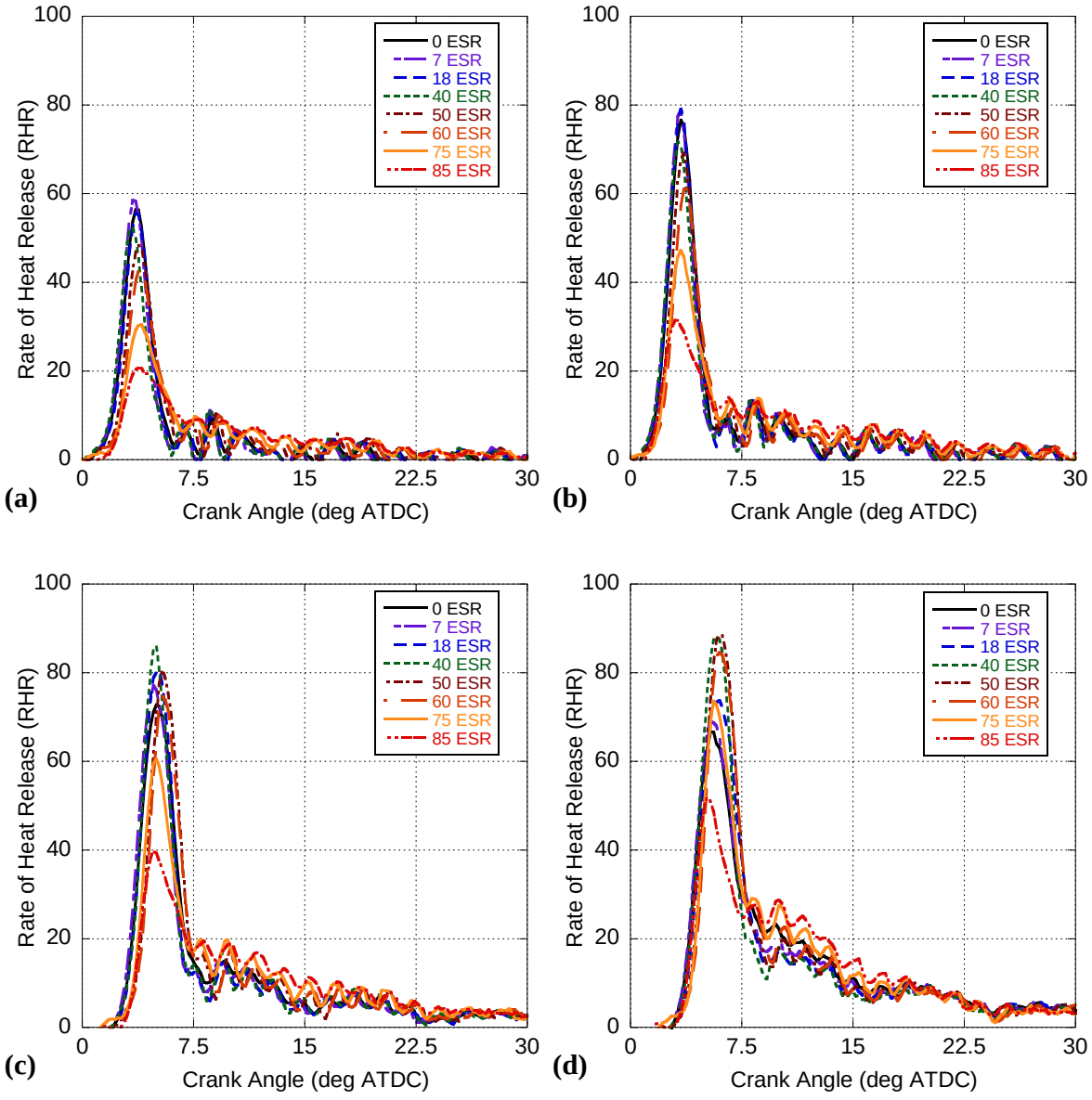

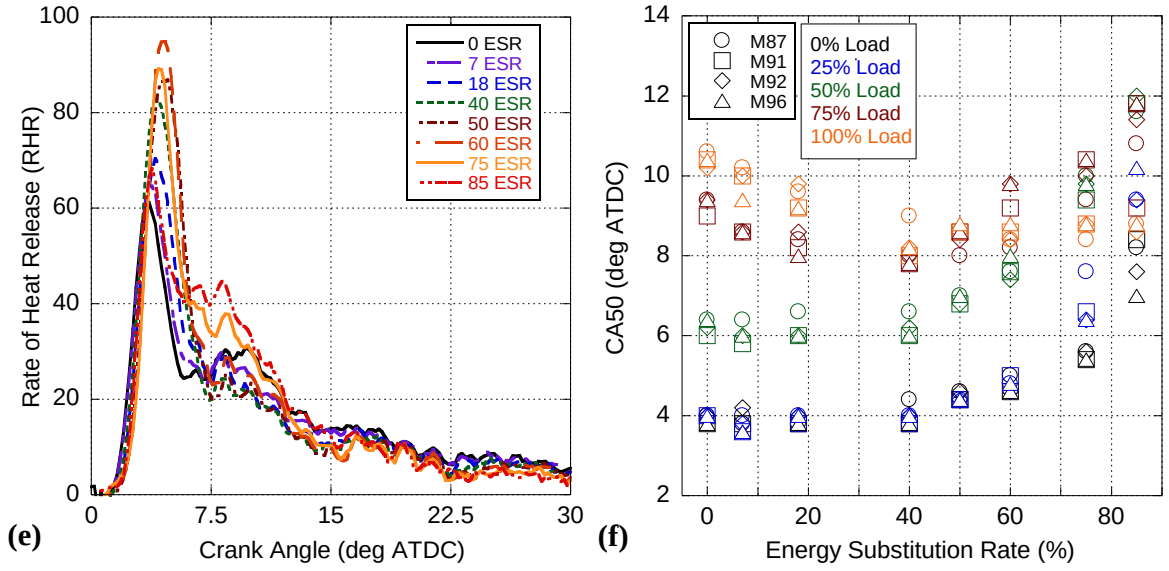

Figure 9. Calculated RHR for M92 gas mixture at varying *ESR*s at 0% (a), 25% (b), 50% (c), 75% (d), and 100% (e) of rated engine load, as well as the CA50 timing for all fuels, *ESR*s, and loads (f).

However, beyond this intermediate *ESR* range the peak RHR falls dramatically. This again highlights the added difficulties in combusting relatively large amounts of CNG, such that at 9.0 N-m the peak RHR for operation at 85% *ESR* is around half of that for operation in between 18 and 50% *ESR*. In addition, as *ESR* increases, the RHR profiles seem to indicate a rise in later-stage heat release (particularly beyond 7.5˚ after TDC), normally indicative of diffusion dominated combustion. This diffusion burn comes in spite of the fact that most of the fuel has no need to atomize or vaporize; i.e., 75% or more of the fuel energy is entering the engine in a gaseous state. Furthermore, increasing *ESR* leads to lowered ULSD usage, meaning higher *ESR*s will have more optimal atomization of the injected liquid fuel. Here, it is possible that flame quenching inhibits complete combustion of the fuel-air charge. Moreover, this may indicate that a significant amount of the CNG remaining (particularly methane) cannot survive the high-temperature environment and at least partially combusts, even after the combustion event has largely ceased.

At higher loads, added CNG usage results in combustion behavior being generally closer to what is expected from a gaseous fuel. As *ESR* rises, peak RHR also increases, and diffusion-dominated combustion is mitigated because more fuel prepares and burns in the premixed phase. However, for high

*ESR*s the RHR begins to experience more post-premixed combustion above that of ULSD, before falling below the diffusion combustion phase of ULSD (beyond 10˚ after TDC) while subsequently becoming more similar to the other *ESR*s. Finally, at 85% *ESR* the engine struggles to operate and the peak RHR recedes to a level more comparable to (but still greater than) operation with ULSD. In addition, operation at 85% *ESR* experiences the highest amount of initial diffusion burn, although this is largely mitigated beyond 10˚ after TDC.

Next, the cylinder-averaged temperature profiles for the M92 mixture are presented in Figure 10 (Appendix A11-A15), again at 0% (a), 25% (b), 50% (c), 75% (d), and 100% (e) of rated load. Similar to previous results, low-to-moderate usage of CNG encounters a temperature profile that is not too dissimilar from combustion with ULSD. In particular, at low and middling engine loads both peak cylinder and later expansion temperatures follow the same path as operation with ULSD, respectively. However, for high CNG substitution and moderate engine loads, peak cylinder temperatures are generally lower while being delayed further from TDC. This again highlights the difficulties in combusting relatively large amounts of CNG, and implies that a significant amount of flame quenching may be taking place. In addition, temperatures during expansion generally rise with added CNG usage, in keeping with the growth in combustion levels seen after the premixed spike at these loads.

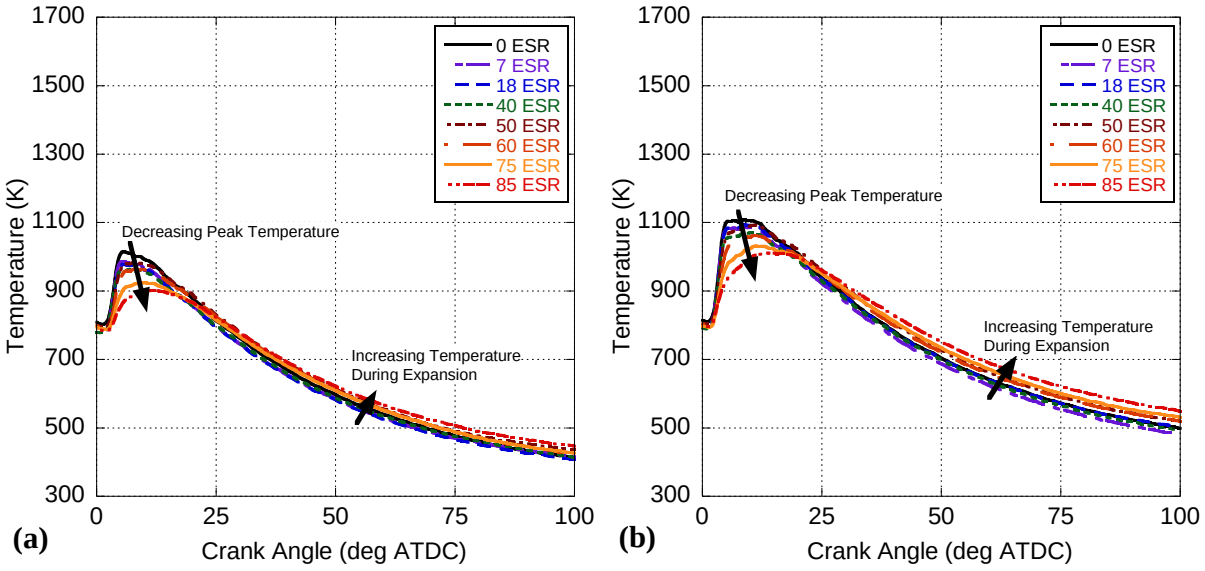

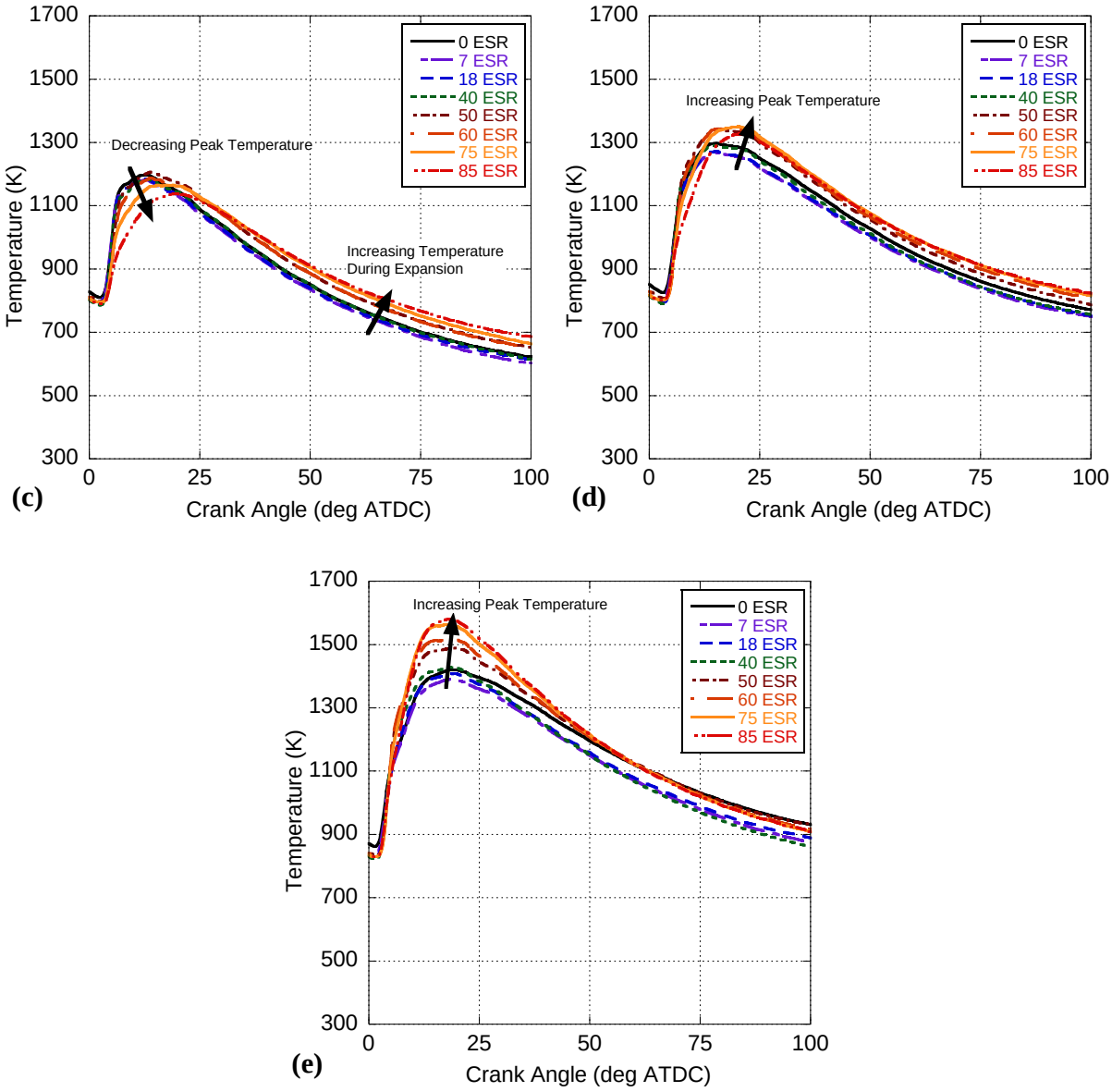

Figure 10. Calculated temperature profile for M92 gas mixture at varying *ESR*s at 0% (a), 25% (b), 50% (c), 75% (d), and 100% (e) of rated engine load.

For 13.5 to 18.0 N-m, operation with moderate amounts of CNG generally leads to similar (although possibly slightly cooler) combustion to ULSD only, both in terms of peak and expansion temperatures. However, as more CNG is used, peak cylinder temperatures not only rise to meet operation with ULSD, but also significantly exceed it due to more CNG being consumed in the premixed spike or immediately afterwards. Furthermore, moderate-to-high CNG usage results in significantly hotter cylinder temperatures during piston expansion until around 40-50˚ after TDC. Around this crank angle range, the

relatively greater amount of diffusion burn encountered in the ULSD only tests begins to heat the working fluid to the same level as the CNG tests. Moreover, the high *ESR* tests promote greater rates of initial heat transfer (albeit over a relatively short period); hence, a later heat release (ULSD only) will put more energy into the working fluid rather than lost to the ambient through the cylinder walls.

Altogether, the pressure, RHR, and temperature results suggest that for moderate *ESR*s (and greater loads) CNG usage will result in a greater premixed combustion event; thus, faster overall combustion. However, utilizing CNG at lower loads or at higher *ESR* levels can result in less idealized combustion likely resulting in a significant amount of combustible species surviving until the exhaust blowdown event. In addition, it appears that nearly all scenarios utilizing CNG will result in varying levels of flame quenching throughout the cylinder. In order to highlight these facets further, the measured hydrocarbon (HC) emissions of the engine are shown in Figure 11 via methane (a) and non-methane (b) hydrocarbons (NMHC). Unsurprisingly, all HC emissions grow significantly with CNG usage. For low *ESR*s, emissions of methane grow significantly; however, this growth largely tapers off for moderate substitution of CNG. Furthermore, the rate of growth in methane emissions past 40% *ESR* falls as a function of engine load, such that at 18.0 N-m methane emissions are relatively flat. At the highest *ESR*s, a slight increase in methane emissions is seen as the engine struggles to combust all of the methane present in the cylinder.

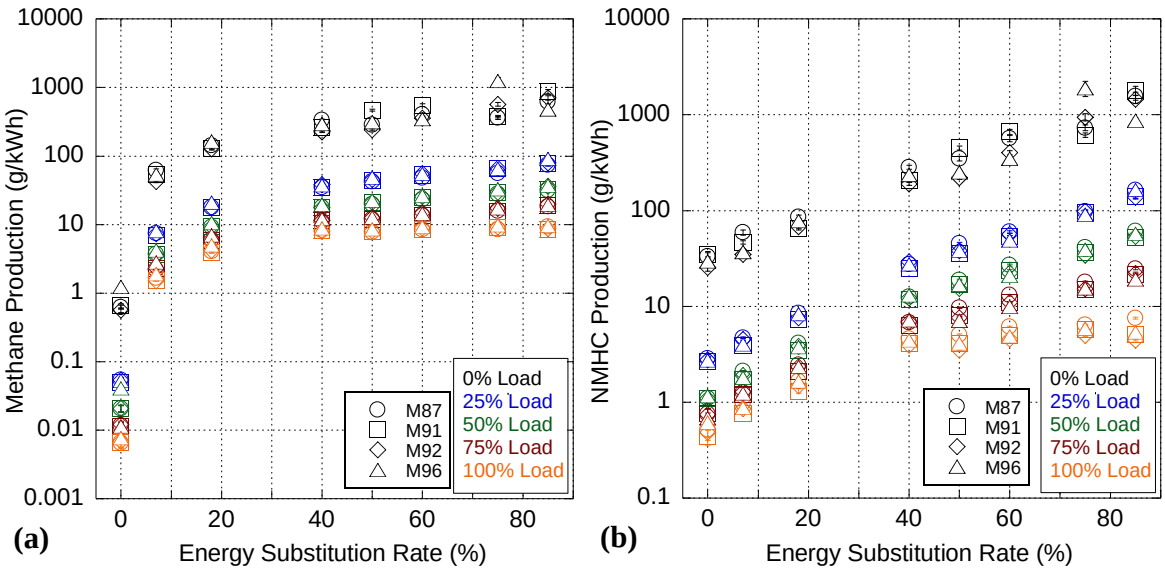

Figure 11. Brake specific methane (a) and non-methane (b) hydrocarbon emissions for all *ESR*s, mixtures, and engine loads.

Across all *ESR*s, the growth of NMHC emissions is relatively consistent with respect to engine load. However, this intensification is slightly less pronounced for the highest *ESR*s, as the relatively hotter temperature environment appears to consume some HC species prior to exhaustion. Further sources of HC emissions could be due to a greater flow of CNG into the crevices of the combustion chamber or past the piston, only to be released back into the working fluid during expansion at lower temperatures and eventually exhausted to the atmosphere. In addition, while oxygen starvation is likely not widespread throughout the cylinder, the lowered amount of oxygen present with heightened *ESR* may promote flame quenching and partial combustion of the fuel. Finally, the relatively significant amount of emitted HCs at lower loads (particularly idle) highlights a shortcoming of the dual-fuel system, in that temperatures are not sufficient to fully combust the natural gas present in the cylinder. As a result, dual-fuel combustion is particularly advantageous when operating at greater engine loads, where elevated combustion temperatures promote more premixed (and complete) combustion, as well more thorough combustion of methane that survives the premixed combustion event.

Engine-out soot emissions are shown in Figure 12 and appears to be the most straightforward of all of the various emissions species to characterize since soot is a direct result of the efficacy of liquid fuel

atomization. Across all engine loads, utilization of CNG will result in a decreased reliance on the liquid fuel pilot. As a result, raising *ESR*s lowers the amount of liquid fuel that can form soot; hence, CNG usage causes soot emissions to fall outright. Similarly, for any given *ESR*, soot emissions rise as a function of engine load (other than idle) due to a raised amount of liquid fuel that must be injected into the cylinder in order to meet the overall energy demand of the engine at that particular load.

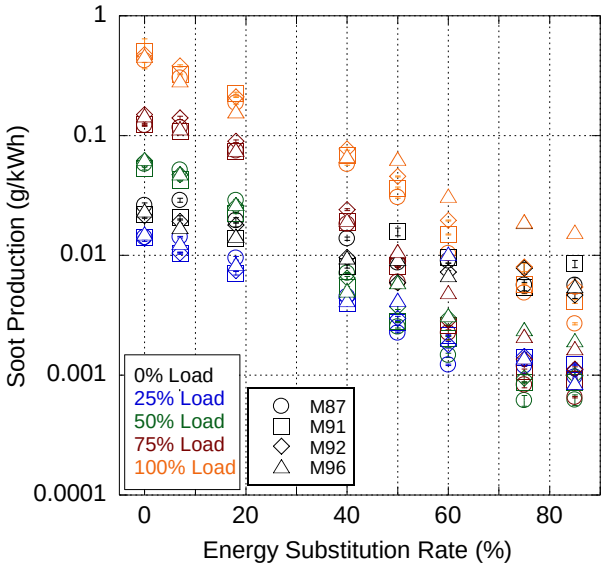

Figure 12. Brake specific soot emissions for all *ESR*s, mixtures, and engine loads.

Figure 13 details NO_x emissions, decoupled into NO (a) and NO_2 (b), respectively. In contrast to soot, emissions of NO are relatively more complicated with complex relationships between engine load and *ESR*. For low amounts of CNG substitution, NO emissions slightly decrease for all but the highest engine loads, as the lowered engine temperatures associated with CNG usage leads to reduced thermal NO kinetics. However, there is an increased likelihood of prompt NO formation due to the larger number of CH radicals present in the cylinder with added CNG. The overall trend may be explained by a greater prevalence of lower local cylinder temperatures, particularly closer to the cylinder walls, subsequently indicating that quenching of the flame front (where NO forms) may be occurring and halting flame propagation [6, 77-79].

However, as *ESR* rises past 40%, NO emissions largely split into three trends. For engine loads at or below 9.0 N-m, the experiments indicate a significant fall in NO emissions with added CNG. In

contrast, operation at 18.0 N-m results in a relatively steady NO emission rate, climbing slightly as a function of *ESR*. Finally, operation between 9.0 and 18.0 N-m splits the gulf with a net decrease in NO emissions as *ESR* grows, but not at the same rate as the lower engine loads. In the case of low loads and high *ESR*s, large degrees of flame quenching, lower overall temperatures, and a relative decrease in available oxygen and nitrogen (i.e., air is displaced by CNG) needed to form NO all play a role in keeping NO emissions lower than standard operation with ULSD, even at 50% of rated load.

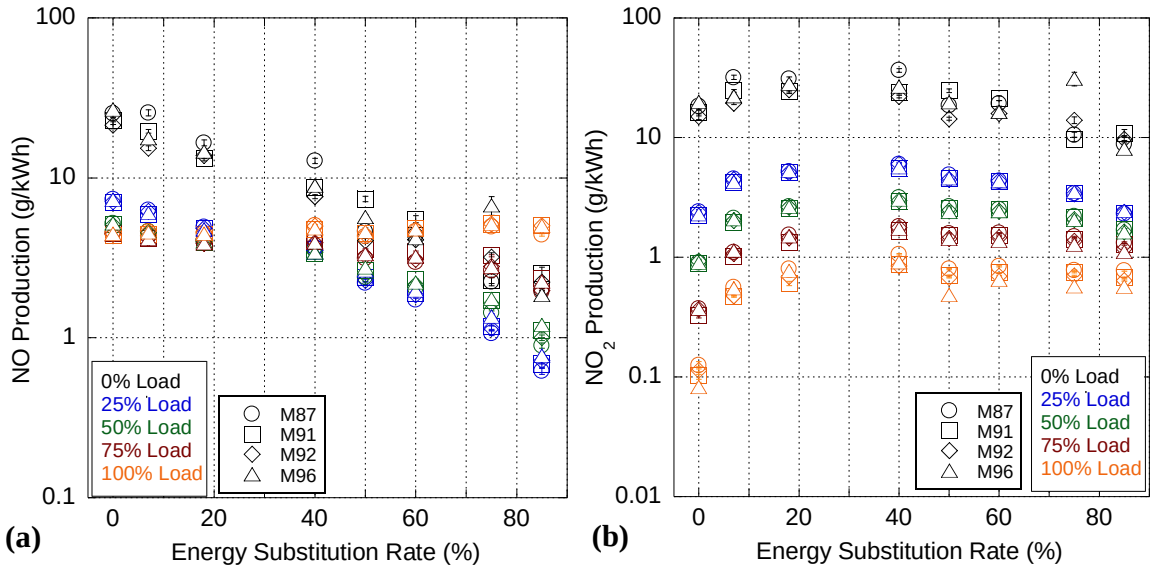

Figure 13. Brake specific NO (a) and NO_2 (b) emissions for all *ESR*s, mixtures, and engine loads.

As engine load increases, less inhibition of flame propagation takes place, but temperatures may still be slightly too low for substantial flame-based combustion. Hence, while global equivalence ratios (Figure 7) may favor NO emissions, only the region immediately around the ignition source may see temperatures significantly high enough for NO formation. However, this ignition source is the liquid fuel spray that is in a region significantly more fuel-rich than the rest of the cylinder. This region becomes smaller as more CNG is utilized and the flame front (potentially) quenches faster. Furthermore, this region becomes richer as *ESR* rises thanks to the large amount of CNG available globally throughout the cylinder. As a result, the only region where NO has suitable temperatures to form may not have the prerequisite nitrogen and oxygen. In contrast, the combinations of high loads with large *ESR*s may expand the regions of high temperatures enough to promote the right conditions for NO formation. Nevertheless,

at 18.0 N-m and high *ESR*s, the peak rate of heat release appears shift forward and a shorter ignition delay may be seen (Figure 8b does not illustrate a definitive trend). As a result, the premixed spike may decrease resulting in reduced NO formation during this phase. Overall, seeing lower NO emissions at 13.5 N-m and 75-85% *ESR* illustrates that it may be possible to achieve significant (if not peak) engine loads without increasing NO emissions in comparison to operation with ULSD.

In contrast, NO_2 emissions are relatively more consistent, with a universal fall in NO_2 as a function of engine load for all *ESR*s. This is largely because of the rise in cylinder temperatures as load increases. NO_2 is typically formed in the periphery of the cylinder and away from fuel spray as it requires relatively rapid cooling in order to maintain itself. Instead, in the high temperature environment, NO_2 will decompose back into NO; thus, regardless of *ESR*, rising engine loads will dissuade NO_2 production [80].

With usage of CNG, NO_2 emissions climb for low-to-moderate *ESR*s. Here, the promotion of flame quenching by CNG usage allows more NO_2 to cool quickly and maintain itself rather than become NO; hence, emissions of NO_2 increase alongside *ESR* [6]. For moderate *ESR* ranges, however, NO_2 formation begins to generally fall away. At lower engine loads, this is largely related to the similar decrease in NO emissions; lower temperatures begin to dissuade all NO_x formation. Whereas, at high loads this is again due to high temperatures prompting NO emissions at the direct expense of NO_2. Both of these trends continue as *ESR* rises to the high-substitution range, where flame quenching and lower local temperatures continue to impede all NO_x formation except at the highest engine loads.

Of note, while NO and NO_2 emissions both fluctuate over varying *ESR*s, emissions of each species at 18.0 N-m and moderate-to-high *ESR*s are relatively consistent. In this scenario, increased CNG usage can result in a significant rise in temperature that appears to promote the formation of NO_x and NO from NO_2 by thermal decomposition. However, this same CNG induces more flame quenching, promoting the existence of cooler areas in the periphery of the cylinder where NO_2 can form more readily. For full load, it would appear that these two aspects of NO_x formation are relatively balanced against each other; hence, NO and NO_2 emissions are relatively constant above 40% *ESR* (see Figure 14).

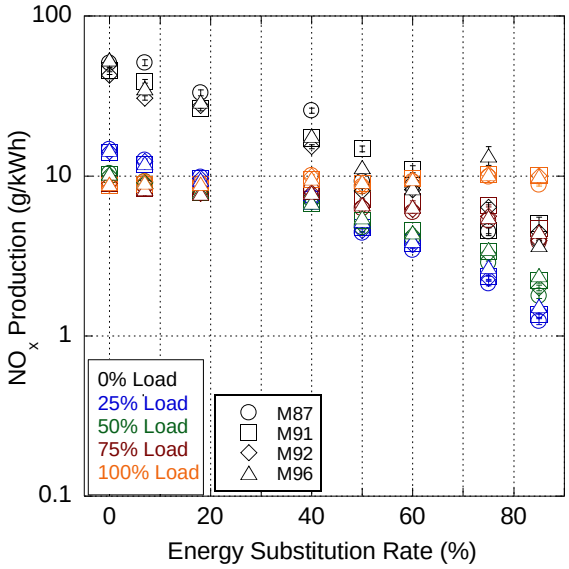

Figure 14. Brake specific NO_x emissions for all *ESR*s, mixtures, and engine loads.

Figure 15 showcases combustion (a) and thermal (b) efficiencies of the engine for all loads, mixtures, and *ESR*s. As implied by the HC emissions, combustion efficiency (almost) universally falls with higher *ESR*s, as the amount of unburned fuel in the exhaust grows. This effect is due to the greater likelihood of flame quenching as a function of *ESR*, as the relatively high stability and activation energy of methane serves to inhibit flame propagation, particularly in the periphery of the engine cylinder.

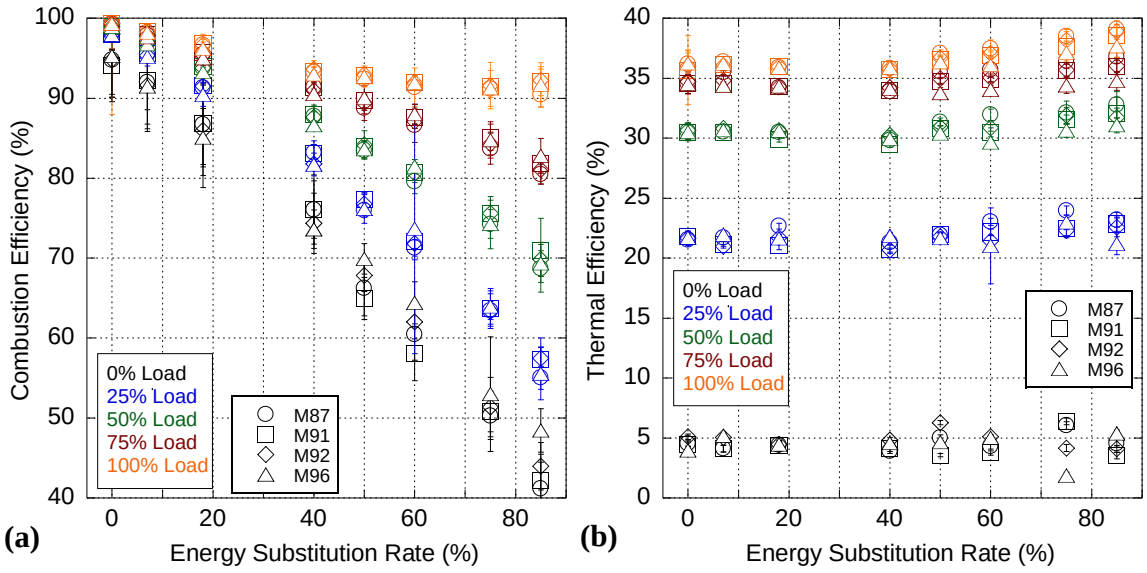

Figure 15. Measured combustion (a) and calculated thermal (b) efficiencies for all *ESR*s, mixtures, and engine loads.

Furthermore, increasing engine load serves to keep combustion efficiency relatively high by raising local temperatures. Thus, combustion efficiency increases with engine load and is able to exceed 90% at peak engine load even for the greatest *ESR*s. Interestingly, in spite of the decreasing general efficacy of the engine combustion process as a function of *ESR*, these augmented temperatures promote (mostly) higher thermal efficiencies. Here, it is important to recall that thermal efficiency measures the engine's usage of thermal energy actually added to the cylinder, and not the chemical potential energy of the burned (or unburned) fuel [14]. Thus, while raising the *ESR* generally leads to increasingly poor usage of fuel chemical potential energy, the engine will inevitably use the potential energy that is successfully converted more efficiently. This is inherently due to the greater amount of premixed (i.e., constant volume) combustion within the engine with added CNG usage.

Finally, Figure 16 features the brake specific fuel (BSFC, a) and energy (BSEC, b) consumption rates of the engine. Generally, both BSFC and BSEC decrease with engine load as the engine is operating more thermodynamically efficient. For low-to-moderate amounts of CNG usage, both the BSFC and BSEC tend to rise slightly with *ESR*, as engine combustion becomes less efficient overall. However, in the case of BSFC, this is countered by the higher energy content of CNG and lower amount of fuel mass needed to meet a certain amount of required fuel potential energy.

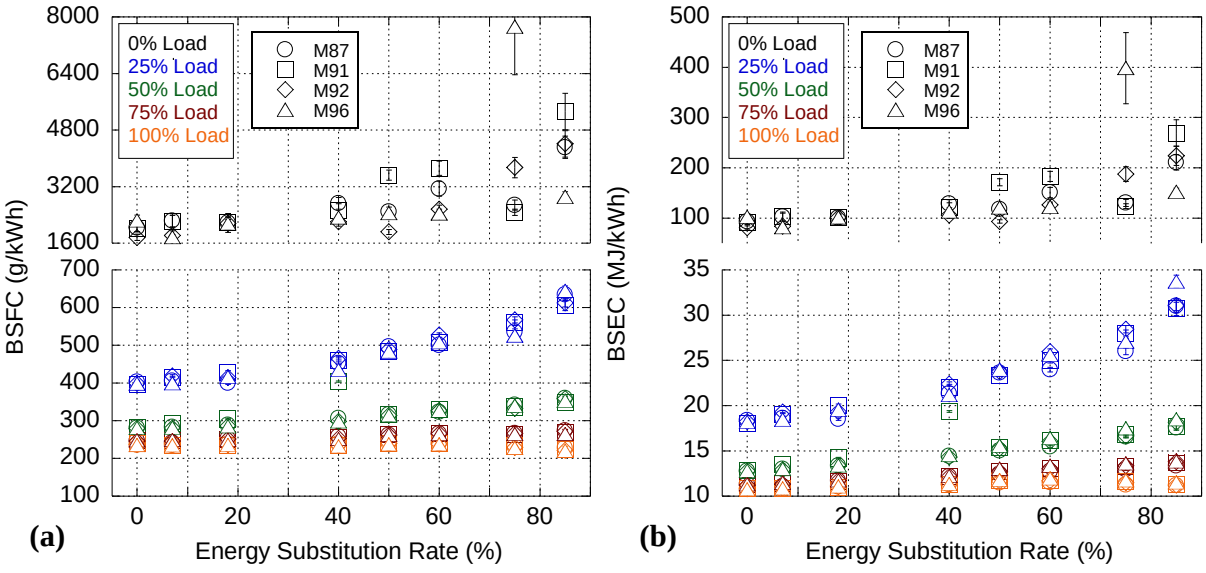

Figure 16. Brake-specific fuel (a) and energy consumption (b) rates for all *ESR*s, mixtures, and engine loads.

Thus, in some cases, BSFC does not significantly grow or may actually fall below that of operation with ULSD only. For *ESR*s above 40%, increasingly inefficient combustion primarily leads to a rise in both BSFC and BSEC that is reflected in higher HC emissions. However, for operation at peak engine load, this loss of efficiency is mitigated, as the combination of high thermal and combustion efficiencies leads to a relatively consistent fuel and energy consumption for all *ESR*s. Thus, while fuel consumption mainly grows overall with *ESR*, this increase is relatively less significant at higher engine loads.

2.5 Conclusions

Dual-fuel combustion with CNG presents a reasonable alternative to ULSD-fueled CI engines without extensive physical engine modifications. Specifically, utilization of CNG in a dual-fuel combustion scenario has the potential to offset ULSD usage and costs while decreasing soot emissions and possibly lowering NO_x emissions in some operational scenarios. However, a major roadblock to modification of existing CI engines for dual-fuel operation is the knowledge of the different combustion regimes, particularly with respect to engine retuning and emissions. Therefore, it is necessary to determine and categorize dual-fuel combustion over a wide variety of potential operational modes and offer clear subdivisions between these modes. To that end, four separate CNG mixtures were tested in a high compression ratio single-cylinder CI engine, utilizing a wide range of *ESR*s ranging from 7% to 85%, alongside operation with neat ULSD.

However, to allow for dual-fuel combustion, heat release models must be adjusted to allow for changes in fuel and combustion chemistry. The model presented augments the standard heat release analysis in accounting for gases being added to the engine via the intake, and correctly computes changes in engine behavior under dual-fuel operation. The model also shows the anticipated increase in premixed combustion (and decrease in diffusion burn) when utilizing higher amounts of CNG. Of note, ignition delay calculations utilizing the pressure trace only generally work well on the Yanmar L100V, likely

related to its high compression ratio and the resulting overlap in combustion of each of the two fuel types used. Experimentation on engines with lower compression ratios may yield a clearer boundary between combustion of the pilot and gaseous fuel charges, and as a result may require more novel ignition delay calculations, but this is not able to be explored in the engine at present.

Operation within the low *ESR* (0-18%) range was found to generally mimic ULSD combustion, such that ignition delays are not suitably changed and engine retuning is not necessary. Within this range, engine operation became slightly less efficient overall, with worsened HC emissions associated with even the smallest amounts of CNG tested because of the difficulty in igniting methane. However, this was coupled with generally lower NO_x emissions through flame quenching, although NO_2 emissions increase. Furthermore, soot emissions drop dramatically due to a shift from liquid to gaseous fuel combustion. Of note, increase methane emissions may be a significant issue for some emissions regulatory agencies, necessitating some means to counter methane emissions (e.g. exhaust aftertreatment, or exhaust gas combustion in a secondary reactor in the same manner as syngas).

Midrange *ESR*s (40-60%) were associated with improvements to engine thermal efficiency as the premixed combustion phase grows. However, this is tied to increasing combustion inefficiencies and unburned fuel lost to the exhaust, particularly at low engine loads; hence, fuel consumption grows. Again, a dramatic drop in soot emissions is seen with NO_x emissions slightly decreasing or remaining constant (both NO and NO_2). Over this *ESR* range, low loads do not have sufficient temperatures to promote NO_x production in comparison to ULSD; whereas, high loads may be too fuel-rich near the fuel spray to allow for significant NO_x production. Furthermore, these moderate substitution rates changed ignition delay and combustion timing; thus, retuning the engine to operate within this regime is recommended.

Finally, high CNG usage (75-85% *ESR*) was found to result in inadequate combustion at all but the peak engine load, with significant flame quenching and cooler temperatures leading to low combustion efficiencies, raised fuel consumption rates and greater HC emissions albeit with relatively low soot emissions. Moreover, a significant shift in combustion timing required modification to the ULSD injection timing. However, the combination of high *ESR* and high engine loads produced

reasonable engine operation, with high thermal efficiencies, lessened increases to HC emissions in comparison to other *ESR*s and loads, and a relatively consistent NO_x production and fuel energy consumption profile.

Chapter III: First Law Analysis of Dual-Fuel Combustion of Biodiesel and Syngas

Material published as "Usage of Glycerin-Derived, Hydrogen-Rich Syngas Augmented by Soybean Biodiesel to Power a Biodiesel Production Facility," International Journal of Hydrogen Energy, August 24, 2016.

3.1 Abstract

A single-cylinder compression ignition engine undergoing dual-fuel operation with soybean biodiesel and an artificial hydrogen-rich syngas (postulated from glycerol reformation) was tested at varying engine loads and gaseous/liquid fuel flowrates. Overall, increasing syngas usage promotes premixed combustion, with only relatively small deviations in injection timing required to maintain efficient engine operation. Fuel consumption increased while emissions of particulates fell with greater syngas usage due largely to a shift to flame propagation-controlled combustion. Increases in nitrogen dioxide emissions are tied closely to syngas usage, and composed an unusually large portion of all nitrogen oxide emissions via greater levels of flame quenching. The experimental results are combined with an energy analysis of a biodiesel production process in order to determine the amount of glycerol (subsequently converted to a syngas) and biodiesel required for a small-scale plant to be self-sufficient. Calculations indicate that only 10.88% of the glycerol by-product generated and 3.65% of the biodiesel produced by the facility is needed to provide all of the plant's energy requirements.

3.2 Introduction

Given the potential climate change from the continued use of fossil fuels, an increased need exists for renewable energy sources produced from non-petroleum supplies. One such source is biodiesel fuel derived from existing feedstocks of biomass, most commonly through transesterification [81]. This process combines a lipid-heavy material (e.g., soybean oil) with an alcohol to form biodiesel in the form of fatty-acid methyl (using methanol) or ethyl (using ethanol) esters. During this process, biodiesel and glycerol (an odorless and colorless by-product [34]) are generated at an amount of 38 and 10 gallons, respectively, per 50 gallons of feedstock oil [82]. The recent rise of biodiesel production because of the

United States Environmental Protection Agency's continuing emphasis on renewable fuels has resulted in a sudden glut of glycerol on the market, leading to a significant decrease in its price [83, 84]. Furthermore, this fall in price could continue, as the Department of Energy estimates that for every 2% of petroleum replaced with biodiesel per year, another 800 million pounds of glycerol is produced [34]. As a result, the economic viability of refining, storage, and sale of pure glycerol created from biodiesel production is decreasing [85]. This reduces the ability of biodiesel to compete with petroleum-based fuels.

In its pure form glycerol is too viscous to be injected directly, and may settle and solidify within the fuel lines [86]. When used as a fuel additive, glycerol has been shown to have difficulty atomizing. As a result, combustion including glycerol has exhibited increased carbon monoxide (CO) and total hydrocarbon (THC) emissions, characteristic of partial combustion, while also causing increased production of oxides of nitrogen (NO_x) [34, 87, 88]. In order to utilize glycerol's high hydrogen content, it may need to be partially oxidized (typically in the presence of a catalyst) into a hydrogen-rich synthetic gas (aka syngas) [89]. This syngas can then be employed in a direct combustion manner with a spark ignition (SI) engine. For a compression ignition (CI) engine, the combustion of syngas alone is difficult due to the lack of precision in controlling the ignition timing and duration; a problem in CI engine operation with all gaseous fuels. However, syngas may be used in a CI engine with the addition of a pilot charge of liquid fuel, in the same manner as dual-fuel combustion of ultra-low sulfur diesel (ULSD) and compressed natural gas (CNG) [8].

Previous studies in hydrogen-rich syngas dual-fuel CI combustion have found the potential to decrease NOx emissions while possibly increasing thermal efficiency and in-cylinder pressure, so long as the amount of hydrogen is limited to prevent pre-ignition and early or excessive premixed heat release rate [90]. Combustion of hydrogen also benefits from a wide-ranging flammability limit and low ignition energy, but may also increase the overall auto-ignition temperature of the mixture. Furthermore, hydrogen possesses a lower overall quenching distance, being able to burn much closer to the cylinder wall, subsequently leading to further increases in thermal efficiency over other gaseous fuels [90]. This earlier work highlighted a possible operational ceiling of 30% hydrogen content by volume in the intake charge,

past which pre-ignition of the hydrogen becomes severe [90, 91]. In addition, syngas addition beyond 35% (by total fuel energy content) has been found to lead to inefficiencies due to a general lack of oxygen available for complete combustion [92]. More recent work has universally shown a decrease in engine fuel conversion efficiency and increase in fuel consumption as additional syngas is used [92-100]. This behavior is likely related to combustion efficiency degradation (particularly at low engine loads) when utilizing gaseous fuels [92, 95, 100]. However, the decreased combustion efficiency and increased CO and THC emissions is due entirely to unburned gaseous fuel, and does not appear to reflect a decrease in liquid fuel combustion efficiency [92, 100]. Emissions of PM have also been found to generally decrease with additional gaseous fuel usage, while emissions of NO_x compounds either remained somewhat constant or increased, particularly in the form of NO_2 [8, 92-95, 97, 100].

Between differing gaseous fuels species, methane content has been linked to larger CO and THC emissions, while hydrogen content is more associated with NO_x emissions [92, 95, 100]. In addition, it has been found that increasing hydrogen content in methane-dominated mixtures will aid in reducing CO and THC emissions by increasing combustion efficiency. In contrast, increasing methane content in primarily-hydrogen gaseous fuels mitigates NO_x emissions by promoting cooler combustion that inhibits the thermal NO mechanism [93]. Finally, when using biodiesel as the liquid pilot in place of ULSD, researchers have found a general increase in NO_x emissions [94], although that may be related to combustion phasing effects instead of fuel chemistry [19].

To that end, this work uses a hydrogen-rich gas chosen to approximate the syngas produced at an existing glycerol reformation station. A single-cylinder CI engine was then operated at a constant speed and varying fractions of the ratio of this syngas to soybean biodiesel was employed at different loads in order to maintain constant engine power. This engine utilized a modern, high-pressure liquid injection system that allows for normalization of combustion timing, and reinvestigates the authors' earlier findings that employed a mechanical injection system [90]. Testing included monitoring the engine's performance and in-cylinder pressure characteristics while recording a comprehensive emissions profile as a function of both fuel flow rates. Subsequent post-processing included a heat release analysis for understanding pre-

mixed and diffusion burn characteristics. Over the following sections, the details of this experimental process are discussed including the resulting pressure traces, rates of heat release (RHR), emissions, and efficiency data gained from testing. A subsequent discussion then expands on the initial results by estimating the effectiveness in using syngas-assisted biodiesel combustion as an energy source for the biodiesel production process [82, 101]. In specific, biodiesel production requires a source of power for various processes (e.g. heating and filtering the feedstock, powering the reactor, etc.), and the potential exists to supply the energy required through the dual-combustion of syngas (from the glycerol by-product) and the produced biodiesel. Finally, this analysis also includes a comparison to previous successful (but inefficient) reformation and combustion of actual syngas in a larger SI engine [82].

3.3 Experimental Methodology

Currently, a unique glycerol-based power generation system is installed at the University of Kansas that includes a full-scale reformer along with a Chevrolet 350 in^3 V8 engine and Mecc-Alte ECO32-2L/4 generator [82]. The reformer utilizes a relatively low-cost nickel-alumina catalyst and various flow rates of glycerol in order to explore the ranges of syngas reformation and combustion for power. Of note, an 80/20% glycerol/water mixture is employed in the full-scale reformer in order to reduce the viscosity of glycerol while promoting the water gas shift reaction to generate more hydrogen in the reforming process. However, to allow for the combustion of syngas in a CI engine at a separate location on campus, the syngas in this effort comes as a tank gas since the reformer effluent cannot be bottled on-site given the explosion hazards involved. As a result, the artificial syngas mixture was created by Matheson Tri-Gas to match the average mixture generated by glycerol reformation as shown in Table 4 [82]. The resulting artificial syngas had a lower heating value of 10.75 MJ/kg (31.55 if only flammable species are considered), a constant pressure specific heat of 1395.6 J/kg-K, a ratio of specific heats of 1.355, and a gas constant of 364.6 J/kg-K [82].

Table 4: Composition of the original (observed) syngas and the artificial mixture, expressed in volume % [75, 82].

Mixture Component	Volume Fraction (Dry)	Volume Fraction (Wet)	Artificial Mixture
Hydrogen	32.4	28.7	28.7
Methane	5.8	5.1	5.1
Carbon Monoxide	18.1	16.0	16.0
Carbon Dioxide	7.2	6.3	17.7
Water	-	11.4	-
Ethylene	4.8	4.3	4.3
Ethane	2.6	2.3	2.3
Nitrogen (assumed)	29.1	25.9	25.9

Of note, the actual syngas mixture contains a relatively high water content that cannot be easily replicated in the artificial syngas, as the water would condense out of the overall mixture. To achieve the desired composition, the carbon dioxide (CO_2) content in the artificial syngas mixture was increased to account for both the CO_2 and water content of the original gas. As a result, the lower heating value of the combustible material remained constant at 31.50 MJ/kg, and the ratio of specific heats of the mixture was lowered slightly (from 1.360). The choice of using additional CO_2 over N_2 to represent the inert water in the mixture was to maintain the ratio of specific heats as closely to the initial mixture as possible; both water and CO_2 are triatomic molecules and using N_2 would have raised the ratio of specific heats to 1.372. Moreover, this prevents a further increase N_2 concentration that would have impacted NO_x emissions through the thermal NO mechanism (a significant focus of regulation standards). This should provide a realistic characterization of syngas combustion; however, emissions will be slightly different (promotes CO instead of H_2 production) since H_2O dissociation and the water gas shift reaction ($CO + H_2O \Leftrightarrow H_2 + CO_2$) will not be as accurately portrayed.

Experiments with the artificial syngas were performed using a Yanmar L100V single-cylinder CI engine [73]. The engine was operated with the manufacturer's Exhaust Gas Recirculation (EGR) port blocked. In addition, the engine's standard mechanical injection system was replaced with a modern high-pressure single rail injection system controlled electronically with a Bosch MS15.1 engine control unit using Bosch Modas Sport. Finally, engine speed was controlled using a Dyne Systems Dymond Series alternating current dynamometer rated for a maximum torque of 21.1 ft-lbs, and a maximum speed of

7500 RPM [102]. Engine operation was monitored and recorded using National Instruments (NI) LabVIEW systems. The first of these systems was utilized to capture the in-cylinder pressure trace at a resolution of 0.2° of crank angle, using 60 consecutive thermodynamic cycles (120 engine revolutions) in order to offset cyclic variations. The second system collected other engine operating data every 0.1 seconds over the course of two minutes. Finally, a third NI system was used to facilitate communication with an AVL smoke meter and SESAM-FTIR emissions analyzer, in order to provide a complete characterization of the engine-out emissions profile. The emissions analyzer was set to record a full emissions profile every second over the course of three minutes of engine operation at steady-state (defined by changes in oil and exhaust temperatures of less than 1% over the previous 60 seconds) [73].

The syngas was tested at three separate Energy Substitution Rates (*ESR*), or the fraction of the total energy used for combustion that is added by the syngas. The *ESR* is defined mathematically as follows:

Energy Substitution Ratio	$ESR = \frac{\dot{m}_g Q_{LHV_g}}{\dot{m}_g Q_{LHV_g} + \dot{m}_p Q_{LHV_p}}$	(20)

where m is the mass flow rate of fuel, and Q_{LHV} is the lower heating value, and the subscripts g and p are used to differentiate between syngas and pilot (liquid) fuel charges, respectively [8]. The three separate *ESR*s used in testing were 10%, 20%, and 35% at all engine loads other than the peak rated load, at which point the maximum amount of syngas that could be added to the intake was maximized at 30% *ESR*. The bottled syngas mixture was attached to a gaseous mixing box on the intake-side of the engine, allowing for complete mixing of the intake air and gaseous fuel. Flow of the gaseous fuel was monitored and controlled using a Brooks mass flow controller (model #SLA5850s) [8].

The syngas mixture was tested at 1800 RPM, and by varying engine load from 0.5 N-m (engine idle) to 18.0 N-m (peak load at 1800 RPM), to separate and identify the varying effects of increasing the syngas component of fuel energy in both the premixed and diffusion burn portions of the engine cycle. This engine speed was chosen based on prior testing efforts that demonstrate conditions of primarily pre-mixed burn to mostly diffusion burn based on load. For testing, the engine was brought to a given engine

load using soybean biodiesel only (henceforth, 0% *ESR*), with an energy content of 39.88 MJ/kg, and with other properties approximated in Table 5 via earlier efforts.

Table 5: Soybean biodiesel properties.

Cetane Number	48.1 ± 4.7
Energy Content [MJ/kg]	39.88 ± 0.044
Density [kg/m3 at 298.15 K]	875.58 ± 0.01
Kinematic Viscosity [cSt]	4.218 ± 0.001
Dynamic Viscosity [cP]	3.693 ± 0.001
Oxygen Content [% wt.]	9.9 ± 0.3
H:C Molar Ratio	1.87 ± 0.04

This operation was continued until the engine achieved steady-state, at which point the engine operational data was collected. Next, the amount of biodiesel being injected was reduced, and the syngas was allowed to flow into the intake to reach a desired *ESR*. After the engine had re-acquired steady-state, the new operational data was collected. Following this, the process was repeated until all of the desired *ESR*s for a given load had been achieved. At this point, the flow of syngas was stopped and the rate of biodiesel fuel injection increased in order to achieve the next engine load, with testing occurring at idle (0.5 N-m), 25% (4.5 N-m), 50% (9.0 N-m), 75% (13.5 N-m), and 100% of rated engine load (18.0 N-m). The common-rail injection system was held at 48±0.5 MPa, and injection timing was varied (when necessary) in order to realign the timing of peak cylinder pressure during dual-fuel operation to that of operation with biodiesel only. Post-processing included filtering and compilation of the acquired in-cylinder data, as well as the use of an equilibrium-based heat release model [11, 73, 103].

3.4 Experimental Results

The pressure traces for engine operation at 0.5 N-m (Figure 17a) and 4.5 N-m (Figure 17b) exhibit similar behavior, and dual-fuel operation is not too dissimilar to traditional engine operation with biodiesel. Of note, all data presented corresponds to normalized combustion, with respect to peak pressure being maintained at a consistent crank angle location. In each case, the most significant difference is the general lowering of cylinder pressure with an increase in *ESR*. This is related closely to the change in the ratio of specific heats of the bulk gas within the cylinder. In specific, the pressure at top-dead center

(PTDC) is related directly to the pressure within the cylinder when the intake valve is closed (PIVC), the compression ratio of the engine (r), and the ratio of specific heats of the bulk gas (γ) if isentropic compression is assumed [8]:

Isentropic Compression	$P_{TDC} = P_{IVC} r^{\gamma}$	(21)

Here, the engine compression ratio is constant, and the changes in intake pressure are negligible. However, the ratio of specific heats decreases from 1.40 (for air) towards 1.357 (for syngas) as the *ESR* increases and dilutes the greater bulk gas mixture. This depresses the peak cylinder pressure during compression, subsequently lowering the combustion pressure.

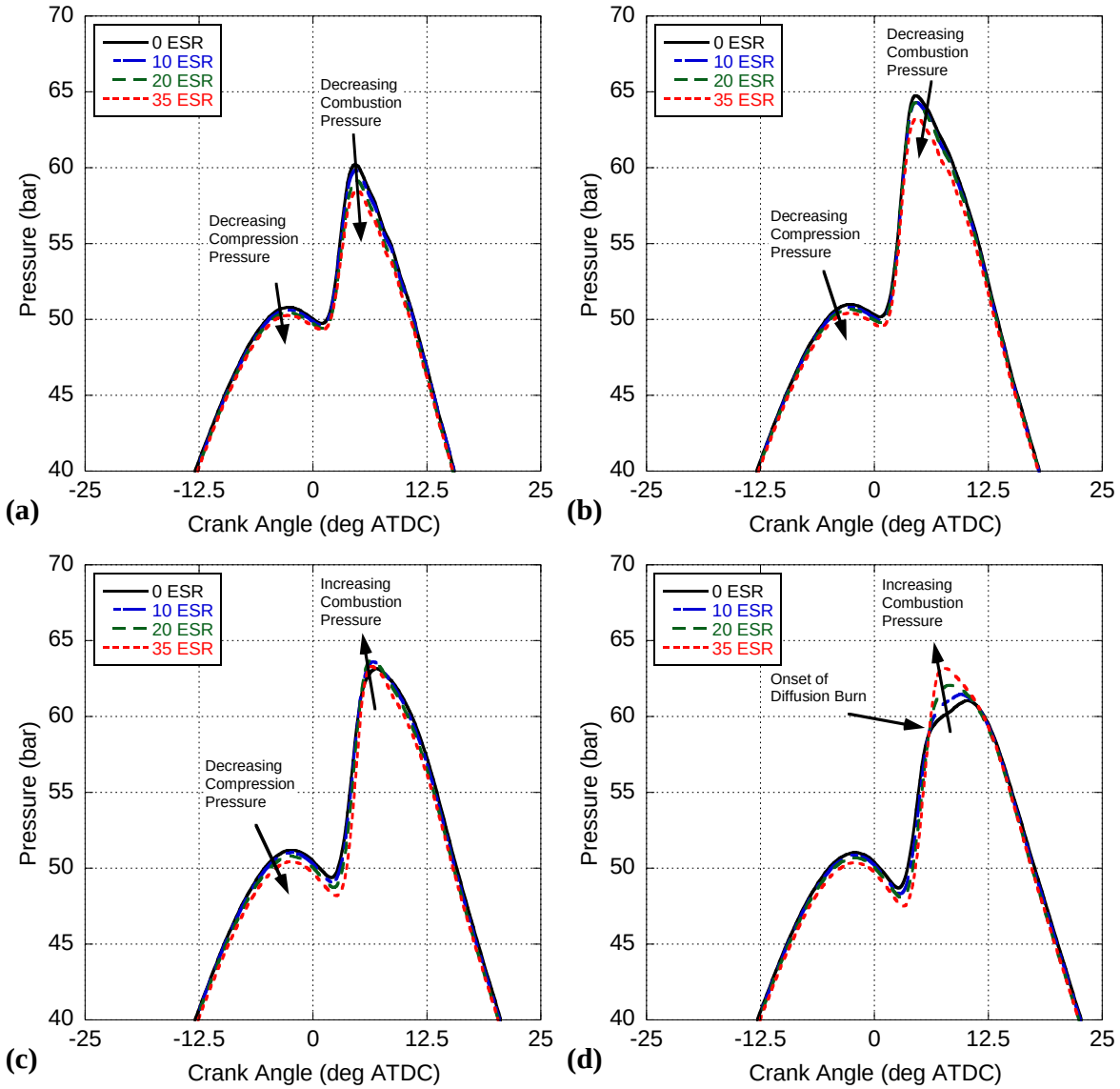

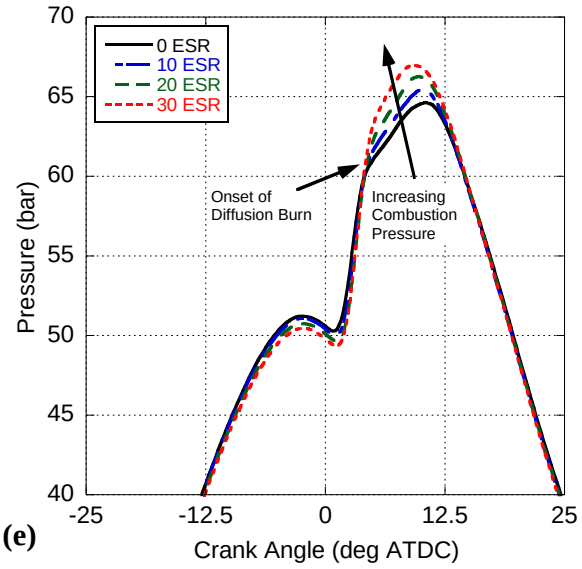

Figure 17: Measured in-cylinder pressure traces for operation with biodiesel and three *ESR*s at 0.5 N-m (a), 4.5 N-m (b), 9.0 N-m (c), 13.5 N-m (d), and 18.0 N-m (e).

At 9.0 N-m (Figure 17c), the lowering of peak cylinder pressure due to compression is still seen; however, after combustion begins, increasing *ESR* led to a slight growth in peak cylinder pressure. This amplification of combustion pressure is further evident at the higher loads of 13.5 N-m (Figure 17d) and 18.0 N-m (Figure 17e). Previous efforts with this engine involving soybean biodiesel have illustrated that at 1800 RPM, combustion is largely pre-mixed burn up to 9.0 N-m. Hence, all liquid fuel added is sufficiently prepared for combustion within the ignition delay of the fuel. At and above this load, diffusion burn starts to play a more prominent role with 13.5 N-m and 18.0 N-m results transitioning to significant amounts of diffusion burn. Therefore, as *ESR* increases, the level of pre-mixed combustion increases (and so does peak pressure) because the intake-added syngas does not suffer from the phenomena associated with the physical ignition delay in liquid fuels. This is quite noticeable due to the sudden change in the upward slope of the pressure rise, seen at approximately 4-6° after top-dead center (ATDC) in Figure 17d. With increasing amounts of syngas, this slope continues to rise further illustrating greater levels of pre-mixed combustion. Calculation of ignition delay via the second derivative of the pressure trace found that the syngas did not greatly affect the ignition delay of the fuel mixture; hence, it will not appreciably influence the relative amounts of pre-mixed and diffusion burn. When needed, changes to injection timing and ignition delay were approximately 0.1-0.3, and 0.2-0.7 crank angle

degrees, respectively. This is because both hydrogen and methane are difficult to auto-ignite; hence, ignition delay is governed primarily by the biodiesel chosen and not the syngas.

Investigating the RHR as *ESR* is increased in Figure 18 finds that the diffusion-burn phase is dramatically reduced, even at light loads besides idle where all combustion is overwhelmingly pre-mixed. As load and *ESR* increases, a noticeable growth in the pre-mixed phase is found with a corresponding decrease in diffusion burn. This behavior highlights the characteristic shortcoming of liquid fuels; the inability of the injected fuel to fully prepare prior to combustion. In order to meet a desired load, the engine must lengthen the injection event at a given injector pressure in order to allow more fuel to enter the engine, subsequently promoting diffusion burn. The addition of syngas provides the needed energy at a given load during the pre-mixed burn phase since it enters through the intake with the air.

Furthermore, previous research on CNG-assisted combustion indicates that an increase in *ESR* results in a more homogeneous fuel-air mixture and the transitioning of combustion to a flame-propagation type of event [8, 90]. Given the wide flammability limit and significantly fast flame speeds of hydrogen mixtures, it is possible that there is a greater level of biodiesel pre-mixed burn as the level of hydrogen increases. For instance, biodiesel on the periphery that would not be combusted at 0% *ESR* could now be potentially ignited by the hydrogen flame front as it propagates at 35% *ESR*. This may explain the delay in pre-mixed spike (e.g., 5° to 6.5° ATDC at 13.5 N-m) with *ESR* as the flame front propagates and continues to burn biodiesel fuel in the periphery. Moreover, the distinct combustion phase peaks at higher loads are now blending as (a) less biodiesel fuel is needed with higher *ESR* levels, subsequently reducing the potential for diffusion burn and (b) flame propagation may be aiding the now more homogeneous diffusion-burn combustion process.

The in-cylinder temperature, calculated from the pressure trace and composition of the bulk gas, serves as a final means to express the relationships between pressure, heat release, and the varying stages of combustion, and is shown in Figure 19. Similar to the in-cylinder pressure traces, a slight decrease in temperature during the compression can be related to the change in ratio of specific heats within the cylinder. At lower engine loads, the similarity across various *ESR*s is apparent in the relatively identical

temperature profiles due to combustion being nearly all pre-mixed (Figure 3a). When diffusion burn plays a more prominent role at higher loads, increasing the *ESR* level results in temperatures greater than ULSD. This is due to the dramatic increase in the pre-mixed combustion phase around TDC.

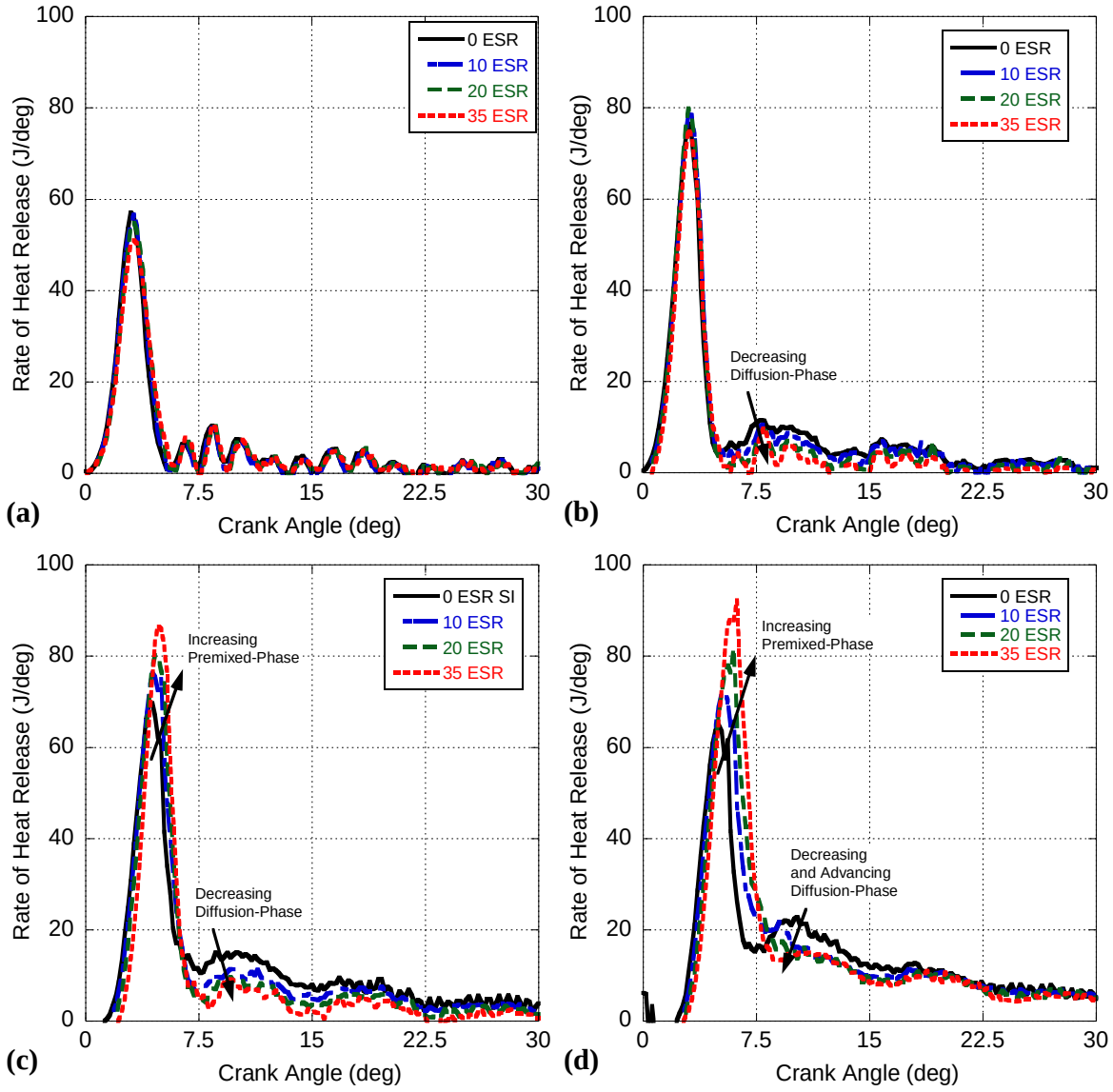

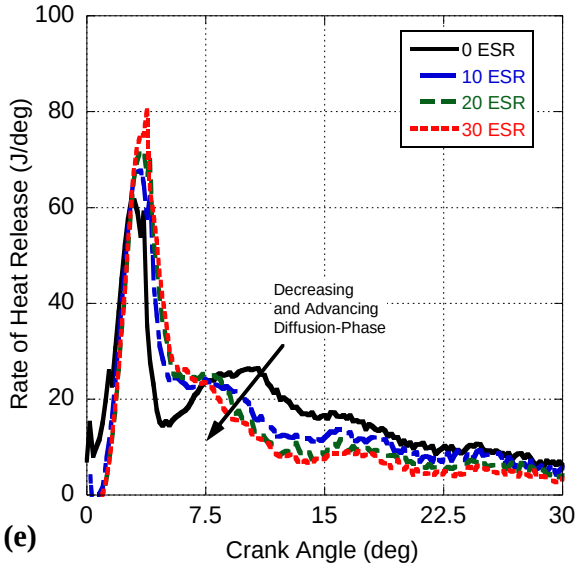

Figure 18: Fuel Rate of Heat Release for biodiesel and three *ESR*s at 0.5 N-m (a), 4.5 N-m (b), 9.0 N-m (c), 13.5 N-m (d), and 18.0 N-m (e).

The in-cylinder temperature, calculated from the pressure trace and composition of the bulk gas, serves as a final means to express the relationships between pressure, heat release, and the varying stages of combustion, and is shown in Figure 19. Similar to the in-cylinder pressure traces, a slight decrease in temperature during the compression can be related to the change in ratio of specific heats within the cylinder. At lower engine loads, the similarity across various *ESR*s is apparent in the relatively identical temperature profiles due to combustion being nearly all pre-mixed (Figure 3a). When diffusion burn plays a more prominent role at higher loads, increasing the *ESR* level results in temperatures greater than ULSD. This is due to the dramatic increase in the pre-mixed combustion phase around TDC.

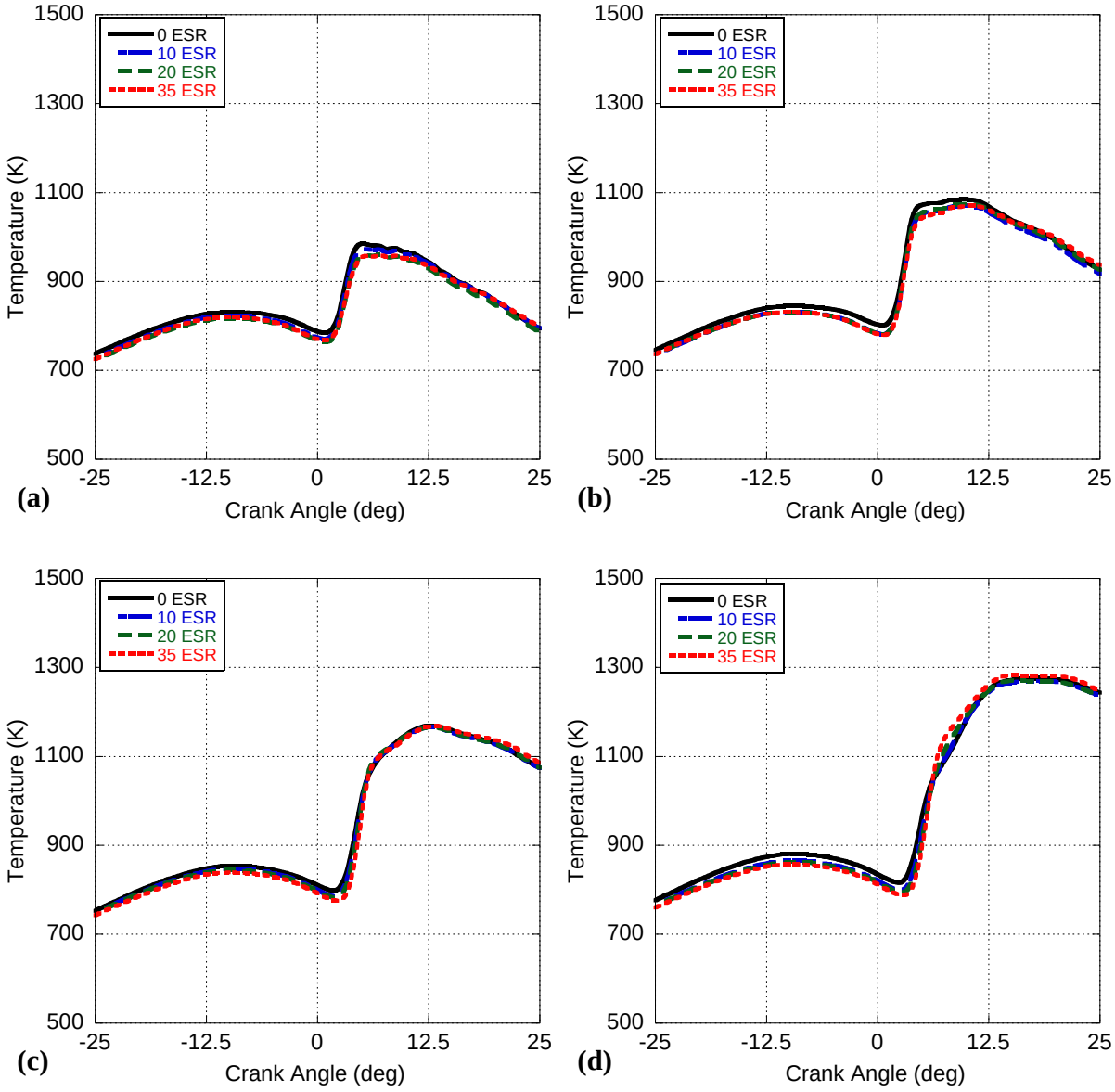
0 ESR
10 ESR
20 ESR
35 ESR
Temperature (K)
Crank Angle (deg)
(a)
(b)
(c)
(d)

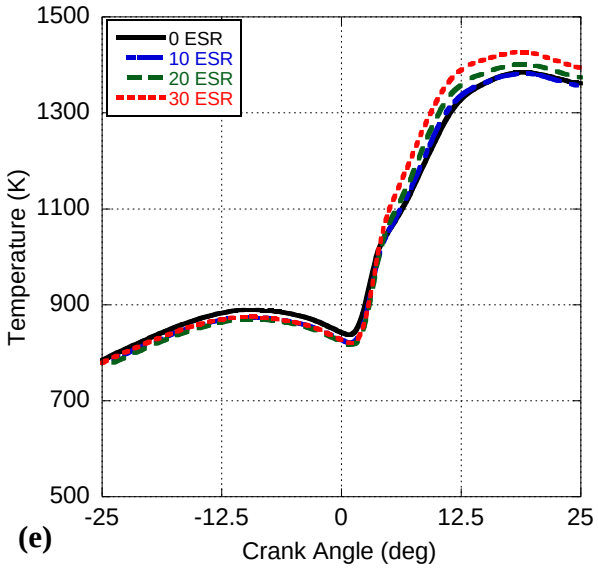

Figure 19: Calculated in-cylinder temperature profiles for biodiesel and three *ESR*s at 0.5 N-m (a), 4.5 N-m (b), 9.0 N-m (c), 13.5 N-m (d), and 18.0 N-m (e).

The next point of consideration lies with the changes in engine operational efficiency with respect to load and *ESR*. Mass flow rates of both syngas and biodiesel, as well as the potential energy content of the syngas mixture and biodiesel, are found in Table 6. The general trend shows the expected linear rise in gaseous fuel consumption (and a fall in liquid consumption) as *ESR* was increased. However, the brake specific consumption of both fuel (BSFC) and energy (BSEC) of the engine as a whole increased with higher *ESR* even though the level of the more efficient pre-mixed combustion phase grows. To understand this finding, one must look towards the decrease in volumetric efficiency with *ESR* as illustrated in Figure 20a. The added syngas is reducing the amount of oxygen entering the engine promoting reduced combustion efficiency. Furthermore, combustion is transitioning from auto-ignition (i.e., CI combustion) to flame propagation (i.e., SI combustion) as *ESR* grows. Hence, overall combustion becomes less constant-volume like that could lead to a reduction in engine efficiency. So, while the pre-mixed phase grows, combustion in general might take longer to finish. These findings are reflected in the growth of the global equivalence ratio with *ESR* in Figure 20b.

Table 6: Liquid and gaseous fuel flow rates and energy contents for all loads and *ESR*s tested.

		Biodiesel		Syngas		Brake Specific Consumption	
Engine Load	*ESR* [%]	Flowrate [g/s]	Power [kW]	Flowrate [g/s]	Power [kW]	Fuel [g/kWh]	Energy [kJ/kWh]
0.5 N-m (0.094 kW)	0	0.078	3.111	0	0	2412.99	96230
	10	0.068	2.725	0.029	0.309	8956.69	279935
	20	0.068	2.716	0.066	0.712	5315.07	135603
	35	0.060	2.393	0.128	1.379	6795.71	136153
4.5 N-m (0.848 kW)	0	0.112	4.481	0	0	477.22	19059
	10	0.106	4.217	0.045	0.487	627.21	19536
	20	0.097	3.884	0.094	1.006	798.19	20437
	35	0.083	3.309	0.178	1.914	1064.39	21300
9.0 N-m (1.696 kW)	0	0.156	6.202	0	0	325.25	12984
	10	0.144	5.752	0.063	0.681	430.18	13333
	20	0.130	5.166	0.127	1.362	546.30	13917
	35	0.109	4.364	0.229	2.466	718.94	14493
13.5 N-m (2.545 kW)	0	0.201	8.033	0	0	288.81	11532
	10	0.186	7.427	0.081	0.876	380.41	11806
	20	0.167	6.644	0.166	1.784	477.00	12088
	35	0.137	5.481	0.293	3.146	615.16	12339
18.0 N-m (3.393 kW)	0	0.258	10.305	0	0	274.75	10980
	10	0.232	9.247	0.103	1.103	359.74	11132
	20	0.209	8.334	0.202	2.173	440.76	11265
	30	0.184	7.335	0.299	3.210	520.47	11374

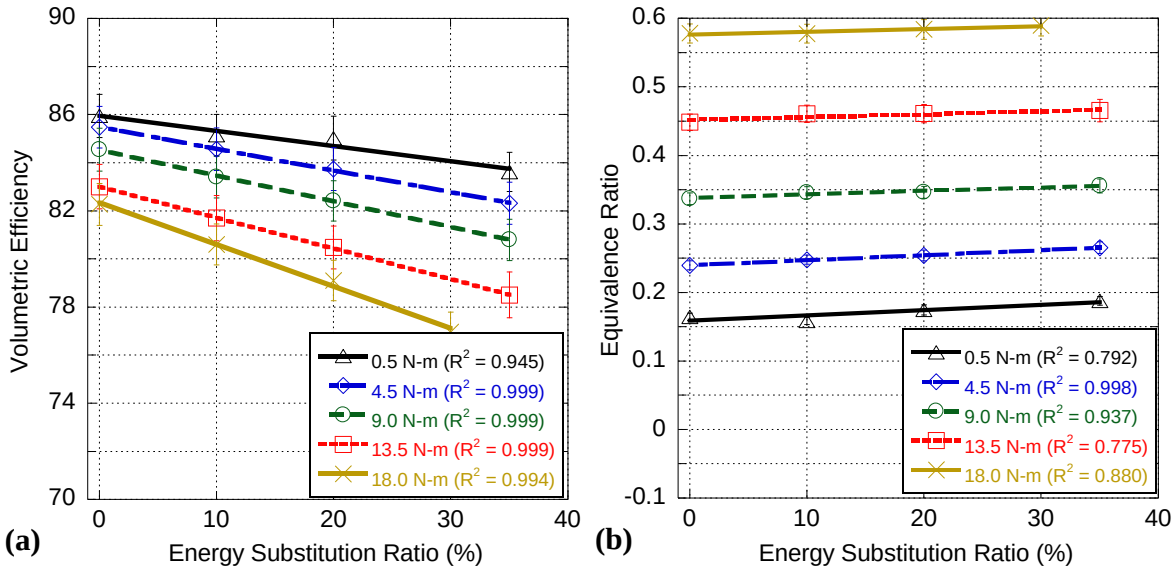

Figure 20: Calculated volumetric efficiency (a) and global equivalence ratio (b) with respect to *ESR* at each engine load tested.

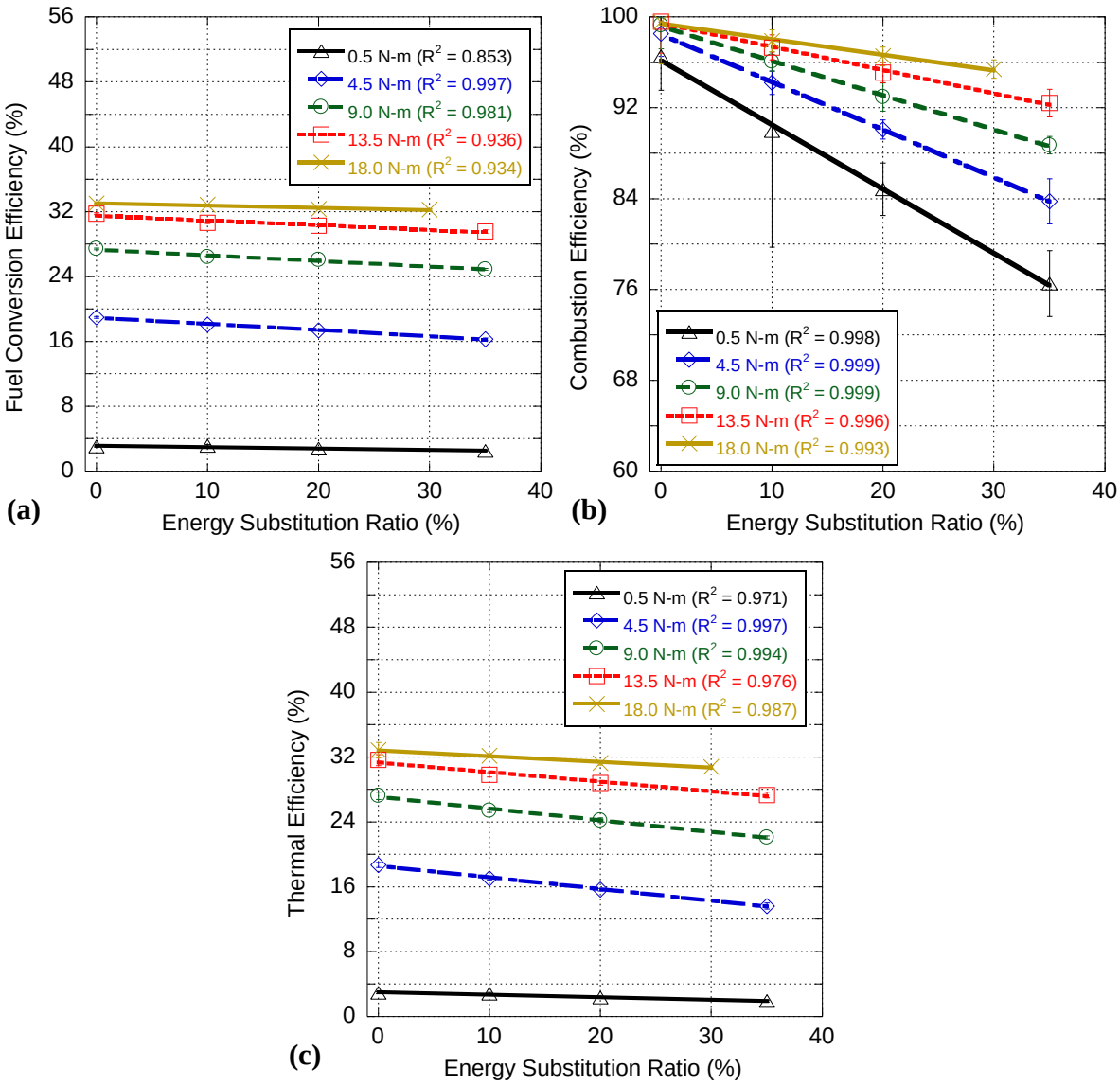

Figure 21: Fuel conversion efficiency (a), combustion efficiency (b), and thermal efficiency (c) with respect to *ESR* at each engine load tested.

To illustrate this last thought more clearly, the changes to fuel conversion, combustion, and thermal efficiency with *ESR* are presented in Figure 21. Fuel conversion efficiency is computed from the fuel flow rates and follows the trend of BSFC; i.e., decreasing with added *ESR*. Combustion efficiency is calculated from the exhaust gas speciation and demonstrates a reduction with respect to *ESR* addition. This is counterintuitive since more combustion is happening sooner (i.e., pre-mixed) providing for more combustion time and in-cylinder temperatures generally increase with *ESR* suggesting a hotter combustion process. Hence, this reduction is likely due to the transition to flame-propagation combustion

of a mixture containing a significant fraction of methane gas. While hydrogen has a high flammability limit, previous efforts with CNG dual-fuel combustion illustrate that methane is more likely to remain stable within the cylinder, particularly in the cooler regions of the cylinder where combustion is less pronounced (either due to poor flame front propagation, poor air-fuel mixing, or potential flame quenching near the wall) [104-106]. Furthermore, the syngas artificially adds Exhaust Gas Recirculation (EGR) species (i.e., N_2 and CO_2) into the intake with *ESR* that acts as diluent, subsequently lowering combustion efficiency by reducing flame propagation [107]. Finally, investigating thermal efficiency (as calculated from the fuel conversion and combustion efficiencies) finds that it generally trends lower with *ESR* addition. This is probably the most illustrative finding with respect to the influence of flame-propagation on the results. Figure 18 demonstrates a significant rise in pre-mixed burn suggesting higher engine thermal efficiencies; however, the transition to a flame-propagation combustion event along with effectively adding EGR (that slows flame propagation) overwhelms the large increase in pre-mixed burn. This result differs from the prior efforts of the authors where the syngas consisted of only H_2 and CO and an increase in thermal efficiency was seen at a few engine loads.

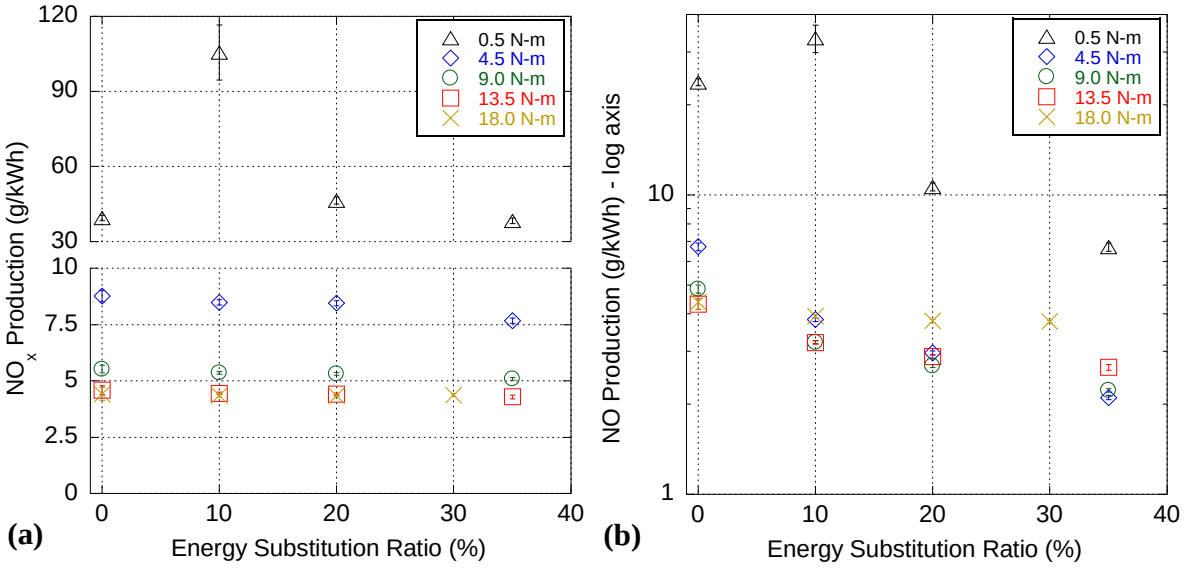

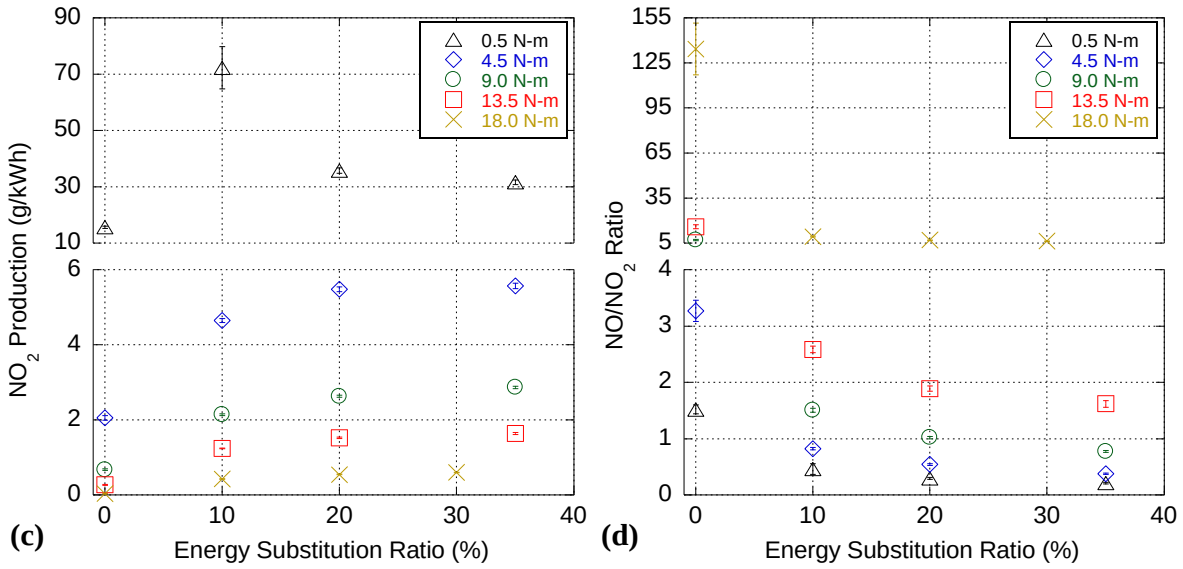

Figure 22: Brake-specific production of NO_x (a), NO (b), NO_2 (c), and the ratio of NO to NO_2 (d) with respect to *ESR* for each engine load tested.

Engine-out brake-specific NO_x production (see Figure 22a) showed a general decrease with respect to engine load, regardless of *ESR* used. This behavior is in keeping with prior results and is due to the increase in engine efficiency with load (Figure 21). With an increase in *ESR* at a given load, NO_x production appeared to either remain unchanged or decrease very slightly. Investigating NO (Figure 22b), one would expect that an increase in pre-mixed burn (Figure 18) and in-cylinder temperatures (Figure 19) while having a global equivalence ratio closer to peak NO_x production (Figure 20b) would lead to higher levels of NO due to the thermal NO mechanism (more time and temperatures to promote the kinetics). Furthermore, due to the higher hydrogen-to-carbon ratio caused by the addition of the methane- and hydrogen-dominated syngas, increased NO production through the prompt NO mechanism is possible as *ESR* is increased. However, the trend found was opposite; moreover, NO_2 goes up with *ESR* (Figure 22c), whereas convention would state it should go down. Investigating the relative ratio of NO/NO_2 in Figure 22d demonstrates that the overall tendency is to promote NO_2 production over NO with *ESR*.

This behavior can be explained through the increasing homogeneity of the combustion process as *ESR* is increased, smoothing the temperature gradient (i.e., allowing combustion to spread further away from the pilot fuel spray), and increasing the likelihood of flame quenching near the cylinder walls. This promotion of flame quenching leads to a growth of NO_2 over NO; i.e., normally NO_2 quickly reverts back

to NO, but on the periphery of a flame when NO_2 sees relatively colder temperatures, it can freeze at its current concentration. Similar NO_x findings have been previously documented with dual-fuel combustion of CNG and ULSD [8, 105, 106, 108]. Of note, as load continues to increase, the rising temperatures with *ESR* may eventually cause thermal NO production to win out over NO_2 quenching [109].

Brake-specific particulate matter (PM) emissions demonstrated a gradual increase in overall production with greater load, while also showing substantial decreases with added *ESR* (see Figure 23). Both of these behaviors are representative of the changes in the fuels being used with different combinations of load and *ESR*. For higher loads, more biodiesel fuel is utilized either as the primary source of energy or as the pilot fuel for the syngas mixture, leading directly to an increase in PM production through higher levels of diffusion burn (Figure 18). As *ESR* is increased, the total amount of liquid fuel utilized decreases, causing a direct decrease in the total amount of liquid fuel available to form PM. In addition, the decrease in PM emissions by addition of syngas is not entirely a linear relationship. This is due to the homogenizing effect of syngas that decreases fuel stratification directly; hence, a linear increase in *ESR* results in an exponential decrease in PM production.

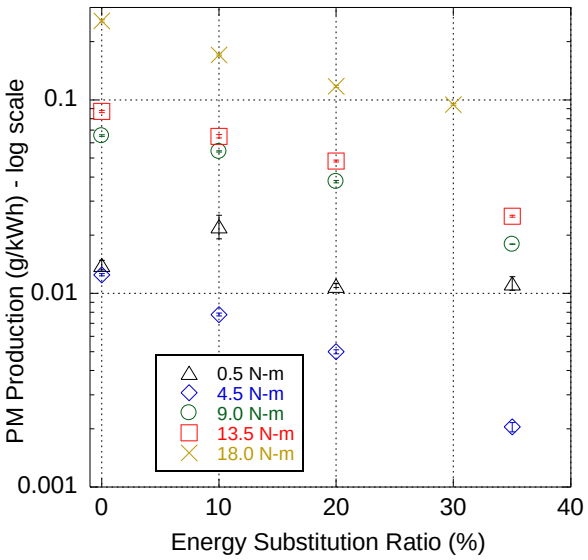

Figure 23: Brake-specific production of PM with respect to *ESR* at each engine load tested.

THC emissions generally decreased with engine load for each *ESR* tested as shown in Figure 24a, consistent with the trend of combustion efficiency (Figure 21b). However, THC emissions gradually

increased alongside *ESR*, suggesting an overall increase in the number of hydrocarbon species surviving combustion as gaseous fuel composed a greater fraction of the overall mass. This is again due to the transition to flame propagation and higher likelihood of flame quenching leaving THCs on the periphery of the mixture. Moreover, since the engine is now compressing the syngas along with air, there is the added potential of crevice flow leading to HCs re-emerging during exhaust valve opening.

As shown in Figure 24b, methane follows the same trend with *ESR* while also forming a significant fraction of roughly a quarter of the engine-out THC emissions (see Figure 24c); whereas, it only constituted 5.1% by volume of the initial syngas mixture (Table 4). This is likely due to methane's stability at high temperatures relative to other hydrocarbons [104]. Emissions of hydrogen gas (H_2) were also calculated via considering the water-gas shift reaction, and these emissions followed the same trends as those of methane, serving as further evidence that flame quenching on the periphery of the cylinder reduces combustion effectiveness [105, 106].

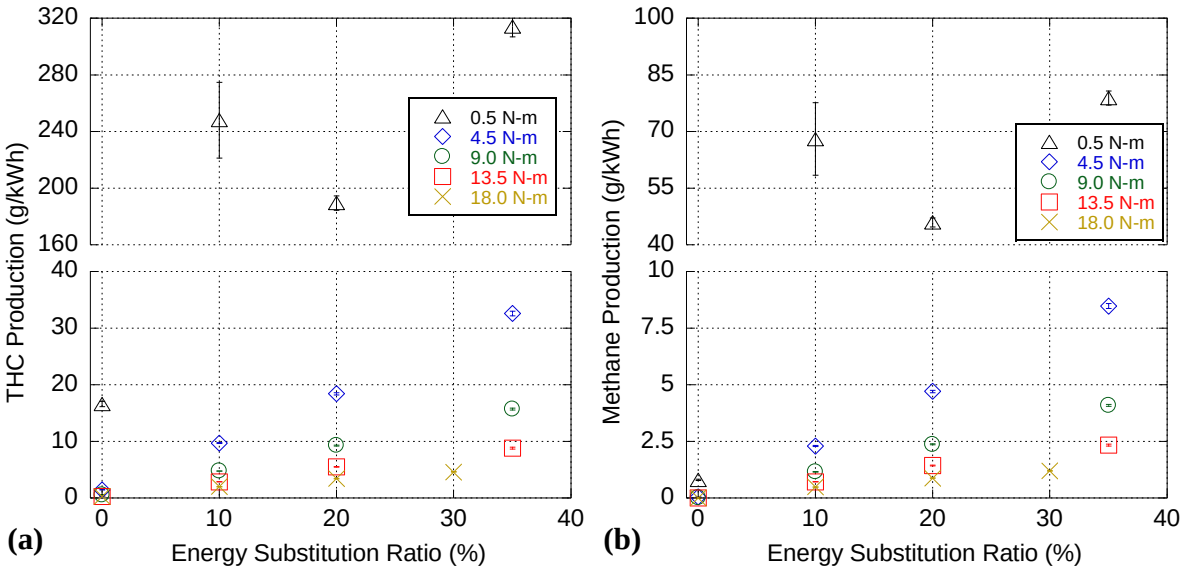

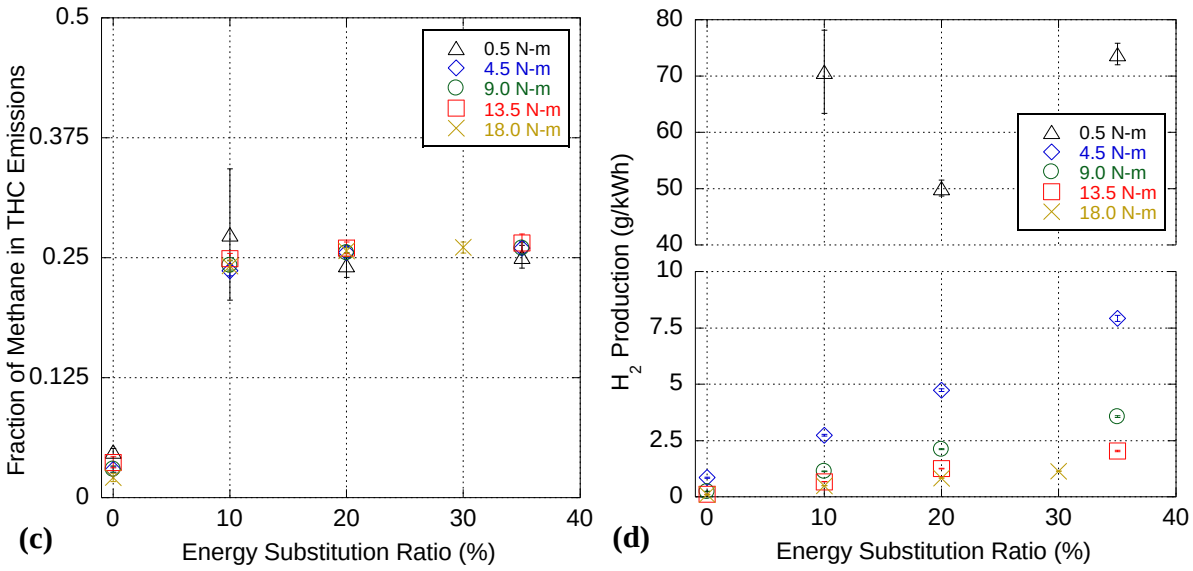

Figure 24: Brake-specific production of THCs (a) and methane (b), the fraction of methane in THC emissions (c), and brake-specific production of H2 (d), with respect to *ESR* at each load tested.

3.5 Syngas-Powered Biodiesel Production

It is apparent that the usage of a hydrogen-rich syngas in a dual-fuel combustion manner with biodiesel is achievable for a small-scale, modern CI engine. Given that a potentially sustainable source of syngas is through the reformation of the biodiesel by-product glycerol, this dual-fuel operation is of interest within the field of biodiesel production as it would potentially remove the need to dispose of (or sell) glycerol. At the University of Kansas, a biodiesel production facility (KU Biodiesel Initiative) converts oil into biodiesel and glycerol through a transesterification (batch) process. In order to power the entire process, 14.9 kWh of energy is utilized at various rates (ranging from 0.153 kW to 2.792 kW) over the course of nearly 17 hours as shown in Table 7. Tests involving the flow rates to run the previously mentioned Chevy 350 in3 V8 engine while measuring the power produced from the Mecc-Alte ECO32-2L/4 generator determined that it would take 70.56 gallons of glycerol (after factoring in a 20% water content) in order to produce 38 gallons of biodiesel product and 10 gallons of crude waste glycerol. However, the continuous energy requirements of the process never rises above 2.80 kW, making the Chevrolet 350 engine (capable of 150 kW) much too large for this small-scale biodiesel production

facility. This results in the Chevy engine running at lower engine speeds and loads than optimal, subsequently requiring a glycerol usage seven times higher than what is produced in the process [82].

Table 7: Energy and glycerol flow rates (after accounting for 20% water content) for biodiesel production [82].

Phase	Time [hours]	Continuous Power Required [kW]	Glycerol Flow Rate [gal/hour]	Glycerol Required [gal]
Oil Filter Stage 1	3.00	1.28	4.29	12.86
Oil Filter Stage 2	2.50	2.79	4.64	11.60
Reactor Pump	6.00	0.39	4.08	24.45
Catalyst Mixer Pump	0.33	0.36	4.07	1.36
Fluid Transfer Pumps	1.00	0.15	4.02	16.28
Dryer Pump	4.00	0.37	4.07	16.28
Total	16.83	-	-	70.56

If the engine were to be replaced with a single-cylinder CI engine, such as the one used for the preceding experiments, the potential exists to reduce the required glycerol amount. The Yanmar L100V engine has a peak output of 3.4 kW at 1800 RPM (6.2 kW at 3600 RPM); hence, it is able to meet the continuous energy requirements for biodiesel production at the given facility. In the original reformation system, the V8 SI engine utilized only syngas in order to fuel combustion and drive a generator, and was extremely inefficient as the engine was operating close to idle. By utilizing the much smaller Yanmar, it is conceivable that the engine would be able to make more efficient use of the energy content of the syngas mixture while relying on the produced biodiesel fuel to initiate the dual-fuel combustion process.

In order to allow for a comparison between the two engines, it is necessary to provide an expression to link the rate at which glycerol is reformed to the energy content of the produced syngas, or the total effectiveness of the reformation process. The original V8 engine required an input flowrate of 7.975 gal/hour of the glycerol/water mix (or 6.380 gal/hour of raw glycerol) in order to produce syngas at a rate of 14.716 g/s (or 158.2 kW of chemical potential energy) to produce 3.6 kW of power [82]. From this, it is possible to generate the following expression:

Syngas Reformation Effectiveness	$E_g = \frac{\dot{m}_s Q_{LHV,s}}{\dot{m}_g}$	(22)

where the mass flow rate of syngas (in g/s), the lower heating value of the syngas (in kJ/g), and the rate of consumption of the glycerol (m_s, in gal/hour) are used to evaluate the glycerol reformation effectiveness

(E_g) of 24.80 kWh/gal. This effectiveness may then be utilized to estimate the necessary glycerol reformation rates needed to meet the syngas consumption rates utilized in testing with the Yanmar L100V (see Table 6), by reordering Equation 22:

Required Syngas Reformation Rate for Given Fuel Usage	$\dot{m}_g = \frac{\dot{m}_s Q_{LHV,s}}{E_g}$	(23)

To this end, a second analysis was performed for glycerol reformation and combustion using the Yanmar L100V operating at 30% *ESR* and 1800 RPM. The power production rates utilized in Table 7 were scaled uniformly by a factor of 1.219 to be constrained to the engine's operational limits; i.e., the 2nd oil filtering stage now draws a constant 3.4 kW, or 100% rated engine load at 1800 RPM. This further ensures that the Yanmar was running at engine loads higher than idle where measurement uncertainty is generally the greatest. Required syngas and biodiesel flow (and energy) rates into the engine to achieve given power production rates were scaled using linear interpolation of the data given in Table 6. Finally, the necessary reformation rates of glycerol for each stage of the biodiesel production process were solved using Equation 23 and are given in Table 8.

Table 8: Power production of optimized Yanmar L100V operating at 1800 RPM and 30% *ESR*.

Phase	Output Power [kW]	Biodiesel Flowrate [g/s]	Syngas Flowrate [g/s]	Syngas Power [kW]	Glycerol Flow Rate [gal/hour]
Oil Filter Stage 1	1.56	0.105	0.220	2.367	0.095
Oil Filter Stage 2	3.40	0.187	0.304	3.270	0.132
Reactor Pump	0.48	0.069	0.147	1.580	0.064
Catalyst Mixer Pump	0.44	0.067	0.144	1.551	0.063
Fluid Transfer Pumps	0.18	0.059	0.127	1.366	0.055
Dryer Pump	0.45	0.068	0.145	1.558	0.063

The result of this analysis is a large increase in the expected efficiency when utilizing the smaller Yanmar engine. In the 2nd Oil Filtering stage alone, the Yanmar utilizes a reformation rate of only 0.132 gal/hour (to the V8's 4.64 gal/hour), while also producing 3.4 kW of output power (to the V8's 2.79 kW). This obviously comes at a price of shifting the energy burden onto the biodiesel fuel, but the power input of the biodiesel (7.335 kW) and the syngas (3.270 kW) together is only 10.605 kW. Using Equation 23 and solving for the necessary syngas flowrate, the V8 engine is shown to consume syngas at a rate of 10.7 g/s, or 115.05 kW, a full order of magnitude higher than the total energy consumption rate of the Yanmar.

From the known glycerol reformation rates, the total amount of glycerol needed to power the entire reformation process can be ascertained in Table 9. In addition, the required biodiesel fuel flow rates were also solved for each phase of the process through linear interpolation. In total, the optimized reformation process utilizing the Yanmar L100V engine would use 1.326 gallons of glycerol and 1.688 gallons of biodiesel, while producing 12.186 gallons of glycerol and 46.308 gallons of biodiesel, yielding a net gain of 10.860 and 44.620 gallons of glycerol and biodiesel, respectively. In addition, the process would require 0.265 gallons of water to mix with the pure glycerol prior to reformation. Plotting the comparative glycerol reformation rates of the two engines (see Figure 25) shows that, while it is capped at a maximum power output of 3.4 kW at 1800 RPM, the optimized Yanmar L100V serves as a more efficient platform when the necessary power output of the system is relatively small. This is because of the shift to lean CI combustion from stoichiometric SI operation, and engine friction is significantly reduced moving from eight cylinders down to one.

Table 9: Energy and glycerol/water flow rates for optimized biodiesel production in a Yanmar L100V engine.

Phase	Pure Glycerol [gal]	Water [gal]	Biodiesel [gal]
Oil Filter Stage 1	0.286	0.057	0.343
Oil Filter Stage 2	0.330	0.066	0.511
Reactor Pump	0.382	0.076	0.449
Catalyst Mixer Pump	0.021	0.004	0.025
Fluid Transfer Pumps	0.055	0.011	0.065
Dryer Pump	0.251	0.050	0.295
Total Required	1.326	0.265	1.688
Total Produced	12.186	-	46.308
Net Gain	10.860	-0.265	44.620

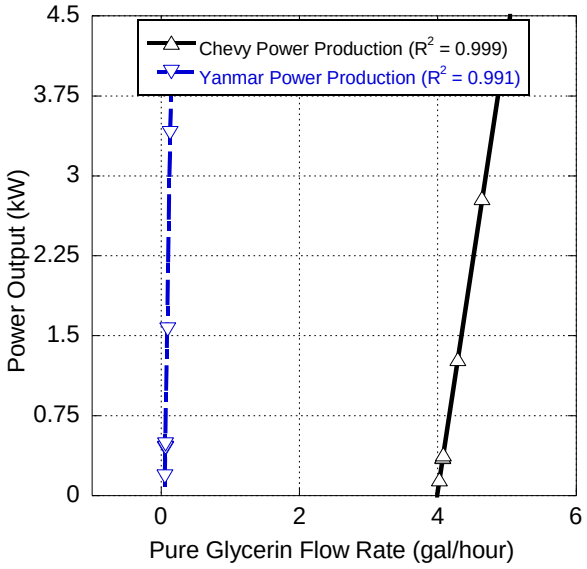

Figure 25: Comparison of glycerol reformation rates needed for equivalent power production using the original Chevrolet 350 and the Yanmar L100V engines [82].

In this scenario, a small biodiesel production facility utilizing this optimized process would be able to provide suitable power to run the entirety of the reformation process off biodiesel and reformed syngas, while only utilizing 10.88% of the total glycerol by-product and 3.65% of the biodiesel. Increasing power production to exhaust the supply of glycerol could be possible by operating the engine at peak load (and efficiency) to produce 279.7 kWh of energy. Using up the entirety of the glycerol supply in this manner would take approximately 82 hours, and require the use of 2.17 additional gallons of water while consuming another 16.82 gallons of biodiesel fuel.

The primary obstacle for this process is the large variation in the required glycerol reformation rate from 5.3% of rated load during the fluid transfer process to 100% during the 2nd oil filtration stage. However, a potential solution could be the inclusion of battery-electric charging, keeping the engine running at or near 100% of rated engine load, thus, maximizing its efficiency. This system could then discharge the batteries when a relatively lower energy supply is required. Alternatively, the Yanmar could be kept running at rated load at all times, and any excess power could be used for other purposes or diverted to the electrical grid and sold via a net metering scenario.

3.6 Conclusions

Glycerol reformation into a hydrogen-rich syngas that is subsequently burned for energy generation provides a means to power a biodiesel production facility. Usage of this syngas within a CI engine is possible with minimal engine modifications through dual-fuel usage with biodiesel. The behavior of this dual-fuel combustion is largely a function of the quantity of syngas being utilized, along with the engine load. Increasing the amount of syngas leads to a growth of cylinder peak pressure, subsequently increasing the amount of pre-mixed combustion. This is due to the effects of the syngas homogenizing the fuel content throughout the cylinder, promoting prompt combustion. Despite these changes, the net change in ignition delay is minor as *ESR* increases because of the high auto-ignition temperatures of hydrogen and methane (the primary fuels in the syngas); hence, minimal adjustments to injection timing are required to maintain efficient engine operation, and the most important aspect to the prediction of ignition timing is through the preparation of the biodiesel fuel pilot.

Changes in fuel consumption of biodiesel and syngas are linear with respect to changes in *ESR*, and overall fuel and energy consumption increases with *ESR* as engine volumetric efficiency (and overall oxygen content) decreases, inhibiting the dual-fuel combustion process. This, along with a transition to flame-propagation controlled combustion, leads to increased methane, hydrogen, and THC emissions. Furthermore, emissions of PM increase with engine load, but decrease significantly with added *ESR* due to the lesser amounts of liquid fuel injected and the transition from heterogeneous to homogeneous combustion. Emissions of NO_x compounds were subject to complex behaviors and (on average) were unchanged as *ESR* increased. Most significantly, emissions of NO_2 were dominant and generally increased with *ESR*. Overall, relatively low ratios of NO to NO_2 were emitted for all *ESR*s tested, except at high engine loads. This behavior is largely due to the nature of the syngas combustion (i.e., homogeneous flame propagation) that smooths the temperature gradient by moving combustion away from the fuel spray region, leading to an increase in flame quenching near the wall. This behavior may change at higher loads, where in-cylinder temperatures may begin to favor NO over NO_2.

Glycerol reformation using previously established techniques produces 24.80 kWh worth of syngas for every gallon of glycerol used. This reformation effectiveness is a useful tool for sizing the operation of a biodiesel production facility. Optimization of dual-fuel combustion for an appropriately sized facility using the tested single-cylinder engine leads to significant increases in process efficiency over previous efforts. Only 10.88% of the total glycerol by-product generated and 3.65% of the biodiesel produced by the biodiesel facility is required for self-sufficiency. However, the significant variation in glycerol reformation rates suggests the requirement of a battery storage system or connection to the electrical grid to sell the excess power in a net metering scenario for more efficient engine utilization. Ultimately, the potential exists for efficient power production from dual-fuel operation with biodiesel and syngas, with a single-cylinder CI engine useful for small-scale biodiesel production.

Chapter IV: Diesel Engine Knock and Noise Analysis

Material published as "Comparison of Injection Systems with Respect to Compression Ignition Engine Knock," SAE International, Technical Paper 2018-01-0219, April 10th, 2018

4.1 Abstract

Diesel knock and ringing combustion in compression ignition (CI) engines are largely an unavoidable phenomenon and are partially related to the overall effectiveness of the fuel injection process. Modern electronic fuel injection systems have been effective at reducing the intensity of knock in CI engines, largely through optimization of fuel injection timing, as well as higher operating pressures that promote enhanced fuel and air mixing. In this effort, a single-cylinder CI engine was tested under a number of different combustion strategies, including a comparison of mechanical and electronic injection systems, increasing fuel injection pressures for biodiesel fuels, and the usage of dual-fuel combustion with compressed natural gas (CNG). Using in-cylinder pressure traces and engine operational data, the difference in injection mechanisms, fuel preparation, and their effects on knock intensity is clearly illustrated. This allows a means of comparison across multiple engine combustion modes, including mechanical vs. electronic injection, injection of various fuels through a common injection system, and standard operation against dual-fuel operation. In particular, the effect of higher injection pressures and fuel flow rates on reducing knock in some cases is highlighted. In addition, cyclic variability in the severity of ringing combustion appears to be a function of the ability of the fuel system to re-pressurize between engine cycles. This offers a potential means to provide for diagnosis of engine fuel pressurization system deficiencies through variability in ringing combustion, even if these deficiencies would not be discernible from normal measured operational characteristics.

4.2 Introduction

Within spark ignition (SI) internal combustion engines, unwanted autoignition of the fuel-air mixture, aka knock, is a constant, but controllable, side effect of combustion [1, 110]. While usually

easily mitigated, uncontrolled or prolonged engine knocking can result in increasing damage to the engine. Compression ignition (CI) engines also suffer from a more limited form of knock, as while spontaneous ignition of the entire fuel-air mixture at once is highly unlikely, smaller pockets of fuel and air will still produce a milder (but still potentially damaging) autoignition if heavily compressed by combustion [111, 112]. Therefore, it is of importance to characterize the severity and intensity of engine knock within CI engines.

One common indicator of knocking combustion, particularly for CI engines, is the formation of high frequency pressure waves [1]. These waves are characterized as pressure ringing; hence, CI engine knock is often known as ringing combustion. This knocking behavior is largely linked to premixed combustion and subsequent rapid pressure rises; thus, CI knock is extremely common. These pressure oscillations can be readily observed within in-cylinder pressure traces, as a waveform visible on the trailing edge of the pressure rise from combustion (see Figure 26) [1].

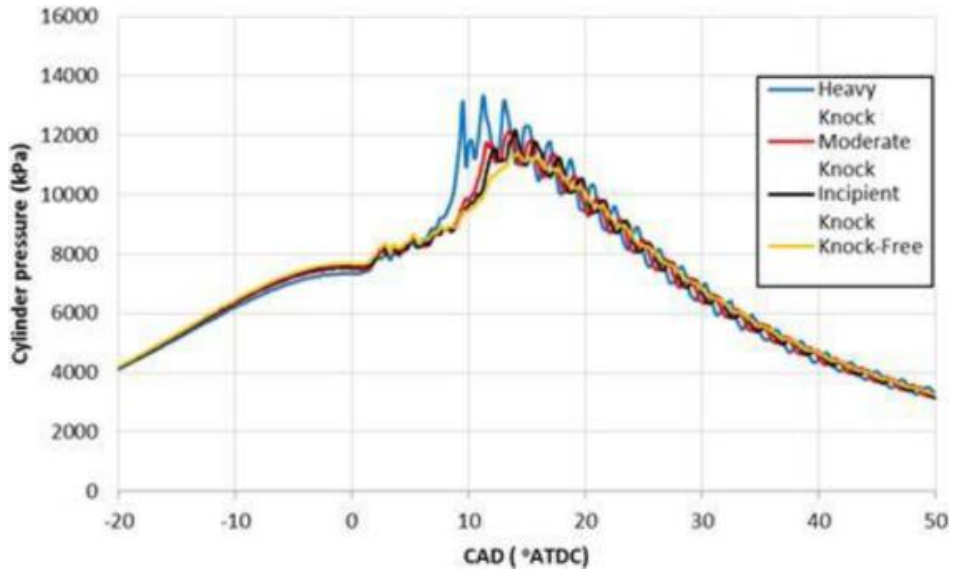

Figure 26. In-Cylinder Pressure Traces for a CI engine undergoing various amounts of knocking combustion [113].

This behavior is further accentuated in CI engines operating under dual-fuel regimes, often with the addition of gaseous fuels like compressed natural gas and hydrogen-rich syngas [114]. In these cases, the rising amount of fuel energy provided by the gaseous fuel leads to an increase in the amount of fuel prepared for combustion at ignition, as gaseous fuels do not have to undergo injection, atomization, or

vaporization like liquid hydrocarbon fuels. Therefore, with more fuel prepared prior to ignition, premixed combustion is enhanced. While this would normally be advantageous by smoothing the in-cylinder pressure rise from combustion, these gaseous fuels typically have higher autoignition points. Therefore, they will only autoignite due to compression from combustion, and not from the compression stroke of the engine. As a result, if gaseous fuels experience engine knock at all, the process will generally be much more intense than during operation consisting of only liquid fuels.

The frequencies of knocking combustion are identified through the creation of a signal power spectrum from the in-cylinder pressure trace, commonly using Fast Fourier Transform (FFT) algorithms. Figure 27 showcases one such power spectrum of a single-cylinder engine under operation at 3300 RPM and 75% load. Areas where the emission spectrum peaks represent frequencies of particularly strong signals within the unfiltered dataset; here, the local peaks occur at 0.63, 6.2, 9.5, and 12.9 kHz. These individual signals are largely washed out of the dataset without filtering, due to the overwhelming presence of lower-frequency signals. Here, the primary signal is at 27.5 Hz, corresponding to the compression, combustion, and expansion events occurring once every two cycles at 3300 RPM (55 Hz). Other local peaks have the potential to wash out the high-frequency signals within the dataset, such as the signal at 0.63 kHz due to fuel injection. Therefore, in order to remove the influence of the low-frequency signals, a filter is required, ideally a high-pass or band-pass filter to remove frequencies below 4-6 kHz [1].

Overall, since CI knock is a function of the amount of premixed combustion present in a given engine cycle, knock can be characterized as being dependent on the controllable parameters affecting the onset and intensity of combustion; injection pressure, injection timing, and fuel flow rate. Generally, experimentation has shown that increasing or advancing these operational parameters leads to a growth in knocking combustion [111, 112, 115-117].

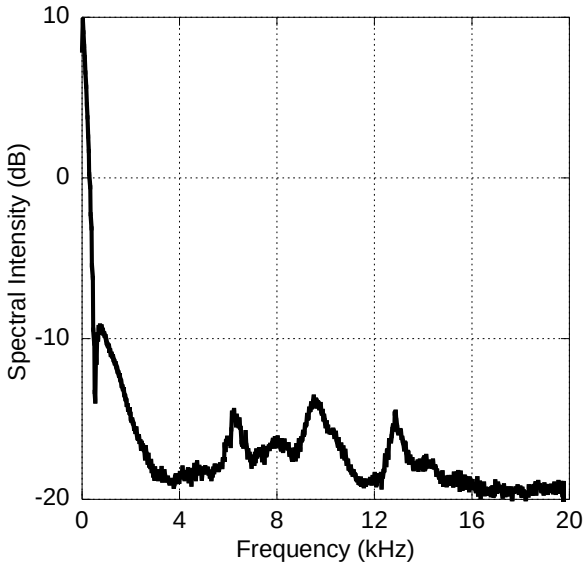

Figure 27. Sample power spectrum of a Yanmar L100V operating at 3300 RPM and 75% of rated load, from measured pressure trace.

Two primary strategies governing fuel injection have been commonly implemented on CI engines; mechanical fuel injection, and common-rail electronic injection technologies. Older mechanical systems are driven entirely by their parent engines via the crankshaft or timing belt, and are relatively simpler to manufacture and use. While mechanical injection is no longer utilized for modern automotive applications, they are still in use within generators or aircraft engines, where engine operation is typically limited to a relatively small speed range and finer engine controls are either prohibitively expensive or simply unneeded [35]. Such mechanical systems typically operate at lower injection pressures than modern systems. In addition, mechanical injection pump systems are largely limited to a single injection event per engine cycle [35]. As such, the static and unchanging nature of mechanical systems means they can be manufactured to avoid knock, but also lack any techniques to mitigate knock should it occur.

Modern electronic injection systems are computer-controlled, utilizing the engine control unit (ECU) to modulate fuel flow rate into the cylinder. Utilizing direct electronic control allows for fine control of an engine over wide speed and load ranges [35]. As a result, variable injection timings and higher injection pressures may be utilized. Furthermore, modern electronic systems have the ability to undergo multiple injection events per engine cycle. A negative result of this, though, is that increased

injection pressures may lead to more intense CI knock. However, this is commonly mitigated by utilizing pilot injections to smooth the rise in pressure during the premixed spike.

This work details a direct comparison between mechanical and electronic injection knock within a high-compression ratio, single cylinder CI engine, with the electronic injection system undergoing only one injection event per cycle to increase the parity between the two operational modes. As such, the advantages of electronic fuel injection technologies over mechanical technologies with respect to knock are highlighted. At the same time, the potential dangers associated with the electronic system are also made apparent, particularly at midrange engine loads where premixed combustion is most readily apparent. Furthermore, findings in relation to fuel injection pressure and CNG-assisted diesel combustion for the electronic injection system are presented highlighting the impact of fuel preparation on knock.

4.3 Experimental Setup

To investigate the effects of injection strategy on ringing combustion and engine knock, engine testing on the same single cylinder engine was accomplished. The characteristics of the engine, a Yanmar L100V coupled with a DyneSystems Dymond Series alternating current (AC) dynamometer, are given in Table 10, while a comparison of the two injection systems is provided in Table 11. Of note, all tests utilized ultra-low sulfur diesel (ULSD) with a density of 837 kg/m3, and a lower heating value of 41.53 MJ/kg. In addition, the engine's standard exhaust gas recirculation (EGR) port in the cylinder head was blocked.

Engine operation was monitored through a National Instruments (NI) LabVIEW program, gathering data at 10 Hz over two minutes. A second LabVIEW system was utilized for capturing the in-cylinder pressure trace, recording 60 consecutive engine cycles (or 120 revolutions), at a resolution of 0.2° of crank angle [73]. A third NI system was also utilized to log emissions data from an AVL SESAM-FTIR emissions analyzer. While not presented here, this emissions data was collected at a rate of 1 Hz over a five minute period, and was used to characterize the cyclic combustion efficiency values utilized in

calibrating a model to calculate the engine-out rate of heat release (RHR) utilized within this work [13, 118].

Table 10. Engine and Dynamometer Specifications [73].

Engine Manufacturer/Model	Yanmar L100V
Type	Vertical Direct-Injected
Intake	Naturally Aspirated
Cooling	Air-Cooled
Cycle	4-Stroke
Displacement [cc]	435
Number of Cylinders	1
Number of Valves	2 (1 intake, 1 exhaust)
Bore [mm]	86
Stroke [mm]	75
Connecting Rod Length [mm]	118
Crank Radius [mm]	38
Clearance Volume [cm^3]	21.611
Piston Area [cm^2]	58.088
Compression Ratio	21.2
Continuous Rated Output [hp]	8.3
Rated Speed [RPM]	3600
Engine Oil Used	Shell 15W-40
Dynamometer Manufacturer/Model	DyneSystems, Inc. Dymond Series 12
Continuous Rated Torque [N-m]	28.61
Continuous Power [hp]	12
Maximum Speed [RPM]	7500
Voltage [VAC]	480
Phase	Three Phase
Frequency [Hz]	60
Controller	DyneSystems, In. Linter-Loc V OCS

Table 11. Fuel Injector System Comparison [35, 73].

Type	Mechanical	Electronic
Part #	71430-53100	0-445-10-183
Injection Timing [° BTDC]	15.5	Variable
Injection Pressure [MPa]	19.8	Variable, under 200
Controller	Engine Governor	Bosch MS15.1 ECU

Engine torque is measured with a FUTEK transducer (Model #TRS-705) installed between the engine output and dynamometer input shafts. Fuel flow is measured through a Micro-Motion Coriolis flow meter (Model #CMF010M), and inlet air flow is catalogued through a Merriam laminar flow element (Model #50MW20-2) with an Omega differential pressure transducer (Model #PX277-30D5V). A combination of a Kistler pressure transducer (Model #6052c) and encoder (Model #2614B) are utilized

to acquire in-cylinder pressure measurements. Further hardware specifications for this experimental setup may be found in Langness et al. [73].

Operation with the mechanical injection system was achieved at 3600 RPM, with the speed determined by the constraints of the mechanical injector and the engine's built-in speed governor. Engine load control was provided by the AC dynamometer with the built-in governor responding to the dynamometer's load by increasing or decreasing the required fuel flow rate [35, 119]. The mechanical injector and speed governor were later removed in favor of the electronic injection system controlled by a Bosch MS15.1 ECU, with ECU monitoring and operation provided by Bosch Modas Sport. Here, engine operation was reduced to 1800 RPM, and the AC dynamometer was instead used to control engine speed. Engine load was adjusted directly by the user through an engine torque command, causing the ECU to increase or decrease in fuel flow rate in order to meet the required demand. Engine injection timings were adjusted in order to keep the engine operating at maximum brake torque (MBT) for that engine load [16]. The electronic injection system was also held to an operating pressure of 42±0.5 MPa unless otherwise noted.

To facilitate combustion of gaseous fuels for dual-fuel operation, bottled gaseous fuels are introduced to a mixing box mounted on the intake-side of the engine, allowing for adequate mixing of gaseous fuel and fresh air to create an essentially homogeneous mixture [43, 73]. Flow of gaseous fuels are controlled and monitored through a Brooks mass flow controller (Model #SLA5850s) mounted between the gas cylinder and mixing box [73].

The engine was operated at a fraction of the rated engine load at each speed, which was 18.0 N-m for both operational settings [16, 119]. The fractions of engine load, therefore, are referred to as idle (0.5 N-m, to reduce the variability of testing an 'unloaded' engine), 25% (4.5 N-m), 50% (9.0 N-m), 75% (13.5 N-m), and 100% (18.0 N-m). Engine operation was monitored until the engine reached steady-state operation, characterized as a change in exhaust and oil temperatures of less than 1% over a 60 second period [73]. The engine was run with only a single injection event per cycle so as to provide a direct

comparison between the two injection systems, as the mechanical system is limited to only a single injection event per cycle.

Filtering of the in-cylinder pressure traces was achieved through application of a high-pass filter to attenuate frequencies below 4 kHz [1]. For each individual experiment, the high-pass filter was applied to each of the 60 individual engine cycles in order to maintain the oscillatory behavior of each cycle. After filtering, the highest amplitude of oscillation within the pressure trace in the vicinity of top dead center (i.e., excluding valve events) was catalogued for each cycle. Finally, the average and standard deviation of oscillation for each experiment were calculated. Design and application of the filter was achieved through the *filtfilt* and *fft* commands within MATLAB, respectively. In addition to the pressure filtering, the pressure data was run through a MATLAB program developed by Shahlari et al. in order to calculate the amount of combustion noise present in engine operation [120].

4.4 Comparison of Mechanical and Electronic Injection Systems

Figure 28 shows the pressure traces for each injection system, and each engine load, given as a function of crank angle. At idle and 25% load (see Figure 28(a) and (b)), the deviation between in-cylinder pressure is due entirely to the difference in injection timings, injection pressures, and in-cylinder temperatures. In particular, while the electronic injection system is optimized for each engine load individually (10-12.5° BTDC), the mechanical injection system is reliant on a static injection timing that is held constant across all engine loads (15.5° BTDC).

This delay in injection timing for the electronic system results in slightly later atomization, despite the differences in injection pressure. This deviation decreases as engine load increases, to the point that the pressure traces are nearly identical past 50% load, likely related to the fact that the mechanical injection system was optimized for the higher engine loads (i.e., its injection timing was set to achieve MBT at 100% of rated engine load). When the electronic system was installed, optimal injection timings for each engine load had to be reacquired. As a result, the deviation between the mechanical and electronic injection systems is likely a combination of possible error in the MBT analysis, and inability of

the mechanical injection system to achieve optimal operation at lower loads. In either case, this deviation decreases substantially as engine load increases, indicating that the MBT analysis approaches the factory optimization of the engine with added load.

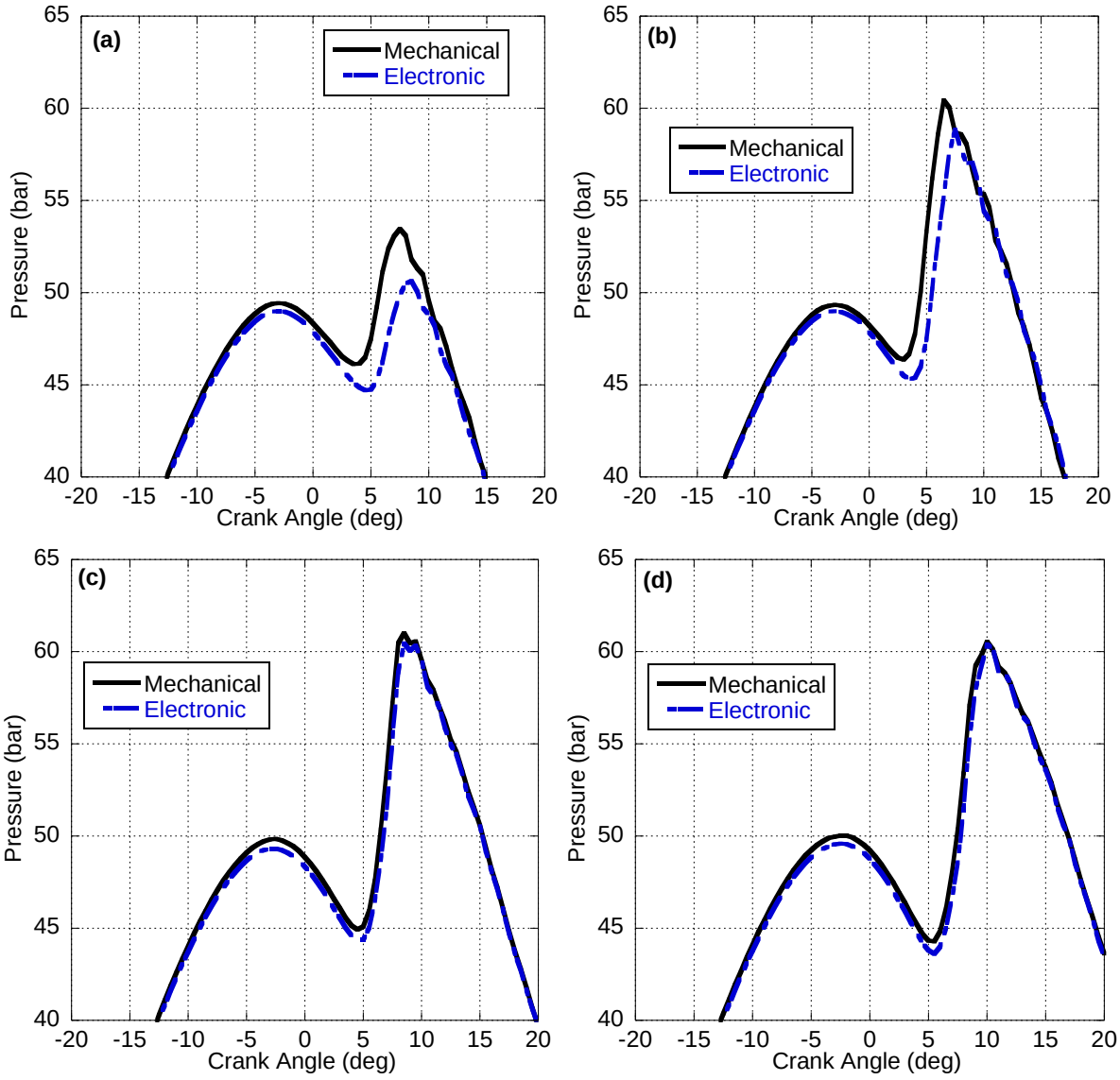

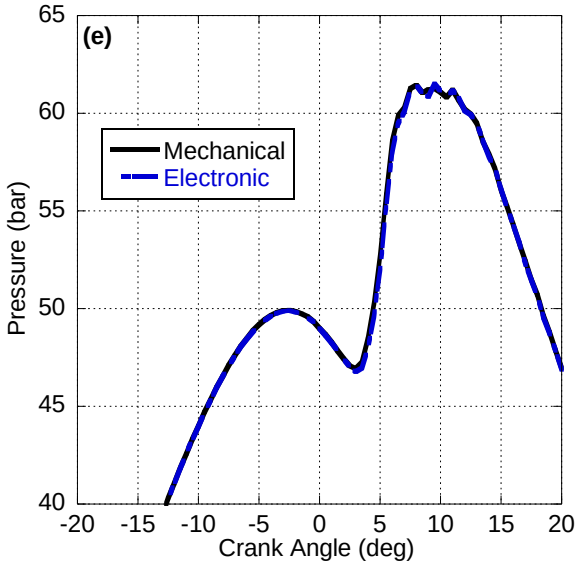

Figure 28. Measured in-cylinder Pressure Traces with respect to Crank Angle for (a) 0%, (b) 25%, (c) 50%, (d) 75%, and (e) 100% load for mechanical and electronic injection systems.

In addition, peak cylinder pressures near TDC for operation with the mechanical injection system are slightly higher than those of operation with the electronic system, approximately 0.5-0.8 bar. This effect is assumed to be due to the decreased engine speed (leaving more time for heat transfer in the vicinity of TDC, albeit at a lower level of turbulence) when testing with the electronic injection system, and tends to decrease with engine loading as the engine comes up to higher operational temperatures.

Figure 29 shows the RHR of the engine for each injection system as a function of crank angle. For every operational load, it can be seen that the mechanical injection system experiences slightly more diffusion-based combustion. In both systems, diffusion-dominated combustion is a function of increasingly poor fuel mixing and atomization, as the engine struggles to inject and prepare enough fuel prior to (and sometimes during) the premixed combustion phase. The difficulties of the mechanical injection system are due in part to its lower injection pressure, which limits the ability of the fuel to atomize and vaporize as a part of the physical ignition delay process. In addition, the higher speed of testing with the mechanical injection system provides a smaller window of time for the injected fuel to prepare fully prior to the onset of combustion; although increased levels of turbulence will facilitate enhanced mixing. However, the mechanical injection system also injects earlier adding to the necessary time required to prepare the fuel.

For the electronic injection system, increasing load up to 9.0 N-m leads to a direct increase in the premixed combustion phase, with a limited growth in the amount of diffusion burn. Above 9.0 N-m, the electronic system begins to encounter the same ignition delay issues as the mechanical system; i.e., not enough fuel can be added to the cylinder prior to the onset of combustion. Thus, at 13.5 and 18.0 N-m, the engine experiences a limitation in the peak RHR from the premixed spike, and whatever additional energy is required to meet the given load must come from diffusion-dominated combustion. As a result, despite the difference in engine speed and injection strategy, the RHR at 18.0 N-m for the two engine injection systems begins to resemble each other.

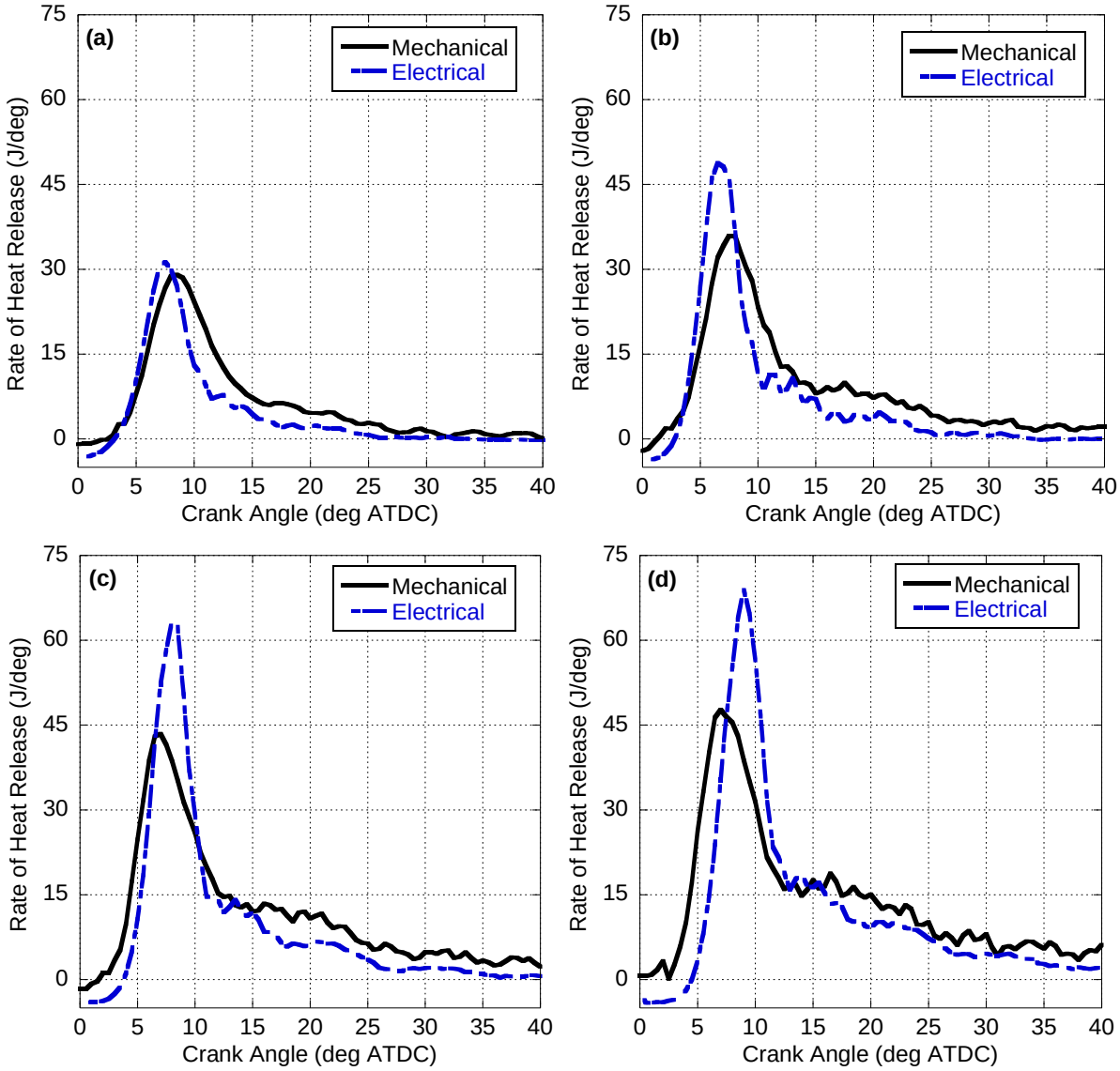

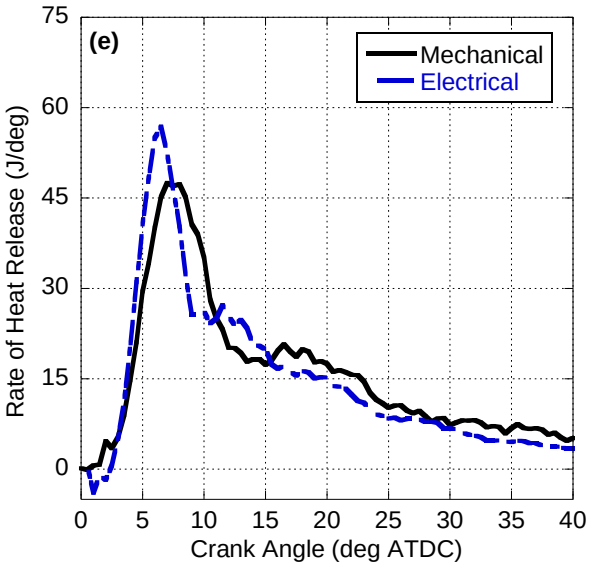

Figure 29. Rate of Heat Release with respect to Crank Angle for (a) idle, (b) 25%, (c) 50%, (d) 75%, and (e) 100% load for mechanical and electronic injection systems.

The overall cycle-averaged noise for the mechanical and electronic injection systems is shown in Table 12, calculated using an algorithm by Shahlari et al. [120]. While the mechanical and electronic injection systems will deviate in terms of overall engine noise relative to each other (due to the change in engine speeds), the noise from combustion itself should remain relatively consistent with respect to changing engine speeds. As a result, in order to remove the effects of engine speed, only combustion noise is considered, which is calculated directly from the pressure trace. Between the mechanical and electronic injection systems, the mechanical system has a higher amount of combustion noise, indicative of higher degrees of knock and ringing combustion. For each system, the overall combustion noise increases from idle to 50% of rated load, and then is reduced from 50% to 100% of rated load. This is consistent with the RHR results, and indicates a rise in combustion noise (and likely CI knock) as a function of the magnitude of the premixed combustion phase. Past 50% load, diffusion-dominated combustion contributes a significant amount to the total fuel heat release, and thus a lower amount of combustion noise, indicative of less engine knock relative to operation at 9.0 N-m.

Table 12. Cycle-averaged Combustion Noise for mechanical and electronic injection systems.

Engine Load [N-m]	Noise (Mech. Inj.) [dB]	Noise (Elec. Inj.) [dB]
0.5	95.65	87.14
4.5	98.96	92.17
9.0	100.20	93.61
13.5	99.99	92.79
18.0	98.00	90.98

The average pressure traces for the engine after filtering is applied, as well as the peak amplitude of oscillation for each individual engine cycle, are shown for idle (Figure 30), 25% (Figure 31), 50% (Figure 32), 75% (Figure 33), and 100% (Figure 34) of rated engine load. In addition, the average peak amplitude across the 60 thermodynamic cycles, and the absolute and relative standard deviation in those peak amplitudes for mechanical and electronic injection, are provided in Table 13 and Table 14, respectively.

At engine idle, the engine is unsurprisingly operating with the least amount of ringing combustion, with the average amplitude of engine ringing being the lowest for both the mechanical and electronic systems. Here, the mechanical system experiences ringing oscillations of approximately 2.90 bar, while the electronic system only experiences 1.03 bar of oscillations. This muting in ringing is directly related to the low flow rate of fuel entering the engine, and the ease with which both injection systems can adequately mix the fuel. This lesser amount of ringing combustion is also evidenced by the relatively small standard deviation away from the average (±0.40 and ±0.36 bar for mechanical and electronic, respectively). In this case, while the engine cyclic variability is relatively high (mainly as a function of the low engine load), this variability does not appear to translate into absolute variability of combustion ringing. However, while oscillations are smaller in an absolute sense, the relative standard deviation (as a percentage of the total knocking amplitude) is more significant in the electronic system than the mechanical system. While this relative variability in the electronic injection is the most extreme among all loads tested, it is likely that the engine's low load is making a significant contribution to the amount of variability seen in the pressure oscillations of both injection systems, and thus skewing the variability of the knock readings.

Table 13. Magnitude of pressure oscillations for engine operation with mechanical injection.

Engine Load [N-m]	Average Ringing Amplitude [bar]	Standard Deviation of Ringing [bar]	Relative Standard Deviation [%]
0.5	2.90	0.40	13.91
4.5	4.99	0.59	11.84
9.0	5.37	0.76	14.16
13.5	4.24	0.57	13.44
18.0	3.92	0.59	15.16

Table 14. Magnitude of pressure oscillations for engine operation with electronic injection.

Engine Load [N-m]	Average Ringing Amplitude [bar]	Standard Deviation of Ringing [bar]	Relative Standard Deviation [%]
0.5	1.03	0.36	34.51
4.5	1.92	0.55	28.27
9.0	2.11	0.73	34.36
13.5	1.87	0.50	26.61
18.0	2.01	0.58	28.74

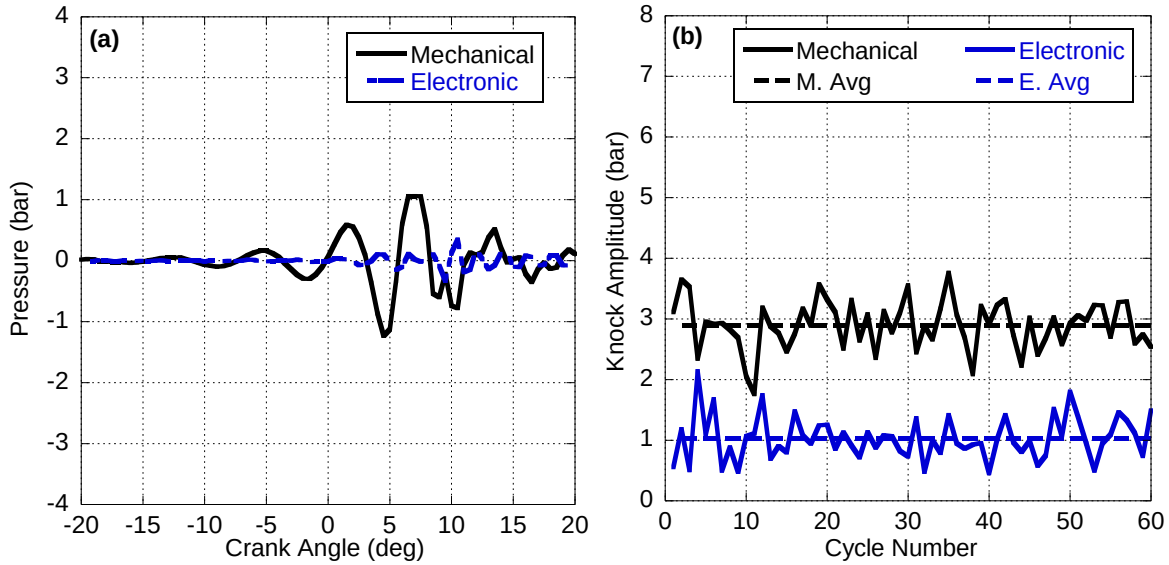

Figure 30. Averaged pressure oscillations (a) and cyclic peak oscillation (b) at 0.5 N-m.

At 25% engine load, ringing combustion increases significantly, with the mechanical system experiencing an average amplitude of 4.99 bar, and the electronic system encountering 1.92 bar. Variability between the mechanical and electronic systems also grew, with standard deviations of ±0.59 and ±0.55 bar, respectively. In both systems, increasing the fuel flow rate results in a significant intensification of the amount of energy added to the cylinder, augmenting the amount of premixed combustion and adding to the severity of knock. Both injection strategies are dealing with a relatively low

amount of overall fuel added to the cylinder, and so unburned atomized fuel is less likely to exist in the periphery of the cylinder in sufficient quantities and air/fuel ratios to lead to significant knock. As a result, ringing combustion remains relatively minor. Again, the relative variability of engine knock is more significant for the electronic injection system.

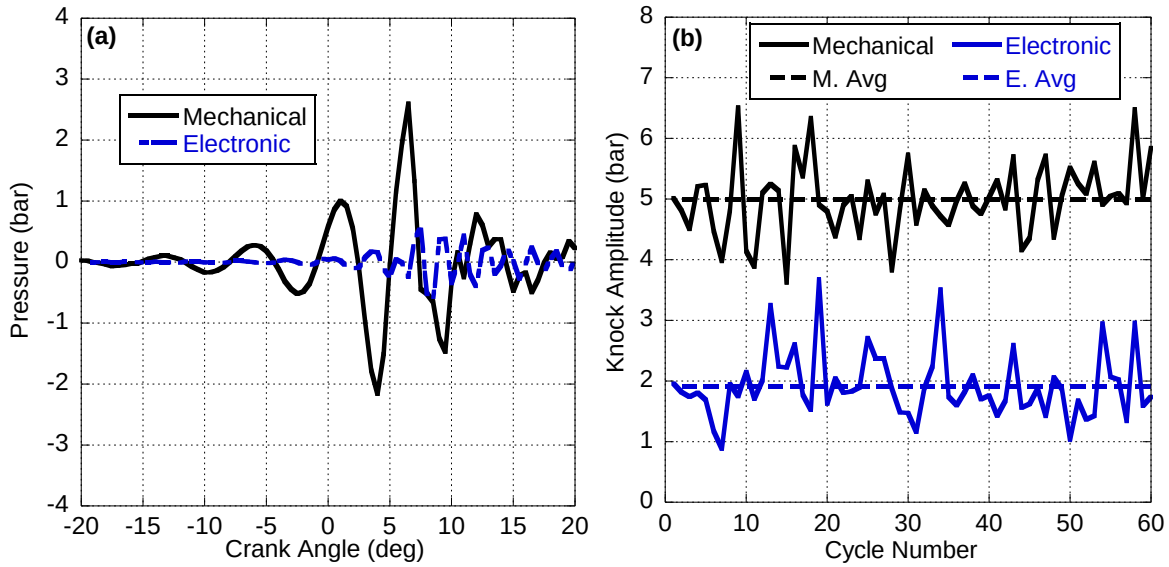

Figure 31. Averaged pressure oscillations (a) and cyclic peak oscillation (b) at 4.5 N-m.

At 50% of rated load, the engine experiences the most variable and violent ringing combustion of all of the engine loads tested, in keeping with the combustion noise and heat release data. Here, the mechanical and electronic systems encounter wave oscillations at amplitudes of 5.37 and 2.11 bar, respectively. In addition, the standard deviation of ringing amplitude between engine cycles of the mechanical and electronic systems amount to ±0.76 and ±0.73 bar, respectively. While the two systems experience relatively equal variability in an absolute sense, the unevenness of the electronic system is much greater relative to its average amplitude of oscillation.

In both systems, the fuel is relatively well-mixed, resulting in conditions highly prone to engine knock. Similar to the previous load, the higher average amplitudes of cylinder pressure oscillations is indicative of the added energy content. While the electronic system still outperforms its mechanical competition in terms of mitigating engine knock, its high cyclic variability may be related to the relative operating pressures of the two fuel systems. The mechanical system experiences a lower peak operating

pressure; hence, the fall in line pressure due to the injection event is relatively easier to overcome in time for the next engine cycle (i.e., the engine is more likely to maintain an even injection pressure between cycles). In comparison, the electronic injection system, operating at around twice the line pressure, will experience higher changes in injection pressure, particularly as the load increases. As a result, this may increase the likelihood that the injector system will not be able to maintain its ideal operating pressure, and so the amount of variability between engine cycles increases. This then causes variation in the amount of fuel prepared at the onset of combustion, changing the level of the premixed combustion phase. In essence, while the electronic fuel injection system is generally better able to mitigate the various effects that lead to engine knock, it is also less able to do so in a consistent manner. This is also demonstrated by the operation of the mechanical system, where the difference in relative variation between cycles is at its largest (other than at idle), further highlighting the relatively high amount of cyclic variation within the mechanical system (see Table 13 and Table 14). As the fuel flow rate into the cylinder increases, the pressures within both injection systems are less able to maintain consistent operation.

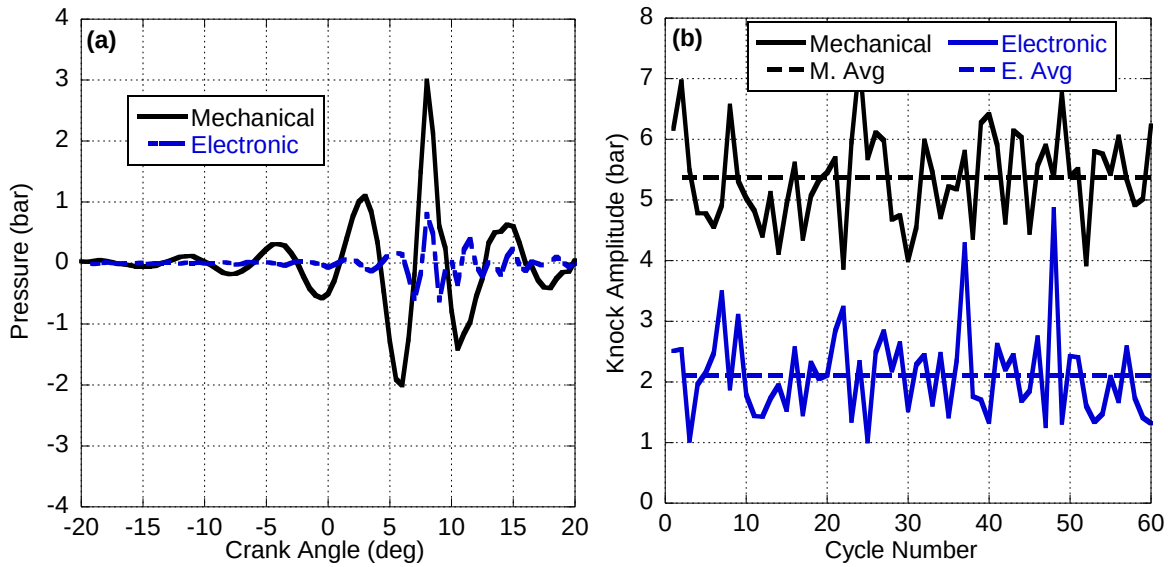

Figure 32. Averaged pressure oscillations (a) and cyclic peak oscillation (b) at 9.0 N-m.

Compared to 50% load, pressure oscillations at 75% load are much less pronounced, with the mechanical and electronic systems experiencing an average of 4.24 and 1.87 bar oscillation, respectively.

This again reflects the decrease in combustion noise seen for operation with both injectors (see Table 12). As mentioned before, this decrease is likely due to the onset of significant diffusion-dominated combustion for both injection systems. This slightly stifles ringing combustion by spreading out the rate of combustion and muddying the pressure oscillations. In addition, the smoothing of knock also reduces the overall cyclic variability of the oscillations, with standard deviations of ±0.57 and ±0.50 bar across the 60 cycles examined for mechanical and electronic injection, respectively. Relative cyclic variability is also reduced from 50% load, although the variability in the electronic system is still larger relative to the average oscillation.

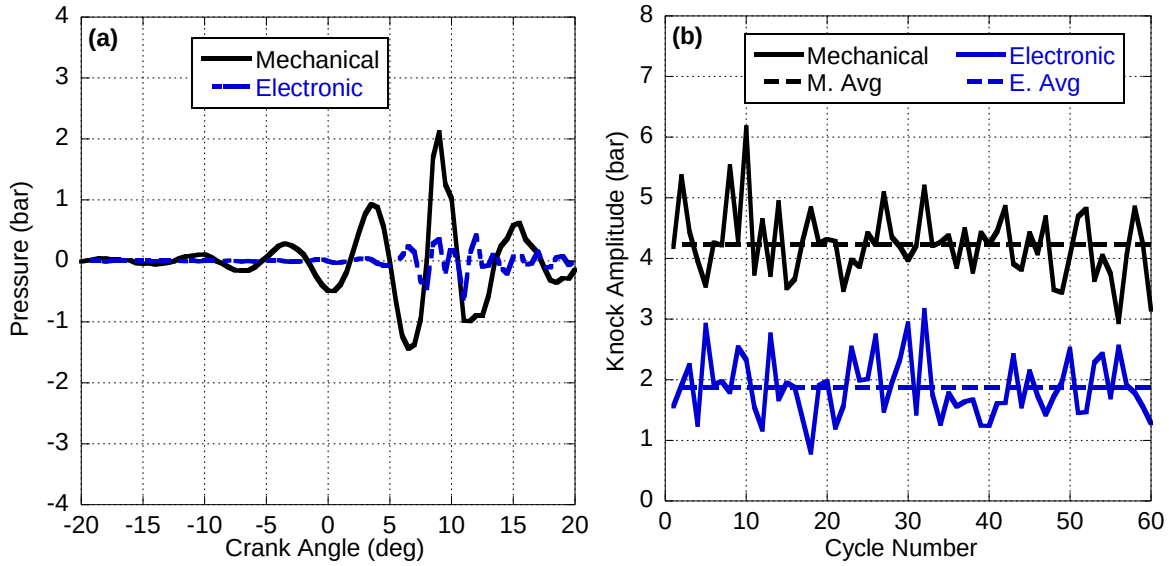

Figure 33. Averaged pressure oscillations (a) and cyclic peak oscillation (b) at 13.5 N-m.

In comparison to operation at 75% engine load, when increased to 100% load the amplitude of pressure oscillations decrease for the mechanical injection system (3.92±0.59 bar); however, the oscillations for the electronic system increase slightly (2.01±0.58 bar). Lower calculated noise values suggest that the increased level of diffusion-dominated combustion for both injection strategies helps to stifle CI knock. The increase seen in the ringing amplitude for the electronic case is likely a function of the advancement of injection slightly to achieve MBT (from 10° BTDC at 13.5 N-m to 11° BTDC at full load). As a result, more fuel is prepared in time for the initial premixed phase, followed by relatively good mixing of the later injected fuel, and a higher and earlier diffusion burn phase (see Figure 29(e)). Thus,

engine knock experiences a high initial oscillation due to the high amount of premixed fuel in the cylinder (and which may actually be more severe than in operation at 75% load), but this effect is immediately stifled (or potentially hidden) by more intense diffusion burn, resulting in the lower "averaged" engine knock and combustion noise of the cycle. Finally, because of the need to add significantly more fuel to achieve 100% load, the standard deviation of ringing increases for both injection strategies over 75% load as the fuel lines require continual re-pressurization.

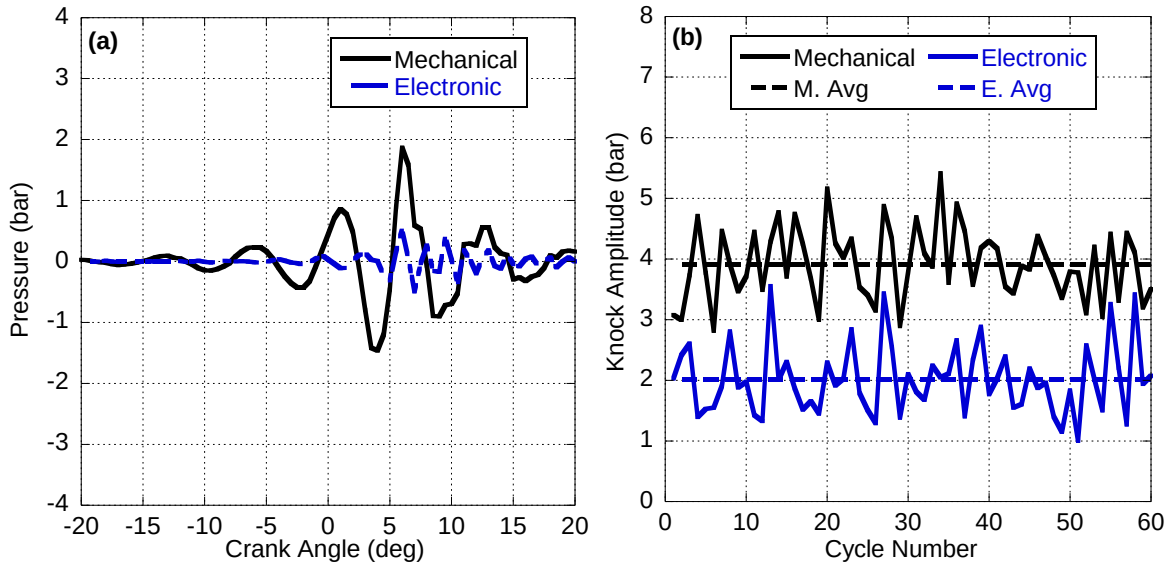

Figure 34. Averaged pressure oscillations (a) and cyclic peak oscillation (b) at 18.0 N-m.

Overall, the electronic injection system generally outperforms its mechanical counterpart. Initial inspection would expect the electronic injection system and its greater premixed burn phase to result in a larger level of CI knock. However, the ability of this injection system to increase atomization and homogeneity throughout the cylinder will lead to a more global (aka uniform) equivalence ratio. Hence, the packets of greater fuel-to-air ratios in the mechanical system can lead to local events of a more energetic (and noisy) combustion process. The trends with load between the two injection systems are similar as noise/ringing amplitude grows to the point of maximum pre-mixed burn and then falls due to a stifling effect of diffusion-dominated combustion. However, the electronic injection system undergoes a relatively higher cyclic variability in the magnitude of the pressure oscillations, ranging from 26.6% to 34.5%; opposed to only 11.8% to 15.2% for the mechanical injection system. This may be related to the

pressurization requirement in the fuel injector line. For the mechanical unit injection system, a lower pressure is required and the system can achieve this more readily. Whereas, in the electronic system, the relatively high pressure required results in more oscillations within the line subsequently finding their way into the ringing pressure analysis. As a result, operation of the electronic injection system with increased injection pressures at the same speed and load should lead to the presence of more intense knocking combustion as the injector system undergoes more cyclic oscillation, and fuel is prepared more quickly leading to a greater rate of pressure rise. This will also lower the amount of diffusion burn present in the cylinder that serves to stifle or mask the severity of ringing combustion.

4.5 Electronic Injection Pressure Variation

To further explore the nature of injection pressure on engine knock, the authors have considered a separate data set concerning variation in fuel injection pressure as a means to normalize biodiesel combustion [121]. Since biodiesel fuels typically have higher viscosities, they tend towards greater degrees of diffusion burn than ULSD under the same engine operating conditions. This manifests as a lower premixed spike apparent within the RHR, and as a lower overall peak operating pressure when utilizing fuel blends with higher biodiesel contents. Therefore, biodiesel fuels require greater fuel injection pressures in order to counteract the negative aspects of their higher viscosities; however, these same higher injection pressures may introduce more significant knocking combustion.

For these tests, the Yanmar L100V engine was operated using neat and blended Waste Cooking Oil (WCO) biodiesel, with ULSD as a control fuel. The properties of these various fuels are shown in Table 15 [121]. In each case, the engine was operated at 1800 RPM, and the injection pressure was increased from the control pressure (50.0 MPa) until the peak operating pressure of the engine matched that of the engine operating on ULSD. In all cases, injection timings were adjusted in order to maintain the same timing of peak pressure as was achieved with ULSD operation. For brevity, only the results of the fuel blends containing 20% biodiesel content or higher at 9.0 and 18.0 N-m are presented, as it is at

these loads that the interactions between fuel injection pressure, premixed combustion, diffusion burn, and engine knock are all significant and highly visible within the available data.

Table 15. ULSD and biodiesel fuel properties.

Characteristic	ULSD	W20	W50	W100
Biodiesel Composition [%]	0	20	50	100
Density [kg/m^3]	837.58	848.66	859.66	878.00
Kinematic Viscosity [cSt]	2.74	2.85	3.39	4.61
Dynamic Viscosity [cP]	2.31	2.42	2.91	4.05
Cetane Number [-]	48.61	49.45	50.71	52.80
Lower Heating Value [MJ/kg]	45.60	43.78	40.94	36.21
Energy Density [MJ/m^3]	38.42	37.15	35.19	31.79

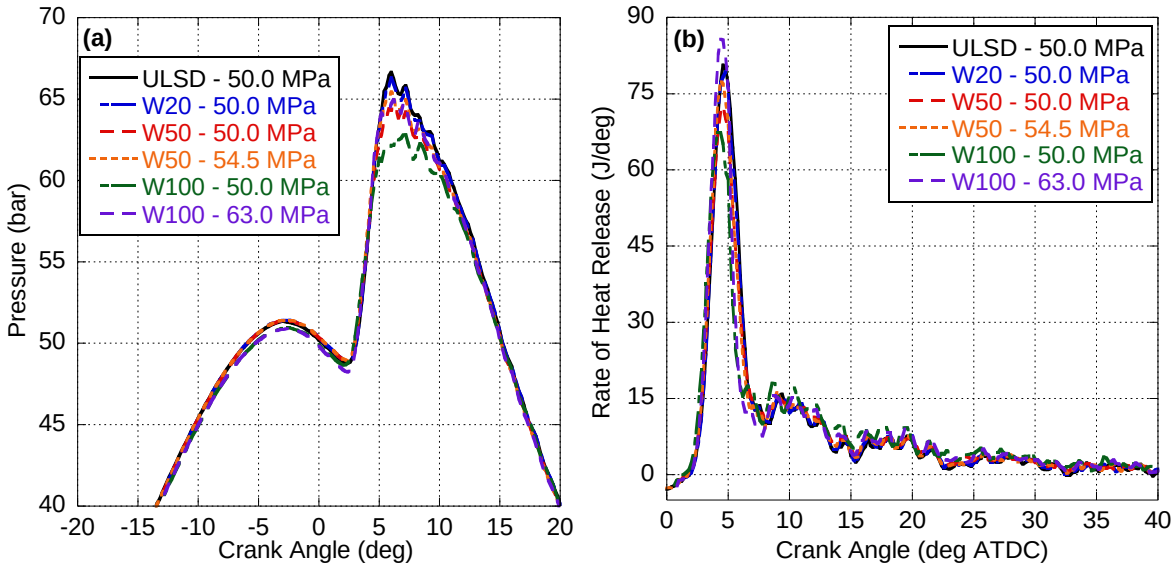

Figure 35. Measured In-Cylinder Pressure Traces (a) and Calculated Rate of Heat Release (b) with respect to Crank Angle for engine operation with high-percentage blends of ULSD and WCO biodiesel at 9.0 N-m.

At 9.0 N-m, the changes in in-cylinder pressure and overall RHR between differing fuel injection pressures are not readily apparent, except for the most extreme case (i.e., neat biodiesel, see Figure 35). Here, an increase in fuel viscosity leads to a subtle downward shift in peak cylinder pressure for constant fuel injection pressures, as well as a slightly depressed peak RHR. However, for all fuels tested, once the injection pressure was raised, peak cylinder pressures were brought back into the window expected from ULSD combustion, and peak RHR was raised slightly higher than that of ULSD. In all cases, this indicates that the injector is able to meet the demand for entirely premixed combustion. However, at the

same time the slight rise in diffusion burn for the neat biodiesel tests at 50.0 MPa illustrates that the injector is at its ideal performance limit, in that any further fuel flow rates will add to the diffusion-dominated regime, rather than the premixed spike.

Using both the standard filtering, as well as the algorithm developed by Shahlari et al., the magnitude of pressure oscillations and the cycle-averaged combustion noise were calculated and provided in Table 16. Overall, increasing biodiesel content and fuel viscosity was met with a decrease in average ringing amplitude and combustion noise intensity, likely pointing to the growth of diffusion-dominated combustion. By comparison, when fuel injection pressures rose to mimic the performance of ULSD, average ringing amplitude increased overall, and generally approached or slightly exceeded the knock performance figures of ULSD. This indicates a more severe ignition event as more fuel is injected and prepared, as to be expected. In addition, deviation in ringing also increased, pointing to higher cyclic variability related to the injection system struggling to maintain greater injection pressures, and a larger operational variation in pressure cycle-to-cycle (i.e., due to the difference in line pressure between the start of injection and immediately following it). With the pressure adjustment, combustion noise also rose, but stayed universally lower than combustion noise with ULSD (and slightly higher than combustion noise at lower injection pressures for the same loading, as shown in Table 11). Altogether, this information points to the injection pressure increase performing almost exactly as intended. In specific, increasing the fuel injection pressure for biodiesel fuels to mimic ULSD performance comes with both positive (i.e., higher RHR, less diffusion burn, higher cylinder pressures) and negative (i.e., greater knock from a larger premixed combustion) aspects.

Table 16. Pressure oscillations and combustion noise with biodiesel blends at 9.0 N-m.

Fuel Used	Injection Pressure [MPa]	Average Ringing Amplitude [bar]	Standard Deviation of Ringing [bar]	Combustion Noise Intensity [dB]
ULSD	50.0	2.48	0.63	94.36
W20	50.0	2.35	0.70	94.11
W50	50.0	2.05	0.50	93.04
	54.5	2.30	0.54	93.67
W100	50.0	1.79	0.46	91.53
	63.0	2.50	0.65	93.95

This same analysis was repeated for operation at 18.0 N-m, where diffusion-dominated combustion with all fuels is significantly more pronounced, with the pressure trace and RHR from experimentation presented in Figure 36. Here, the effects of viscosity are apparent, as the more viscous fuels suffer from lower peak cylinder pressures, lower peak RHR, and a more pronounced diffusion burn. This is all due to the inability of the injector to meet the engine's demand for fuel. However, like the cases at 9.0 N-m, increases in injection pressure are largely able to increase fuel atomization and breakup, such that the higher-viscosity fuels can still be made to perform similarly to ULSD.

Again, both the standard filter and Shahlari, et al. algorithm were used to evaluate the intensity of ringing and combustion noise, with results presented in Table 17. It should also be noted that engine operation, across the board, is on the order of 3 dB quieter than equivalent operation at 9.0 N-m. In addition, average ringing amplitude and ringing deviation are both largely equivalent to operation at 9.0 N-m, despite the increase in fuel flow rate and peak cylinder pressure. In both cases, this is due to the overall increase in diffusion-dominated combustion for operation beyond 9.0 N-m leading to an overall stifling of ringing combustion, and masking deviation in ringing normally associated with higher fuel flow rates.

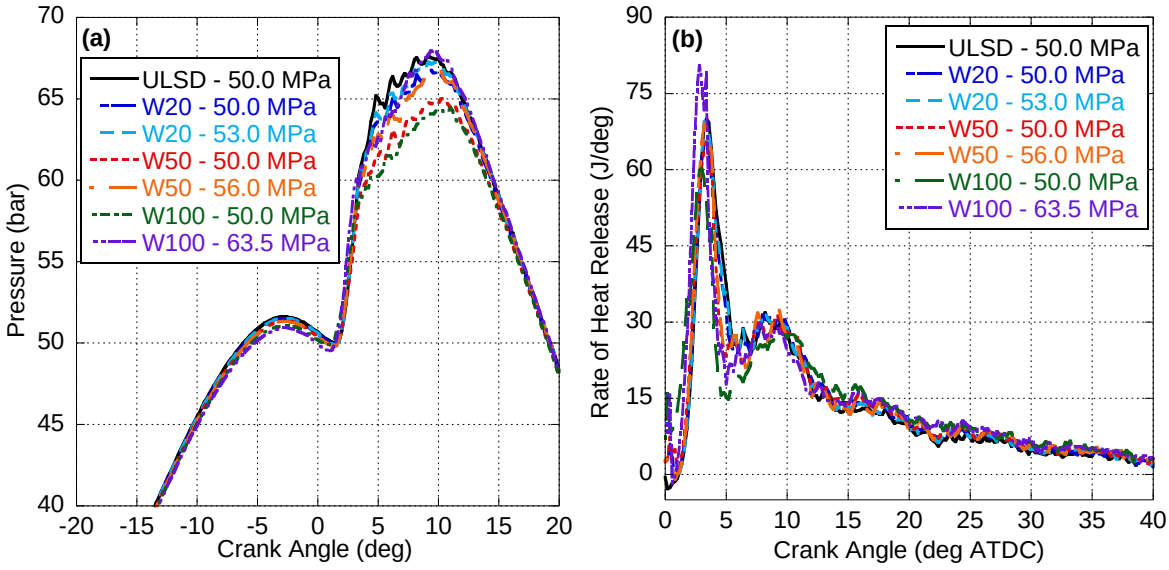

Figure 36. Measured In-Cylinder Pressure Traces (a) and Calculated Rate of Heat Release (b) with respect to Crank Angle for engine operation with high-percentage blends of ULSD and WCO biodiesel at 18.0 N-m.

Table 17. Pressure oscillations and combustion noise with biodiesel blends at 18.0 N-m.

Fuel Used	Injection Pressure [MPa]	Average Ringing Amplitude [bar]	Standard Deviation of Ringing [bar]	Combustion Noise Intensity [dB]
ULSD	50.0	2.54	0.54	91.54
W20	50.0	2.09	0.62	90.88
	53.0	2.47	0.73	91.14
W50	50.0	2.07	0.52	89.82
	56.0	2.28	0.63	90.62
W100	50.0	1.66	0.45	88.74
	63.5	2.47	0.71	90.61

Here, without an injection pressure increase, the heightened viscosity of the fuels tested leads to an overall decrease in pressure ringing, and a significant diminution in noise intensity. For example, the W100 fuel achieved a drop in combustion noise of approximately 2.80 dB in comparison to ULSD, as diffusion burn is raised further above that of standard operation, subsequently stifling CI knock. Like operation at 9.0 N-m, once fuel injection pressures are increased sufficiently enough for the biodiesel to approximate standard operation with ULSD, both the positive and negative aspects of this regime of combustion are generally achieved. In particular, higher premixed combustion is observed, leading to greater peak RHR and peak cylinder pressures, but this is accompanied with augmented CI knock amplitude, ringing deviation, and noise intensity. In addition, these negative traits all approach or (broadly) match those of ULSD, except for combustion noise, which generally remains below that of standard operation.

Recalling the earlier discussion, it is believed that operation of the electronic fuel injection system at peak load should produce greater knock due to a prolonged fuel injection event during the premixed combustion phase; however, this combustion is being stifled and masked by the onset of significant diffusion burn. This effect is more visible with the change in injection pressures, and works to counter the potential decrease in knock from the increase in homogeneity. Raising the injection pressure leads to a higher fuel flow rate, increasing the amount of fuel present within the cylinder to burn in the premixed combustion phase. In addition, by shifting a greater fraction of the total heat release into the premixed

event, less fuel is available to burn within the diffusion phase. As a direct result, knocking combustion is less stifled from diffusion-related effects, causing a further apparent increase in the severity of ringing.

To highlight this, it is necessary to consider combustion regimes in which the amount of fuel present and prepared at ignition is more extreme, leading to a more violent premixed combustion event. In addition, it is preferred here that fuel injection pressure be held constant, so as to remove potential increases to ringing from increased liquid fuel flow rates while lowering cyclic variability in engine knock inherent to the fuel injection system itself.

4.6 Dual-Fuel Operation and Knock

To highlight the relationship between knocking combustion and the amount of premixed fuel available in the cylinder, the authors consider a final study utilizing dual-fuel operation of ULSD with CNG [43]. Here, the addition of CNG does not suffer from fuel viscosity issues, as it is added to the intake stream as a gas. As a result, CNG requires no physical fuel breakup or atomization. In addition, since CNG is added to the intake stream prior to entering the engine, it is more likely to be well-mixed in the engine prior to combustion, subsequently increasing the amount of fuel potentially able to ignite and burn at the onset of combustion. Hence, dual-fuel combustion is more prone to CI knock, and so the amount of knock and ringing combustion will generally increase with growing amounts of CNG [43, 113, 114]. This also means that utilizing CNG can increase cylinder homogeneity, which acts to counter slightly the level of CI knock by proving a more uniform (and in some cases flame-propagated) burn.

To illustrate this, the Yanmar L100V was run at 1800 RPM using ULSD and CNG in dual-fuel operation, with ULSD-only operation serving as the control [43]. For a given load, the ULSD fuel flow rate was reduced and the CNG flow rate was increased in order to maintain a given Energy Substitution Ratio (*ESR*), or a set percentage of combustion energy provided by the CNG. Four separate CNG mixtures were considered, with their mixture compositions shown in Table 18. Here, fuel injection pressure was held constant at 50 MPa and fuel injection timings were again varied as needed to keep the peak pressure timings consistent across all tests. For this study, only testing at 100% of rated load is

discussed because this load serves to illustrate the interplay between premixed- and diffusion-dominated combustion phases. Moreover, it is at this load that the shift towards increasing premixed combustion with increasing CNG usage is most visible.

Table 18. ULSD and CNG fuel properties [43].

Characteristic	ULSD	M87	M91	M92	M96
Methane [%]	-	87.00	91.67	92.00	96.00
Ethane [%]	-	5.10	4.08	3.50	1.80
Propane [%]	-	1.50	0.71	0.80	0.20
Isobutane [%]	-	0.29	0.01	0.15	0.30
Nitrogen [%]	-	5.60	1.00	2.85	1.30
Carbon Dioxide [%]	-	0.51	2.53	0.70	0.40
Density [kg/m^3]	837.58	0.76	0.73	0.72	0.70
Lower Heating Value [MJ/kg]	45.60	49.50	51.48	51.62	53.50
Energy Density [MJ/m^3]	-	37.30	37.30	37.30	37.30
Ratio of Specific Heats	-	37.07	36.75	36.62	36.29
Cetane Number	48.61	-	-	-	-
Octane Number	-	49.50	49.60	49.80	50.00

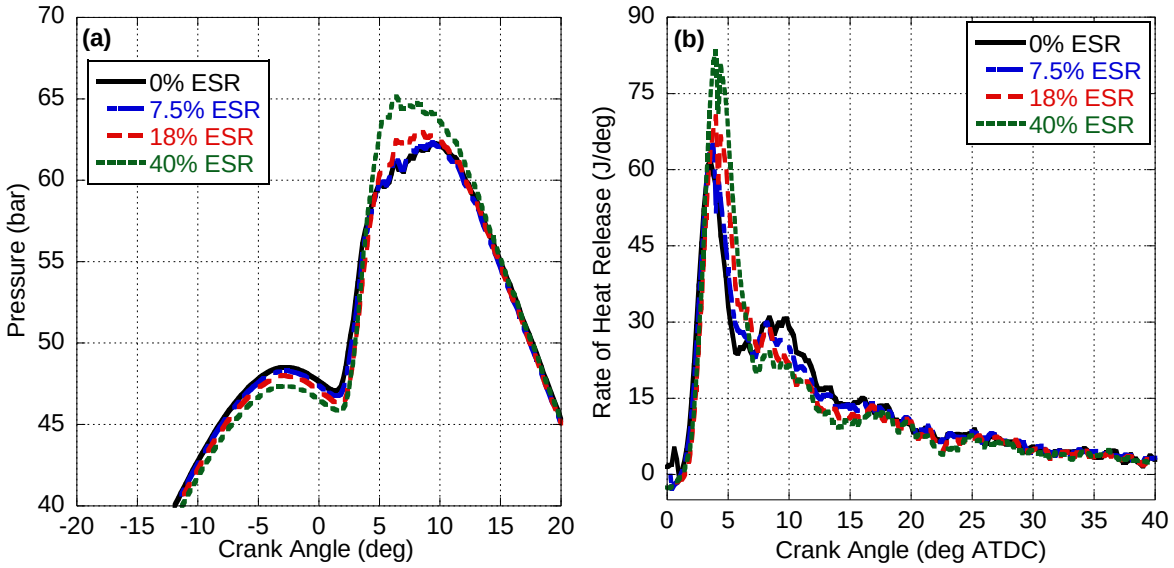

Figure 37. Measured In-Cylinder Pressure Traces (a) and Calculated Rate of Heat Release (b) with respect to Crank Angle for dual-fuel engine operation with moderate amounts of CNG at 18.0 N-m.

As *ESR* is increased at full load, the peak in-cylinder pressure and RHR both grow since they are related directly to the higher amount of fuel fully prepared for combustion by the time ignition occurs. This can be seen in Figure 37 for the M91 natural gas mixture (the pressure and RHR plots for the other mixtures are excluded for brevity, but follow the same overall trends, and are available upon request). Note that the decrease in cylinder pressure at TDC prior to combustion is representative of the changing

mixture composition with *ESR*. Overall, increasing *ESR* leads to a lower ratio of specific heats, which in turn will lead to a decrease in unfired cylinder pressure [9, 43]. Necessarily, the growth in premixed combustion is accompanied by a decline in diffusion-dominated combustion, as more less fuel mass is leftover after the premixed phase is completed.

Using the standard filter and the program by Shahlari et al., the ringing amplitude, ringing deviation, and combustion noise intensity were tabulated and are shown for all CNG fuels in Table 19. As CNG is initially added, the average ringing amplitude appears to decrease (not considering experimental error) even though the pre-mixed spike increases (slightly) running counter to the notion that CNG usage should increase CI knock. It is postulated this relatively low level of *ESR* may be (a) mimicking the small amount of fuel present from pilot injections in standard CI engines, (b) increasing the homogeneity of the mixture, and (c) transitioning some of the CI combustion to more like a SI flame-propagated regime all acting to reduce ringing amplitude. However, combustion noise does increase slightly; therefore, no definitive conclusion can be made at low *ESR* levels. For higher *ESR*s with larger fuel-to-air mixtures throughout the cylinder prior to combustion, ringing amplitude and combustion noise both grow as to be expected with the enlargement of the pre-mixed combustion spike.

Curiously, the standard deviation of ringing appears to follow no overall trend with respect to *ESR*, alternatively experiencing more or less cyclic variation than standard operation with ULSD only. Based on the discussion from the prior sections, it would be expected that cyclic variation should decrease, as ULSD fuel flow rates decrease with *ESR*, and the injection system experiences a lower overall difference in pressure, aiding it in its ability to maintain a consistent pressure between cycles. Instead, it is possible that the growth in pre-mixed combustion with CNG mitigates the assumed reduction in injection pressure variability.

Table 19. Pressure oscillations and combustion noise for dual-fuel operation with CNG at 18.0 N-m.

ESR (%)	CNG Fuel	Average Ringing Amplitude [bar]	Standard Deviation of Ringing [bar]	Combustion Noise Intensity [dB]
0	N/A	2.04	0.54	90.10
7.5	M87	1.86	0.51	90.61
	M91	2.07	0.54	90.31
	M92	1.99	0.51	90.88
	M96	1.97	0.63	90.53
18	M87	2.08	0.57	91.10
	M91	1.99	0.53	91.17
	M92	1.96	0.56	90.88
	M96	2.00	0.60	90.53
40	M87	2.31	0.58	93.45
	M91	2.30	0.59	93.15
	M92	2.03	0.45	93.04
	M96	2.05	0.49	93.38

In addition, any standard deviation in ringing combustion intensity when utilizing CNG may now be more indicative of engine-wide cyclic variability, rather than variability of the fuel system itself, that is related to a decrease in combustion efficiency when adding CNG. It then follows that, if this engine-wide variability can be reliably separated from the injection system variability, deficiencies in fuel system operation may be able to be diagnosed from the degree of knocking combustion apparent within the in-cylinder pressure trace. Assuming a "baseline" of engine knocking variability may be found, any significant increase in cyclic variability can point to injector re-pressurization issues, even if the average amount of engine knock does not significantly change.

4.7 Conclusions

Knock in CI engines is a common destructive phenomenon, necessitating advanced fuel injection strategies. Using a spectral analysis and filtering, as well as combustion noise calculation, the presence and intensity of ringing combustion can be clearly shown for a given engine. In comparison to mechanical systems, electronic injection leads to a more homogeneous air-fuel mixture, ensuring that localized areas where more severe engine knock is possible are less likely to form, and providing a general reduction in knock. Overall, engine knock is made steadily more violent with the addition and preparation of greater amounts of fuel prior to ignition. This effect is seen both in modern electronic injection systems, with

higher operating pressures that increase the rate of fuel flow into the cylinder, as well as in engines utilizing dual-fuel operation, as the added gaseous fuels require minimal preparation prior to combustion, and so are easily ignited and combusted in the premixed combustion event.

For the fuel injection systems tested in the single-cylinder engine, the electronic injection system is shown to produce a more variable amount of engine knock. In particular, the electronic injection system experiences peak instability at around 50% engine load, where premixed combustion and diffusion burn are contributing the most and least, respectively, to the heat release rate of the engine. In all cases, this variability is due to cyclic variation within the injector system itself, and which is worsened with higher fuel flow rates, and higher injection pressures. Below mid-load, the problems associated with cyclic variability are somewhat avoided by low overall fuel flow rates, and above this load, diffusion-dominated combustion takes a larger role in the heat release rate, stifling knocking combustion, and masking variability in knocking combustion between cycles. Increasing fuel injection pressure heightens the amount of overall variability, but utilization of gaseous fuels will not, as the amount of premixing that leads to engine knock is decided more by the gaseous fuel than by the efficacy of liquid fuel injection. As this fuel injection variability may be tracked across multiple cycles, any repeatable deviation in this variability away from normal operation may be used to diagnose fuel system deficiencies, particularly if this variation can be separated from normal engine variability.

Chapter V: Construction and Implementation of a Second Law Heat Release Analysis

Some material published as "Second-Law Heat Release Modeling of a Compression Ignition Engine Fueled with Blends of Palm Biodiesel," ASME Journal of Engineering for Gas Turbines and Power, Technical Paper GTP-16-1008, March 30, 2016

Some material published as "First and Second Law Heat Release Analysis in a Single Cylinder Engine," SAE International Journal of Engines, Technical Paper 2016-01-0559, April 5, 2016

Some material published as "Second Law Analysis of Waste Cooking Oil Biodiesel versus ULSD during operation of a CI engine," Fuel, Accepted July, 2019

5.1 Abstract

Engine-out heat release is of immense importance for engine combustion research, particularly in a diagnostic role. The variation in fuel properties such as viscosity, energy content, or density seen in most fuels fit for combustion in compression ignition engines brings about distinct and important changes in the combustion behavior of these fuels. This is particularly true for fuels with more extreme viscosities (both higher and lower). This behavior results in changing rates of heat release, and thus changes in the pressure and temperature conditions within the engine cylinder. Through the use of in-cylinder pressure measurement, the rate of heat release can be deduced, and the effect of these various properties expressed in a relatively straightforward manner. Traditionally, heat release is catalogued only through the 1st Law of Thermodynamics. However, this analysis can be expanded to include the 2nd Law of Thermodynamics, in order to account for the effects of entropy generation. In doing so, the heat release analysis now details the flow of availability throughout the system, and accounts for the losses of availability associated with entropy.

This work details the creation of a multi-zone (fuel, burned, and unburned) diagnostic 2nd Law Heat Release model, built around an older 1st Law analysis, allowing for the simultaneous calculation of energy and exergy flow through the engine system due to engine combustion. The created model is then utilized to categorize combustion of diesel fuel alongside numerous neat fuels, and also in blends of

varying constituencies with palm biodiesel, with an emphasis on the changes in fuel behavior as a function of the differing properties of the fuels utilized. The 2nd Law model is found to provide additional clarity in understanding combustion than the older 1st Law model, particularly with respect to fuel viscosity effects. The exergy model also details how high viscosity fuels lead to a more delayed and prolonged combustion event, which adds availability to the working fluid later in the expansion stroke. Of importance, this later availability addition is still quite useful and suffers from relatively low entropy generation, and while it is inherently wasted as it is added far too late in the expansion stroke, it is still potentially useful and harnessable from a thermodynamic perspective.

5.2 Introduction

The modeling of thermodynamic processes within internal combustion engines is of importance in classifying and categorizing the behavior of both engine and fuel(s) [2, 60]. One such model is through the calculation of the compression ignition (CI) engine-out rate of heat release (RHR), and is an extremely useful tool in combustion research because it categorizes the changes in combustion rate of the fuel(s) used and clearly identifies the periods of premixed- and diffusion-dominated combustion.

Heat release (HR) calculation is commonly achieved in one of two ways; either the computational modeling of in-cylinder phenomenon [62], or through simplified models that take advantage of measured engine data (i.e., in-cylinder pressure trace) [61, 122]. The latter models typically operate by employing the 1st Law of Thermodynamics, and are often referred to as Equilibrium HR models. Within these models, the bulk mass of gas within the cylinder may be subdivided into multiple component zones (e.g., unburned mass, burned mass, fuel mass, blow-by, etc.), with varying degrees of independence (or interdependence) from each other [61, 123]. This allows for simplified but time-efficient diagnostic modeling of in-cylinder phenomenon based on measured engine performance data. In specific, variations in liquid fuel usage leads to differences in the HR profile of the engine itself because of dissimilar fuel physical and chemical properties. This is particularly important within the study of biodiesel fuels and blends, where changes in combustion behavior are closely linked to viscosity, density, and the energy

content of a given fuel. This necessitates adjustments in engine control systems (i.e., fuel injection pressure and timing) both to optimize engine operation and to mitigate production of harmful emissions as a function of fuel input.

An extension of RHR modeling is to allow for the analysis of CI engine combustion through the 2nd Law of Thermodynamics [124, 125], generally referred to as an availability analysis. Similar to the 1st Law models, the 2nd Law analysis is typically achieved with either complex computational modeling in a predictive analysis [126-128], or through simplified modeling in a diagnostic role [129, 130]. These models are largely concerned with analyzing and quantifying sources of inefficiency within the engine cycle, and are centered on the creation and flow of entropy into, out of, or within the bulk gas. This helps identify the peak availability and, therefore, the ideal period to extract energy from the engine as work, which are not as readily apparent when using 1st Law modeling of engine combustion. In addition, the rates and pathways by which availability are used or lost are analyzed, potentially aiding in both engine control and design.

This effort details the expansion of an existing HR model to allow for the analysis of CI engine combustion using the 2nd Law of Thermodynamics. The previously published model serves as the basis of the work providing a comprehensive 1st Law of Thermodynamics analysis [11]. This prior work delineates the net rate of HR into its components, namely the rates of energy used for work, lost to heat transfer, retained by the working fluid as internal energy, or otherwise changed by mass transfer into or out of the cylinder (e.g., fuel injection, blow-by, etc.). Using the Equilibrium HR model as a foundation, the expansion into the 2nd Law analysis allows for the calculation of entropy generation and loss of availability to each of the component energy pathways associated with the HR rate of the engine.

Unlike other zero-dimensional multi-zone HR models, the presented work utilizes an Arrhenius equation to govern the rate at which combustion proceeds (calibrated to a known cycle combustion efficiency from exhaust hydrocarbon measurements), combined with continued adjustment of the thermodynamic properties of the working fluid through analysis of the in-cylinder pressure trace. As a demonstration, the 2nd Law analysis is used to categorize the efficacy of combustion of ultra-low sulfur

diesel, palm biodiesel fuel, and their blends. This highlights the effects of biodiesel on engine efficiency, particularly with respect to the increase in fuel viscosity, and the resulting decreases in efficiency, as the composition of biodiesel within the fuel blend increases. In addition, the 2nd Law analysis offers a stronger insight into the fuel combustion process than prior 1st Law modeling by identifying the areas of availability losses, particularly in the increasing losses of availability to the exhaust gas due to the interrelations between biodiesel blend percentage, fuel viscosity, diffusion-dominated combustion, and combustion temperatures.

5.3 Model Equations

For a 1st Law-based HR analysis, the fundamental equation to be balanced is the conservation of energy [11, 60]:

1st Law Rate of Heat Release	$\frac{dQ_{hr}}{d\theta} = \frac{dU_{cv}}{d\theta} + \frac{dW_{cv}}{d\theta} + \frac{dQ_{ht}}{d\theta} + \sum h \frac{dm_{cv}}{d\theta}$	(24)

where the amount of heat released by combustion of the fuel (Q_{hr}) is a function of the internal energy of the control volume (U_{cv}), the amount of work done by the bulk gas on the piston at a given point in time (W_{cv}), the net amount of heat transfer out of the cylinder (Q_{ht}), and also energy losses through mass transfer ($dm_{cv}/d\theta$), such as injection or blow-by.

The evaluation of the internal energy, work, and mass transfer terms occurs as a function model zones. All chemical species within the cylinder are subdivided into one of three zones; an unburned zone for air and recycled gases, a fuel zone for unburned fuel, and a burned zone for the products of combustion. The mass of each of the three zones is held constant at all times, with the only exceptions being the addition of mass to the fuel zone through injection, and the transfer of mass from the unburned and fuel zones into the burned zone due to combustion. These separate processes are modeled individually, and are covered in detail as follows.

For a 2nd Law availability analysis, a similar equation exists to quantify the individual components of the change in cylinder availability [125]:

2nd Law Rate of Change of Availability	$\frac{dA_g}{d\theta} = \frac{dA_c}{d\theta} - \left(\frac{dA_w}{d\theta} + \frac{dA_{ht}}{d\theta} + \frac{dA_{ir}}{d\theta} \right)$	(25)

where the total amount of availability of the bulk gas (A_g) is expressed as a function of the net rate of availability addition through the combustion of fuel into the cylinder (A_c), and the transfer of availability out of the cylinder through work done on the piston (A_w), the losses associated with heat transfer (A_{ht}), and the amount of availability that is not recoverable (A_{ir}) due to irreversibilities. So long as the component terms of Equation 25 can be found, the net change in availability may be solved.

The rate of availability transfer by work in Equation 25 is given by the following [14, 125]:

Availability Transfer by Work	$\frac{dA_w}{d\theta} = \frac{dW_{cv}}{d\theta} - p_0 \frac{dV}{d\theta}$	(26)

where V is the cylinder volume, and p0 is the ambient pressure. Here, the total amount of work done by (or on) the bulk gas is compared against the amount of work done by the atmosphere against the piston. Using the 1st Law model as a basis, this rate of availability may be calculated either within a given zone, or across the entire cylinder at once.

The rate of availability loss through heat transfer in Equation 25 is expressed as follows [14, 125]:

Availability Loss by Heat Transfer	$\frac{dA_{ht}}{d\theta} = \frac{dQ_{ht}}{d\theta} \left(1 - \frac{T_0}{T_w} \right)$	(27)

where Q_{ht} is the total amount of heat transfer at a given moment, T_0 is the ambient temperature, and T_w is the cylinder wall temperature. The heat transfer term itself may be broken into multiple components [11]:

Rate of Heat Transfer	$\frac{dQ_{ht}}{d\theta} = \frac{dQ_c}{d\theta} + \frac{dQ_r}{d\theta} + \sum h \frac{dm_{cv}}{d\theta}$	(28)

where the individual components represent heat transfer losses by convection (Q_c), radiation (Q_r), and mass transfer. Note that the final term on the right hand side is zero if injection is discounted.

Within internal combustion engine modeling, the total rate of availability loss due to irreversible phenomenon is given as [125, 131, 132]:

Availability Loss by Entropy Generation	$\frac{dA_{ir}}{d\theta} = T_0 \frac{dS}{d\theta} - \frac{T_0}{T_w} \frac{dQ_{ht}}{d\theta} \geq 0$	(29)

where S refers the entropy generated at a given moment. Given that the only useful measure of irreversibility is the amount of energy contained within the cylinder, the second term of Equation 29 serves to discount irreversibility associated with heat transfer (note: it is accounted separately here in Equation 28). As a result, Equation 29 is a measure of internal irreversibilities (i.e., entropy generation that is contained within the working fluid).

Finally, the rate of availability addition through combustion is given by the following [125]:

Availability Addition from Combustion	$\frac{dA_c}{d\theta} = e_c \frac{dm_c}{d\theta}$	(30)

where e_c is the chemical exergy content of the fuel, and mc is the mass of fuel consumed. The fuel exergy content is closely related to the lower heating value (Q_{lhv}) of the fuel [133, 134]:

Ratio of Fuel Exergy to Fuel Energy for Diesel Fuel	$\frac{e_c}{Q_{lhv}} = r \approx 1.065$	(31)

where the proportionality constant r varies depending on the chemical composition of the fuel molecule, and has been tabulated by various authors for ultra-low sulfur diesel (ULSD) [15, 133, 135]. With its components known, the rate of availability transfer (Equation 30) may be solved via individual processes similar to the RHR (Equation 24).

For more exotic fuels (such as biodiesel), it is necessary to calculate the availability content directly [136, 137]:

Ratio of Fuel Exergy to Fuel Energy as a Function of Fuel Chemistry	$r = 1.0401 + 0.1728\frac{y_H}{y_C} + 0.0432\frac{y_O}{y_C} + 0.2169\frac{y_S}{y_C}\left(1 - 2.0628\frac{y_H}{y_C}\right)$	(32)

where y is the mass fraction of hydrogen (H), oxygen (O), carbon (C), or sulfur (S) within the fuel molecule.

The model discussed herein is focused on the application of Equations 25-32 within an existing HR model [11], allowing the addition of functions to handle the new analysis rather than an entirely novel model. For brevity, this work will only discuss the additions to the original model required for the

availability analysis, and will not dictate portions of the prior model that will otherwise go unused (see the author's Master's Thesis, and Chapter II of this document) [138].

The calculation of the individual terms of Equations 24 and 25 are reliant on the analysis of the changes in thermodynamic properties between timesteps, such as molar constant pressure specific heat (c_p), enthalpy (h), or standard-state entropy (s_0). For this, the model utilizes seven coefficients tabulated within the CHEMKIN-III model [63]. Within the model, it is assumed that component gases of a given zone are all at a uniform temperature, allowing the model to express a thermodynamic quality of a mixture of species as a single value. Using entropy as an example:

CHEMKIN-III Equation for Molar Entropy	$\frac{\bar{s}}{R_{univ}} = \frac{x_i}{R_{univ}} \sum \bar{s}_i^0 - \ln\left(x_i\right) - \ln\left(\frac{p}{p_0}\right)$	(33)

where Runiv is the Universal Gas Constant, x_i is the mole fraction of a given species within the mixture, and $\bar{s}_i^0$ is the standard-state molar entropy of that species. In effect, Equation 33 serves to account for entropy of mixing, as well as the pressure-based entropy terms as recommended by Kee et al. [63]. This leads to an expression whereby the individual coefficients utilized by the model are expressed as a function of the constituency of a given zone:

Lumped Gas Coefficient	$a_j = \sum x_i a_i$	(34)

where a_i is one of the seven coefficients utilized by the CHEMKIN-III model for a given species, and aj is the resulting coefficient for the bulk gas mixture. As a result, the model is able to evaluate changes in entropy of a given zone (and of the bulk gas) for a given timestep, as a function of the temperature and speciation of that zone. In addition, this allows for the calculation of the rate of availability losses due to irreversible phenomenon in the bulk cylinder gas given in Equation 34 once the entropy has been converted to a mass basis:

Rate of Change of Entropy	$\frac{dS}{d\theta} = m\frac{ds}{d\theta}$	(35)

However, Equation 35 may only be utilized for situations where the mass within the bulk zone is constant (i.e., excluding fuel injection or blow-by). In addition, Equation 35 is unable to resolve the

transfer of mass between zones. Because of these deficiencies, Equation 35 is recast to allow for mass transfer:

Rate of Change of Entropy with Mass Transfer	$\frac{dS_j}{d\theta} = m_j \frac{ds_j}{d\theta} + s_j \frac{dm_j}{d\theta}$	(36)

where the subscript *j* may represent the changes within a given zone, or within the bulk gas as a whole.

To resolve the varying rates of heat transfer in Equation 28, the model uses an average between the heat transfer correlations provided by Woschni [139] and Hohenberg [140], while the radiative heat transfer component is calculated from the emissivity of the exhaust gas using a methodology by Bahadori et al. [141]. Finally, all forms of mass transfer into or out of the cylinder are ignored, other than mass addition through injection, and the associated rate of heat transfer is given as follows [11]:

Injection Heat Transfer Rate	$\sum h \frac{dm_{cv}}{d\theta} = h_{inj} \frac{dm_{inj}}{d\theta}$	(37)

where h_{inj} is the enthalpy associated with injection and vaporization [11]:

Enthalpy of Injection	$h_{inj} = h_{fg} + c_f \left(T_{vap} - T_{inj}\right) + c_{p,f} \left(T_f - T_{vap}\right)$	(38)

where h_{fg} is the enthalpy of vaporization of the fuel, c_f and $c_{p,f}$ are the specific heating values of the fuel in its liquid and vaporized forms (respectively), and T_{inj}, T_{vap}, and T_f are the temperature of fuel at injection, vaporization, and as a vapor within the fuel zone, respectively. For this calculation, it is assumed that injected fuel is injected, atomizes, vaporizes, and comes up to the temperature of the fuel zone instantaneously, while accounting for the necessary heat transfer into the fuel zone.

Next, the rate of mass addition by injection is given as follows [60]:

Rate of Liquid Fuel Mass Addition by Injection	$\frac{dm_{inj}}{d\theta} = C_d A_n n_h n_{inj} \left(2\rho_f \Delta p\right)^{0.5}$	(39)

where the injection process is defined through the area of the injector nozzle holes (An), the number of holes per injector (n_h), the number of injectors (n_{inj}), the density of the fuel (ρ_f), and the change in pressure (Δp) between the fuel rail and the cylinder. In addition, Equation 39 is calibrated by the injector coefficient of discharge (C_d) which is nominally set to 0.39 [60]. This mass of fuel injection can then be used in conjunction with Equations 33-36, using CHEMKIN coefficients of the chosen fuel or blend

(either directly in the case of ULSD, or indirectly through the fatty-acid methyl ester composition in the case of biodiesel).

Finally, the rate of combustion of fuel is determined by an Arrhenius reaction rate [64]:

Rate of Combustion of Fuel	$\frac{dm_c}{d\theta} \approx K \rho_{cv} V y_f y_{O_2}^5 e^{-E_a/(R_{univ}T)}$	(40)

and is expressed as a function of the density of the bulk gas mixture (ρ_{cv}), the cylinder volume, the relative mass fractions of fuel (y_f) and oxygen (y_{O_2}), the activation energy of the fuel (E_a), the universal gas constant, and the temperature of the bulk gas. The combustion process then consumes a set amount of oxygen, and leads to the production of nitrogen, carbon dioxide, and water, all in a stoichiometric manner, with the consumed air and fuel being moved from the unburned and fuel zones into the burned zone, along with their byproducts from combustion [11]. Partial combustion products (i.e., carbon monoxide, hydrocarbons) and other resultant species (e.g., oxides of nitrogen) are ignored, as they make up a relatively small portion of the bulk gas, and do not significantly affect the thermodynamic characteristics of the bulk gas itself.

In addition, the reaction rate given in Equation 40 is controlled using the dimensionless constant *K*, which is calibrated in order to ensure that the cumulative amount of heat released is equal to the energy content of the consumed fuel:

Cumulative Heat Release	$Q_{hr} = \eta_c m_f Q_{lhv}$	(41)

where m_f is the mass of fuel injected, and η_c is the combustion efficiency of the engine cycle, calculated from the hydrocarbon content of the engine's exhaust emissions [11].

The solution process of the model is iterative and is based on evaluation of the components of the Ideal Gas equation of state:

Ideal Gas State Equation	$pV = mRT$	(42)

where *p* is the measured cylinder pressure, and *m* and *R* are the mass and (speciated) gas constant of the mixture of fuel, air, and exhaust products within the cylinder. At each step (covering a fraction of crank angle degree), the component variables of the equation of state are solved both within the individual

zones and on a cylinder-wide scale over the closed portion of the engine cycle (i.e., Intake Valve Closing to Exhaust Valve Opening).

This solution process utilizes the measured pressure trace in order to solve for the necessary rates of mass transfer and changes in speciation (and gas constant) due to combustion. Finally, temperature is found through a 1st Law balance using Newton's linear method, and the volumes of the individual zones are solved directly through the state equation. The entire process is then iterated to ensure conversion of the anticipated and modeled amount of energy released by the fuel, including the total amount of heat transfer out of the cylinder.

Once the 1st Law model is completed, the 2nd Law model utilizes the same thermodynamic variables in order to quantify the components of Equation 25 through the changes in availability due to fuel combustion, work, heat transfer, and entropy generation. In addition, the model then calculates the 2nd Law Efficiency (or exergetic efficiency) [14, 15]:

2nd Law Efficiency	$\eta_e = \frac{A_w}{A_c} = 1 - \frac{\left(A_g + A_{ht} + A_{ir}\right)}{A_c} = 1 - \frac{A_{loss}}{A_c}$	(43)

where A_{loss} is the total amount of availability not utilized by the engine for work either through heat transfer, irreversibility, or wasted availability of the exhaust gases.

5.4 Validation and Modeling of Conventional Diesel Combustion

Experimentation with ULSD was performed using a naturally-aspirated air-cooled Yanmar L100V single cylinder engine, coupled with a Dyne Systems Dymond Series alternating current dynamometer. The Yanmar engine was operated with the built-in EGR port blocked (an external cooled EGR system is available but was not utilized). In addition, the Yanmar was upgraded to a high-pressure single-rail electronic system [73]. Additional specifications for the engine and dynamometer can be found in Table 20 and Table 21.

Table 20. Yanmar L100V Engine Specifications.

Displacement [cc]	435
Valve Number/Type	1 Intake, 1 Exhaust
Bore [mm]	86
Stroke [mm]	75
Connecting Rod Length [mm]	118
Crank Radius [mm]	38
Compression Ratio	21.2
Injection Timing	Variable
Injection Pressure	Variable, Maximum 200 MPa
Continuous Rated Output [kw]	3.4
Rated Speed [RPM]	3600
ULSD Heating Value [kJ/g]	42.8
ULSD Cetane Number	40
IVC [° ATDC]	-122
EVO [° ATDC]	144

Table 21. Dynamometer Specifications.

Model	Dymond Series 12
Rated Torque [N-m]	28.6
Rated Power [hp]	8.95
Speed Range [RPM]	0-7500
Voltage [V]	480
Phase	Three-Phase
Frequency [Hz]	60
Controller	DyneSystems Inter-Loc V OCS

Engine operation was monitored and measured through a number of National Instruments LabVIEW systems, recording engine performance characteristics at 10 Hz over two minutes and engine emissions from an AVL SESAM-FTIR emissions analyzer to provide for the combustion efficiency calibrations needed for the model (see Equation 41). Finally, a third LabVIEW system was utilized for capturing the in-cylinder pressure trace, recording 60 consecutive engine cycles (120 revolutions) at a resolution of 0.5° of crank angle [19, 73].

The engine tests were run at 1800 RPM and five separate engine loads, each representing a fraction of total rated load; 0.5 N-m (idle, or 0%), 4.5 N-m (25%), 9.0 N-m (50%), 13.5 N-m (75%), and

18.0 N-m (100%). Engine data was collected after the engine had reached steady-state operation, defined by a change in oil and exhaust temperatures of less than 1% over 60 seconds. Injection pressure was held constant at 43±0.5 MPa, and injection timings were prescribed in order to achieve peak engine efficiency as found by a previous analysis [10, 19].

The results of ULSD testing are shown in Figure 38(a) (cylinder pressure) and Figure 38(b) (RHR). Of note, the RHR generally increases and shifts further away from top-dead center (TDC) as load is increased (in order to retain peak engine efficiency); whereas, the peak pressure remains relatively constant when shifting away from TDC. Moreover, the amount of heat release from the diffusion burn portion of the cycle also increases, and at 18.0 N-m, the engine combustion becomes dominated by diffusion burn; whereas, for loads at 9.0 N-m and below combustion is primarily pre-mixed. This behavior is due to the growing length of the injection period with greater load (and thus fuel flowrate), in turn increasing the total amount of fuel that cannot be prepared quickly enough to be consumed by premixed combustion. Therefore, peak-pressure is often defined by the maximum amount of pre-mixed combustion possible and the width of the pressure trace defined by the amount of diffusion burn.

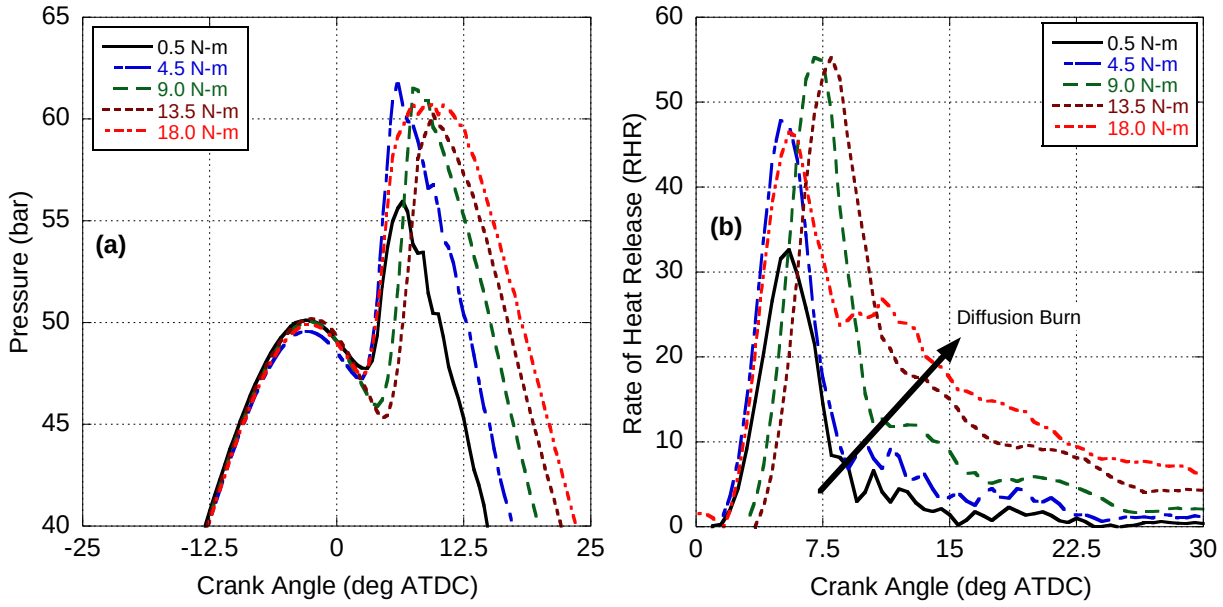

Figure 38: Measured In-Cylinder Pressure (a) and Calculated 1st Law RHR (b) for Conventional Diesel Combustion with ULSD.

In order to keep the engine operating at peak efficiency, the timing of injection was advanced at higher loads [10]. The result of this is that the heat release profile differs from the trend at 18.0 N-m (increasing premixed peak shifting away from TDC) given the significant increase in diffusion burn at this load. The net effect results in a more prolonged period of peak cylinder pressure (see Figure 38b) and optimal power production [10]. For a more detailed analysis of ULSD (and biodiesel) in-cylinder pressure and first law HR results, please consult the following reference [142].

The corresponding rate of change and cumulative change in availability at 18.0 N-m were calculated using the 2nd Law analysis, as shown in Figure 39 and Figure 40. This highlights the various pathways by which availability is transferred within the system. Here, positive availability values for irreversibility and heat transfer represent immediate losses within and out of the cylinder (respectively), while positive availability in the exhaust gas represents the addition of energy (first by compression, and then by combustion) to the working fluid that may be extracted as work. Negative work availability represents availability that must be transferred in (by compressing the working fluid). However, the work put into the system must be balanced by the corresponding rise in internal energy of the working fluid (with any differences offset by heat transfer into or out of the cylinder), and so the net availability transfer remains nearly zero before ignition, with the remainder of availability transfer attributed to irreversibility and entropy generation.

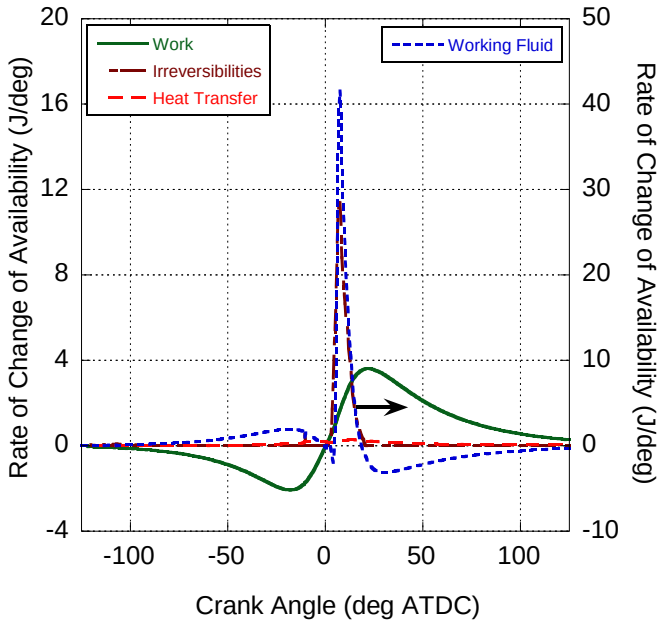

Figure 39: Calculated Rate of Change in Availability at 18.0 N-m for Engine Operation with ULSD.

Ignition and combustion (approximately 0-20° ATDC) leads to the transfer of chemical availability within the fuel to thermal availability in the working fluid, combined with a significant rise in entropy production and resulting irreversibility. Post-combustion, the availability of the working fluid is reduced, as availability is transferred out of the cylinder through work and heat transfer. Not all of the available energy may be extracted with the remaining availability of the working fluid (285.1 J at EVO) exiting the cylinder during the exhaust stroke.

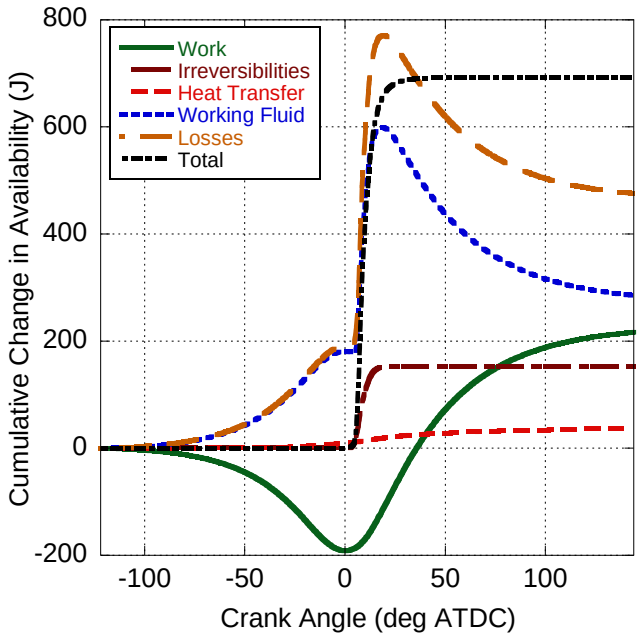

Figure 40: Calculated Cumulative Change in Availability at 18.0 N-m for Yanmar Engine Operation with ULSD.

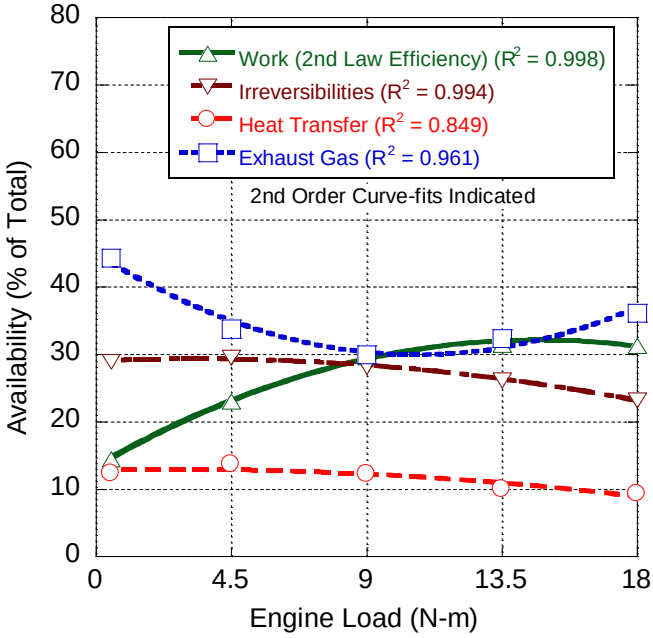

Figure 41: Percentage of Calculated Total Availability via Components of Equation 25 at EVO for Engine Operation with ULSD.

The component percentages of availability transfer at EVO for all engine loads may be seen in Figure 41. As engine load is increased, the percentage of availability lost to irreversibility and heat transfer generally trend downwards, while the amount of availability transferred as work increases. In

addition, the changes in percentage of availability lost through the exhaust gas are lowest at 9.0 N-m, and trend upwards as engine load moves further from the midrange loads. All four means of availability transfer follow (roughly) 2nd order behavior.

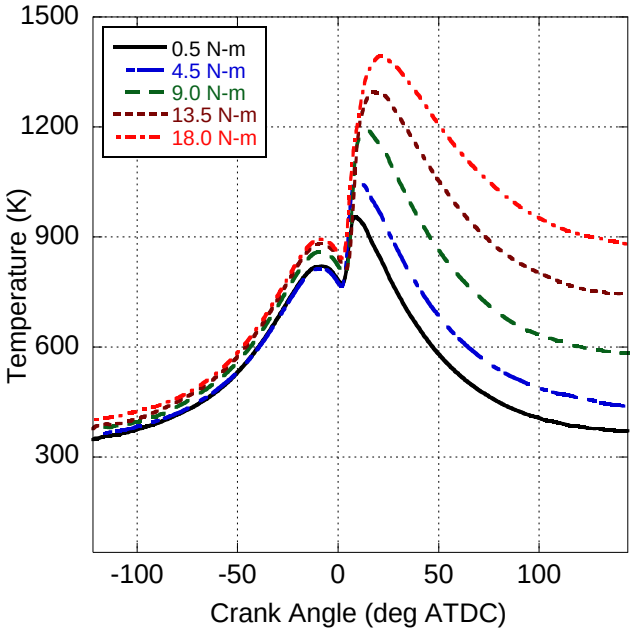

Figure 42: Calculated In-Cylinder Temperature Profile for Engine Operation with ULSD.

At all engine loads, the fractions of availability lost to heat transfer and irreversibilities are somewhat constant for lower loads, and trend downwards at higher loads, with heat transfer peaking at 13.7% of availability at 4.5 N-m, and irreversibility at 29.5% at the same load. On an absolute scale, heat transfer increases with load as higher temperatures promote a greater thermal gradient between the gas and the wall. Heat transfer is also a strong function of the turbulence of the gas, set-up through the engine speed. Since the engine was run at a singular speed, heat transfer availability trends downwards as the changes in the other availability components are more dramatic than an increased level of heat transfer due to a greater temperature difference (see Figure 42). In effect, while the peak temperatures increase with load, less of the total availability is lost to heat transfer (typically in favor of increased work extraction).

Irreversibilities also decrease as engine load is increased because the engine becomes more thermally efficient in translating energy released through combustion into actual work. In specific, the high temperature reservoir (Figure 42) effectively increases as heat release grows (Figure 38b); hence, a higher potential Carnot efficiency. Therefore, even though more fuel is being combusted promoting entropy generation, the temperature differences between the lower and higher thermal reservoirs increases and irreversibility goes down with respect to the other availabilities.

The total fraction of availability within the working fluid trends downward as load is increased from idle to mid-range, while the amount of availability extracted as work increases over the same range. For increases in load past 9.0 N-m, however, the fraction of availability transferred to the exhaust gas rises while work remains relatively constant. This is because past 9.0 N-m the increasing diffusion burn (Figure 38b) leads to availability being added later in the expansion stroke, cooling the working fluid. Hence, load goes up but the fraction of availability that is extracted as work remains constant, and the fraction remaining within the working fluid increases. Therefore, through this availability analysis, it appears that the most efficient set point of the engine is at 9.0 N-m where exhaust gas availability is minimized. This makes sense according to the first law HR analysis (Figure 38b) because this is the engine combustion regime that has maximized pre-mixed combustion (i.e., constant volume combustion) while minimizing diffusion burn. In other words, as the engine continues to add energy in a constant volume manner up to 9.0 N-m, exhaust gas availability decreases and work availability increases. However, beyond this load, diffusion burn (i.e., slower, later combustion) begins to dominate and more energy is added at a less advantageous time resulting in an increase in exhaust gas availability without an appreciable gain in work availability.

5.4.1 2nd Law Behavior and Variation in Fuel Properties

The fuels utilized during experimentation were Jet A, an aviation fuel derived from renewable through hydroprocessing (R-8), and two biodiesel fuels derived from beef tallow and jatropha oils. The characteristics for these fuels can be found in Table 22 [5, 25]. In addition, standard ULSD was utilized as

a control. The engine was operated without added turbocharging, and without multiple injection events per cycle, in order to simplify the comparisons in engine operation between each fuel.

Table 22. Properties of Neat Fuels Tested [5, 25].

Property	ULSD	Jet A	R-8	Tallow Biodiesel	Jatropha Biodiesel
Density (kg/m^3)	837.58	801.02	758.54	870.98	876.81
Kinematic Viscosity (cSt)	2.578	1.431	1.542	4.70	4.44
Dynamic Viscosity (cP)	2.159	1.146	1.170	4.094	3.893
Cetane Number	40.0	43.4	68.8	61.0	52.0
Energy Content (kJ/kg)	41530	42700	43101	39933	39809
Volumetric Energy Content (MJ/m^3)	34785	34204	32694	34781	34905

Engine operation and performance was monitored through a system created through LabVIEW, recording at a rate of 10 Hz for 120 seconds of engine operation. A second LabVIEW system was used in order to capture the in-cylinder pressure trace, recording 120 consecutive engine revolutions (amounting to 60 engine cycles) at a resolution of 0.5° of crank angle. Finally, a third LabVIEW system was used with an AVL SESAM-FTIR emissions analysis module recording at a rate of 1 Hz over 300 seconds, which was utilized to capture the amount of unburned fuel species, in order to calculate the combustion efficiency of the engine cycle for use within the RHR and 2^{nd} Law models [73].

All tests were run at 1800 RPM and loading was varied between 0.5 N-m (idle) and 18.0 N-m (100% of rated load) in increments of 4.5 N-m, corresponding to the engine operating unloaded, and at 25%, 50%, 75%, and 100% of rated engine load, allowing a visualization of both premixed- and diffusion-dominated combustion, as well as the transition between these operating states. Testing of alternative fuels was preceded with engine operation with ULSD [5, 25]. In all cases, fuel injection was increased to bring the engine to a given desired percentage of engine load, and was allowed to come to steady-state operation as defined by changes in oil and exhaust temperatures of less than 1% over the 60

seconds of operation. Next, engine performance and emissions data were collected, as well as the in-cylinder pressure trace.

After data collection, engine load was increased to the next desired level, and process was repeated. Fuel injection parameters were controlled through a Bosch MS15.1 Diesel Electronic Control Unit utilizing Bosch ModasSport. For the ULSD testing, fuel injection timing was set to predetermined points known to maximize engine efficiency at each load [16]. For testing of the other fuels, injection timing was adjusted to align the timing of peak pressure with the timing of peak pressure when operating with ULSD. The injection timings utilized for all fuels can be seen in Table 23 (note that for the baseline ULSD testing, injection timing reverses direction at full load, due to the magnitude of diffusion-dominated combustion and its effect on thermal efficiency). For all fuels, fuel injection pressure was held constant at 40±0.5 MPa.

Table 23. Injection Timings (° before TDC) used for Tested Fuels.

Engine Load	ULSD	Jet A	R-8	Tallow Biodiesel	Jatropha Biodiesel
0.5 N-m	12.5	12.1	10.5	10.4	11.2
4.5 N-m	12.5	12.1	10.5	10.6	11.4
9.0 N-m	11.0	10.6	9.4	9.5	10.1
13.5 N-m	10.0	9.6	8.6	8.5	9.2
18.0 N-m	11.0	10.7	9.9	9.6	10.2

The pressure traces for engine combustion at 4.5 N-m, 9.0 N-m, 13.5 N-m, and 18.0 N-m (corresponding to 25%, 50%, 75%, and 100% of rated engine load) are presented in Figure 43. Note that the motoring pressure prior to combustion peaks around 2.5° before TDC, due to cylinder cooling effects in the vicinity of TDC [11, 143]. Combustion using ULSD and Jet A produced largely identical results. It appears the drop in viscosity for Jet A that promotes better mixing is balanced by its growth in cetane number that subsequently reduces the amount of fuel prepared prior to combustion. Since both fuels have similar volumetric energy contents, combustion ends up being relatively comparable.

R-8 and both biodiesel fuels had noticeably lower peak pressures than ULSD and Jet A. Investigating R-8, while it has a lower viscosity its significantly high cetane number and lower volumetric energy content results in a reduced amount of early combustion and a decrease in peak pressure as

compared to ULSD. However, for the biodiesel fuels their greater fuel viscosity leads to a decreased atomization process resulting in worse mixing. This, combined with a higher cetane number, results in a reduction in peak pressure over ULSD even though they have equivalent or slightly higher volumetric energy content. Hence, combustion for R-8 and both biodiesels will shift until later in the thermodynamic cycle at less optimum crank angles. Tallow biodiesel has the lowest combustion pressure because it has the highest viscosity with the second highest cetane number.

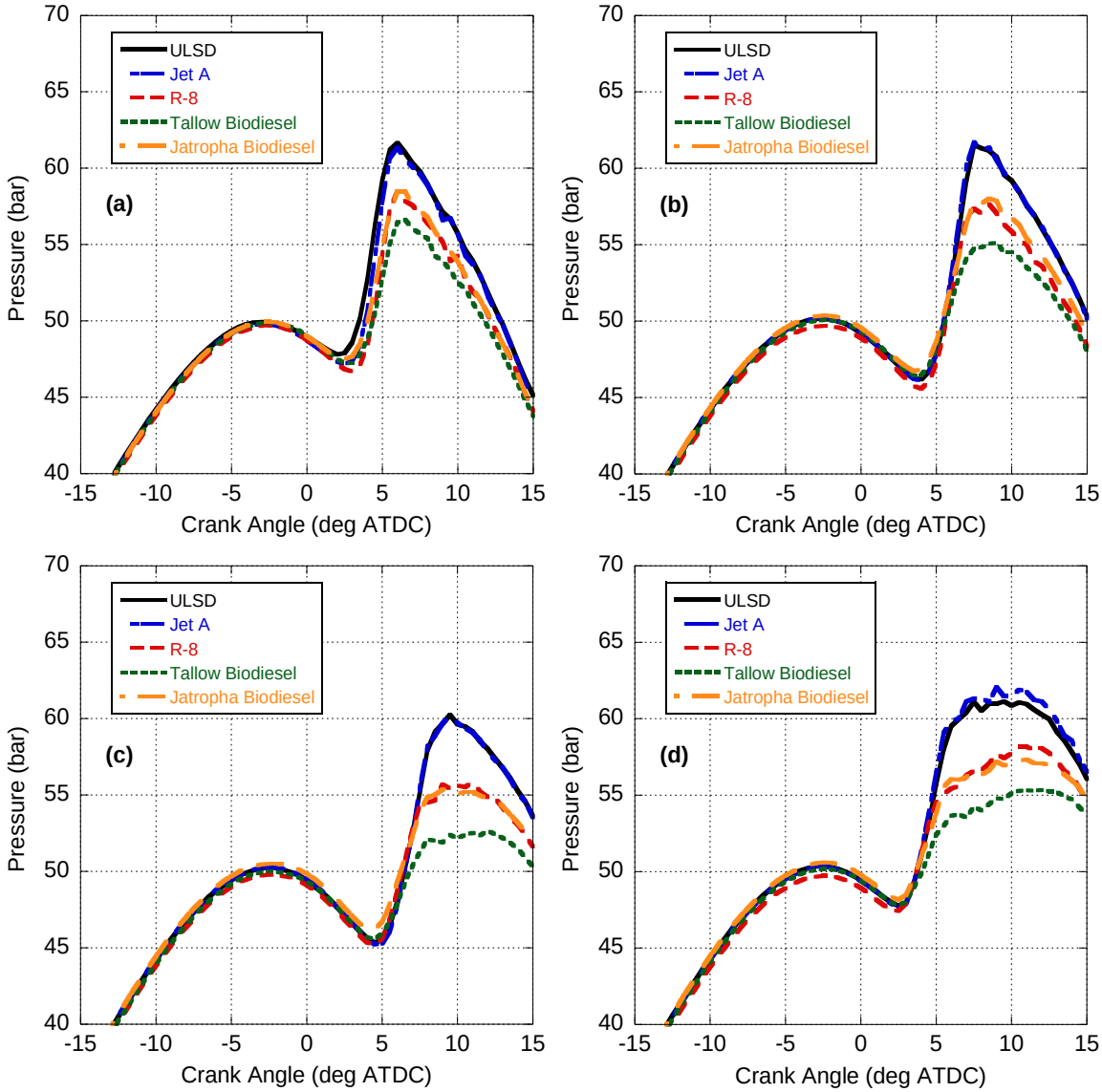

Figure 43. Measured In-Cylinder Pressure Traces with respect to Crank Angle for (a) 4.5 N-m, (b) 9.0 N-m, (c) 13.5 N-m%, and (d) 18.0 N-m for various neat fuels.

The 1st Law RHR results mirror the same trends seen in the pressure traces, and are given for the 25%, 50%, 75%, and 100% load conditions in Figure 44. Combustion with ULSD and Jet A are shown to have the highest peak RHR, followed by R-8 and jatropha biodiesel, and then finally the tallow biodiesel. These peak RHR values are seen in the premixed combustion phase, where injected fuel has had sufficient time to atomize and prepare for combustion. However, for higher engine loads, the ignition delay period between injection and ignition is not enough time to add enough fuel to achieve the desired engine loads, and for the more volatile fuels can be seen to decrease significantly (see Table 24). As a result, with increasing load comes the onset of diffusion-dominated combustion, where fuel combusts as soon as it prepared and mixed with sufficient oxygen. Of note, the trend seen within the premixed phase is now reversed for the diffusion phase at loads below 18.0 N-m; tallow biodiesel is observed to have the highest RHR, followed by R-8 and jatropha, and finally ULSD and Jet A. The reversal of this trend is due to the how the power requirements of the engine are met in the premixed phase; if more fuel can be combusted in the premixed phase, less will be needed in the diffusion phase in order to meet the desired load.

Table 24. Ignition Delays (° of crank angle) of Tested Fuels.

Engine Load	ULSD	Jet A	R-8	Tallow Biodiesel	Jatropha Biodiesel
0.5 N-m	13.5	13.6	12.0	12.4	12.7
4.5 N-m	13.0	13.1	12.0	12.1	12.4
9.0 N-m	13.0	13.1	11.9	11.5	12.1
13.5 N-m	13.0	12.6	11.6	11.5	12.2
18.0 N-m	13.0	11.7	11.9	11.1	11.2

At 18.0 N-m, there is a noticeable difference in diffusion burn between the fuels. Initially, starting at around 8° after TDC, the RHR of the ULSD, Jet A, and R-8 fuels increase, while the RHR of the jatropha and tallow biodiesels remain relatively low or continue to decrease. This surge in energy is temporary, however, as the RHR of both biodiesels soon surpass the other fuels at around 15° after TDC, after which point the RHR of the ULSD, Jet A, and R-8 fuels is lower than that of both biodiesels. This difference is likely due to the effect of fuel viscosity and late injection at higher fuel loads. Here, the low viscosity fuels are able to combust shortly after injection because they quickly break up, mix with the

surrounding air (sufficient oxygen due to lean operation), and are brought to ignition due to the heat of prior combustion. Chemical ignition delay and cetane number now no longer play a large role, as the fuel is able to prepare chemically for combustion quickly in the high temperature environment. However, the biodiesel fuels both suffer from higher viscosities and need more time to atomize, vaporize, and mix after injection.

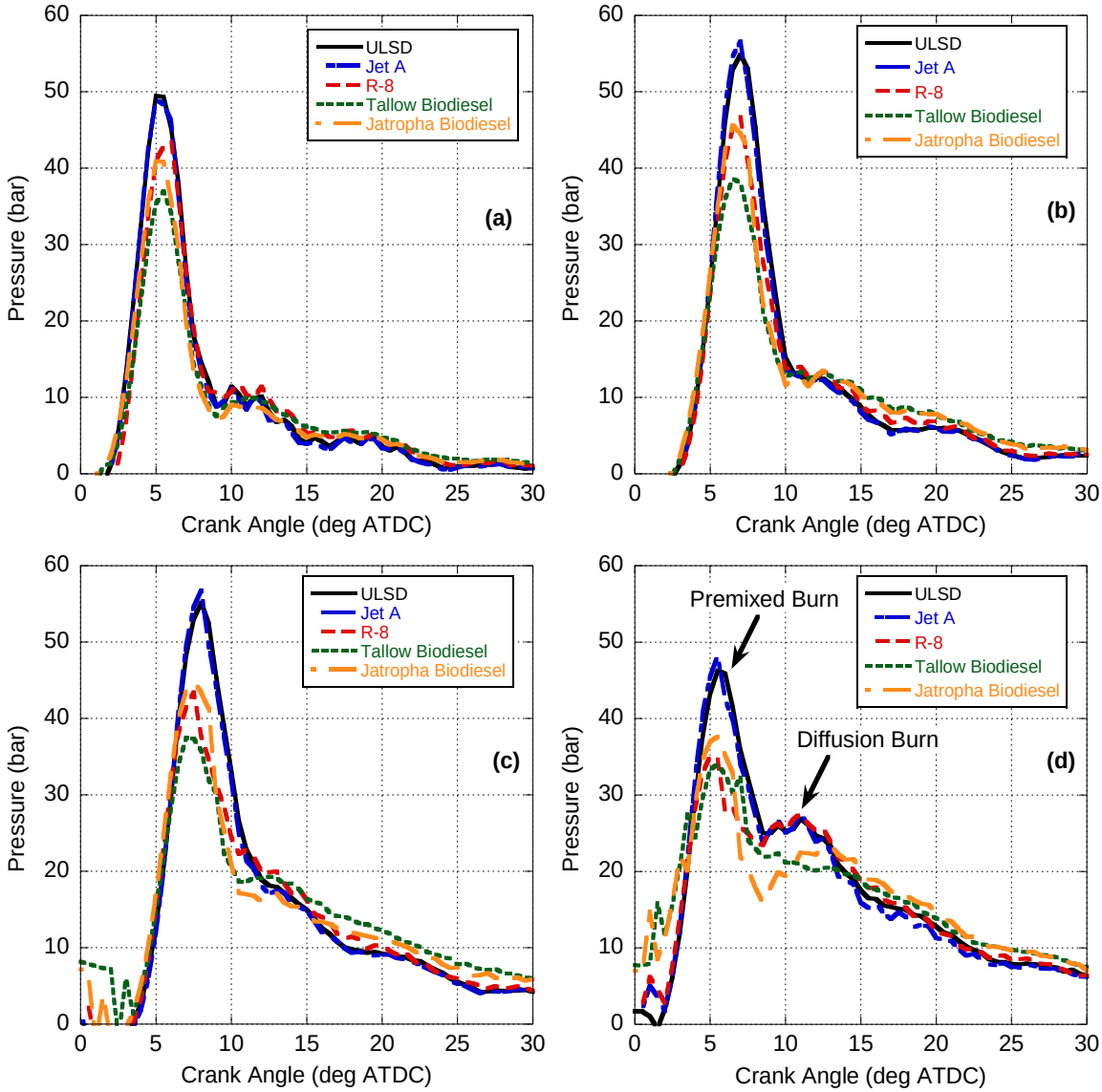

Figure 44. 1st Law RHR with respect to Crank Angle for (a) 4.5 N-m (b) 9.0 N-m, (c) 13.5 N-m, and (d) 18.0 N-m, for various neat fuels.

Brake specific fuel consumption (BSFC) and energy consumption (BSEC) were calculated from the measured fuel flow rates for all engine loads, and are shown in Figure 45. Overall, BSFC and BSEC

decreased with engine load. Fuel consumption was highest for the biodiesels, and lowest for the aviation fuels, and largely followed the same trends seen in the pressure and RHR results. Of note, the lowest BSFC for each engine load was the R-8 aviation fuel, despite its lower amount of premixed combustion, and higher amounts of diffusion burn. This also comes in spite of the low volumetric energy density of the R-8 fuel. Since fuel injection is on a volumetric basis for our system, R-8 has the lowest flow rate of fuel potential energy into the cylinder during injection, subsequently lowering the premixed spike and peak pressure. However, the R-8 fuel also carries the highest energy density, allowing the injector to deliver the needed amount of energy for combustion without requiring a large mass of fuel. Therefore, even though it has a lower added energy rate, overall less mass is used to achieve the required engine load.

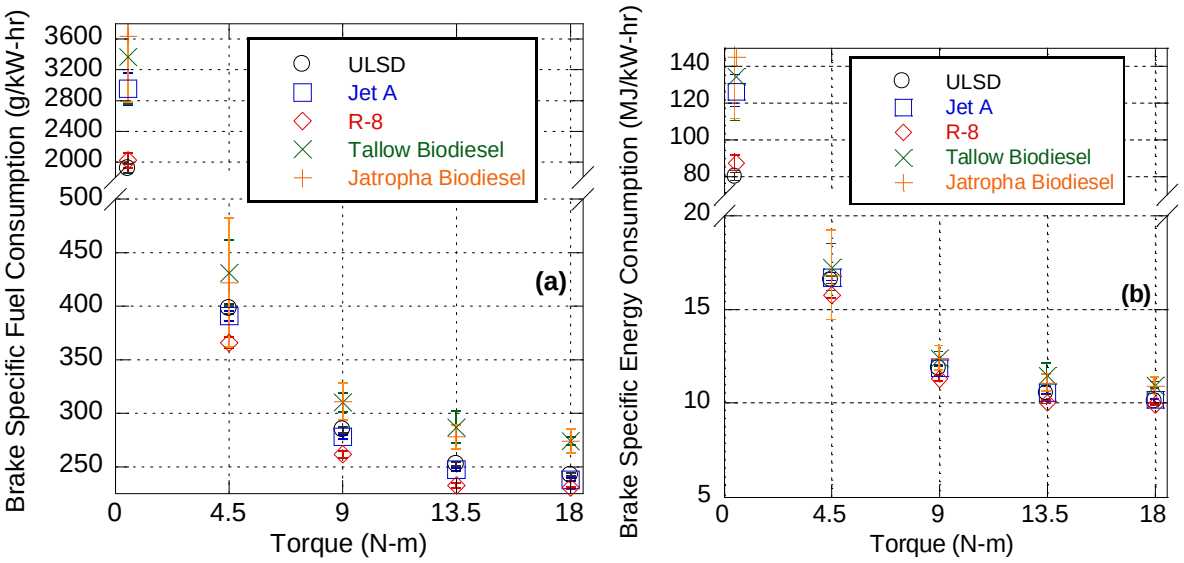

Figure 45. BSFC (a) and BSEC (b) for various neat fuels at all engine loads.

The reverse of this trend occurs for the biodiesel fuels; their higher volumetric energy content allows the injectors to deliver a greater rate of fuel energy into the cylinder for combustion. However, the low energy content means that the total amount of fuel mass required will increase significantly when operating with biodiesel, resulting in their high BSFC. In addition, the increasing viscosity of the biodiesel fuels has the effect of increasing inefficiencies, slowing the rate of combustion and stunting the rise in cylinder pressure (particularly in the case of tallow biodiesel). As a result, the distribution in BSFC between fuels increases further, and also appears within the BSEC, where the differences in fuel energy

content are largely removed. As a result, while the amount of energy injected per event may be the same (or less, in the case of R-8), the fact that the biodiesel fuels have less energy per unit mass results in a greater amount needed to achieve the desired engine load. R-8 additionally moves closer to the other fuels when investigating BSEC because the amount of energy needed to achieve each engine load should be similar between all fuels.

The low fuel mass requirement of the R-8 fuel results in it having the highest fuel conversion efficiency; whereas, biodiesels have the lowest (see Figure 46a). Fuel conversion efficiency serves as a measure of the fuel potential energy added by injection that is successfully released by combustion. Here, R-8 is the best fuel overall, owing to the lower amount of fuel that must be added to the cylinder, shortening the time needed for injection. In addition, R-8's decreased viscosity promotes better mixture preparation, allowing more of the fuel energy to be released closer to Top Dead Center (TDC), where work energy can be extracted more efficiently (seen later in total availability extracted as work). By comparison, the biodiesel fuels exhibit prolonged combustion due to their higher viscosity, releasing fuel energy later in the power stroke, lowering efficiency overall.

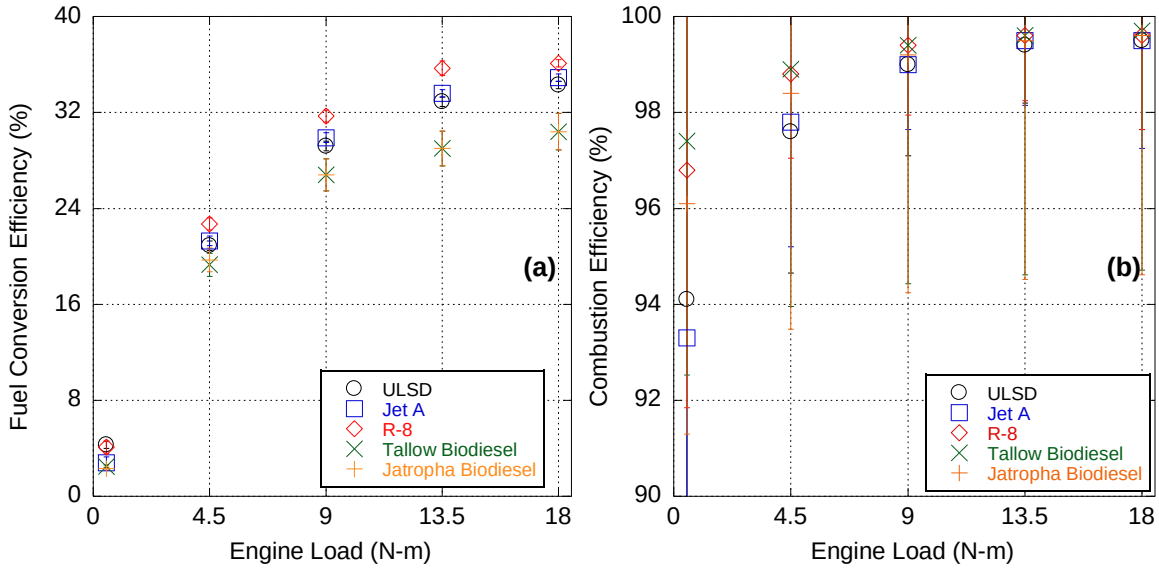

Figure 46. Fuel Conversion (a) and Combustion (b) Efficiencies for all fuels and engine loads for various neat fuels.

The next measure of cycle efficiency is the engine combustion efficiency in Figure 46b that measures the actual fraction of fuel mass consumed by the combustion process. Overall, Jet A and ULSD

exhibited the lowest overall combustion efficiency (investigating trends without error bars), caused by a tendency of these fuels to undergo richer combustion in spite of lower viscosities in comparison to the biodiesels. Tallow and jatropha biodiesel had the greatest overall combustion efficiency, despite their high viscosities and prevalence towards diffusion-dominated combustion. Each of the biodiesel fuels carries significant amounts of oxygen embedded in the fuel molecules, reducing the effective local fuel-air ratios. Moreover, biodiesel fuels have been shown to have greater in-cylinder temperatures (Figure 47) due to a higher adiabatic flame temperature, subsequently promoting combustion efficiency [19].

Unlike the ULSD and Jet A fuels, R-8 also had relatively high combustion efficiencies, comparable to the biodiesels. This is due to its low density complimenting its lower viscosity, promoting air mixing beyond the ULSD and Jet A. In addition, use of R-8 was found to increase in-cylinder temperatures because its diffusion burn rate is faster than ULSD and Jet A [25]. However, a reduced deviation in combustion efficiency is seen as engine load increases, as higher engine temperatures promote vaporization and combustion, regardless of fuel properties.

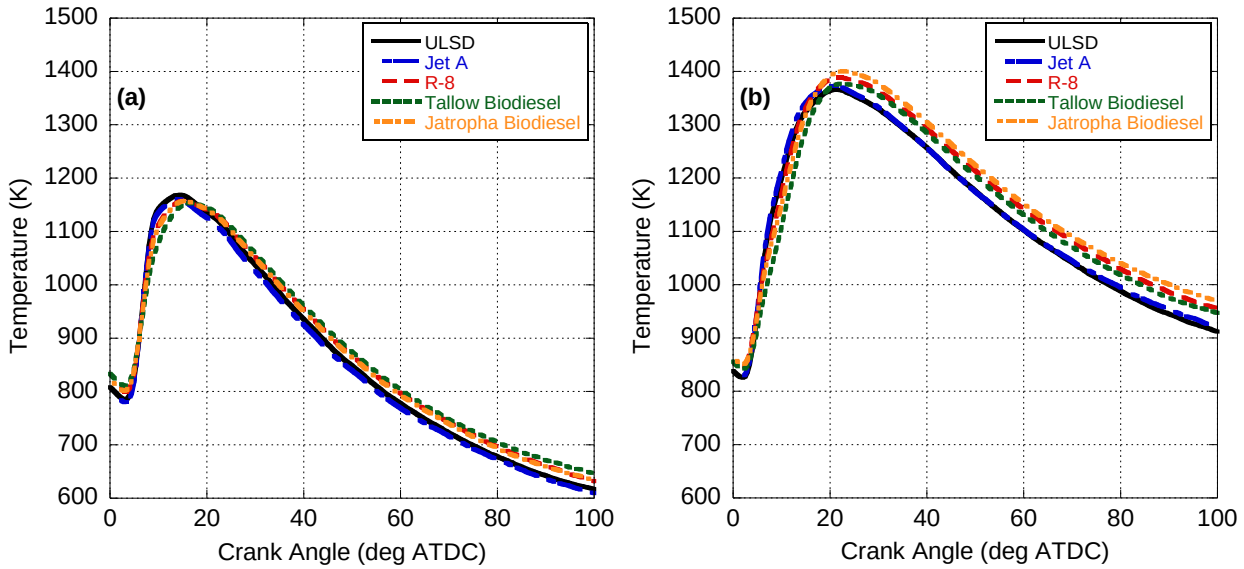

Figure 47. In-Cylinder Temperatures with respect to crank angle for (a) 9-0 N-m and (b) 18.0 N-m for various neat fuels.

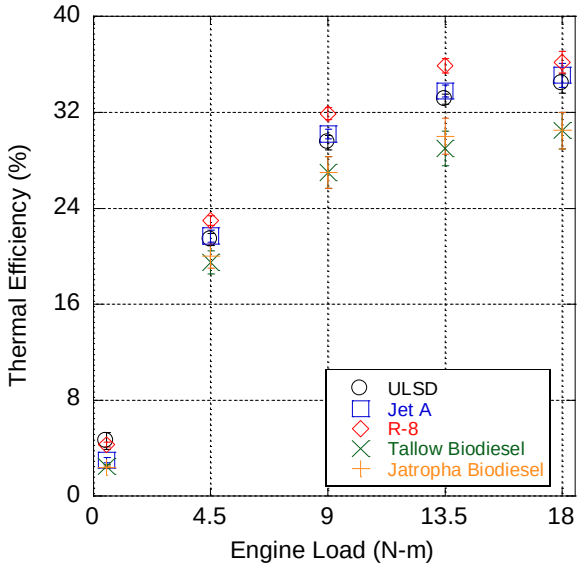

Figure 48. Thermal Efficiencies for all fuels and engine loads for various neat fuels.

The final means of understanding 1st Law-based engine efficiency is through the thermal efficiency, calculated as the ratio between the fuel conversion and combustion efficiencies. This efficiency serves as a measure of the fraction of energy liberated by combustion that is extracted as work (see Figure 48). Like the fuel conversion efficiency, the biodiesel fuels show the lowest overall values, despite their higher combustion efficiency (ignoring the error bars). This highlights the prolonged combustion time of the biodiesel fuels, which adds thermal energy later in the engine cycle where it cannot be extracted as efficiently. By comparison, the aviation fuels and ULSD exhibit larger amounts of combustion closer to TDC, where work is more easily extracted, thus leading to higher thermal efficiencies. R-8 is again the highest with its enhanced combustion efficiency improving its thermal efficiency over and above that of ULSD and Jet A.

Within the 2nd Law Analysis, the net addition of fuel availability in Figure 49 is closely tied to BSFC and BSEC. Overall, the fuel availability added to the cylinder increased linearly as engine load was increased. This is related to the linear increase in fuel flow rate needed to meet each prescribed engine load. The biodiesel fuels required higher net availability addition at all loads, corroborating their higher BSFC and BSEC results discussed earlier, subsequently reflected in their fuel conversion efficiency.

Furthermore, R-8 required a lower net availability addition at all loads, in keeping with its lower BSFC and BSEC (and improved fuel conversion efficiency).

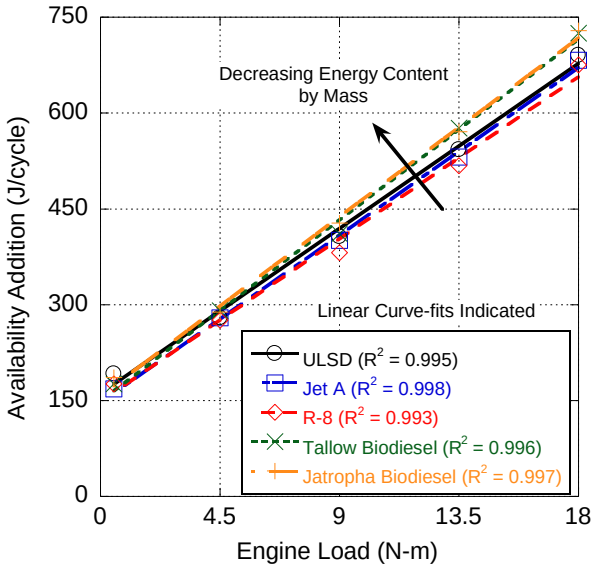

Figure 49. Availability Addition for various neat fuels.

The percentage of availability extracted as work represents the 2nd Law efficiency of the engine cycle (shown in Figure 50), and is the counterpart to the thermal efficiency (also commonly known as the 1st Law efficiency). Similar to thermal efficiency, the 2nd Law efficiency generally is maximized for the aviation fuels and ULSD, and is minimized for the biodiesel fuels. Overall, the deviation in 2nd Law efficiency between the fuels increases with engine load, with the two biodiesel fuels performing significantly worse than the ULSD, Jet A, and R-8 fuels at peak load. Altogether, this indicates a direct relationship linking 2nd Law efficiency to the changes in viscosity between the tested fuels. Of note, the 2nd Law efficiency highlights a difference between the biodiesel fuels, indicating that the tallow biodiesel is slightly less efficient, particularly at high loads (not distinguishable in thermal efficiency). In addition, the 2nd Law efficiency shows essentially no difference between operation with Jet A or ULSD, in support of the thermal efficiency results (when the measurement uncertainty is included). Hence, incorporating the 2nd Law efficiency helps further identify the trends between the different fuels over and above a standard RHR analysis.

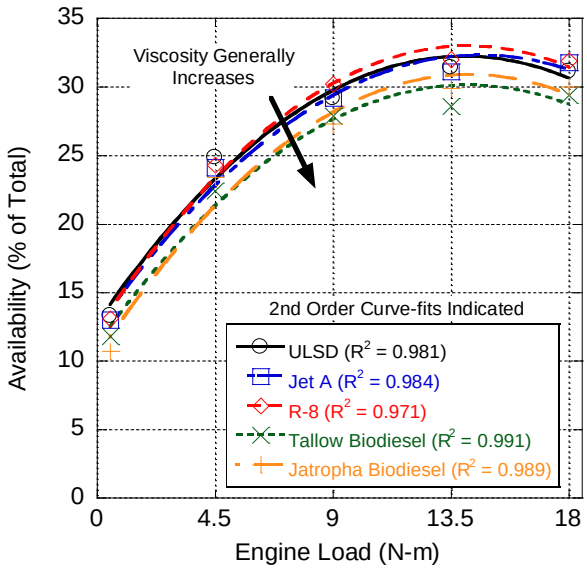

Figure 50. Percentage of Total Availability extracted as Work for various neat fuels.

The first means by which availability is lost is through heat transfer out of the engine cylinder, which is fundamentally a function of the in-cylinder temperature profile (see Figure 47). Here, the biodiesel fuels exhibit higher in-cylinder temperatures, particularly later in the engine cycle. This is due to their prolonged combustion caused by their high viscosity promoting diffusion burn, subsequently intensifying peak cylinder temperatures later in the expansion stroke (particularly at 18.0 N-m). In comparison, the R-8 fuel also had relatively high in-cylinder temperatures. This is due to its energy content by mass, as well as its higher combustion efficiency promoting a more complete extraction of fuel energy. In addition, while the ULSD and Jet A had higher peak cylinder temperatures for brief periods, their reduced diffusion burn phase lowered later in-cylinder temperatures. As a result, the distribution of in-cylinder temperatures can then be used to understand the relative amounts of heat transfer for each of the fuels tested as shown in Figure 51. Overall, the biodiesel fuels and R-8 had the highest rates of heat transfer, owing to their higher combustion temperatures. The ULSD and Jet A fuels, with their cooler combustion temperatures and less pronounced diffusion burn periods, exhibited less total heat transfer.

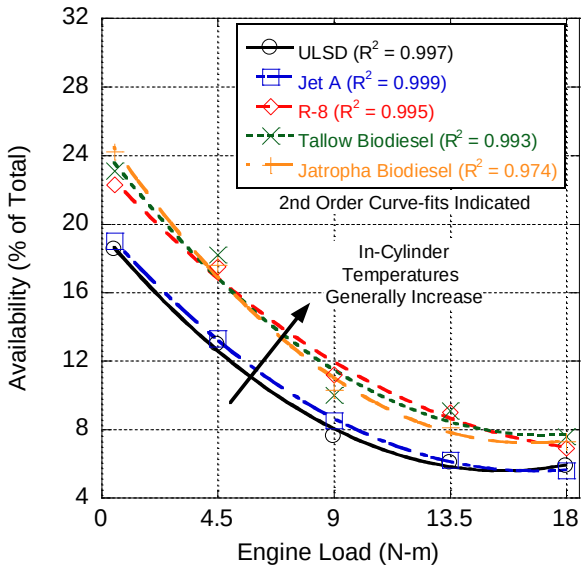

Figure 51. Percentage of Total Availability lost to Heat Transfer for various neat fuels.

The percentage of availability destroyed, or the amount of irreversibility within the working fluid, decreased slightly with increasing engine load as seen in Figure 52. Overall, Jet A had the highest amount of availability destruction, with ULSD somewhat lower, and the two biodiesels and R-8 all considerably lower. This result is linked to the same distribution of temperatures seen in the heat transfer profiles. Given that the calculation of availability is dependent on the temperature difference between the hot and cold side of the system, higher temperature differences lead to lower irreversibilities. As a result, increasing the temperature leads to a larger fraction of the total availability that may be extracted from the working fluid, which would otherwise be destroyed. The biodiesel and R-8 fuels also exhibited higher overall combustion efficiencies, due to oxygen content in the biodiesels, and high energy content by mass of R-8. Ultimately, ULSD and Jet A burn cooler than the other fuels, leading to a greater level of irreversibility, particularly at the highest engine loads.

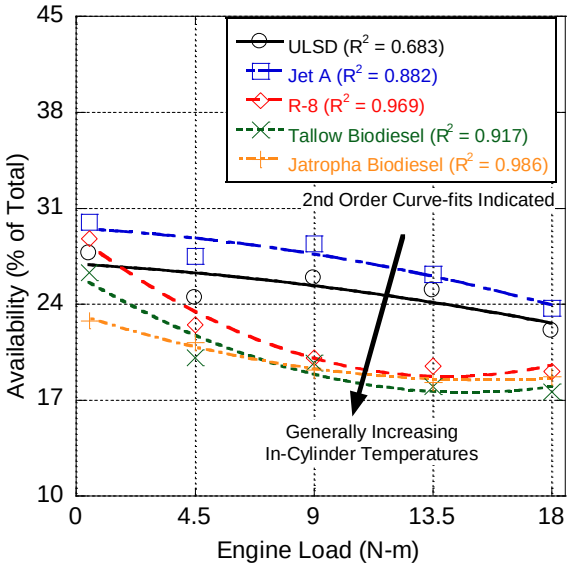

Figure 52. Percentage of Total Availability lost to Entropy Generation for various neat fuels.

In this way, the combined availability losses through heat transfer and internal irreversibilities in Figure 53 may be used as a means to derive and decompose efficiency information from the in-cylinder temperature profile, over and above the 1st Law analysis. At low engine loads, fuels are generally ordered by viscosity, with the least viscous fuels exhibiting the most irreversibility. Increased viscosities will lead to more prolonged and delayed combustion, increasing cylinder temperatures overall. At higher loads, losses to irreversibilities begin to array themselves in a fashion that viscosity alone cannot explain (particularly in the case of the R-8 fuel), implying that multiple fuel properties affect the net irreversibility at high load. Here, the R-8 fuel's higher combustion temperatures lead to a greater in-cylinder temperature. At all loads, despite these cylinder temperatures increasing the losses due to heat transfer, the losses are outweighed by the decreasing destruction of availability within the working fluid itself. In essence, the net irreversibility loss of the cycle is essentially a function of temperature only; e.g., Equations 27 and 29. This is probably why other authors have linked these two equations into a single expression for analysis. As a result, the 2nd Law analysis allows another means to link fuel properties to combustion results. In addition, the fraction of availability lost to all irreversibilities forms the 2nd Law analogue of the combustion efficiency, as it reflects the advantages of both the high heat of combustion and the complete consumption of fuel.

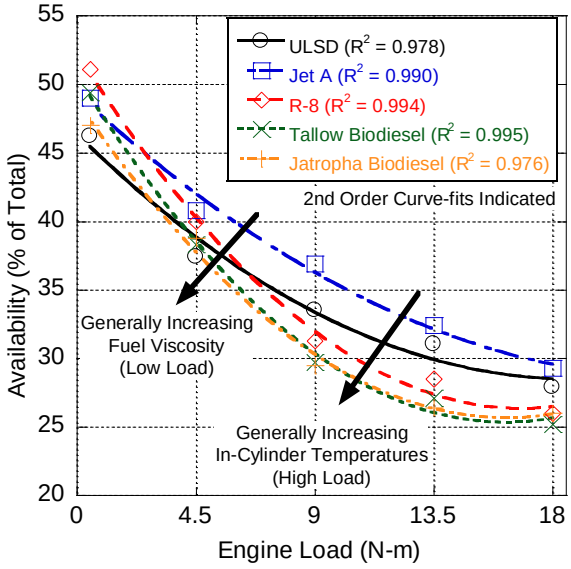

Figure 53. Percentage of Total Availability lost to all Irreversibilities for various neat fuels.

Overall, the availability retained by the working fluid in Figure 54 generally accounted for around 35-45% of the total availability added to the cylinder. The amount of availability retained slightly decreased with load, representing the ability of the engine to take further advantage of the growing temperature of the working fluid as more fuel energy/availability is added to the cylinder primarily in a premixed burn scenario (Figure 2). For high loads, increasing diffusion burn prolongs the duration of combustion, and causes the addition of availability later in the engine cycle, where the cylinder is rapidly expanding and cooling. As a result, this later availability addition is wasted, as it is at a relatively lower temperature, and the engine cannot effectively extract it as work.

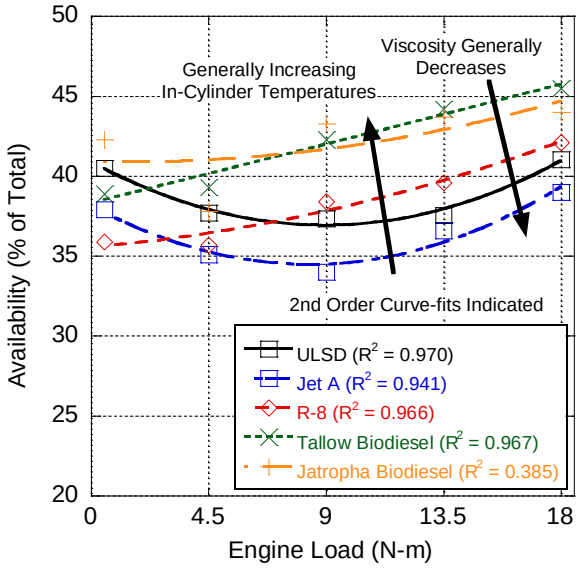

Figure 54. Percentage of Total Availability retained by Exhaust Gases for various neat fuels.

Here, the effect of viscosity and energy content on diffusion-dominated combustion is additionally seen. In particular, the increased viscosity of the biodiesel fuels decreases the ability of the fuel to break up after injection, slowing combustion while increasing diffusion-dominated combustion and moving it further from TDC. By comparison, the decreasing viscosity of the Jet A and ULSD leads to more advantageous fuel break up, moving diffusion-dominated combustion closer to TDC, subsequently leading to a higher work extraction. In the case of R-8, its higher combustion temperatures lead to a greater fraction of availability left in the exhaust than in the ULSD or Jet A fuels. However, R-8's greater energy content by mass promotes more prompt combustion, meaning more fuel energy is released closer to TDC where the engine may extract work more efficiently, and leads to lower amounts availability than is encountered in the biodiesel fuels. This shows a similar result (at high loads) to the net irreversibility losses. Here the competing effects of viscosity and in-cylinder temperature can be seen; while in-cylinder temperatures take precedence overall as a measure of the availability added to the working fluid, fuel viscosity affects the timing of this availability addition.

5.4.2 2nd Law Behavior of ULSD-Biodiesel Blends

In tandem with this testing, a palm-oil derived biodiesel fuel was also analyzed in order to further examine the changes in fuel properties and their effects on the 2nd Law analysis. In particularly, given that

the fuel viscosity, density, and energy content are essentially a linear function of composition of the fuel blend, this allows a consistent and predictable shift in fuel properties and 2nd Law phenomena. The characteristics of both the palm biodiesel (P100) and ULSD (P0) may be found in Table 25. Biodiesel and diesel fuel were blended, producing fuel mixtures with biodiesel contents of 5% (P5), 10% (P10), 20% (P20), and 50% (P50) by volume. Of note, representative viscosity measurements from a different batch of palm biodiesel and ULSD blends is provided in Table 26 for discussion purposes (details of these tests are available from the authors). Injection timings for the fuel blends were adjusted as necessary (advanced towards TDC) in order to retain peak engine efficiency, based on the alignment of peak cylinder pressure timing [10, 19]. Using Equation 32, the availability content of the biodiesel was found to be 1.076 times the energy content of the fuel [134, 136], while assuming the overall sulfur content of the biodiesel was negligible. The overall increase in proportionality between ULSD (at 1.065 times the energy content) and the palm biodiesel is primarily due to the oxygen content of the fuel, promoting more complete combustion (and addition of availability).

Table 25: ULSD and Biodiesel Properties [19].

Fuel	ULSD	Palm Biodiesel
Cetane Number	40	60
Density @ 20°C [kg/m^3]	837.58	872.63
Lower Heating Value [kJ/g]	42.8	40.5
Kinematic Viscosity [cSt]	2.58	4.61
Flash Point [°C]	55.8	184.8
Oxygen Content [% wt.]	-	10.17±0.29
Carbon Content [% wt.]	86.34±0.20	76.57±0.13
Hydrogen Content [% wt.]	14.27±0.20	13.27±0.16

Table 26: ULSD and Biodiesel Blend Properties from Experiments [19].

Fuel	Kinematic Viscosity (cSt)
ULSD	2.578±0.008
- Palm -	-
5%	2.608±0.008
10%	2.714±0.008
20%	2.849±0.009
50%	3.395±0.010
100%	4.605±0.014

As with the ULSD presented earlier, the 1st Law analysis was run first, and the resulting rates of heat release for the biodiesel blends at 9.0 N-m and 18.0 N-m are shown in Figure 55(a) and Figure 55(b), respectively. Of note, increasing the composition of biodiesel in the fuel blend leads to a decrease in the magnitude of the premixed spike, in addition to a gradual shift forward in the timing of the peak RHR. This is paired with an increase in the magnitude of the diffusion burn. This is because the higher cetane number (and lower ignition delay) of biodiesel blends results in less fuel being prepared prior to ignition. Moreover, an increase in fuel viscosity with biodiesel composition further serves to inhibit fuel atomization and vaporization. Therefore, premixed combustion decreases with blend subsequently leading to a growth in mixture-controlled diffusion combustion [19, 144].

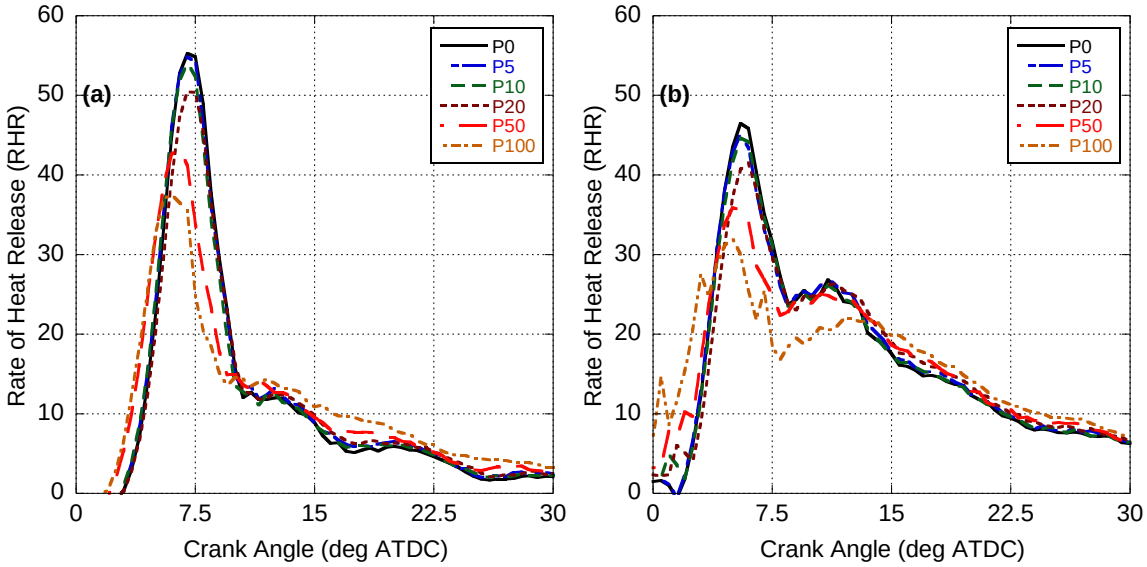

Figure 55: Calculated Rates of Heat Release for ULSD, Palm Biodiesel, and Blends at 9.0 N-m (a) and 18.0 N-m (b).

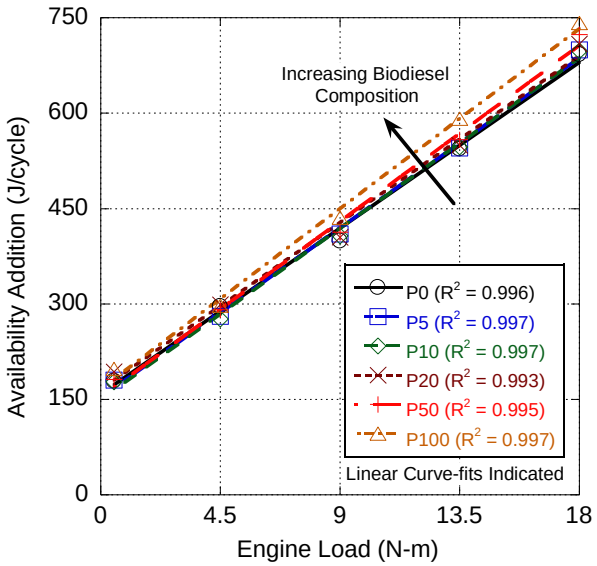

Figure 56: Availability Addition for ULSD, Palm Biodiesel, and Blends.

As the engine load increases, the overall period of premixed combustion broadens and is lowered as biodiesel content is increased. The diffusion-dominated portion of combustion becomes more prominent and lasts slightly longer with increasing biodiesel content, but does not significantly diverge from the behavior of ULSD until the biodiesel content reaches 50%. The cause of this behavior is closely linked to the increased viscosity of the biodiesel, which inhibits fuel breakup and atomization subsequently increasing ignition delay. In specific, investigating Table 26, the viscosities of biodiesel blends at and below 20% are relatively close to that of ULSD. As a result, for high engine loads where fuel injection is more prolonged, this increased fuel breakup time limits the ability of the engine to consume the fuel in the premixed combustion phase. This behavior is integral to understanding the 2nd Law analysis.

The net changes in availability added into the cylinder (i.e., injection of fuel) are shown in Figure 56. Overall, increasing biodiesel composition (that itself has a higher availability) in the injected fuel leads to a greater availability needed by the engine to meet the desired load, in turn requiring further fuel injection. This is due to the inhibiting effects of biodiesel viscosity and the lower energy content of biodiesel, subsequently noted in the experiments by an increase in fuel consumption with biodiesel blends. Moreover, there is little change in availability addition with 20% blends and less. This initially

corroborates the 1st Law HR findings with respect to blends that could be substituted for ULSD with little difference noted.

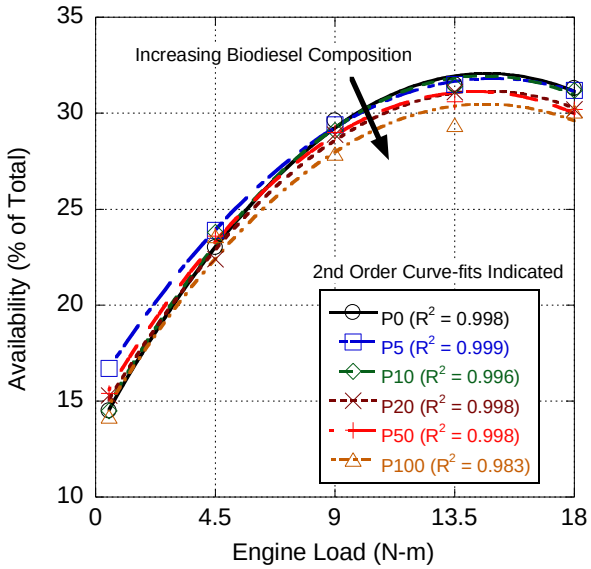

Figure 57: Percentage of Calculated Total Availability transferred as Work for Biodiesel Blends.

The increasing inefficiencies of utilizing biodiesel fuel is most apparent when considering the 2nd Law efficiency of the engine cycle, or the percentage of availability transferred as work (see Figure 57). Here, there is a decreasing level of availability as a function of biodiesel blend. Interestingly, the behavior of the biodiesel blends at full engine load seems to converge on one of two extremes. For blends with 10% biodiesel content or less, the efficiency decreases are marginal, and the behavior of the blend is largely the same as ULSD. However, at or above 20% biodiesel content, all of the tested blends exhibit a lowered efficiency.

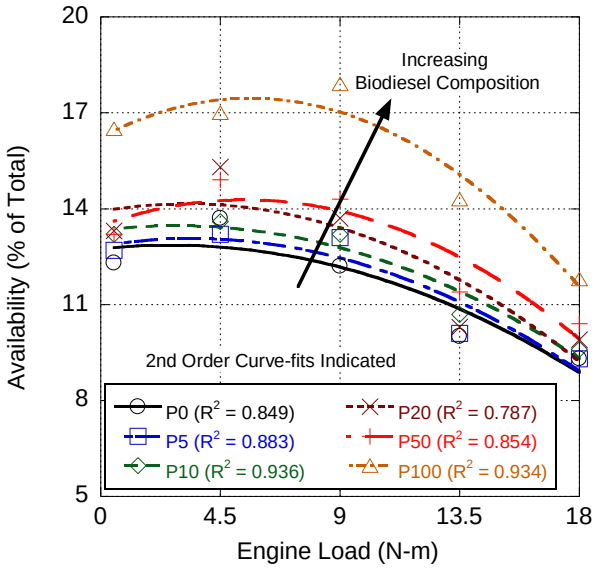

Figure 58: Percentage of Calculated Total Availability lost to Heat Transfer for Biodiesel Blends.

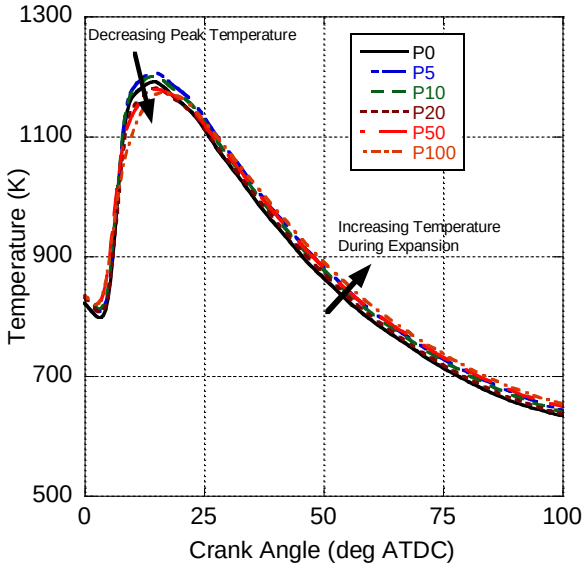

Figure 59: Calculated In-Cylinder Temperature profile for Biodiesel Blends at 9.0 N-m.

This behavior can be explained through the increase in viscosity with biodiesel content. In prior testing (utilizing only the 1st Law HR analysis) it appeared that 50% biodiesel composition was the tipping point of the blend acting dissimilar to ULSD [19]. However, in the 2nd Law HR analysis, it appears that for blends below 20%, the increased viscosity is marginal and does not greatly affect fuel atomization. At 20% and higher, the viscosity effects of the biodiesel begin to dominate, noticeably decreasing (using availability) the more efficient premixed combustion phase. For neat biodiesel, the

effects of viscosity are even more pronounced, such that the stunting of the premixed spike begins to manifest earlier (see Figure 55). This illustrates the advantage of performing both a first and second law HR analysis; i.e., finding the tipping point of biodiesel blends performing similarly to neat ULSD.

The first source of availability losses is through heat transfer out of the cylinder as shown in Figure 58. In general, the total amount of heat transfer increases with biodiesel content in the fuel. This behavior is likely linked to the higher combustion temperatures commonly seen when utilizing biodiesel fuel [19, 144-146]. This is corroborated in Figure 59 that illustrates a decrease in peak temperature due to a less energetic pre-mixed combustion phase, but a hotter expansion stroke with biodiesel composition. It appears that the losses due to heat transfer peak between 4.5 and 9.0 N-m. This is because the combustion event is largely pre-mixed and relatively short providing ample time for heat transfer to the walls. As diffusion burn begins to dominate, the losses due to heat transfer decrease in a relative manner because combustion is happening later in the cycle resulting in less physical time for heat transfer.

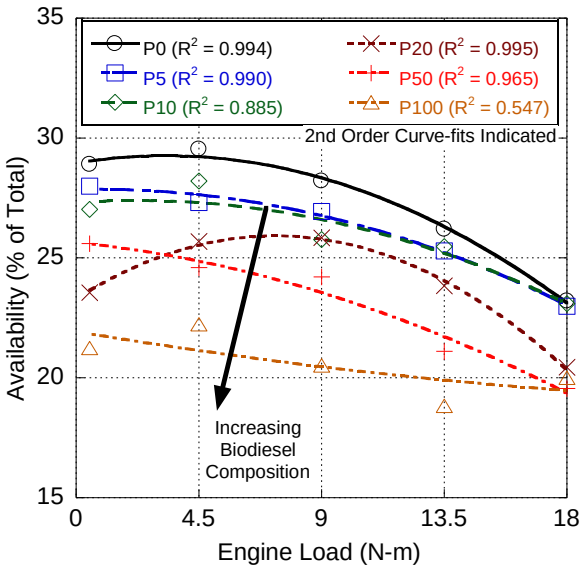

Figure 60: Percentage of Calculated Total Availability lost through Entropy Generation for Biodiesel Blends.

The second source of availability losses is through the destruction of availability by entropy generation within the working fluid, seen in Figure 60. Overall, the total amount of irreversibilities decreases with engine load (as described earlier for ULSD), regardless of the biodiesel fuel composition. However, internal irreversibility exhibits an overall decrease with respect to increasing biodiesel

composition. This reduction is again linked to the higher in-cylinder temperatures of the biodiesel fuel. By further increasing the temperature of the working fluid above the ambient (in comparison to ULSD), the addition of chemical availability increases the temperature difference between the two thermal reservoirs, increasing the thermal efficiency (as discussed prior) and leads to an increase in the fraction of availability that may be extracted as work instead of being lost to irreversibilities. In addition, the oxygen content in biodiesel provides an added combustion enhancer helping to improve combustion efficiency by ensuring that oxygen is near more carbon and hydrogen bonds, especially during the diffusion burn phase. Therefore, irreversibility decreases as the combustion process becomes more efficient even though viscosity increases (i.e., atomization decreases) with biodiesel content.

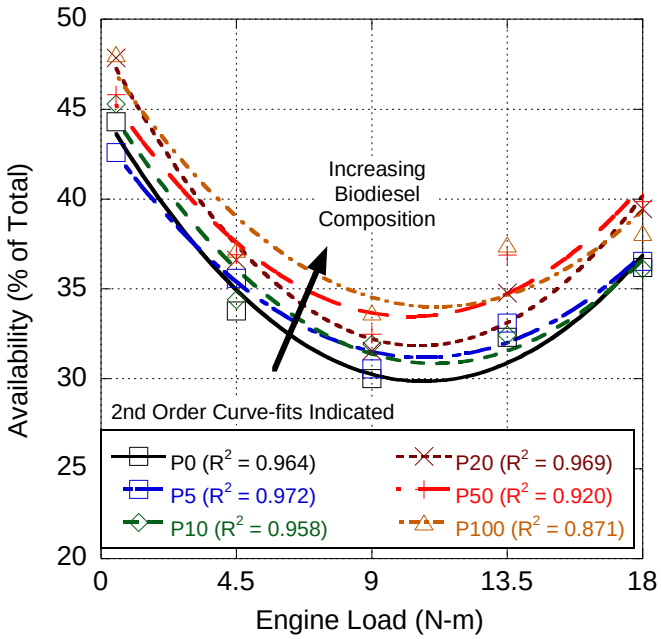

Figure 61: Percentage of Total Availability retained by the Exhaust Gas for Biodiesel Blends.

The final means for availability to be lost from the system is in the unused energy contained within the exhaust gases as they exit the cylinder, shown in Figure 61. Overall, increasing the biodiesel content leads to an increase in unused availability. This is partially due to the increased in-cylinder temperatures with added biodiesel composition; i.e., more thermal energy left in the exhaust gases at Exhaust Valve Opening as seen in Figure 59. However, the more important factor is the increasingly prolonged combustion of biodiesel fuel due to viscosity, leading to the addition of availability to the

working fluid later in the engine cycle. In this state, where the engine cylinder is already rapidly expanding (and cooling), this late availability addition is largely wasted by the engine's inability to extract it.

5.4.3 Operation at Lower Compression Ratios

As a final examination of the model, it is of importance to examine the potential effects of the model on engines with compression ratios lower than that of the Yanmar L100V. In general, lowering the compression ratio serves to reduce in-cylinder pressures and temperatures. In addition to generally reducing engine efficiency (as a direct result of Carnot's Law), this also directly reduces the efficacy of fuel injection and dispersion into the cylinder, resulting in a more difficult fuel break-up period [147]. This, in turn, will generally decrease efficiency, increase fuel consumption, and promote incomplete combustion and emissions of hydrocarbons and particulate matter.

The engine used for this particular study was a naturally-aspirated four-stroke AVL5402 single cylinder CI research engine, coupled with an AVL DynaRoad202 dynamometer with engine and dynamometer specifications presented in Table 27, located at the Technical University of Cluj-Napoca, Romania [148]. The testbed used for the study features an AVL Rapid Prototyping Engine Management System (RPEMS) and ETK7 engine management system that allows a flexible engine control. Specifically, this enables the user to change the injection timing and quantity for up to four injection sequences (two pilots, main, and post injection), as well as the fuel pressure in the common rail. Here, only a main injection event was utilized. Furthermore, the testbed is equipped with a fuel conditioning unit for control of the experiments. This includes an AVL735 Fuel Mass Flow Meter for fuel flow rate and density (±0.12% kg/h, ±0.0005 g/cm^3) with the fuel consumption measured as a difference between the fuel feed line and the fuel return line along with an AVL753 Temperature Control unit for fuel temperature control. Operating conditions are further regulated with the aid of an AVL577 conditioning unit that enables a control of the coolant flow and temperature (5-120°C ±1°C) while also modulating the oil flow, temperature, and pressure.

Table 27. Engine and Dynamometer Specifications [148].

Engine			
Model	AVL 5402	Bore	85 mm
Intake	Natural Aspirated	Stroke	90 mm
Cooling	Water-Cooled	Fuel Pump	Bosch CP4.1
Cycle	4-Stroke	Fuel System	Common Rail Direct Injection
Displacement	510.7 cm^3	Max Injection Pressure	180 MPa
No. of Cylinders	1	Engine Management	AVL RPEMS + ETK7
Compression Ratio	17.1:1	Rated Power	6 kW
Number of Valves	2 Intake, 2 Exhaust	Rated Speed	4200 RPM
AC-Dynamometer			
Model	AVL DynaRoad 202	Nominal Power	198 kW
Maximum Speed	12000 RPM	Nominal Torque	473 N-m

The engine was equipped with a glow-plug type AVL GU22C pressure transducer (0 to 250 bar, linearity ±0.3%, thermal sensitivity ±1%) for in-cylinder pressure measurements at a variable sampling interval over an engine cycle. For this study, the authors opted for a sampling interval of 0.1 °CA (crank angle) between 30 °CA BTDC (before top dead center) and 70 °CA ATDC (after top dead center), and 1 °CA for the rest of the cycle. The pressure trace, which is an average of 101 thermodynamic cycles, was then analyzed using the first and second laws of thermodynamics to determine the rate of heat release and in-cylinder temperatures [12, 118]. Additional sensors allow the measurement of the ambient temperature (accuracy ±1.5°C), pressure (accuracy ±0.2%) and relative humidity (RH; accuracy ±0.6% for 0-5% RH and ±1% for 5-80% RH), intake air temperature (PT100; accuracy ±0.15+0.002×temperature) and pressure (PTX 1400; accuracy ±2% from -20 to 80°C), as well as exhaust gas temperature and pressure (same as intake). The intake air mass flow is measured using a Sensyflow P thermal mass flow meter (accuracy ±1% of reading; repeatability error ±0.25% of reading).

Table 28. Properties of WCO Biodiesel and Diesel Fuel [146].

Property	ULSD	Biodiesel
CN	51	52.8
Energy Content (kJ/kg)	43000	39663
Density (kg/m^3 at 298.15 K)	826	860
Kinematic Viscosity (cSt at 40º C)	4.50	6.56
Dynamic Viscosity (cP at 40º C)	3.717	5.79
Oxygen Content	N/A	10.5

Two fuels were used for this study: ULSD (with the properties specified according to the quality assurance sheet of the fuel, except for density that was measured using the AVL 735 and the energy content that was taken from the European Fuel Quality Legislation [149]), and a WCO biodiesel (produced according to the methodology presented by Cecrle et al. in [146]) with the main properties estimated to be similar to those presented in Table 28. For the tests, the engine was operated at 2000 rpm at five different loads: 0, 25, 50, 75 and 100% load. The ULSD was tested first, as a reference. For the WCO biodiesel, the injection quantity was increased to obtain the equivalent load, while the injection timing was adjusted to maintain the same crank angle position of the peak cylinder pressure for normalized combustion phasing between the test fuels (discussed later). The fuel injection pressure was the same in both cases and the test parameters are presented in Table 29. Ambient conditions were also controlled, with the following values measured during the tests: 28-35 ºC ambient temperature, 973-981 mbar ambient pressure, 13.3-17.3% relative humidity, and 23-29 ºC intake air temperature. Finally, the emissions were measured using a Bosch BEA350 system as follows: after the engine reached steady state, defined when engine oil and exhaust temperatures changed by less than one percent over a 60 second period, emission values for CO, CO_2, NO_x, and HC were recorded every 10 seconds for 1 minute. The obtained values were averaged and converted to brake specific quantities.

Table 29. Test Parameters for Study [148].

		ULSD			WCO Biodiesel			
Speed	Load	Injection Quantity	Injection Timing	Injection Pressure	Injection Quantity	Injection Timing	Injection Pressure	Normalized Injection
RPM	%	mg	°CA BTDC	MPa	mg	°CA BTDC	MPa	°CA
2000	0	9	7.5	60	13.6	5.6	60	+1.9
	25	12.6	7.9	60	18.5	6.0	60	+1.9
	50	16.4	8.2	70	22.2	6.4	70	+1.8
	75	21.4	9.0	70	29.4	7.9	70	+1.1
	100	27.4	11.6	70	36.3	12.4	70	-0.8

The first analysis primarily concerned the effect of WCO biodiesel on this engine without changing injection timing in order to realign the timing of peak pressure. In specific, after setting the injection timing and pressure to the same ULSD test values, the injection quantity of WCO biodiesel was increased gradually until the BMEP of the engine was equated to that of ULSD. This led to an increase of 53.4, 49.1, 37.4, 39.8, and 35.0% in fuel mass injected for 0, 25, 50, 75, and 100% load, respectively, when using WCO biodiesel. This is largely due to its reduced energy content even though it has a greater density as highlighted in Table 28. In other words, since the engine injection system adds fuel on a volumetric basis, WCO biodiesel is being added at a reduced volumetric energy level of around 34,110 MJ/m3 in comparison to 35,518 MJ/m^3 for ULSD.

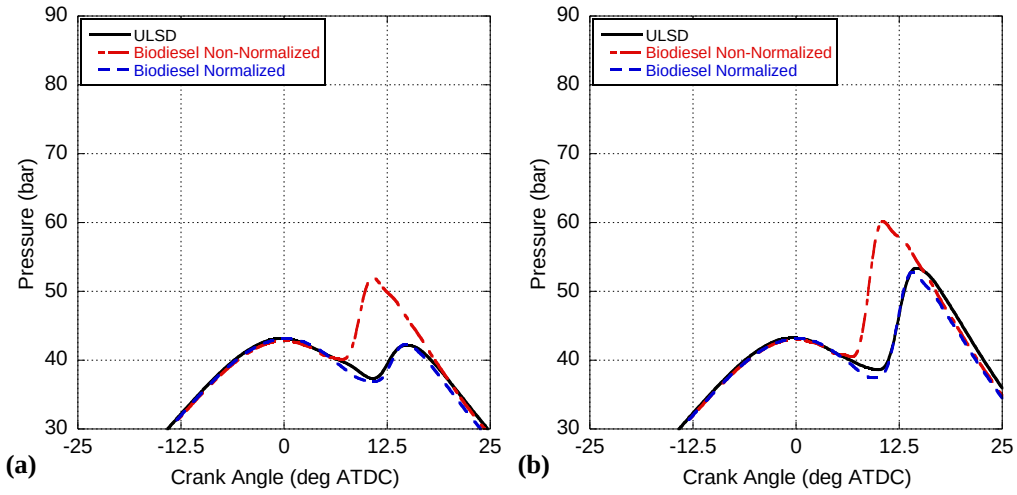

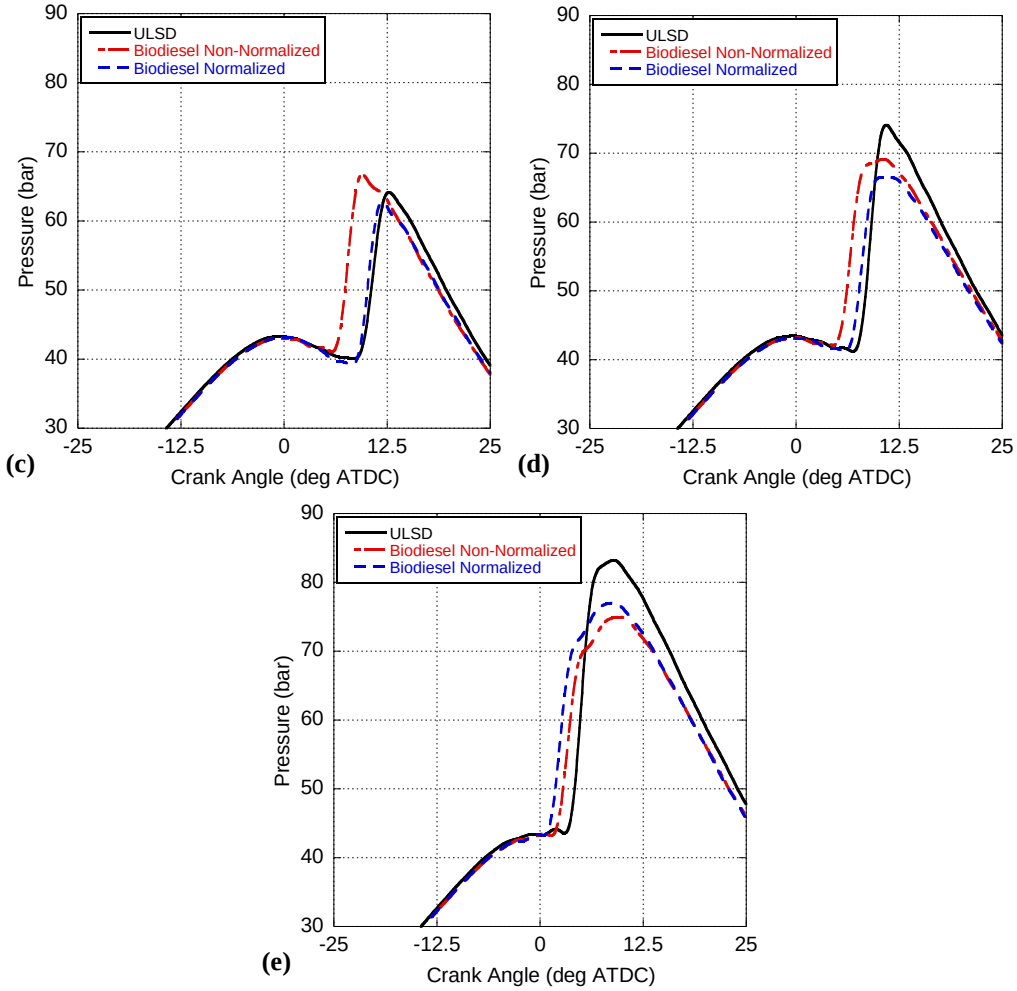

Figure 62: Measured and Filtered in-cylinder pressure trace at (a) 0% Load, (b) 25% Load, (c) 50% Load, (d) 75% Load, and (e) 100% Load for AVL 5402 engine.

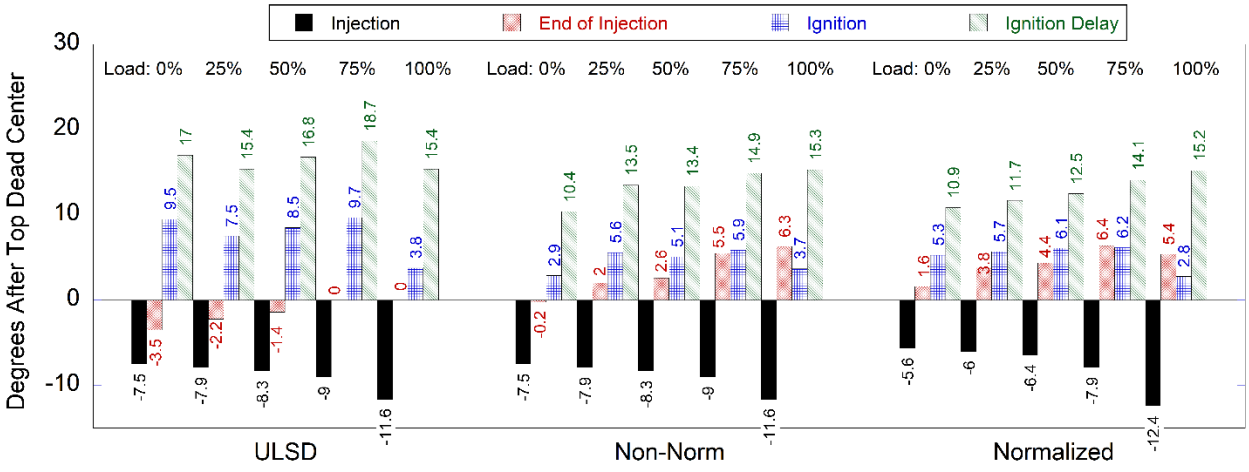

Figure 63: Injection and Ignition Parameters.

As demonstrated in Figure 62, employing the same injection timing for WCO biodiesel as ULSD led to an advance of the combustion process. To further elucidate on combustion timing differences, a comparison of the injection timings with the start of combustion using the 2nd derivative of pressure determined through the RHR analysis (shown later) provides valuable insight about the ignition delay in Figure 63. It was found that, except at 100% load, combustion of the biodiesel fuel started earlier than ULSD, both in the non-normalized (1.9 to 6.6 °CA advanced) and the normalized (1.8 to 4.2 °CA advanced) cases. This is due primarily to the larger cetane number (CN) of biodiesel, in spite of the increased injection delay (valid for common rail injection systems, but not for mechanical injection systems [150, 151]), poorer atomization, and lowered air-entrainment level, which occurs when changing from ULSD to biodiesel [152-154]. Moreover, the fuel bound oxygen in biodiesel additionally aids in achieving equivalence ratios in the flammability range faster than with ULSD promoting a reduced ignition delay. However, at 100% load, the start of combustion was somewhat comparable between ULSD, non-normalized (0.1 °CA advance) and normalized (1 °CA advance) biodiesel. Here, the need to add a significant amount of fuel to achieve the load required forces the injection process earlier into the compression stroke; hence, each case is given ample opportunity to mix prior to reaching combustion temperatures.

Since combustion that happens sooner results in an earlier heat release, this subsequently influences in-cylinder temperatures and exhaust emissions. Therefore, the rest of the analysis will primarily compare normalized WCO biodiesel and ULSD results by matching the peak pressure crank angle location to (mostly) remove the influence of combustion phasing. This WCO biodiesel normalization process resulted in an increase of 1.6, 0.9, 1.0, 0.7, 7.7% in fuel mass injected for 0, 25, 50, 75, and 100% load, respectively, in comparison to the non-normalized tests.

With the underlying non-normalized tests understood, the normalized tests can be considered. Up to 50% load (Figure 62a, b, and c), delaying the injection timing and matching the BMEP requirements finds that the in-cylinder pressures between normalized biodiesel and ULSD are relatively similar to

slightly lower. However, above 50% load (Figure 62d and e), the peak cylinder pressures for normalized biodiesel drop significantly below that of ULSD. This is likely due to the increased viscosity of biodiesel inhibiting fuel breakup and promoting diffusion burn as a greater level of fuel flow rate is needed to achieve these higher loads. Interestingly, unlike prior results in the literature [5, 19], at 100% load the normalized biodiesel test requires an advanced injection timing in comparison to the non-normalized case. Reviewing these earlier efforts finds that they:

a) employ a higher compression ratio engine (21.2:1 for the Yanmar L100V compared to 17.1:1 for the AVL 5402);

b) the peak pressure for combustion happens sooner;

- Yanmar L100V ignition occurs at 4-5 °CA ATDC with peak pressure at 10 °CA ATDC;
- AVL 5402 ignition occurs 7.5-10 °CA ATDC and peak pressure at 12.5 °CA ATDC or later;

c) while the Yanmar L100V has been upgraded to a common rail electronic injection system, it operates at a respectively lower pressure of 45 MPa as opposed to 60-70 for the AVL 5402.

Here, the set base calibration of the AVL 5402 engine was supplied by the engine manufacturer and not determined as per the maximum thermal efficiency as accomplished for the previous work [16]. Therefore, biodiesel fuel is injected in a relatively less favorable environment for atomization and vaporization. Furthermore, this is compounded by a respectively lower compression ratio that results in a reduced pressure and temperature seen by the fuel as it enters the cylinder. Given biodiesel's higher viscosity, lower volatility, and reduced energy content, it has a more difficult time achieving the 100% load setting, subsequently requiring an earlier and longer injection event.

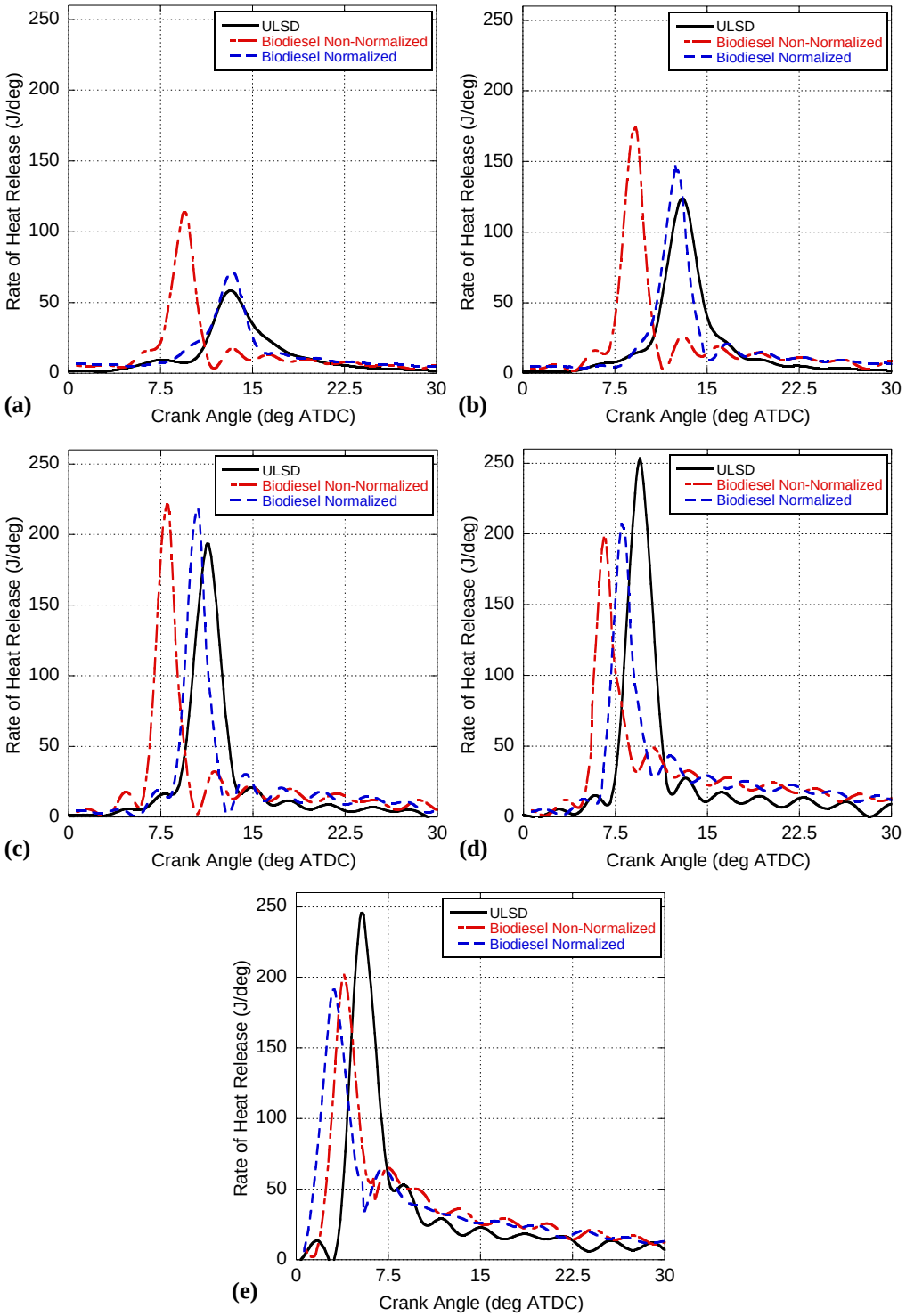

Figure 64: Calculated Rate of Heat Release at (a) 0% Load, (b) 25% Load, (c) 50% Load, (d) 75% Load, and (e) 100% Load for AVL 5402 engine.

Two dissimilar kinds of behavior are seen for the Rate of Heat Release (RHR): one for loads at or below 50% Figure 64a, b, and c), and one for above 50% (Figure 64d and e). Distinctively, below 50%

load, the normalized biodiesel encounters a higher peak RHR with apparently a shorter period of premixed energy liberation. As a result, the process indicates a strong proclivity towards constant volume combustion. Nonetheless, even with this seemingly more energetic and quicker heat release event, the in-cylinder pressures do not exceed that of ULSD. Investigating Figure 63 demonstrates that, except for the 100% load case, all normalized biodiesel injection events begin closer to TDC. Therefore, the fuel injection process is seeing a greater in-cylinder pressure and temperature initially; hence, this should result in a lower spray penetration length (compared to the non-normalized case) but a more spread-out fuel spray that vaporizes quicker. Furthermore, engine coolant temperatures were found to be slightly higher during the biodiesel tests since combustion happens sooner and there is more time for heat transfer (80.4 / 80.6 ℃ for WCO compared to 78.2 / 79.8 ℃ for ULSD; seen in 2nd Law analysis discussed later). Thus, this will additionally promote a slightly enhanced vaporization of the fuel. As a result, there appears to be a better mixing of fuel and air at the beginning of WCO biodiesel's fuel injection process. Combining this with its higher CN, more embedded oxygen (i.e., greater level of equivalence ratios in the flammability zone) and a greater adiabatic flame temperature results in a quicker and apparently more vigorous heat release. However, since significantly more biodiesel fuel must be added because of its reduced energy content, this grows the energy taken away from the working fluid via the latent heat of vaporization. As a result, the in-cylinder pressure and temperature (Figure 65) drops below that of ULSD even as combustion is beginning (Figure 62). Therefore, the biodiesel fuel added towards the end of the injection process sees slightly worse conditions while mixing and vaporizing less well (compounded by its greater viscosity), subsequently showing up as a less efficient diffusion burn (seen in Figure 64), and increasing fuel consumption. Overall, while initially biodiesel burns more effectively, this is not sufficient to overcome a growth in diffusion burn resulting in lower in-cylinder pressures and temperatures. This discussion will be revisited when presenting the second law heat release analysis for further clarification.

After 50% load, the onset of diffusion burn behavior begins and there will be a reduction in efficiency proportional to the increase in pressure trace width. This is due to a combination of a larger fuel mass injected and a poorer mixing of biodiesel with the air inside the combustion chamber, which

leads to a greater amount of fuel that cannot be burnt during the premixed phase. Here, ULSD appears to remain largely pre-mixed because of its respectively lower viscosity and longer ignition delay resulting in an enhanced mixing process. As a result, the trend now switches with ULSD having a higher RHR and shorter combustion event. Some diffusion burn is seen with ULSD at 100% load, but the amount is significantly less than biodiesel.

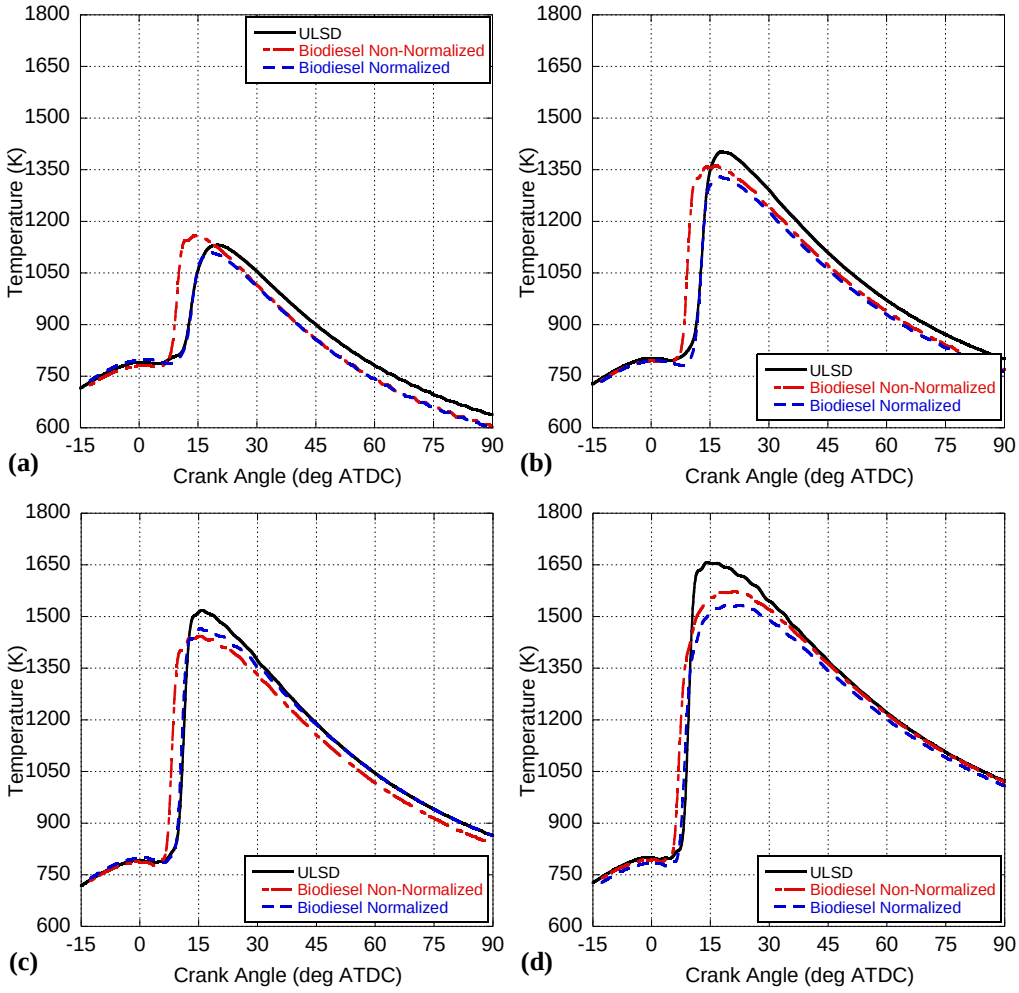

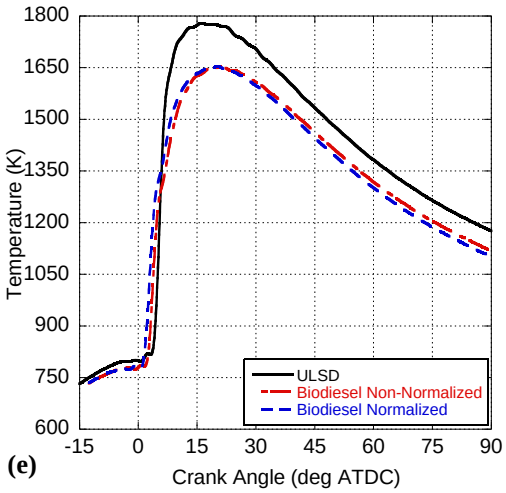

Figure 65: Calculated In-Cylinder Temperatures at (a) 0% Load, (b) 25% Load, (c) 50% Load, (d) 75% Load, and (e) 100% Load for AVL 5402 engine.

In Figure 65, the global in-cylinder temperatures highlight that WCO biodiesel burns at a lower temperature than ULSD after combustion normalization for this engine. This trend of temperature largely follows that of pressure and its associated discussion since they are related through the ideal gas law. Interestingly, at 50% load, the normalized pressure for the WCO biodiesel process is less than the non-normalized case; whereas, the temperature is slightly higher. In this case, it appears that the longer ignition delay (Figure 63) resulting from a later injection helps to prepare slightly more fuel for a premixed burn event that would have otherwise resulted in a diffusion burn. Hence, the peak RHR is similar along with the temperatures. This greater level of premixed burn from a longer ignition delay is also seen at 75% load when comparing the normalized and non-normalized cases. However, since the normalized case is burning later in the cycle with more diffusion burn required to hit the load condition, the global in-cylinder conditions are less a function of the more energetic premixed spike. Therefore, both the temperature and pressure of the normalized case fall below the non-normalized case. Finally, at 100% load, since the normalized case injects fuel before the non-normalized case, this ignition delay trend is reversed, and the peak normalized RHR is smaller. Overall, the significantly lengthened fuel injection process that adds the required amount of fuel at this load results in equivalent temperatures.

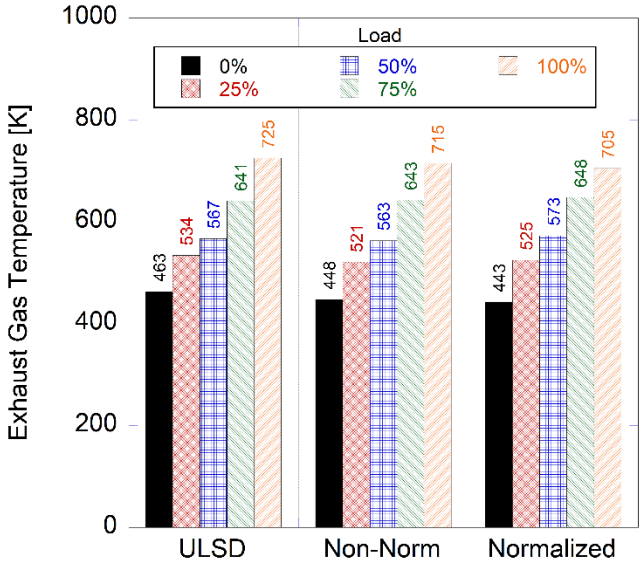

Figure 66: Measured Exhaust Gas Temperatures.

The analysis of the exhaust gas temperatures (Figure 66) showed a similar evolution to that of the in-cylinder temperature with respect to load. However, even though the normalized biodiesel results all maintained a lower in-cylinder temperature than ULSD, higher exhaust temperatures for this fuel were seen for the 50% and 75% load cases. This is due to the larger amount of fuel used and subsequent shift towards diffusion burn when moving to biodiesel, even though the 50% load case had a greater premixed spike. Hence, more fuel is burning closer to the exhaust valve opening (EVO). At 100% load, this trend reverses as the normalized biodiesel was injected before ULSD; therefore, combustion is now happening further away from the EVO event.

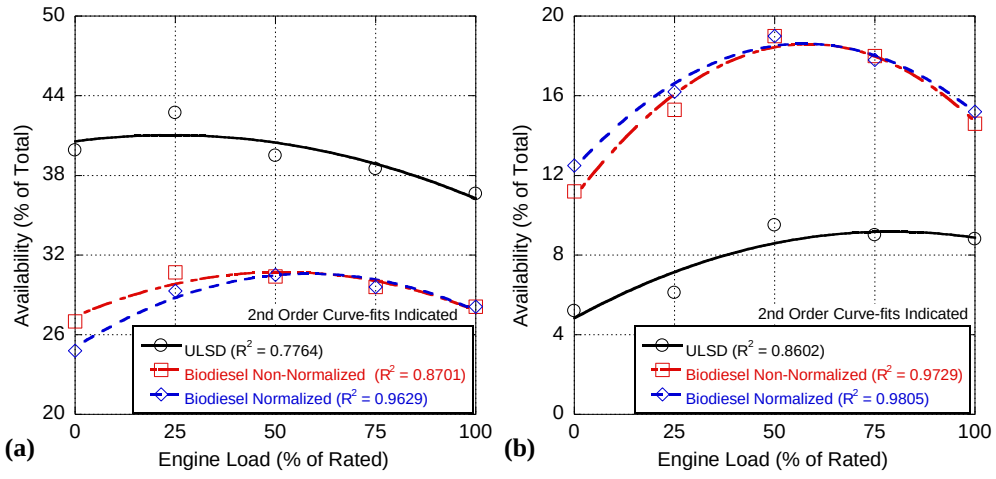

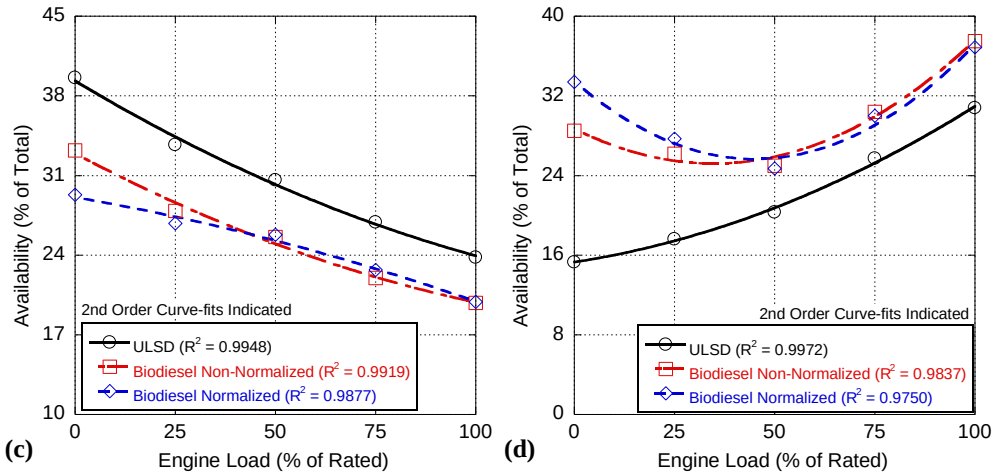

Figure 67: Percentage of Total Thermal Availability (a) extracted as Work, (b) lost through Heat Transfer, (c) destroyed by Entropy generation, or (d) retained by the Exhaust at EVO for AVL 5402 Engine.

This apparent contradiction between the higher biodiesel RHR and its lower in-cylinder pressures and temperatures in comparison to ULSD can be clarified further by investigating the second law of thermodynamics heat release analysis in Figure 67. While operation with biodiesel results in lower peak temperatures within the cylinder, it also causes a longer period of relatively higher temperatures. Generally, biodiesel undergoes a more complete combustion process; hence, the chemical potential availability of the fuel is successfully converted to thermal availability. However, as the load increases, this thermal availability is in the form of diffusion burn that happens later in the expansion stroke, where in-cylinder conditions are rapidly cooling and availability is more challenging to extract. Furthermore, the higher viscosity and lower volatility of biodiesel results in a worse mixing process, moving still more thermal availability production into the diffusion burn phase. Therefore, while fuel potential availability is more likely to be transformed via combustion, that availability is also less likely to be successfully extracted as work (Figure 67a). As a result, this increases the amount of fuel availability lost to heat transfer (Figure 67b) due to prolonged higher temperatures, but this simultaneously results in a decrease in internal entropy production (Figure 67c). Therefore, availability retention increases as a fraction of total availability (Figure 67d) that is exhausted to the atmosphere at the close of the cycle, which may find its way into a greater exhaust temperature (Figure 66). In addition, the energy content of biodiesel

influences the results; i.e., the engine requires more biodiesel fuel availability in order to meet the required load to make up for the fact that the availability is less optimally extracted as work.

Overall, biodiesel (mostly) demonstrates an earlier and greater level of premixed combustion; however, this occurs too early for the biodiesel fuel injected later that cannot prepare fast enough to join in on the premixed event. As a result, premixed combustion is limited in comparison to ULSD, and remaining fuel transitions from premixed (quasi-constant volume) combustion to diffusion (quasi-constant pressure) combustion; thus, peak pressures are limited. This inefficient combustion adds availability later in expansion, where it is less easily extracted, lowering exergetic efficiency (Figure 67a).

Unlike the prior efforts [12, 118], the respectively lower compression ratio of this engine is not quite powerful enough to overcome some of these differences. In addition, this is worsened by the fact that combustion happens later in this engine under a less ideal temperature scenario. Finally, while the performance deviations between biodiesel and ULSD are generally reduced for higher loads where both fuels begin to encounter a greater level of diffusion burn, this engine begins having trouble in mixing biodiesel significantly earlier than with ULSD. In specific, biodiesel diffusion combustion begins to set in just beyond 50% load, whereas ULSD diffusion burn is put off until after 75% load (Figure 64c, d, and e). This results in still worsened performance for the biodiesel fuel, due to the biodiesel entering the less exergetically efficient diffusion phase at lower engine loads.

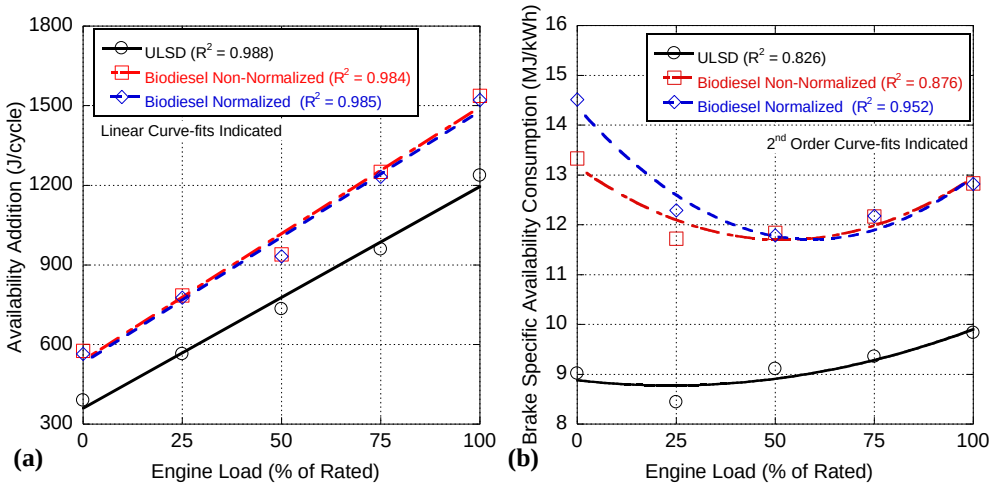

Figure 68: AVL 5402 (a) total thermal availability and (b) brake-specific availability consumption added to the engine cylinder.

As a result of this decreasing overall efficiency, Figure 68a shows the greater amount of availability that must be added when working with biodiesel, which in turn reflects the worsened fuel consumption. Generally, operation with biodiesel seems to require another 120-300 J of thermal availability present in the cylinder. In addition, the deviation in availability generally grows with engine load, highlighting the increasing gulf of performance between the two fueling strategies. In comparison to prior efforts, this is likely linked to the engine compression ratio. In specific, as the compression ratio increases, the importance of fuel viscosity on overall engine performance may decrease so long as the fuel is still able to adequately break up and vaporize. Hence, at higher compression ratios, the performance of an engine might become tied more to the quantity of fuel delivered and less on the quality of that fuel.

Of note, availability addition is related directly to the brake specific availability consumption (BSAC) in Figure 68b) that is the second law analog to brake specific energy consumption. Here, this highlights the amount of availability that is successfully converted to useful work for a given engine cycle. Thus, since the availability addition with biodiesel is higher than with ULSD, the BSAC is greater as well. Moreover, Figure 68b highlights a more dramatic trend with WCO biodiesel illustrating its optimum operational point at 50% load (stated before: highest pre-mixed burn without a significant diffusion burn phase). Hence, the engine appears to be more sensitive to changes in the fuel properties; again, reaffirming the prior statement that at respectively lower compression ratios, performance is tied more closely to fuel properties than fuel quantity.

In order to maintain engine performance when switching to WCO biodiesel operation, it is necessary to increase the injected fuel mass to compensate for its reduced volumetric energy content as compared to ULSD. Therefore, as more fuel is burnt at enhanced combustion efficiencies and because the H/C ratio of biodiesel is similar to that of ULSD, CO_2 emissions (a proxy for fuel consumption, and thus fuel availability addition) generally increase when using WCO biodiesel as presented in Figure 69. However, even if the CO_2 emissions are higher, its overall greenhouse gas footprint can be lower when considering the CO_2 consumption of the plants used as its feedstock [155]. As with all fuels, the potential

CO_2 advantages of WCO biodiesel could be enhanced further by properly matching the fuel injection parameters to the properties of this fuel.

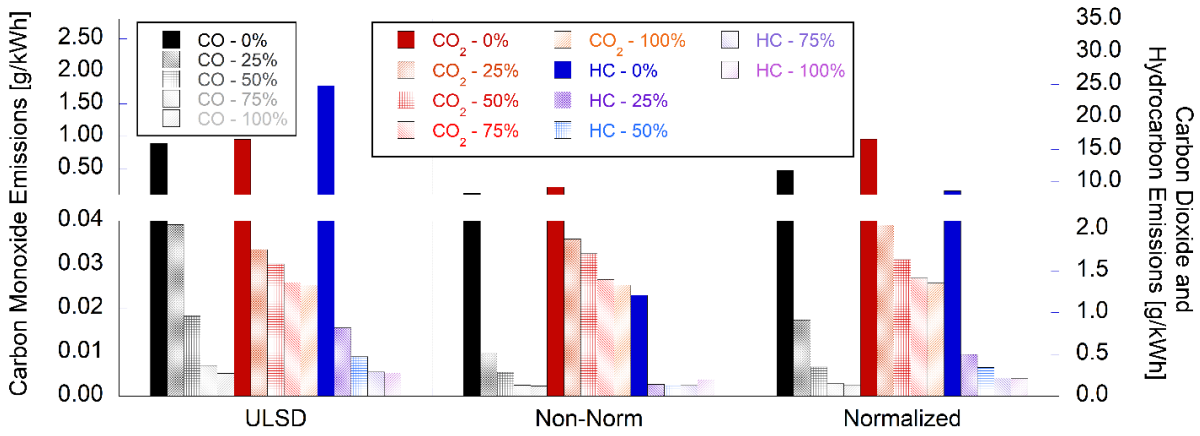

Figure 69: Brake specific CO, CO_2, and HC emissions.

Despite the mixture formation issues caused by a higher viscosity, the fuel bound oxygen content of WCO biodiesel has a beneficial effect on CO emissions in all cases as illustrated in Figure 69. However, this benefit decreases in both the non-normalized and the normalized cases with the growth in engine load as the level of diffusion burn increases at greater equivalence ratios. Moreover, when normalizing the combustion phasing, the combustion process is shifted later in the expansion phase and, as a result, CO emissions increase compared to the non-normalized case. This is due to the slightly less favorable combustion environment, since the combustion time is slightly reduced, and the fuel mass somewhat increases. Since HC emissions emanate primarily from the diffusion burn phase, the trend of HC emissions follows that of CO in Figure 69. Largely, HCs are formed due to a low oxidation rate at reduced temperatures or because of insufficient oxygen being available locally (poor mixing). As shown previously, in-cylinder temperatures are lower when using WCO biodiesel and its mixing process is respectively worse as compared to ULSD. However, its fuel bound oxygen provides some compensation along with locally higher adiabatic flame temperatures; thus, improving the engine out HC values. Again, analogous to CO, HC emissions are larger for the normalized case since combustion happens in a less advantageous situation. Furthermore, these greater CO and HC emissions are tied to the increased thermal availability present in the engine exhaust at EVO; i.e., any partial oxidation species present later in the

engine cycle are essentially unconsumed potential availability. Here, they cannot be effectively extracted as work and do not have the time to be lost via heat transfer; hence, they are retained in the exhaust gases and expelled at EVO.

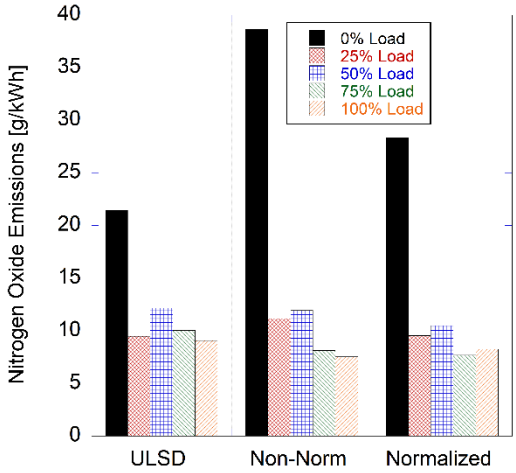

Figure 70: Brake specific NO emissions.

Figure 70 presents the NO emissions and, unfortunately, NO_2 emissions were not available at the time of study. However, since NO_2 emissions are generally a respectively small fraction of NO_x emissions for conventional engine combustion (e.g., 10-30% [1]), the trend of NO emissions will primarily represent that of NO_x. Here, to understand NO_x emissions trends, it is necessary to discuss engine load and calculated in-cylinder temperatures. At 0% and 25% load, there is an increase in NO emissions when using WCO biodiesel as shown in Figure 70. For these cases, even though global in-cylinder temperatures are slightly lower for WCO biodiesel (note: greater in 0% non-normalized), the local availability of oxygen, higher adiabatic flame temperatures, and the fact that combustion happens closer to TDC in a mostly pre-mixed phase all leads to more favorable NO_x formation conditions. However, beginning at 50% load, the NO_x emissions of WCO biodiesel are smaller than those of ULSD with the lowest values for the normalized case (except at 100% load when biodiesel injection timing was advanced). The main reason behind this decrease is its considerably lower in-cylinder temperature. Therefore, as stated prior, even though the early stages of WCO biodiesel combustion happens in a more opportune environment for NO_x emissions, the prolonged fuel injection event due its reduced volumetric energy content and

subsequent growth of diffusion burn combustion finds a less favorable situation. Hence, as more fuel burns later in the engine cycle, this reduces the temperature and time needed for thermal NO kinetics, albeit potentially at the expense of increased NO_2 emissions. Furthermore, WCO's respectively worse mixture formation required an increase in fuel availability; thus, combined with a later burning event (after in-cylinder temperatures have fallen below levels conducive to NO_x formation) results in more availability retained in the exhaust (Figure 66d) and not towards energy release and NO_x emissions. Overall, NO_x is shown to both increase and decrease here in comparison to ULSD, depending on the precise conditions present within the cylinder.

5.5 Conclusions

The model presented serves as an expansion of the more traditional 1st Law RHR model to include a 2nd Law efficiency analysis, presenting a breakdown of the transformation of chemical availability from the combustion of fuel into its components outputs of work, heat transfer, irreversibility, and exhaust gas losses. The model is also useful in identifying the variability of engine operation as a function of fuel characteristics, both as a standalone analysis and in tandem with the 1st Law analysis. These varying properties within the liquid fuels available for CI engine operation are of great importance to researchers. These fuel properties affect the efficacy and duration of combustion, and are instrumental in bringing about premixed- or diffusion-dominated combustion. In particular, fuel viscosity, density, energy content, and cetane number are particularly useful in determining combustion effectiveness. However, modeling of in-cylinder processes is required in order to disseminate and deconstruct the individual effects of these properties.

Using a zero-dimensional equilibrium model, previously collected data from engine operation with various fuels was analyzed, in order to identify the importance of the individual properties of each fuel on combustion. The amount of premixed combustion was largely decided by fuel viscosity that had a significant effect on fuel ignition, as well as the magnitude of premixed combustion, by delaying fuel breakup time. Increases in fuel energy content served to decrease fuel consumption, while increases in

viscosity raised the amount of fuel potential energy required by injection. Diffusion-dominated combustion was largely controlled by fuel viscosity, prolonging ignition delay for late-injected fuels. The effect of cetane number was largely removed, despite the lower ignition delays of the more volatile fuels, thanks to changes in fuel injection timing that prevented it from affecting the premixed spike, and higher temperatures largely overwhelmed chemical barriers to combustion during the diffusion burn period. In the case of both models, fuels with lower viscosity were favored, due to the relationship between high viscosity and increased diffusion burn.

With respect to more consistent changes in fuel properties (typically associated with fuel blending), the resulting changes in engine efficiency seem primarily centered on changes in fuel viscosity and combustion temperatures, and their mutual effects on engine performance. Seen here, biodiesel's higher combustion temperatures result in greater overall heat addition into the working fluid, raising the overall availability of the working fluid (and limiting internal irreversibility by keeping the difference in temperature between the thermal reservoirs high), while also increasing availability losses to the environment through increased heat transfer. However, the heightened viscosity that accompanies higher biodiesel content serves to broaden and lower the premixed combustion phase, while also lengthening and raising the diffusion-dominated combustion phase, particularly for high engine loads and/or high biodiesel content. This serves to move the period of fuel heat release later in the power stroke, limiting the ability of the engine to make use of the higher availability of the working fluid. As a result, increasing biodiesel composition (particularly for blends of 20% or greater biodiesel content) leads to an overall decrease in 2^{nd} Law Efficiency, due to increased heat transfer out of the cylinder, and higher losses of availability to the exhaust gas. More generally, the percentage of availability retained by the working fluid at the exhaust event offers an expression of the effect of fuel properties (most notably, viscosity) on combustion timing and in-cylinder temperatures. Specifically, in the case of biodiesels, fuels with higher viscosities exhibited combustion later into the exhaust stroke, raising the in-cylinder temperature above that of lower-viscosity fuels, but also limiting the ability of the engine to take advantage of those higher

temperatures, resulting in increases to the amount of unused availability present in the working fluid at the exhaust event.

With respect to compression ratio, it is seen that lowering the compression ratio results in not only worsened performance, but an increasing gulf in performance between various fuels, from both a 1st and 2nd Law perspective. In particular, higher viscosity fuels such as biodiesel undergo a less prompt and more difficult injection and ignition delay process, as both the lowered in-cylinder pressures and temperatures do not provide the same idealized environment for fuel breakup. In essence, higher compression ratios serve as an "equalizer" of fuels, overruling (or at least dramatically mitigating) the various negative effects of fuel properties that inhibit fuel preparation processes prior to combustion.

Overall, the 2nd Law model provides measures of engine efficiency beyond what is seen within the 1st Law analysis, providing a more detailed picture overall. While both models were able to identify increasing inefficiencies due to similar effects (usually related to viscosity), the 1st Law model could not identify these effects in biodiesel blend usage above 50%. This added specificity is directly related to the accounting of fuel availability as a function of total chemical potential, and serves to show the 2nd Law analysis to be a powerful tool for diagnostic engine analysis both alone or alongside the 1st Law analysis.

Chapter VI: Second Law Analysis of Dual-Fuel Combustion of ULSD and CNG

Some material published as "Exergy Analysis of Dual-Fuel Operation with Diesel and Moderate Amounts of Compressed Natural Gas in a Single-Cylinder Engine," Journal of Combustion Science and Technology, November 29, 2017

6.1 Abstract

The energy-exergy heat release model described previously is used to analyze dual-fuel combustion in a high compression ratio engine. CNG addition covers a wide range of energy substitution ratios, corresponding to three possible operational cases: 1) low-usage cases where combustion is nearly identical to conventional combustion, 2) medium-usage cases where combustion begins to deviate from conventional combustion but can be brought back under control through engine operational control strategies, and 3) high-usage cases where combustion behavior is significantly different from that of standard diesel combustion. Dual-fuel combustion is highlighted with overall increases in exergetic efficiency, slightly lowered losses to heat transfer and internal entropy generation, and greater exhaust availability. In addition, *ESR* usage is observed to have slightly decreased exergetic fuel conversion efficiencies (except at full load) and high amounts of unburned fuel availability in the exhaust gas, representative of the increasing difficulty of the engine to consume all of the methane-dominant gaseous fuel.

Finally, the 2nd Law Analysis points to the possibility of the engine achieving, or at least approaching, Low Temperature Combustion (LTC) for relatively high gaseous fuel usage rates, as evidenced by large decreases in irreversibility losses. In tandem with the previously observed decrease in NO_x emissions seen in the 1st Law analysis, it can be deduced that at high CNG usage rates the engine is on the periphery of LTC. Identifying and understanding this boundary regime (particularly if combined with other engine control techniques such as Exhaust Gas Recirculation) from the perspective of the 2nd Law analysis may form an extremely powerful tool for achieving control of LTC, particularly in high-compression ratio engines.

6.2 Introduction

Energy consumption remains a vital economic and security concern for the United States (US), particularly within the transportation sector. In specific, over-the-road transportation of heavy freight is a segment of the US automotive fleet that has fewer options for replacements that are less reliant on oil (e.g., full electrification) because automotive power plants require high energy density, significant power output, and long range. Hence, this industry is largely reliant on compression ignition (CI) engine technology [1, 6, 156]. Concurrently, with the recent boom in oil and natural gas extraction through hydraulic fracturing, compressed natural gas (CNG) has become a significantly more economical fuel source capable of generally meeting the demands of the heavy freight fleet. However, this same fleet is currently unable to take advantage of CNG fuels directly, as the high auto-ignition requirements of CNG (which requires heating of the engine intake), as well as its extremely rapid combustion behavior under such conditions, means that it cannot be used as the sole fuel within current CI engines [31, 41, 42]. Instead, CNG may be utilized within these engines via dual-fuel operation, whereby an ingested mixture of a flammable gas and air is ignited through the standard combustion of a liquid pilot fuel. This is typically accomplished with diesel and CNG, but can include other fuels, such as biodiesel or ammonia gas [31, 32, 41, 157]. Employing CNG in this manner may result in increased fuel consumption from unburned fuel, but may also reduce overall fueling expenditures due to the difference in cost between CNG and diesel [6, 9, 17, 32, 43]. Therefore, it is of interest to compare dual-fuel operation of varying CNG mixtures against standard operation with diesel fuel.

One common tool by which this comparison may be made is through the modeling of the engine's rate of heat release (RHR), which explicitly categorizes the rate at which energy is released from the utilized fuel(s) [1, 13]. The RHR itself is cataloged in terms of how it is either extracted as work, lost by heat transfer, or retained by the working fluid. In CI engines, the RHR is commonly subdivided into two primary phases. First is the premixed combustion phase, wherein fuel that has successfully mixed prior to combustion starting is consumed quickly (and typically in an efficient manner). The second is the diffusion-dominated combustion phase, where fuel that was not prepared early enough to combust in the

premixed spike burns as soon as it is able [1]. This is of particular importance to dual-fuel operation, as increasing the fraction of CNG to moderate levels typically results in an increasingly well-mixed fuel-air charge, resulting in an expected growth in the amount of premixed combustion for any given engine load [6, 9, 49, 50, 158, 159].

A useful extension of this analysis is through the calculation of the rate of change of exergy within the cylinder through the 2nd Law of Thermodynamics [12, 118, 133]. Much like the RHR model that is built around the 1st Law of Thermodynamics, the exergy analysis (also commonly known as a 2nd Law or availability analysis) is utilized to ascertain the precise means by which exergy is both added to the engine cylinder and either extracted through work, lost due to heat transfer, or retained by the working fluid and expelled in the exhaust event [12, 14, 15]. However, the 2nd Law analysis is also concerned with the exergy destruction through entropy generation internal to the cylinder, which represents the portion of in-cylinder energy that can no longer be extracted as useful work, and which builds up over the engine cycle as a form of thermodynamic uselessness [14, 15]. This aids in identifying the peak periods of exergy addition and when exergy may be extracted from the engine, while also allowing engine operators to note the conditions under which entropy-related losses are minimized. This latter understanding is a critical quality to ascertain for thermodynamic "bottoming" of the engine cycle, utilizing an organic Rankine cycle (ORC) to recover waste engine heat [12, 160-162]. Despite these benefits, an exergy analysis is significantly less common, and as a result exergetic analyses of dual-fuel combustion are rare [17, 127]. Furthermore, these dual-fuel analyses are somewhat inconclusive, and may be linked closely to the degree of CNG substitution utilized, as well as engine parameters (e.g., compression ratio) that are inherently tied to the degree of thermodynamic advantage enjoyed by the engine [17, 134, 163].

To that end, this effort represents the evaluation of dual-fuel operation of a high compression ratio CI engine with respect to various mixtures and CNG through a heat release model utilizing an analysis built upon both the 1st and 2nd Laws of Thermodynamics [118]. Here, CNG usage with Ultra Low Sulfur Diesel (ULSD) runs the full range of dual-fuel regimes, extending from low usage where operation is not dissimilar from conventional combustion, moderate usage where combustion changes but is

controllable with minor operational modifications, and heavy usage where significant changes in operation are required in order to re-optimize combustion [6, 9, 164]. The four mixtures of CNG utilized herein share an identical volumetric energy content, but differ in terms of actual composition [6]. The four mixtures are all largely dominated by methane, ranging from 87-96% by volume. Overall, operation with CNG is connected with increasing exergetic efficiency, due to the added CNG promoting the more efficient premixed combustion phase over the less desirable diffusion-dominated phase. At the same time, CNG operation leads to an absolute decrease in the cyclic combustion efficiency, due particularly to large amounts of methane surviving the combustion process and being exhausted to the atmosphere. While the 1st Law analysis indicates that operation with CNG leads to an lowered energy efficiency, entirely related to the high fraction of unburned fuel that is lost during the exhaust blowdown event, the 2nd Law analysis indicates that at high loads this loss is more acceptable, due entirely to the combination of the decreased thermodynamic usefulness of the exhausted fuel species with added CNG usage, and the tendency for CNG usage to promote the more efficient premixed combustion phase, albeit with heightened hydrocarbon emissions.

6.3 Experimental Setup

Dual-fuel testing was performed with a Yanmar L100v single-cylinder CI engine, connected to a Dyne Systems Dymond Series 12 hp dynamometer to provide speed and load control (see Table 30) [6, 73]. The single-cylinder engine has undergone some modifications, including blocking the manufacturer's exhaust gas recirculation port in favor of an external system, and replacing the original mechanical fuel system with a modern high-pressure system, with electronic control through a Bosch MS15.1 engine control unit accessed through Bosch ModasSport [73]. The fuel pump for this high-pressure system has been decoupled from the engine, and is powered separately, in order to minimize the effect of the pump on the power output of the engine [73].

Table 30. Engine and Dynamometer Specifications [73].

Engine Manufacturer/Model	Yanmar L100V
Type	Vertical Direct-Injected
Intake	Naturally Aspirated
Cooling	Air-Cooled
Cycle	4-Stroke
Displacement [cc]	435
Number of Cylinders	1
Number of Valves	2 (1 intake, 1 exhaust)
Bore [mm]	86
Stroke [mm]	75
Connecting Rod Length [mm]	118
Crank Radius [mm]	38
Clearance Volume [cm^3]	21.611
Piston Area [cm^2]	58.088
Compression Ratio	21.2
Continuous Rated Output [hp]	8.3
Rated Speed [RPM]	3600
Engine Oil Used	Shell 15W-40
Dynamometer Manufacturer/Model	DyneSystems, Inc. Dymond Series 12
Continuous Rated Torque [N-m]	28.61
Continuous Power [hp]	12
Maximum Speed [RPM]	7500
Voltage [VAC]	480
Phase	Three Phase
Frequency [Hz]	60
Controller	DyneSystems, In. Linter-Loc V OCS

Engine operation was monitored and controlled using a National Instruments LabVIEW system, collecting operating data at a rate of 10 Hz over two minutes of steady state operation, defined as being operation with engine exhaust and oil temperature changes of less than 1% over the course of 60 seconds [6]. In tandem with this system, a second LabVIEW system was utilized to capture the in-cylinder pressure trace from 60 consecutive thermodynamic cycles (120 engine revolutions) to offset engine cyclic variation, recording at a resolution of 0.2˚ of crank angle [6, 73]. Finally, engine-out emissions were recorded using an AVL SESAM-FTIR emissions analyzer recording at a rate of 1 Hz over five minutes. While not presented here, this emissions data was used to ascertain the engine operational combustion efficiency, and was used to calibrate the heat release model [6, 12, 13].

Testing of CNG was performed at 1800 RPM, using engine operational targets ascertained from previous research [16, 73]. For each CNG mixture, the engine was operated using standard ultra low-sulfur diesel (ULSD) fuel in order to establish a control across the four separate mixtures [6, 9]. After each diesel fuel control was established, the amount of diesel was lowered and the CNG increased in order to hit a number of targeted Energy Substitution Ratios, or *ESR*s:

Energy Substitution Ratio	$ESR = \frac{\dot{m}_{CNG} Q_{LHV_{CNG}}}{\dot{m}_{CNG} Q_{LHV_{CNG}} + \dot{m}_{diesel} Q_{LHV_{diesel}}} \times 100\%$	(44)

where $\dot{m}$ is the mass flow rate of either the CNG or diesel fuels, and Q_{LHV} is the lower heating value of the CNG or diesel fuels [6]. Overall, seven separate *ESR*s were utilized, corresponding to approximately 7%, 18%, 40%, 50%, 60%, 75%, and 85% CNG usage. For each test, the timing of injection was adjusted so as to achieve optimum engine efficiency, calculated previously [6, 16]. For higher *ESR*s, typically those at or beyond 40%, injection timings were adjusted in order to maintain optimized combustion behavior [6]. Finally, testing was achieved at five separate engine loads, representing varying percentages of the engine's rated load (18.0 N-m) at 1800 RPM [73].

Table 31. Chemical Composition and Properties of CNG Mixtures and ULSD.

Gas/Mix Title	ULSD	M87	M91	M92	M96
Methane (CH_4)	-	87.00%	91.67%	92.00%	96.00%
Ethane (C_2H_6)	-	5.10%	4.08%	3.50%	1.80%
Propane (C_3H_8)	-	1.50%	0.71%	0.80%	0.20%
Isobutane (C_4H_{10})	-	0.29%	0.01%	0.15%	0.30%
Nitrogen (N_2)	-	5.60%	1.00%	2.85%	1.30%
Carbon Dioxide (CO_2)	-	0.51%	2.53%	0.70%	0.40%
Density @ 20°C (kg/m^3)	837.58	0.755	0.725	0.723	0.698
Heating Value (kJ/kg)	45600	49500	51480	51620	53500
Exergy Content (kJ/kg)	48564	51510	53529	53700	55597
Ratio of Exergy to Energy (kJ/kJ)	1.0650	1.0406	1.0398	1.0403	1.0392
Volumetric Energy Density (kJ/m^3)	-	37300	37300	37300	37300
Constant Pressure Specific Heat (kJ/kg·K)	-	37.07	36.75	36.62	36.29
Ratio of Specific Heats	-	1.297	1.295	1.297	1.298
Cetane Number	40	-	-	-	-
Octane Number	-	118	127	126	133

Injection of gaseous fuel was achieved through a mixing box in the intake of the engine, with CNG released at 50 psi through a Brooks flow controller (model #SLA5850) [6]. Of importance, modeling of the mixing box has shown that the gaseous injection system allows for sufficient time for the fuel-air mixture to become relatively homogeneous prior to entering the engine [74]. The constituencies of the four CNG mixtures are also shown in Table 31. All four mixtures were chosen to have identical volumetric energy content, but with varying constituencies and properties [6]. The variation in combustion behavior between the mixtures was assessed in a separate analysis, and while no significant change in engine behavior was expected between the various mixtures from the perspective of the exergy analysis, their behavior was still measured and modeled for this work [6, 43]. Methane formed the clear majority of the gases, comprising 87% (M87), 91.67% (M91), 92% (M92), and 96% (M96) of each mixture.

6.4 Results and Discussion

For brevity, only the pressure traces, RHR figures, and temperature plots for the M92 CNG mixture are presented with respect to the 1st Law analysis, and only at 50% and 100% of rated engine load. The M92 mixture was chosen for its relatively average characteristics and straightforward behavior. Here, the 1st Law results will be quickly summarized, with thorough findings from these same tests located in prior work [6]. Furthermore, the 1st Law Results for the remaining CNG mixtures can be seen in Appendix A, and a more comprehensive description of the 1st Law Results are given in Chapter II of this document.

The pressure traces for the various dual-fuel tests can be found in Figure 71 for all *ESR*s at 50% (a) and 100% (b) of rated load. Overall, dual-fuel operation at lower *ESR*s is superficially similar to operation with standard ULSD [9]. In general, the in-cylinder pressure traces feature a lowered pressure around Top Dead Center (TDC), the magnitude of which is directly tied to the fraction of methane present in the cylinder. This is related precisely to the ratio of specific heats of the bulk gas, which is lowered significantly with the addition of CNG, resulting in a decrease in the rise in pressure from compressing

the bulk gas. As a result, this also reduces the peak pressure related to combustion, particularly for operation below 9.0 N-m. At 50% engine load, this lowering in peak cylinder pressure is largely mitigated except at high *ESR*s. This reflects the increasing homogeneity of the fuel-air mixture, in turn raising the amount of premixed (aka early) combustion and reducing the total degree of diffusion burn. However, at high *ESR*s the inability to match standard operational pressures of ULSD combustion indicate an increasing struggle to achieve and maintain combustion in the methane-rich environment. Above 9.0 N-m, adding CNG now results in a peak pressure higher than that of operation with ULSD only, again due to the increasing fraction of fuel that is consumed within the premixed combustion phase. This is most extreme at 18.0 N-m, where all CNG mixtures achieve greater peak pressures than in operation with ULSD alone.

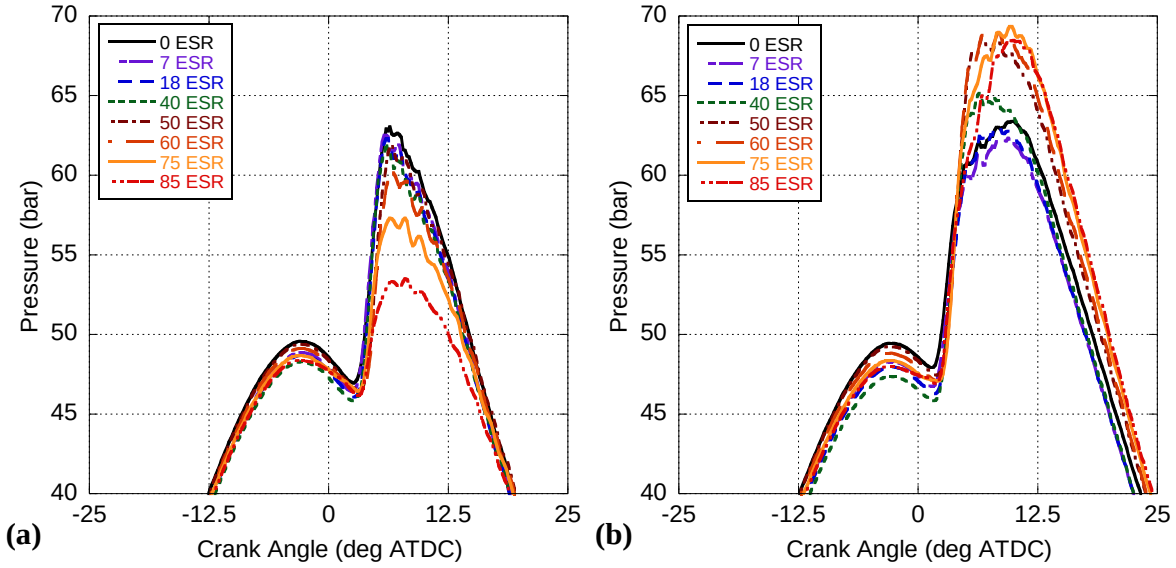

Figure 71. Average of measured in-cylinder pressure traces for M92 gas mixture at varying *ESR*s at 50% (a) and 100% (b) of rated engine load.

The 1st Law RHR results are given in Figure 72, again at 50% (a) and 100% (b) of rated load for the M92 mixture. In general, increasing the *ESR* resulted in a greater magnitude of the premixed spike and a lowering of the extent of diffusion burn. This was particularly noticeable under higher loads where the diffusion burn phase of ULSD is generally quite pronounced. In each case, the addition of gaseous fuel results in a more homogeneous fuel-air mixture because it is able to mix with the air effectively prior

to entering the engine cylinder. In addition, as more CNG is added, the amount of fuel energy (and therefore the amount of fuel mass) that must be delivered by the liquid fuel pilot decreases. This diminished amount of liquid fuel mass is then more easily atomized, vaporized, and mixed into the greater ULSD-air-CNG working fluid within the cylinder. As a result of this augmented mixing process, a flame-propagation-style combustion event becomes more likely as the *ESR* grows [6]. However, at higher loads and very high *ESR*s, the RHR begins to experience more post-premixed combustion beyond what occurs in ULSD-only tests. Peak RHR also recedes for very high *ESR*s, although it is still above what is observed with ULSD.

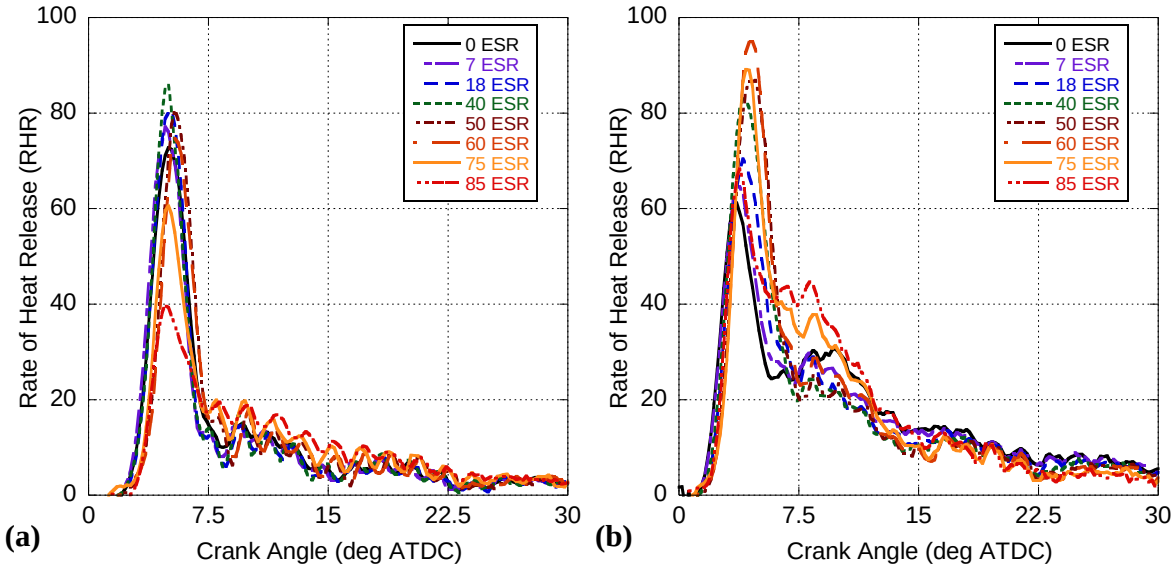

Figure 72. Calculated RHR for M92 gas mixture at varying *ESR*s at 50% (a) and 100% (b) of rated engine load.

With respect to in-cylinder temperatures, dual-fuel combustion is characterized by two primary phenomena; a propensity to increase premixed combustion (raising peak cylinder temperatures), and a tendency to decrease in-cylinder temperatures immediately prior to combustion (i.e., compression temperatures) due to the lower ratio of specific heats of the bulk gas as more CNG is utilized (see Figure 73). As a result, below 9.0 N-m, in-cylinder temperatures are lower with additional CNG usage (as there is not enough heat addition to counter the lessened initial temperature). However, above 9.0 N-m the shift towards premixed combustion with higher *ESR* is most significant, such that the in-cylinder temperature

is generally higher (particularly, the peak temperature). The turning point in this relationship appears to be at or around 9.0 N-m, where the temperature profiles between all of the various *ESR*s are generally uniform except at the greatest ESR rates.

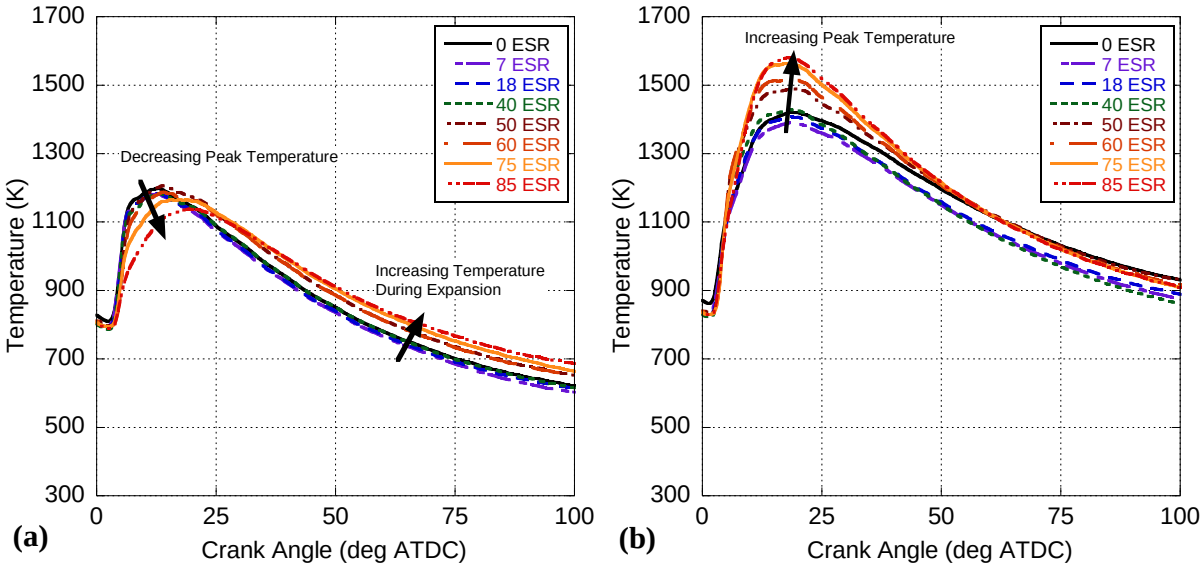

Figure 73. Calculated temperature profile for M92 gas mixture at varying *ESR* at 50% (a) and 100% (b) of rated engine load.

In addition, the temperature profiles indicate a secondary set of phenomena relating to heat addition from diffusion-(and/or flame-) dominated combustion. At low loads, a significant amount of methane survives the premixed combustion phase. While the majority of this methane endures the high temperature environment, some of it will inevitably react, leading to more energy addition (and thus greater temperatures) later on in the expansion phase. However, as engine load increases, more methane is consumed in the premixed phase, leaving less CNG left over to incidentally combust later on. Moreover, combustion temperatures are enhanced promoting more oxidation of CNG (still an overall lean combustion environment). Hence, past 9.0 N-m expansion temperatures are essentially uniform and relatively free of changes to *ESR*.

To characterize the impact of CNG assisted ULSD combustion, operational efficiencies are shown in Figure 74. In general, thermal efficiency grew with engine load, although this rise in efficiency becomes less significant for higher loads as the amount of diffusion burn grows. Thermal efficiency also

climbs when raising the *ESR*. In specific, escalating CNG usage results in a more homogeneous mixture, growing the fraction of combustion that comes during the premixed phase, subsequently enhancing thermal efficiency. Combustion efficiency also grows significantly with engine load, primarily due to intensifying temperatures at higher loads promoting a more thorough consumption of fuel molecules. However, CNG usage at all loads is associated with decreasing combustion efficiency, and is linearly correlated with *ESR*. As stated in a prior effort, this loss is presumed to be tied to the relatively high amount of methane available that may burn more like a spark ignition engine with a flame front [6]. Potential quenching of this flame front prior to consuming all of the CNG may occur on the periphery of the cylinder. Any resulting unburned methane may then encounter some difficulty in reigniting because of its relatively high activation energy and the somewhat lower amount of oxygen present within the cylinder as the added CNG effectively displaces intake air (e.g., higher equivalence ratios are seen [6]). Furthermore, as *ESR* grows, there is a rising potential for CNG to enter the crevices that can also play a role in decreasing combustion efficiency. Together, the thermal and combustion efficiencies then explain the trends in fuel conversion efficiency. Raising engine load results in improved fuel conversion efficiency, but the total fraction of fuel consumed falls with *ESR*, leading to a universal loss in fuel conversion efficiency with greater CNG usage. This is true except for the highest *ESR*s at 100% load where the significantly enhanced premixed burn promotes a growth of in-cylinder temperatures; hence, both thermal and combustion efficiencies tick upwards, and fuel conversion efficiency is also raised.

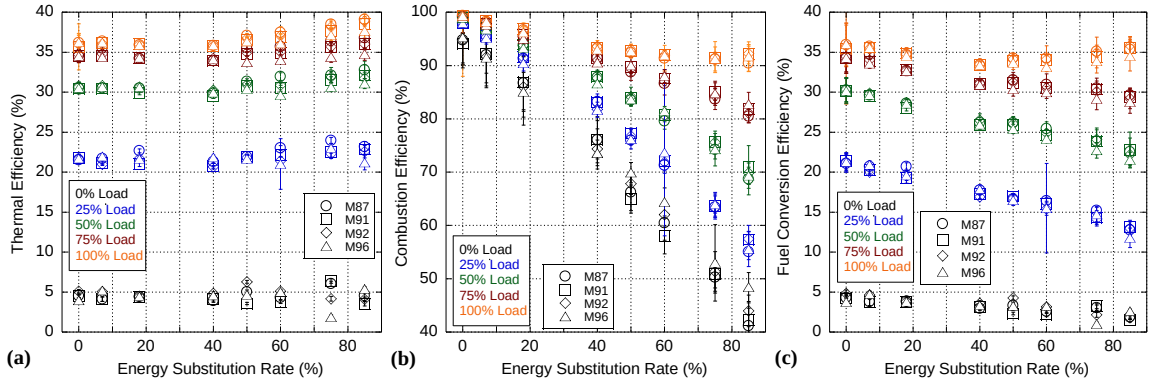

Figure 74. Calculated thermal (a), measured combustion (b), and calculated fuel conversion (c) efficiencies for all *ESR*s, mixtures, and engine loads.

As a final consideration before the exergy analysis can begin, engine brake specific fuel and energy consumption (BSFC and BSEC, respectively) must be examined in Figure 75. Gross BSFC is inversely correlated with fuel conversion efficiency, decreasing with engine load as engine efficiency rises. Furthermore, with variation in *ESR*, BSFC worsens at lower loads. However, at higher *ESR*s this deteriorating behavior becomes less significant, such that BSFC is essentially uniform across all *ESR*s at 75% and 100% of rated load, and begins to resemble more closely the thermal efficiency than the fuel conversion efficiency. The is likely because the engine relies less on the liquid fuel pilot and more on the gaseous fuels, which are more energy-dense (see Table 31); thus, the total amount of fuel mass added to the cylinder falls as *ESR* rises. Furthermore, the usage of CNG promotes the more efficient premixed combustion phase. In essence, while the engine is burning less of the available fuel with higher *ESR*, the fuel that is burning is more useful in producing work, and as a result the less effective operation seen in the fuel conversion efficiency does not manifest itself within the BSFC results at high *ESR*s and high loads. Of note, similar to the various 1st Law Efficiencies, the BSFC sees a slight but consistent shift downwards beyond 75% *ESR* at full load, again due to more enhanced premixed behavior.

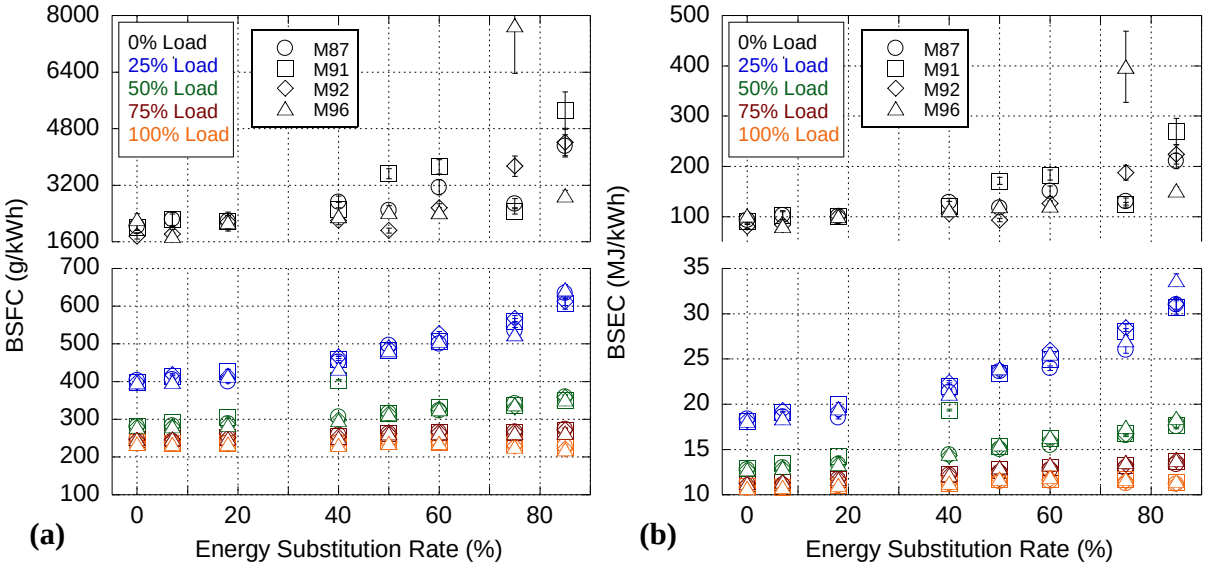

Figure 75. Brake-specific fuel (a) and energy (b) consumption rates for all *ESR*s, mixtures, and engine loads.

BSEC is the rate of fuel energy consumption of the engine, rather than fuel mass. As a result, BSEC ignores the reduction in fuel mass with added CNG usage seen in the BSFC, without affecting the reduction in diffusion combustion in favor of premixed operation. In general, BSEC follows similar overall trends to BSFC with one key exception: BSEC at high loads increases with *ESR*, instead of holding relatively steady like BSFC. This reflects the falling combustion and fuel conversion efficiencies of the engine, and shows that with added CNG usage comes an increased amount of fuel energy that must be made available to the engine. Again, like the other efficiencies and the BSFC, the BSEC is raised for high-*ESR*s and high loads, thanks to more efficient combustion. However, the BSEC does not quite make it back to the same level as with ULSD combustion.

Thus, from the perspective of the 1st Law of Thermodynamics, with added CNG the engine is operating more thermodynamically efficient in converting combusted fuel to work as evidenced through a greater premixed burn, subsequently reflected in a higher thermal efficiency. However, with added *ESR* the process of converting chemical potential into available energy is inhibited as shown through the lessened combustion efficiency. Overall, in a dual-fuel scenario, the engine is leaving a greater portion of energy unutilized with growing *ESR* as seen through the reduced fuel conversion efficiency and increasing BSEC, but the rise in thermal efficiency suggests that this wasted energy content is primarily in the form of chemical potential energy, rather than from thermal energy. At the highest *ESR* levels and 100% load, in-cylinder temperatures rise enough to consume some of this energy and slightly reverse the worsening trend of fuel conversion efficiency with *ESR*.

To begin the exergy analysis, the eight 0% *ESR* (i.e., ULSD only) tests are considered (two sets of ULSD data per gas mixture), in order to establish a control that the dual-fuel results can be assessed against. The distribution of exergy across the tests at the exhaust-valve opening (EVO) event is given in Figure 76, broken down into exergy transfer due to work (a), heat transfer (b, external irreversibilities), entropy generation (c, internal irreversibilities), or lost to the exhaust gas at EVO (d). Overall, the 2nd Law efficiency (work exergy) increased with engine load. As the Yanmar L100v was originally packaged with an electrical generator and meant to be operated near its peak power, this behavior is as anticipated. As

load rises, the change in growth of efficiency is more modest as the fraction of heat released through the diffusion-dominated (and less efficient) combustion phase rises. In synchronicity with the work exergy results, the percentage of thermal exergy lost to heat transfer is (generally) greater at lower loads where the engine is operating more inefficiently. As engine efficiency climbs past 4.5 N-m, heat transfer losses decrease relative to the total thermal exergy, while the absolute amount of heat transfer grows with the rising temperatures of the engine.

The percentage of exergy lost to internal irreversibilities (i.e. entropy generation) within the engine cylinder also falls with engine load, due entirely to the greater operational temperatures of the engine in keeping with Carnot's Theorem [14]. Similar to heat transfer, entropy generation grows in an absolute sense within the cylinder with added load and higher temperatures. However, the greater the temperature difference between the ambient and in-cylinder environments (i.e., Carnot's "cold" and "hot" reservoirs, respectively), then the less the fraction of total exergy lost to entropy generation. Exergy destruction is more prevalent with higher engine loads, but it does not grow at the same rate as exergy addition, and thus the fraction of exergy that is destroyed will fall [14]. The remaining exergy added by combustion is retained, and the warmer the exhaust is relative to the ambient, the more thermodynamic usefulness it possesses. To this end, the percentage of thermal exergy retained by exhaust is reduced as engine load is increased to 9.0 N-m as the engine becomes more effective at extracting thermal exergy. However, beyond this load, the thermal exergy retained by the exhaust grows with greater operational temperatures, and because the engine is adding fuel later in the expansion stroke (i.e., diffusion burn) where it is less likely to be extracted as work. Of note, this exergy is not inherently destroyed and is still potentially useful for work extraction through waste heat recovery systems [162].

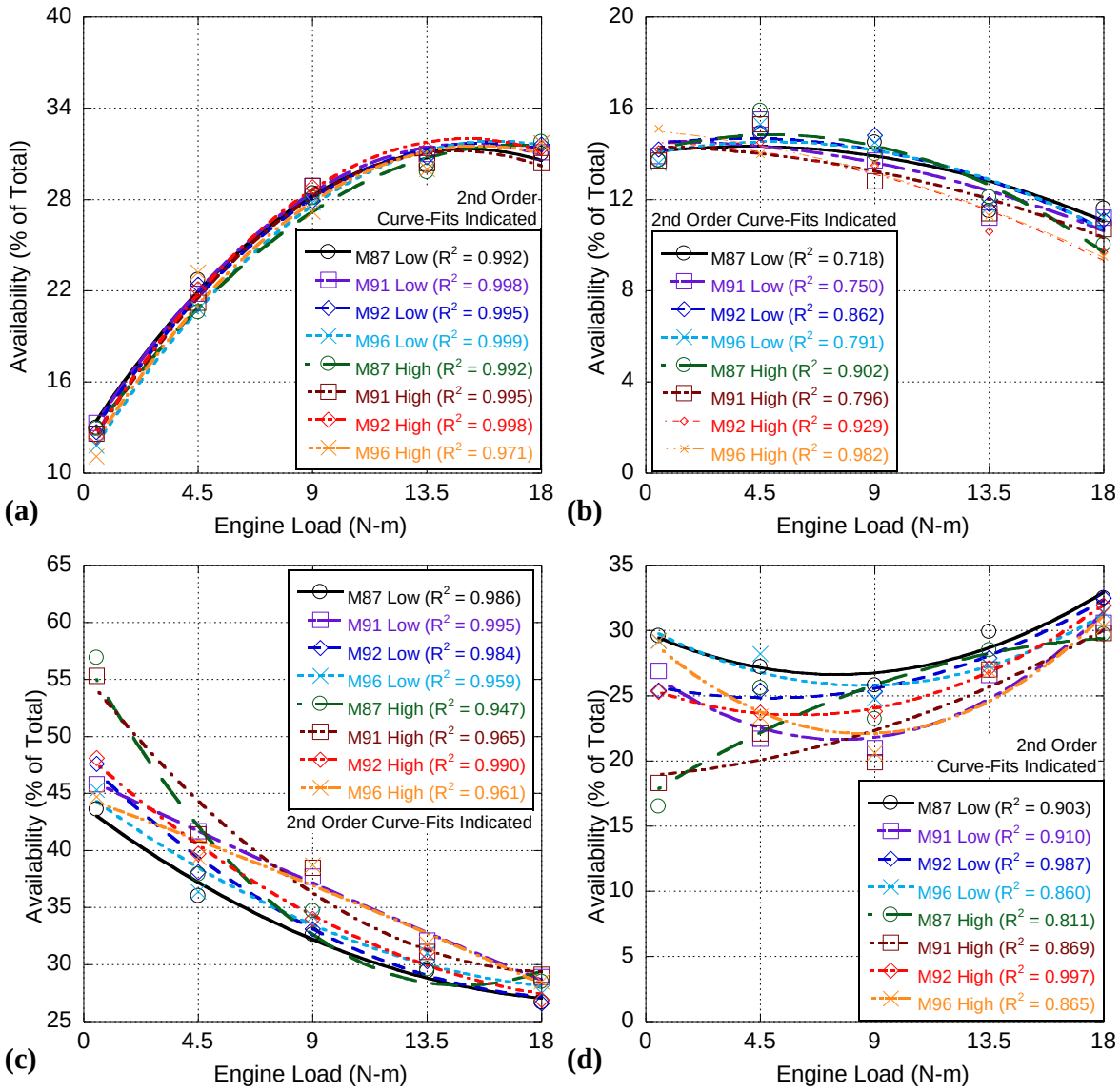

Figure 76. Percentage of Thermal Availability Transferred as Work (a), lost to Heat Transfer (b), lost to Entropy Generation (c), or retained by the Working Fluid at EVO (d) for all 0% *ESR* tests.

With a baseline understanding, it is now possible to compare the various CNG tests more effectively. Overall, the 2nd Law efficiency of each of the CNG mixtures displayed the same overall trend as testing with ULSD only (see Figure 77). In particular, the extracted work exergy grew with *ESR* as the level of the premixed burn phase increased. However, beyond 13.5 N-m the efficiency gains were more modest across all *ESR*s. While diffusion burn becomes a more significant aspect of engine-out RHR past 9.0 N-m, and additional CNG usage serves to counter this by shifting more combustion into the premixed phase, the engine appears to approach a plateau of performance. This may indicate a maximum degree of

premixed combustion possible in the engine given set fuel injection parameters (particularly, injection pressure) that CNG usage does not significantly influence.

Exergy losses due to heat transfer followed a similar trend to those in the ULSD control tests, but diverge more with respect to *ESR* (see Figure 78). Adding *ESR* at low engine loads (all pre-mixed combustion) results in a cooler combustion process and a reduced exergy loss due to heat transfer through a smaller temperature gradient with the atmosphere. This is offset slightly by the higher cylinder temperatures later in the expansion stroke, but these same high temperatures only occur for a portion of the engine cycle; hence, the time for later heat transfer is limited. As engine load increases to 13.5 and 18.0 N-m, the expansion temperatures begin to fall more in line with ULSD, but at the same time the peak cylinder temperatures rise above those of ULSD, all due to the shift from diffusion burn to premixed combustion with higher *ESR*. These raised temperatures exist for a relatively short period (around 20° crank angle, or about 1.9 milliseconds), and so the engine does not experience significant additions to the total amount of heat transfer from these higher temperatures.

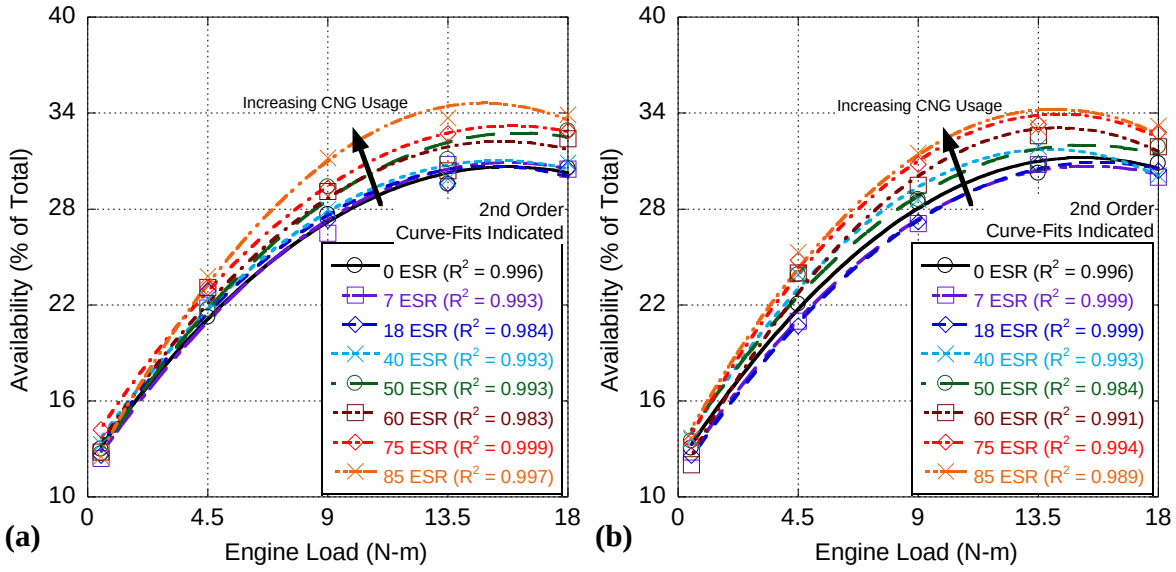

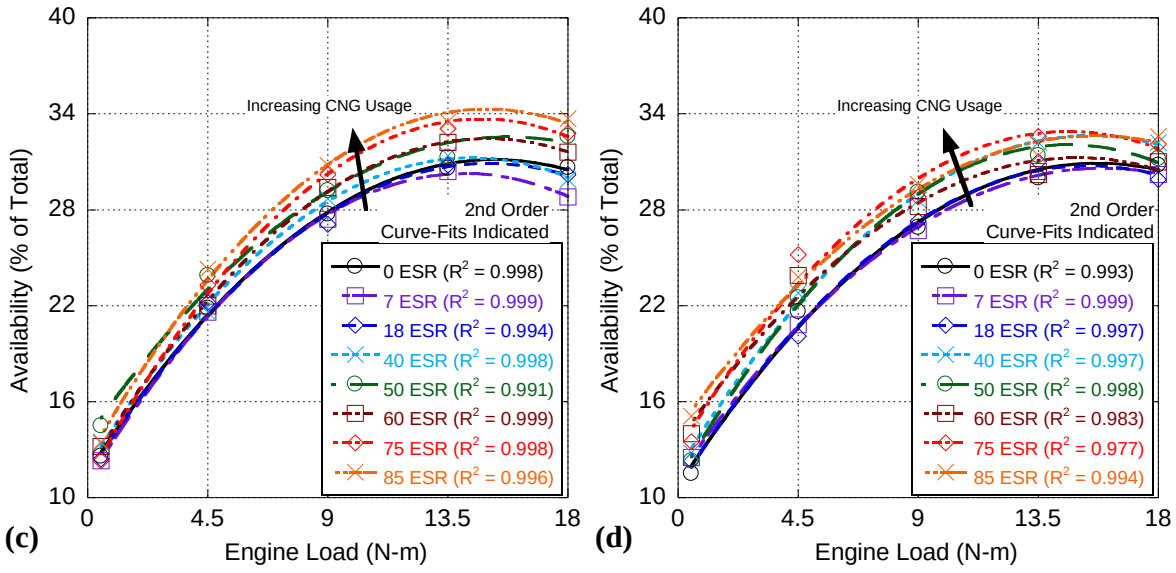

Figure 77. Percentage of Thermal Availability Transferred as Work for the M87 (a), M91 (b), M92 (c), and M96 (d) gas mixtures at all engine loads and *ESR*s.

Furthermore, the engine is operating more efficiently at these higher loads with increasing *ESR*, and so increasing CNG usage will lead to lower heat transfer losses. For the highest *ESR*s, however, heat transfer losses fall significantly, for loads below 18.0 N-m, implying a significant change in combustion behavior. As seen in the 1st Law RHR data, extremely high *ESR* usage is punctuated by a rise in post-premixed combustion, likely due to increasing difficulties in fully combusting the CNG fuel in the premixed combustion event. This is possibly evidence of the engine transitioning from a more typical premixed-diffusion combustion event characteristic of compression ignition engine cycles and more towards a flame propagation event seen in HCCI and RCCI combustion [165-167]. Finally, the total percentage of exergy lost to heat transfer at 18.0 N-m is somewhat consistent across all *ESR*s in comparison to the lower loads as a more efficient combustion process balances the higher temperatures encountered, although the engine still slightly favors higher *ESR*s.

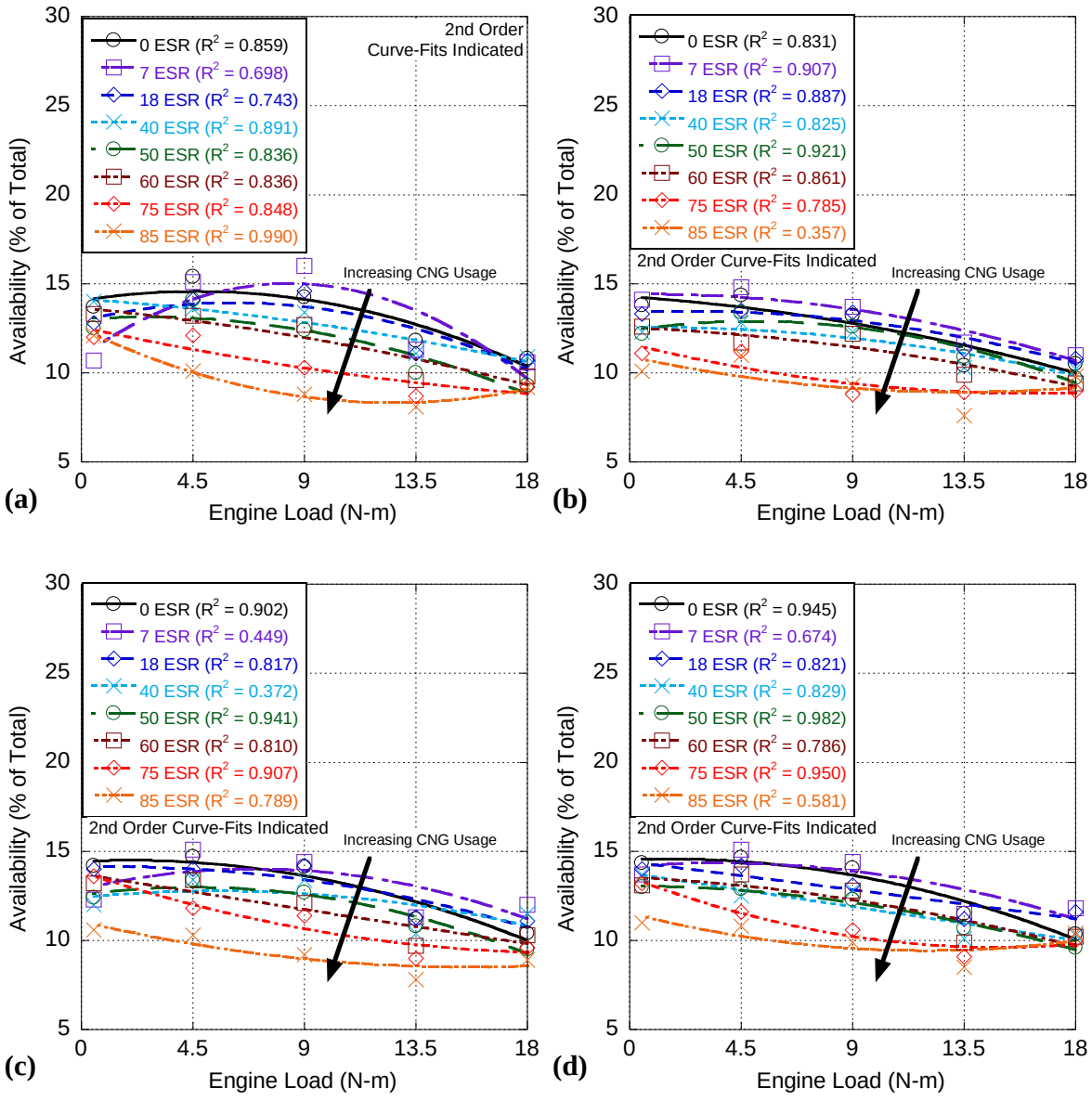

Figure 78. Percentage of Thermal Availability Lost to Heat Transfer for the M87 (a), M91 (b), M92 (c), and M96 (d) gas mixtures at all engine loads and *ESR*s.

Exergy losses from internal entropy generation show a marked decrease as a function of *ESR* across all engine loads, although these losses became more modest for higher *ESR*s (see Figure 79). This is likely linked to more effective mixing as liquid fuel usage is reduced with added CNG. Liquid fuel injection is associated with an unavoidable increase in entropy generation, through a combination of atomization, vaporization, and mixing of fuel and air [168-170]. This may also carry over into the entropy generation due to combustion, as the presence of pockets of poorly-mixed fuel then result in large

contributions to entropy generation [171, 172]. The fuel preparation process within these pockets, after combustion begins, is hurried and incomplete, resulting in further entropy generation. With gaseous fuels, atomization and vaporization are avoided entirely, and mixing of fuel occurs upstream of the engine; thus, more CNG usage results in reduced entropy generation due to a decrease in mixing-related phenomena. Furthermore, utilization of CNG leads to a reduction in both the number and size of the poorly-mixed fuel pockets, as evidenced by the reduction in Particulate Matter emissions that comes alongside CNG usage [6]. Moreover, higher *ESR*s are linked to more premixed combustion, which is already noted for increased efficiency. Altogether, this shows that CNG usage discourages entropy production, entirely because higher *ESR*s do not require as much in-cylinder mixing, generating less entropy before and during the ignition and premixed combustion event, as well as making the premixed event more substantial.

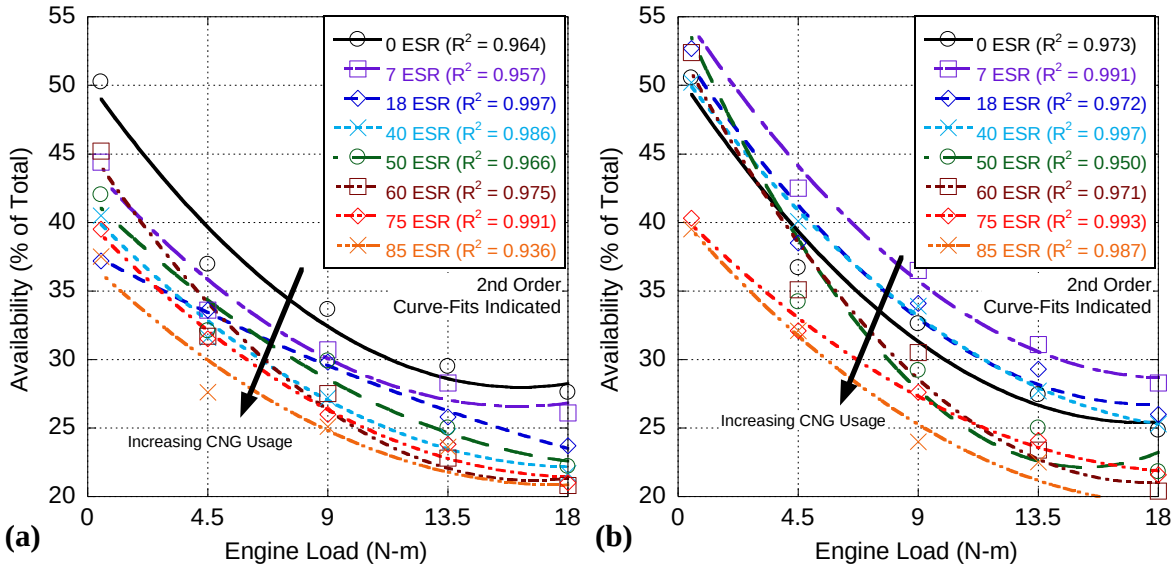

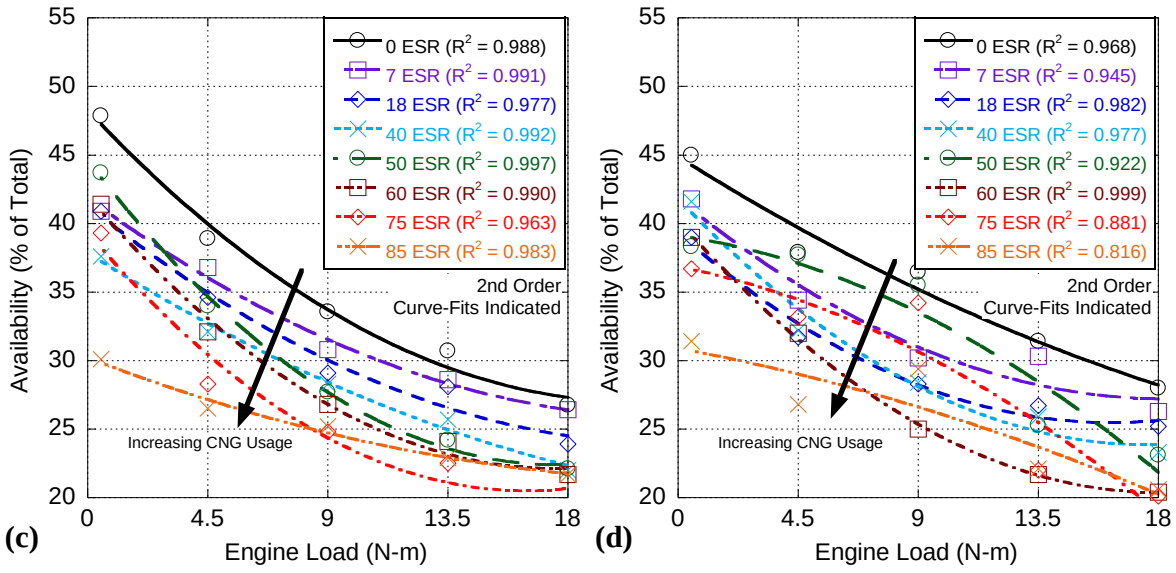

Figure 79. Percentage of Thermal Availability Lost to Entropy Generation for the M87 (a), M91 (b), M92 (c), and M96 (d) gas mixtures at all engine loads and *ESR*s.

Finally, the exergy retained by the exhaust gases behaves similarly to the ULSD control with respect to engine load (see Figure 80). The load at which the local minimum of exergy retained exists (around 9.0 N-m) is more or less independent of the precise mixture of fuels used. Past 9.0 N-m, the exergy remaining in the bulk gas becomes more significant, particularly due to the rising amount of diffusion burn, as this exergy addition is less likely to be extracted by the engine prior to EVO. CNG usage leads to lessened diffusion burn, greater premixed burn, and thus a more efficient addition of exergy to the bulk gas, increasing the overall 2nd Law efficiency of the engine cycle. However, due to the lessened amount of heat transfer and entropy generation discussed earlier along with lower combustion efficiency, the exergy retained by the exhaust gases at EVO rise as more CNG is utilized. Similarly to heat transfer and entropy generation losses, there is a marked shift in availability retention at very high *ESR*s, pointing again to a shift in engine behavior once the engine cylinder becomes sufficiently premixed with fuel.

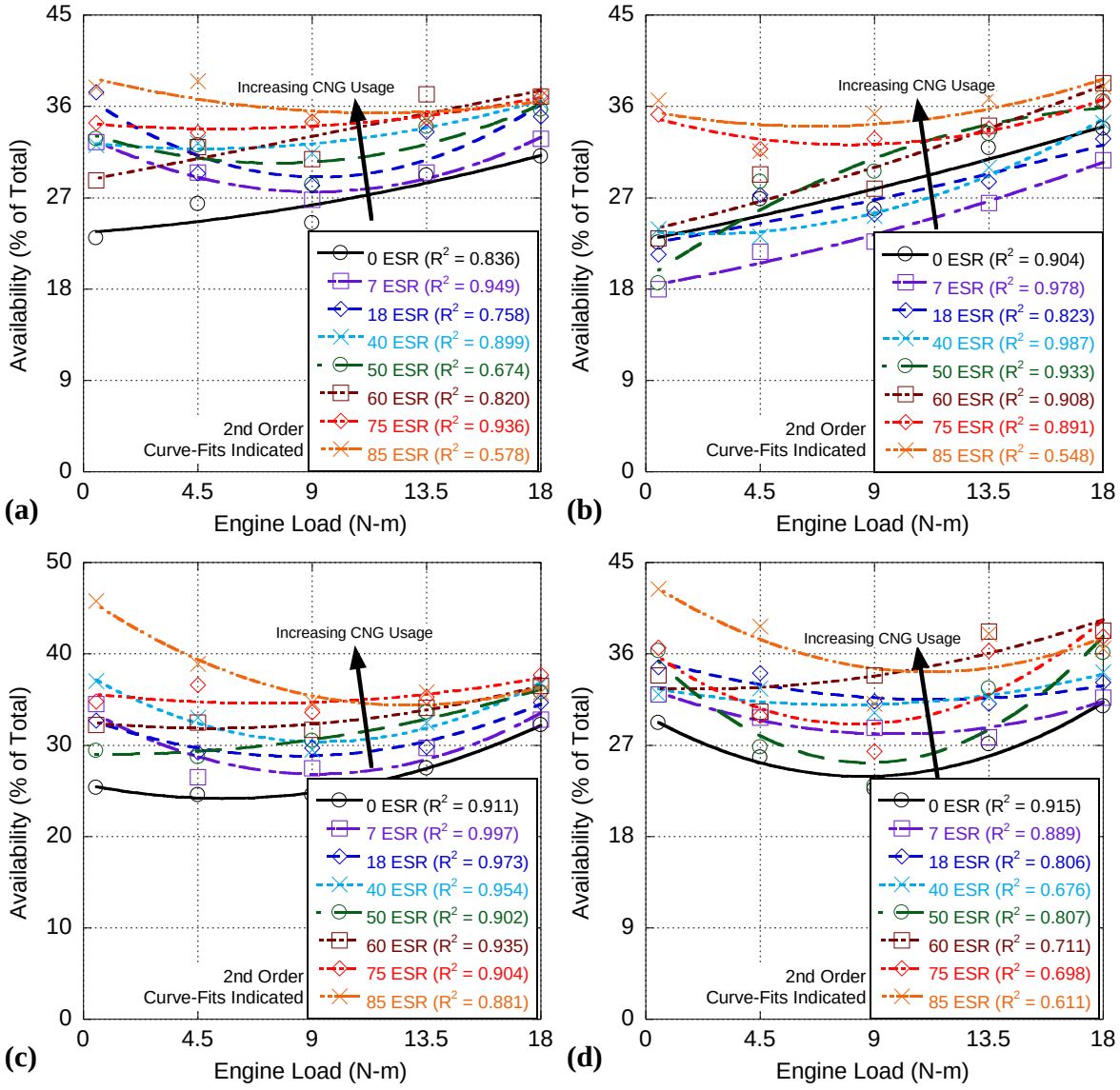

Figure 80. Percentage of Thermal Availability Retained by the Working Fluid for the M87 (a), M91 (b), M92 (c), and M96 (d) gas mixtures at all engine loads and *ESR*s.

The gross 2nd Law efficiency of all of the CNG mixtures at all loads is shown in Figure 81. Overall, the efficiency increases significantly with engine load up to 13.5 N-m, at which point the greater fraction of combustion due to diffusion causes further changes in efficiency with added load to be marginal, in a manner similar to the thermal efficiency from the 1st Law analysis.

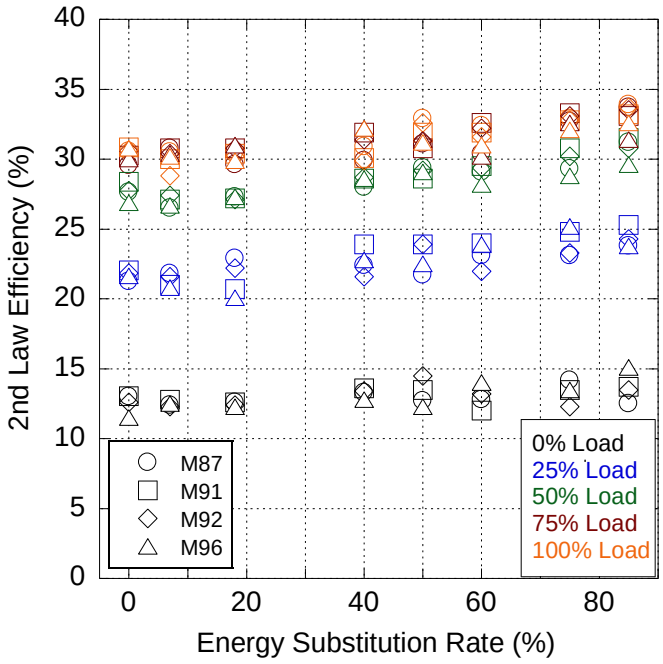

Figure 81. Gross 2nd Law Efficiency as a Function of *ESR* at all loads.

As *ESR* rises, exergetic efficiency also grows slightly, representing the increasingly efficient addition of thermal exergy associated with the greater amount of premixed combustion. However, this only reflects the thermal exergy analysis, and does not fully reflect the chemical exergy added to the cylinder. This is also the case in the 1st Law analysis, and the effect of the decreasing efficacy of combustion at consuming the fuel within the cylinder is only visible through the fuel conversion efficiency (Figure 74). Within the 1st Law Analysis, the fuel conversion and thermal efficiencies are related as follows:

1st Law Efficiency Relation	$\eta_f = \eta_t \eta_c$	(45)

where η_f is the fuel conversion efficiency, η_t is the thermal efficiency, and η_c is the combustion efficiency. Of the three, the thermal efficiency is explicitly defined within the context of the 1st Law of Thermodynamics. However, combustion efficiency exists outside of the 1st Law analysis, as it simply measures the fraction of fuel that is successfully consumed by the combustion event [1]. As a result, combustion efficiency can be utilized outside of the context of the 1st Law analysis alongside the 2nd Law efficiency:

2nd Law Efficiency Relation	$\eta_{ef} = \eta_e \eta_c$	(46)

where η_{ef} is the exergetic fuel conversion efficiency, and η_e is the 2nd Law efficiency.

In this way, just as the exergetic efficiency is analogous to the thermal efficiency, so the exergetic fuel conversion efficiency (shown in Figure 82) is similar to the 1st Law fuel conversion efficiency. Here, the 2nd Law fuel conversion efficiency, like the 2nd Law efficiency (and the 1st Law fuel conversion efficiency discussed earlier), increases with engine load representing the heightened ability of the engine to take advantage of fuel exergy. Also similarly, the rise in 2nd Law fuel conversion efficiency between 13.5 N-m and 18.0 N-m is marginal, due to the difficulty in releasing all of the available fuel exergy in the premixed phase of combustion. Finally, the 2nd Law fuel conversion efficiency shows the anticipated decrease as *ESR* rises, related to the falling fraction of fuel consumed as the engine relies more on CNG for exergy. However, the loss in 2nd Law fuel conversion efficiency is less significant than for the 1st Law fuel conversion efficiency and at 100% of rated load it is nearly constant across all *ESR*s. This is seemingly counterintuitive; the fall in combustion efficiency as *ESR* increases should conceptually lower the 2nd Law fuel conversion efficiency more significantly at higher loads. Of importance; similar to the 1st Law Efficiencies and brake-specific values, the 2nd Law Fuel Conversion Efficiency sees an uptick for 85% *ESR* and full load, again signifying a raised degree of premixed combustion.

To visualize why this occurs, it is necessary to consider the overall exergy addition to the cylinder itself, including all of the components of the exergy analysis, shown in Figure 83 as the average summed thermal and chemical exergy for varying *ESR*s (speciated summed thermal availability addition can be found in Appendix B1). Of note, the thermal exergy is used to categorize the amount of exergy added to the cylinder by the combustion of fuel (burned only); whereas, the chemical exergy refers to the total exergy present in the cylinder in the form of injected fuel (burned and unburned fuel). Therefore, due to combustion inefficiencies, the chemical potential exergy will be higher than the thermal exergy content (see Figure 83b for the average chemical potential availability addition across the four mixtures, and Appendix B2 for speciated chemical potential availability addition). Raising engine load requires a linear increase in exergy addition. However, as *ESR* rises the total amount of thermal exergy added to the

cylinder generally decreased, particularly at or above 9.0 N-m. This is in line with the earlier analysis, and reflects the decrease of diffusion-dominated combustion in favor of premixed combustion as CNG is added. However, like the 2nd Law efficiency, this does not precisely reflect all of the exergy available to the engine, particularly in the form of chemical potential. When this potential is included, it is shown that as engine load rises, the difference in behavior between the various *ESR*s becomes less significant, such that at full load the total exergy addition is effectively constant across all *ESR*s, which highlights a general decease in 1st Law fuel conversion efficiency as more fuel survives and is exhausted at EVO for low-to-moderate *ESR*s.

Of note, however, the total thermal availability also reflects the same increase in efficiency seen in the 1st and 2nd Law Fuel Conversion Efficiencies, as well as the BSFC and BSEC, under full load conditions at 85% *ESR*. Here, the engine is so sufficiently premixed that the negative aspects associated with the combustion of the CNG fuel are diminished. Here, prompt combustion and high temperatures result in a much more thorough combustion event, and thus a much more efficient and effective release of both chemical potential energy and exergy.

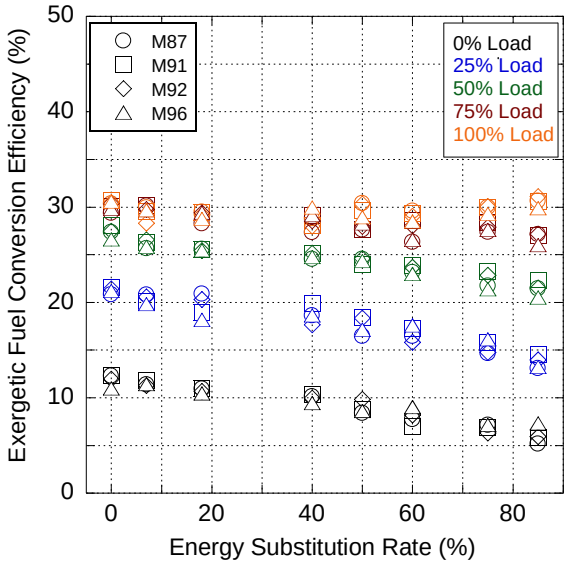

Figure 82. Gross 2nd Law Fuel Conversion Efficiency as a Function of *ESR* at all loads.

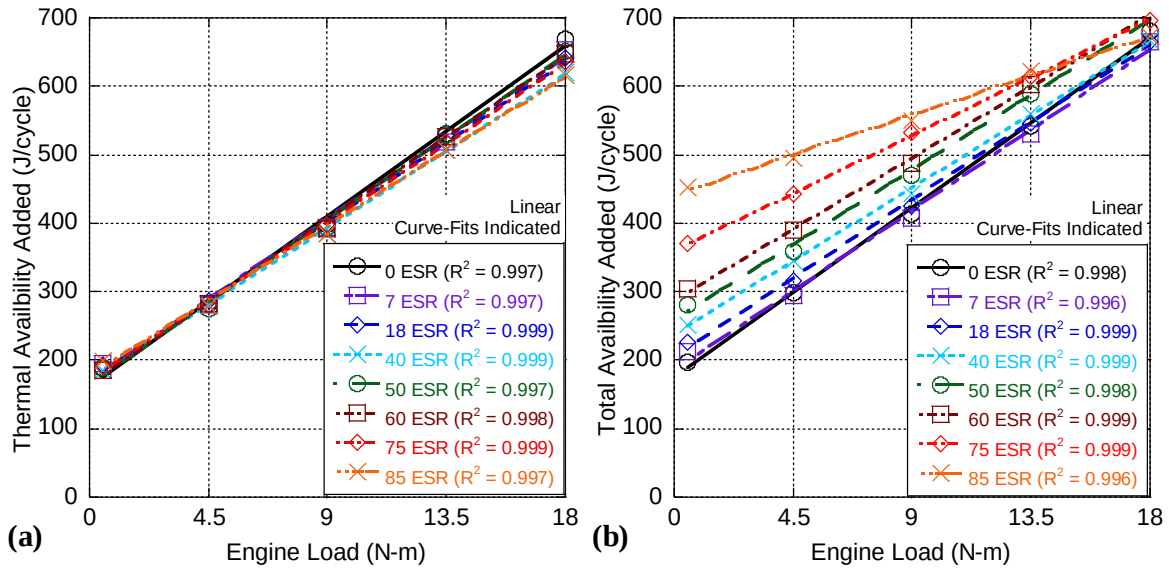

Figure 83. Thermal (a) and Chemical Potential (b) Availability added to the Cylinder, Average of all CNG mixtures.

From the perspective of the 2nd Law analysis, the apparent parity in performance between ULSD and CNG at high loads can be explained through the relationship between the fuel's energy content and exergy. In specific, while more fuel energy is exhausted into the atmosphere as unburned fuel with increasing *ESR*, as evidenced by the falling combustion efficiency, this energy has a lower exergy associated with it due to the reduced ratio of exergy to energy content (see Table 31). In addition, this is offset by the improved 2nd Law efficiency as more CNG is utilized, entirely because of the larger degree of combustion through the premixed phase, as opposed to (and at the expense of) the diffusion phase. Thus, while CNG is less thermodynamically useful in an absolute sense, it is more thermodynamically valuable from a functional perspective entirely because it promotes a more efficient combustion event. Finally, this effect only comes into play at high engine loads, as at lower engine loads the combustion efficiency is too low and significant energy and exergy is expelled in the exhaust blowdown event. However, combining high loads (and hot temperatures) with *ESR*s in excess of 75% results in a much more thorough combustion event, ensuring further combustion of the fuel species in the periphery of the cylinder, and adding to both the premixed and diffusion burn events. Thus, at these high *ESR*s and high

loads the CNG begins to achieve a level of thermodynamic value comparable to, or potentially in excess of, conventional operation with ULSD.

From these results, a description of dual-fuel operation can be ascertained from a 2nd Law perspective. Overall, raising the total amount of CNG leads to more homogeneity in the bulk air-fuel charge, promoting premixed combustion, inhibiting diffusion-dominated combustion, raising the percentage of exergy successfully transferred as work, and thus raising efficiency. Increasing *ESR* results in (generally) cooler temperatures (except at high loads), lowering the overall rate of heat transfer out of the engine, and lowering the percentage of exergy lost to heat transfer. At the same time, raising the *ESR* leads to a greater amount of CNG that survives the premixed spike as the flame front associated with CNG combustion extinguishes prior to consuming all available fuel. While most of the remaining CNG survives the high temperature environment, the rise in temperatures associated with increasing engine load does lower the amount of CNG that survives the entire combustion process stroke and so reacts prior to EVO. Despite peak cylinder temperatures and exhaust temperatures similar to operation with ULSD, the combination of lowered heat transfer losses and lower internal entropy generation causes the exhaust gas to have higher exergy at EVO. Therefore, the total amount of thermal exergy present within the cylinder decreases with added CNG usage, reflecting the improved engine efficiency from the CNG promoting a shift towards premixed combustion. As a result, while the 1st Law analysis determines that operation with CNG is less efficient in terms of energy usage, the engine achieves near-parity of operation from the perspective of the 2nd Law analysis. This comes with a significant caveat. With higher CNG usage comes an increase in the fraction of CNG that survives both the combustion process and the higher temperatures of the expansion process, exiting the engine as unburned fuel (and, in this case, unburned fuel with a significant greenhouse gas potential).

With respect to utilization, the 2nd Law analysis provides a more thorough overall picture of the thermodynamic conditions within the engine cylinder. In particular, the 2nd Law analysis is useful for identifying the degree of usefulness of the entire waste product of the exhaust gas. The thermal component of this exergy is of immense importance to exhaust waste heat recovery through ORC systems,

as it provides an absolute measure of not only the amount of exergy within the exhaust (similar to the energy of the exhaust from the 1st Law analysis), but also a measure of the fraction of exergy that is no longer available. Furthermore, the 2nd Law analysis provides a clear picture where exergy destruction may be identified, which the 1st Law analysis (that is unconcerned with the degree of usefulness of the exhaust gases) cannot. A caveat in this analysis is that the 2nd Law analysis does not inherently account for the chemical potential exergy that is passed out as unburned fuel, as the analysis functions entirely on the addition of thermal exergy by combustion. However, this loss of exergy can still be included by incorporating the combustion efficiency of the cycle, which effectively creates a 2nd Law analogue to the fuel conversion efficiency, allowing the model to pinpoint the final piece of information needed to complete the analysis for comparison of differing engine operational modes; the thermodynamic exergy of the unburned fuel.

6.5 Low Temperature Combustion and Dual-Fuel Operation

Of particular interest is the exergy behavior at very high *ESR*s. Above a certain level (typically 75%), the 2nd Law analysis indicates a marked shift in in-cylinder behavior. While 2nd Law Efficiency (Figure 81) continues to climb at higher *ESR*s, both internal and external irreversibilities (in the form of entropy generation in Figure 79 and heat transfer in Figure 78) fall, and fall more significantly than for changes in operation at lower *ESR*. This results in more availability being retained by the working fluid, and ensuring that the highest fraction of availability is either successfully extracted or retained, and not lost within the engine's processes. This combination of lower entropy generation and reduced heat transfer loss is somewhat contradictory to prior results, particularly when using liquid fuels. Normally, increasing engine temperatures lead to greater losses from heat transfer and decreased losses from entropy generation. While all dual-fuel combustion seems to buck this trend in general, they do not generally result in large shifts in availability transfer and losses until the engine is operating at *ESR*s of 75% or above.

This behavior may all be related to a shift in the upper limit of compression ratio possible for PCCI/RCCI operation in diesel engines, and low-temperature combustion (LTC) in general [172-176]. LTC, particularly in tandem with reactivity-controlled compression ignition (RCCI) combustion, has been associated with lowered heat transfer losses, due to the relative inhomogeneity in comparison to fueling regimes like homogeneous charge compression ignition [7, 18, 30, 177]. This in turn may result in relatively high local temperatures in combination with lowered global temperatures, particularly at the periphery of the cylinder, and therefore the combination of lowered heat transfer losses and lowered internal entropy generation, all due to increased flame propagation and flame quenching while combusting via a more thermodynamically advantageous methodology.

Of note, high compression ratio engines may struggle with achieving LTC [167]. These engines tend to encounter lower ignition delay periods, narrowing the window possible to achieve LTC combustion as the fuel is ignited and consumed before it can mix properly. This normally necessitates the use of EGR to cool the in-cylinder environment, lengthening the ignition delay period and aiding in atomization and vaporization of liquid fuels. This can also be combated by utilizing a fuel more prone to premixing (e.g., ethanol in a direct-injected CI engine because of its low Cetane Number), which is a primary advantage of CNG and gaseous fuels with the intent to achieve RCCI combustion. However, this presents a separate problem; gaseous fuels, in general, are not prone to self-ignition in most compression ignition engines, and must be ignited using the injection of a pilot fuel charge. Then, this returns to the prior mentioned issue; the fuel being injected must have sufficient time to atomize, vaporize, and premix in order for the fuel charge to achieve LTC combustion. As a result, this ability for the pilot charge to premix still forms the primary problem in attempting to achieve RCCI combustion in a dual-fuel regime, and the main characteristics that affect this are the compression ratio of the engine (which promotes prompt ignition) and fuel injection pressure (which promotes fuel breakup and the flowrate of fuel into the cylinder). Thus, for a given combination of fuel injection pressure and compression ratio, even if PCCI combustion is possible at all, it is only feasible for a given amount of fuel (or less). Furthermore, if

the amount of fuel exceeds this allowed maximum, the combustion will be in a transitionary regime in between conventional and LTC operation.

With dual-fuel combustion, the addition of gaseous fuel in the intake has an important effect on this maximum in allowable fuel. By premixing more fuel mass in the cylinder, dual-fuel combustion lessens the amount of premixing that is required from the pilot fuel injection in order to achieve combustion in general. Hence, a greater CNG usage results in less pilot fuel being required to meet a given load. Lowering this fuel mass requirement also makes the engine more likely to premix the pilot charge by completing the injection event far enough ahead of ignition. Therefore, for a given compression ratio and fuel injection pressure, it may be possible to achieve LTC through the usage of sufficiently high *ESR*s, as the CNG effectively counteracts the effects of high compression ratio.

Normally, proving LTC combustion would achieved by a comparison of exhaust emissions across varying *ESR*s. In particular, LTC combustion is noteworthy as a method to "beat" the NO_x/PM tradeoff typically seen in diesel engines, whereby it is generally impossible to achieve high-efficiency combustion in a diesel engine without producing either NO_x or PM. As seen in Chapter II (see Figure 13), operation with increasing amounts of CNG did result in decreased NO emissions and increased NO_2 emissions except at very high *ESR*s, where NO_2 emissions decreased to levels below that of conventional combustion, potentially indicative of LTC. PM emissions also decrease significantly, but this is masked by the lowering of PM emissions associated with gaseous fuels; due to the fact that the fuel is so heavily premixed, and gaseous fuel does not need to undergo fuel breakup. As a result, operation with gaseous fuels will lower PM emissions anyway, and it is difficult to differentiate between PM reductions due to decreased liquid fuel usage and reductions that may be indicative of LTC. Thus, if LTC operation is to be proven with respect to dual-fuel combustion, it must rely on a separate analysis.

The 2nd Law analysis may provide this missing piece. For increasing *ESR*s up to 50-60%, the 2nd Law analysis indicates a gradual increase in efficiency, a decrease in heat transfer and entropy generation losses, and therefore an increase in exhaust availability. Simultaneously, for operation at 9.0 N-m or below, NO emissions generally fall, and NO_2 emissions alternatively rise, while at 13.5 N-m and above

NO and NO_2 emissions are largely constant (see Figure 13). However, past 75% *ESR* for low-to-midrange loads (although particularly at 9.0 N-m), internal and external irreversibilities fall significantly and suddenly, are accompanied by a loss of NO_2 emissions (and thus NO_x emissions overall), and a slight rise in both first and second law thermal efficiencies occurs. For 13.5 N-m, NO_2 emissions decrease (although this decrease is not as significant as at 9.0 N-m), and at 18.0 N-m, NO_2 emissions grow above that of normal levels, and the differences in losses from irreversibilities is less significant overall.

Therefore, operation at 75-85% *ESR* may exhibit a transition from LTC to conventional combustion. At 9.0 N-m, the engine exhibits the combination of high exergetic efficiency and low NO_x emissions characteristic of LTC, thanks to adequate premixing of the pilot fuel charge. As the engine load rises to 13.5 N-m, the increased fuel injection results in a less effective premixed fuel-air charge; the pilot fuel added at the end of injection may barely have enough time to premix adequately prior to ignition, resulting in only slightly lowered NO_x emissions, and a reduced difference in exergetic losses in comparison to conventional combustion. Finally, at 18.0 N-m, the engine has transitioned back into a conventional (if highly premixed) combustion regime, with slightly increased NO_x emissions, and the exergetic losses are only marginally better than ULSD combustion, owing to the highly premixed nature of combustion.

One final piece of evidence for this transition comes in the form of the equivalence ratios of the various *ESR*s and loads tested (see Figure 84). In many conventional combustion scenarios, a net decrease in NO_x emissions can be tied to a general lack of oxygen present within the cylinder, which may be responsible for a similar decrease in NO_x emissions. However, the tested equivalence ratios never exceed 0.6, even for very high *ESR*s and at 18.0 N-m. Furthermore, while equivalence ratio does increase with *ESR* for all loads tested, this increase becomes less significant with higher loads; while there is a need to put in more chemical potential energy at lower loads to compensate for the fact that much of the methane gas will not burn at lower temperatures, the higher temperatures of the higher loads counteract this somewhat. Finally, equivalence ratios for higher *ESR*s at 13.5 N-m are still lower than all tested *ESR*s at full load, and still maintain lower NO_x emissions than the full load conditions. Thus, while some oxygen

limitation is occurring, it is a function primarily of engine load, and not *ESR*, at least not within the suspect high *ESR*s from 9.0 N-m to 13.5 N-m.

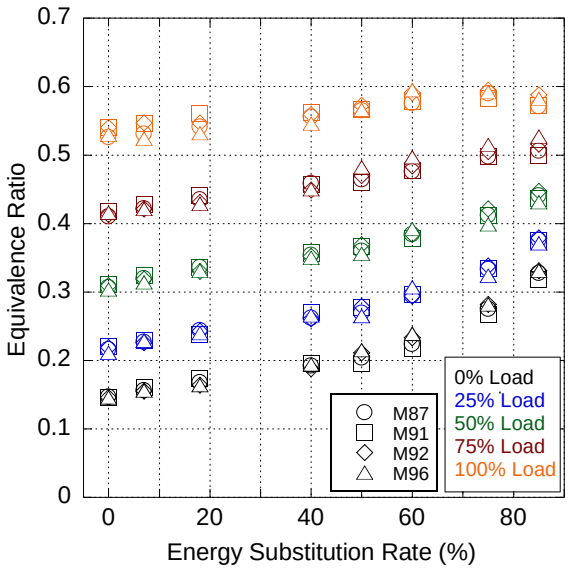

Figure 84. Engine equivalence ratios for all loads, *ESR*s, and CNG mixtures tested [6].

With this information, the possible entrance into the LTC regime can also be (somewhat) observed from the 1st Law RHR results (see Figure 9). Above 9.0 N-m at 75-85% *ESR*, the 1st Law RHR analysis displays a growth in what appears to be diffusion-dominated combustion. However, this is not in keeping with what is anticipated from dual-fuel combustion at such high-*ESR*s; the high amount of mixing should, at least intuitively, lead to a predominately premixed combustion event. The key is showcased in the ignition delay characteristics; for high *ESR*s there is a significant increase in ignition delay (see Figure 8), indicating the increasing difficulty of the ULSD to ignite in the methane-rich environment. Thus, the CNG usage does not produce a large window in which fuel may be injected in order to achieve the entirely premixed combustion necessary for LTC. As load increases, and fuel flow rate grows, the later injected fuel does not have enough time to prepare before combustion begins, and thus combusts (along with unused CNG that survives the initial flame front) after the premixed spike. As a result, thanks to the 2nd Law Analysis, it is possible to identify the fringes of LTC combustion, particularly in the dual-fuel regime, *with the telltale sign being the large reduction in internal and external irreversibilities, in tandem with the reduction in NO_x emissions*. Of importance, this finding may

aid in the exploration of the boundary between conventional and LTC combustion, particularly if paired with other operational characteristics (such as EGR) that may make LTC operation more viable.

6.6 Conclusions

Dual-fuel combustion represents an alternative means of fueling CI engines with relatively inexpensive CNG fuel, and is accessible to CI engines without requiring extensive modifications. A 2nd Law analysis may be used to ascertain the pathways by which fuel combustion adds thermal exergy to the working fluid, and the ways this exergy is alternatively utilized, lost, destroyed, or retained across the engine cycle. To that end, a high compression ratio single-cylinder CI engine was operated in a dual-fuel regime with CNG usage, and a previously constructed exergy model was used to dissect the combustion process and observe CNG operation from the perspective of the 2nd Law of Thermodynamics.

The 2nd Law analysis reveals that dual-fuel operation with moderate CNG usage results in a general rise in the exergetic cycle efficiency, particularly at high engine loads. This is directly due to the increasing homogeneity of the fuel-air charge prior to combustion, and so with higher amounts of CNG more fuel is combusted in the valuable premixed combustion phase rather than the less efficient diffusion-dominated phase. Dual-fuel operation is also noted to generally lower overall heat transfer losses (primarily because of cooler temperatures), inhibit in-cylinder entropy generation (due to the shift towards more efficient exergy addition in the premixed spike and a reduction in losses associated with liquid fuel injection), and thus increase the thermal exergy of exhaust gas upon its ejection into the atmosphere during the blow-down event. This makes operation with higher *ESR*s more exergetically efficient in comparison to operation with ULSD only. In summation, CNG usage results in a lower amount of thermal exergy needed to drive the engine, entirely because additional CNG usage results in an increasing fraction of fuel exergy added in the more efficient premixed combustion phase.

However, CNG usage is also marked by a significant loss in combustion efficiency, believed to be due largely to a combination of quenching of the flame front associated with CNG usage, as well as the relatively sturdy nature of the methane-rich CNG surviving the high-temperature environment during

cylinder expansion. This is not immediately reflected within the 2nd Law analysis, which is primarily concerned with the thermal exergy added to the cylinder; unburned fuel still exists in a relatively low-entropy state, and obviously does not add its exergy unless combusted. However, by augmenting the 2nd Law efficiency values to make use of the combustion efficiency, the exergy content of the unburned fuel is revealed. Overall, while the energy consumption of the engine increases with CNG usage from a 1st Law perspective, the 2nd Law perspective reveals that the exergy consumption of the engine may be essentially equivalent at high engine loads, entirely because of the promotion of premixed combustion, and the lower-quality nature of the potential exergy of the CNG in comparison to ULSD. Thus, the 2nd Law analysis reveals parity in operation across differing amounts of CNG used which the 1st Law analysis is not able to reveal.

Finally, the 2nd Law Analysis may be vital to identifying the onset of LTC combustion. LTC, particularly in RCCI regimes, is noted for significant decreases in both heat transfer and entropy generation-related irreversibilities, and thus a rise in availability retention by the working fluid and/or availability extraction as work. This is particularly apparent when used alongside NO_x emission readings and as an alternative to PM emissions measurements that cannot be relied on due to the normal decrease in PM production with gaseous fuel usage.

Chapter VII: Second Law Analysis of Dual-Fuel Combustion of Biodiesel and Syngas

Some material published as "Availability Analysis of Alternative Fuels for Compression Ignition Engine Combustion," Fourth International Congress of Automotive and Transport Engineering, Accepted June 22nd, 2018

7.1 Abstract

The energy-exergy heat release model is used to analyze dual-fuel combustion in a novel regime, namely the co-combustion of biodiesel with a hydrogen-rich gas. This gas was chosen to mimic the composition and properties of a synthesis gas created from the reformation of glycerol (a byproduct of biodiesel production) in the presence of a catalyst. Overall, biodiesel-syngas combustion is found to produce largely consistent combustion across a variety of gas usage rates, with the differences in 2nd Law behavior being largely mitigated by moving to higher loads. The only significant deviations seen were in the 2nd Law fuel conversion efficiency, due to the engine consuming more fuel to make up for combustion inefficiencies inherent to dual-fuel combustion, and in the heightened availability of the exhaust gas emitted from the engine with increased syngas usage. Overall, the 2nd Law analysis conclusively shows that fuel system optimization is largely unneeded in this specific dual-fuel regime, due to the lack of appreciable change in 2nd Law efficiency as syngas usage was increased. Hence, only in the case of waste heat recovery (where exhaust temperatures and exergies must be kept consistent) are changes to injection strategies absolutely necessary.

7.2 Introduction

The effects of fuel properties on combustion are of central importance to engine testing, and the phenomenon associated with varying fuel properties can be shown through a number of diagnostic models, including 1st Law Rate of Heat Release (RHR) models, and less commonly through 2nd Law Availability models. Generally, 2nd Law analyses are passed over in favor of more simple 1st Law models. However, for increasingly divergent regimes, changing fuel characteristics can incite significant changes to engine combustion. Dual-fuel operation, for example, presents substantial changes in fuel characteristics, due to

the introduction of gaseous fuel far ahead of the engine cylinder, subsequently promoting more effective mixing than what is typically seen with liquid fuels in compression ignition (CI) engines. Because of this departure from conventional CI combustion, it is of importance for dual-fuel combustion regimes to be scrutinized using more advanced combustion modeling, including exergy modeling.

One such potential regime includes dual-fuel use of biogases sourced from byproducts of the creation of renewable fuels. A particular biogas of interest is synthesis gas (syngas), a hydrogen-rich combustible gas created from the partial combustion and reaction of glycerol in a low-oxygen environment with the use of a catalyst. Glycerol is a viscous hydrocarbon-rich substance notable for being an offshoot of the biodiesel production process, and its high viscosity makes it unviable for direct injection (and thus for combustion) in CI engines. Therefore, converting glycerol beforehand into syngas produces a flammable fuel that can be used in a dual-fuel regime. Furthermore, by utilizing the produced biodiesel as the pilot fuel in the dual-fuel regime, the entire combustion process becomes renewable and achievable using both products of biodiesel production.

However, dual-fuel operation is subject to significant variations in the input fuels, and syngas in particular is dependent on both the feedstock and the reformation process. Prior studies with hydrogen-rich syngas have found the potential to increase thermal efficiency and in-cylinder pressures [90]. Combustion of hydrogen also features a wide-range in flammability and low ignition energies. However, the hydrogen and methane content of syngas may lead to increasing difficulty in achieving ignition or maintaining combustion. Hence, a potential outcome of the combustion of syngas can lead to poor combustion efficiency, increased fuel consumption, and lower fuel conversion efficiency [92, 100]. More importantly, usage of syngas has been found to be limited to around 30% hydrogen content by volume, past which pre-ignition and knock issues begin to manifest, and relatively violent combustion presents a danger to operation [90, 91].

In comparison, combustion of biodiesel (both alone and as a pilot fuel for dual-fuel combustion) is noted for increases in diffusion-dominated combustion, thanks its higher viscosity and lower energy content. Conversely, the increased oxygen content inherent to biodiesel also serves to aid in both ignition

and combustion of the syngas, as it offsets the lack of oxygen from atmospheric air displaced by the usage of syngas. Unfortunately, this can result in lowered ignition delays, resulting in the biodiesel igniting earlier than optimal, subsequently requiring reoptimization of engine injection timings.

From a 2nd Law perspective, dual-fuel combustion with syngas is noted for heightened destruction of availability at low engine loads, due to difficulties in maintaining combustion and thus lower operating temperatures. Moreover, it has lessened availability destruction at high loads thanks to increased operating temperatures from the prompt combustion of the hydrogen- and methane-rich gases [158, 178]. Furthermore, the degree of availability retention has been positively correlated to the fraction of hydrogen within the syngas, due to higher degrees of premixed combustion. Other authors have noted that higher fuel-air ratios with increased syngas usage results in greater availability retention by the exhaust and decreased internal availability losses, but also higher heat transfer losses and a decreased 2nd Law efficiency [126-128].

To that end, this paper explores the usage of a diagnostic 2nd Law model to analyze dual-fuel combustion of soybean biodiesel with an artificial syngas. Testing utilized a single-cylinder high compression-ratio CI engine with a modern high-pressure injection system for the liquid pilot fuel, allowing for the normalization of injection and combustion timing. Overall, dual-fuel combustion of syngas with biodiesel is found to be largely identical to combustion of biodiesel alone from a 2nd Law perspective, with exergetic efficiency being fairly constant for varying usage rates at high engine loads. In addition, fuel consumption (and thus, fuel availability consumption) only increased slightly with syngas usage. The most significant deviation in 2nd Law behavior lies in the relative amount of availability retained by the engine exhaust, although this energy can be extracted through the usage of supplemental waste heat recovery systems.

7.3 Experimental Setup

As with prior testing, dual-fuel engine operation was performed using a Yanmar L100V single-cylinder CI engine without exhaust gas recirculation or added turbocharging, and with upgraded

electronic injection in place of the standard mechanical injection system packaged with the original engine [73]. Electronic injection was controlled with a Bosch MS15.1 engine control unit. Engine speed was controlled through a Dyne System Dymond Series alternating current dynamometer [179]. Engine and dynamometer specifications and characteristics can be found in Table 32. All monitoring and data logging were accomplished through a number of National Instruments LabVIEW systems, one to capture the in-cylinder pressure trace at a resolution of 0.2° of crank angle over 60 consecutive thermodynamic cycles, and a second logging engine temperatures, non-cylinder pressures, and other operational characteristics at a rate of 10 Hz.

Table 32. Engine and Dynamometer Specifications [73].

Engine Manufacturer/Model	Yanmar L100V
Type	Vertical Direct-Injected
Intake	Naturally Aspirated
Cooling	Air-Cooled
Cycle	4-Stroke
Displacement [cc]	435
Number of Cylinders	1
Number of Valves	2 (1 intake, 1 exhaust)
Bore [mm]	86
Stroke [mm]	75
Connecting Rod Length [mm]	118
Crank Radius [mm]	38
Clearance Volume [cm^3]	21.611
Piston Area [cm^2]	58.088
Compression Ratio	21.2
Continuous Rated Output [hp]	8.3
Rated Speed [RPM]	3600
Engine Oil Used	Shell 15W-40
Dynamometer Manufacturer/Model	DyneSystems, Inc. Dymond Series 12
Continuous Rated Torque [N-m]	28.61
Continuous Power [hp]	12
Maximum Speed [RPM]	7500
Voltage [VAC]	480
Phase	Three Phase
Frequency [Hz]	60
Controller	DyneSystems, In. Linter-Loc V OCS

For a pilot and baseline liquid fuel, the engine was operated with soybean biodiesel (fuel properties available in Table 33) and with the injection system operating at 48±0.5 MPa. The engine speed was held constant at 1800 RPM, useful for demonstrating both premixed and diffusion-dominated

combustion as a function of engine load. For all loads, the engine was first operated with biodiesel. After achieving a steady-state operational mode (defined as a change in engine and oil temperatures of less than 1% over the course of a minute), engine data was logged. Then, biodiesel injection was reduced, and syngas allowed to flow into the intake in order to achieve a desired Energy Substitution Ratio (*ESR*), or the fraction of total fuel energy added to the cylinder in the form of gaseous fuel (in this case, the syngas), and is represented as follows:

Energy Substitution Ratio	$ESR = \frac{\dot{m}_g Q_{LHV_g}}{\dot{m}_g Q_{LHV_g} + \dot{m}_p Q_{LHV_p}}$	(47)

where $\dot{m}$ is the mass flow rate of fuel, Q_{LHV} is the lower heating value, and the subscripts $_g$ and $_p$ are used to differentiate between gas (syngas) and pilot (biodiesel) fuel charges, respectively [32]. Flow of syngas was monitored and controlled through a Brooks mass flow controller (model #SLA5850s) [32, 73]. Overall, three separate *ESR*s were utilized, corresponding to 10%, 20%, and 35% of total fuel energy. Of note, at 18.0 N-m, the maximum *ESR* was limited to 30%, due to the flow controller operating at its upper limit.

Table 33: Soybean biodiesel properties.

Cetane Number	48.1 ± 4.7
Energy Content [MJ/kg]	39.88 ± 0.044
Exergy Content [MJ/kg]	42.27 ± 0.046
Density [kg/m^3 at 298.15 K]	875.58 ± 0.01
Kinematic Viscosity [cSt]	4.218 ± 0.001
Dynamic Viscosity [cP]	3.693 ± 0.001
Oxygen Content [% wt.]	9.9 ± 0.3
H:C Molar Ratio	1.87 ± 0.04

For operation with syngas, the engine was allowed to re-acquire steady state at the desired load, and new data were collected. The process was then repeated, using steadily less biodiesel and more syngas until the data for maximum *ESR* for a given load were catalogued, at which point syngas operation was halted, and biodiesel usage increased in order to achieve the next desired load. Additionally, fuel injection timings were changed as necessary with each load and syngas operational regime, in order to retain optimized operation with all *ESR*s, as defined by prior operation with biodiesel fuels [32]. Overall, five loads were tested subsequently corresponding to idle (0.5 N-m), 25% (4.5 N-m), 50% (9.0 N-m),

75% (13.5 N-m), and 100% (18.0 N-m) of the Yanmar L100v's rated operational limits at 1800 RPM. Post-processing and filtering of the acquired in-cylinder data was achieved with MATLAB, in addition to the processing of 1st and 2nd Law Heat Release information [12, 13, 35, 73].

The syngas mixture itself is a bottled gas mimicking the observed composition of syngas fuel reformed at a separate site. At present, a glycerol-based power generation system is installed at the University of Kansas using a full-scale reformer to fuel a Chevrolet 350 in^3 V8 engine [82]. This syngas is generated by the reformation of an 80/20% glycerol/water mixture, partially combusted in the presence of a nickel-alumina catalyst. However, the water content of the produced mixture presents a difficulty, as the syngas cannot be effectively or safely bottled on-site, transported to the Yanmar L100V, and combusted. To this extent, an artificial syngas was created in cooperation with Matheson Tri-Gas, intended to match the average mixture compositions as measured by the syngas generator rig, and shown in Table 34 [82]. The resulting artificial syngas had a lower heating value of 10.75 MJ/kg (31.55 if only flammable species are considered), a constant pressure specific heat of 1395.6 J/kg-K, a ratio of specific heats of 1.355, and a gas constant of 364.6 J/kg-K [82].

Table 34: Composition of the original (observed) syngas and the artificial mixture, expressed in volume % [75, 82].

Mixture Component	Volume Fraction (Dry)	Volume Fraction (Wet)	Artificial Mixture
Hydrogen	32.4	28.7	28.7
Methane	5.8	5.1	5.1
Carbon Monoxide	18.1	16.0	16.0
Carbon Dioxide	7.2	6.3	17.7
Water	-	11.4	-
Ethylene	4.8	4.3	4.3
Ethane	2.6	2.3	2.3
Nitrogen (assumed)	29.1	25.9	25.9

To address the issue of the high water content of the original syngas generated by the reforming rig, the carbon dioxide content in the artificial mixture was increased. This, in turn, maintains a consistent lower heating value of the combustible material, but slightly lowered the ratio of specific heats of the mixture. Carbon dioxide was preferred over nitrogen, which would have raised the ratio of specific heats and also may have skewed emissions of oxides of nitrogen (discussed in Chapter III).

7.4 Results and Discussion

To begin, the syngas-biodiesel dual-fuel combustion is considered from the perspective of the 1st Law of Thermodynamics. For brevity, only the results from 9.0 N-m and 18.0 N-m are considered, as these are the primary loads that exemplify the differences in combustion between liquid-only and dual-fuel operation. A more thorough description of the behavior encountered can be seen in Chapter 3 of this document. Pressure behavior at 9.0 N-m and 18.0 N-m can be seen in Figure 85. For low-to-medium loads, biodiesel and dual-fuel operation offer relatively similar performance. Like dual-fuel operation with more conventional gaseous fuels like CNG, the usage of syngas leads to a decrease in the peak motoring pressure (in the vicinity of top dead center, or TDC) due to its reduction in the ratio of specific heats of the air-fuel mixture. Similarly, at low loads, peak firing pressure is also somewhat lower due to a difficulty in combusting the diluent- and methane-rich syngas mixture. However, this is largely mitigated by 9.0 N-m due to increasing in-cylinder temperatures with engine load, such that performance differences between biodiesel combustion and dual-fuel combustion are minimal.

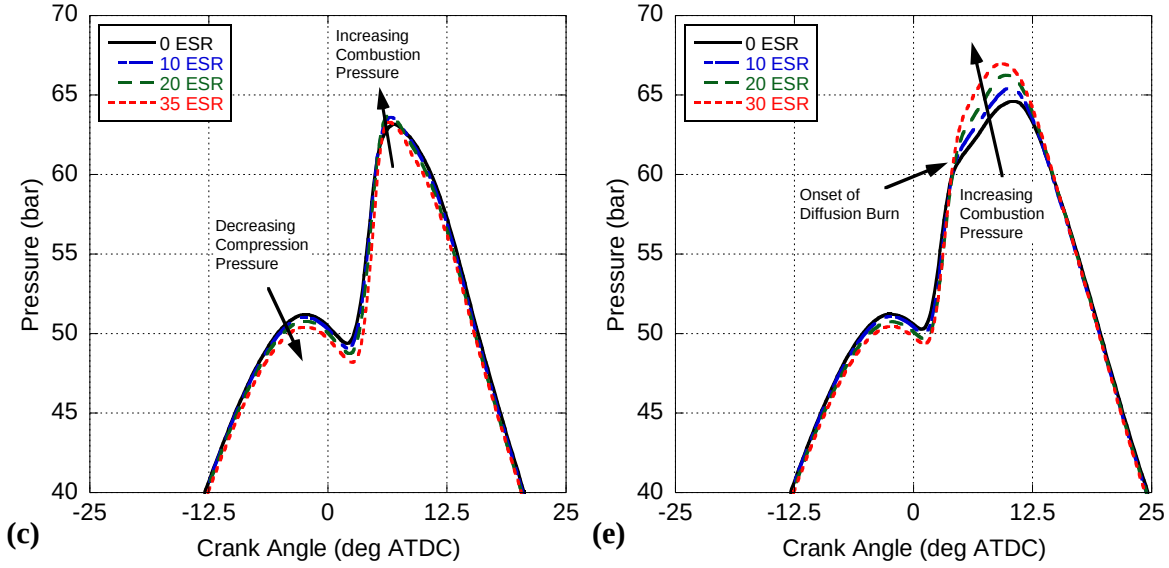

Figure 85: Measured in-cylinder pressure trace for operation with biodiesel and three *ESR*s at 9.0 N-m (a) and 18.0 N-m (b).

As engine load increases past 9.0 N-m, increasing *ESR* leads to a rise in peak firing pressure. Without the limitation to in-cylinder temperatures inhibiting ignition and combustion of the syngas

mixture, the engine is free to take more advantage of the high degree of premixing the syngas affords. As a result, combustion is more premixed, diffusion burn is lessened, and thus peak cylinder pressures are higher. This is made more significant by the usage of biodiesel fuel as the pilot, which is noted for being more viscous; hence, it is less prone to efficient fuel breakup, which itself promotes diffusion burn over ultra low-sulfur diesel. In other words, dual-fuel combustion is more advantageous in promoting premixed combustion when the direct-injected fuel is respectively more difficult to atomize and vaporize.

The calculated 1st Law RHR is shown in Figure 86. For lower loads, dual fuel combustion with syngas is noted for being less prompt, again due to lacking temperatures at lower loads and the inability of the engine to initiate or sustain combustion as easily. At 9.0 N-m, the premixing of syngas results in a higher peak RHR than for combustion with biodiesel alone, allowing the engine to overcome the lower initial pressures prior to combustion and achieve the same peak cylinder pressures as in conventional combustion with biodiesel (see Figure 85a). Similarly, the increase in premixed combustion comes with a relative decrease in diffusion burn. Normally diffusion-dominated combustion would be relatively low at 9.0 N-m, but with the utilization of biodiesel in place of ULSD diffusion burn begins to take a more significant role at loads lower than normal.

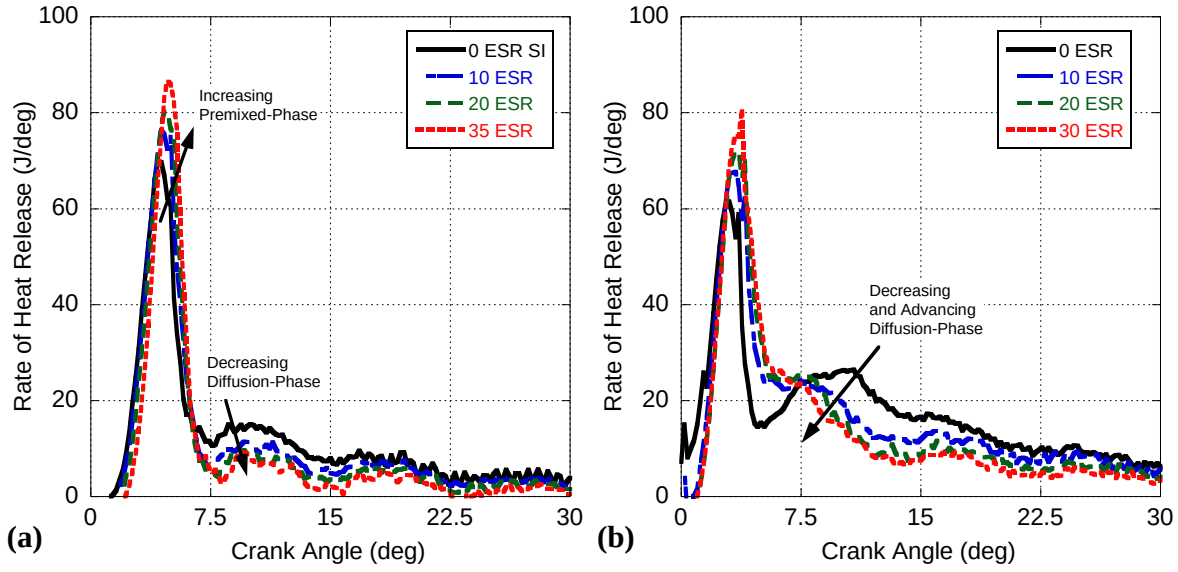

Figure 86: Rate of Heat Release for operation with biodiesel and three *ESR*s at 9.0 N-m (a) and 18.0 N-m (b).

Above 9.0 N-m, dual-fuel combustion results in a universal increase in the degree of premixing present in the engine. Diffusion burn is not totally mitigated, but is generally lower and starts earlier. Interestingly, at 18.0 N-m, the variation between 0 *ESR* and 10 *ESR* is greater than between all of the other syngas-biodiesel dual-fuel regimes, suggesting that even the presence of a small amount of syngas is useful for growing premixed combustion, and limiting diffusion burn, subsequently yielding a significant rise in engine efficiency.

In-cylinder temperatures generally follow the same discussion as the measured in-cylinder pressures. Peak motoring temperatures are universally cooler prior to combustion, again due to the lowered ratio of specific heats as a result of mixing the intake air with syngas. Below 9.0 N-m, peak firing temperatures decrease with added syngas usage, again reflecting the difficulty in igniting and combusting the syngas at low loads. At 9.0 N-m, the increased level of premixed burn allows the engine to overcome the pressure and temperature shortcomings prior to ignition, and as a result, the temperature profile after ignition is generally identical for all *ESR*s. Past 9.0 N-m, the premixed burn grows with *ESR*, and thus temperatures after ignition enlarge alongside syngas usage.

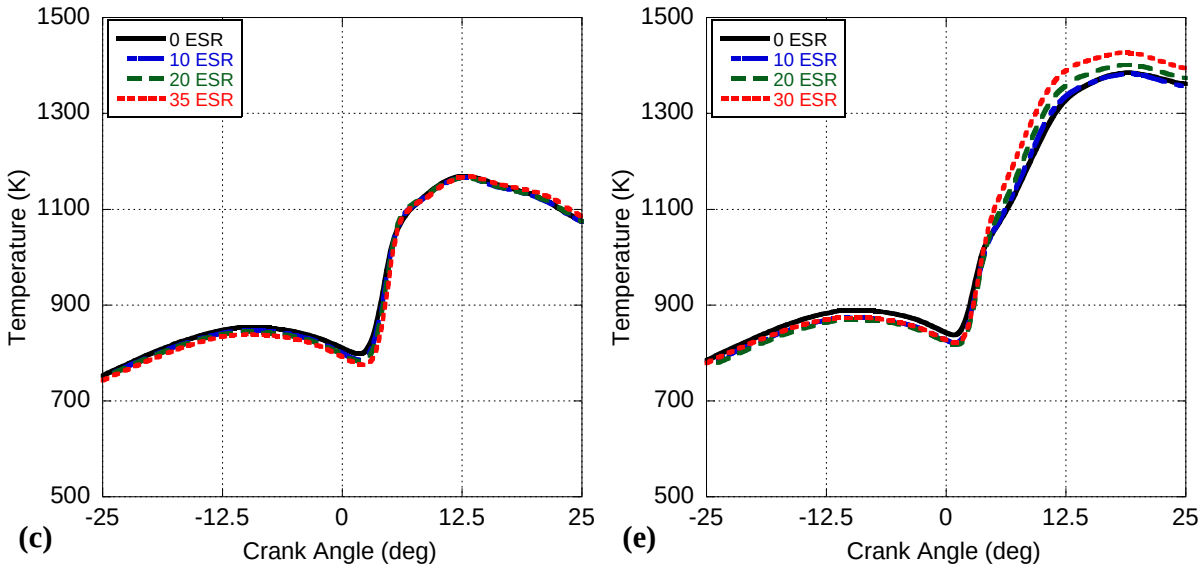

Figure 87: Calculated Temperature Profiles for operation with biodiesel and three *ESR*s at 9.0 N-m (a) and 18.0 N-m (b).

From a 2nd Law perspective, the usage of syngas presents some characteristics that diverge from dual-fuel operation with ULSD and compressed natural gas. First, as seen in Figure 88(a), the fraction of availability successfully transferred as work for any given load is largely uniform at any given *ESR*, with syngas usage being slightly more advantageous at low loads. Normally, dual-fuel behavior is associated with high degrees of the more efficient premixed combustion phase and greater in-cylinder temperatures. Figure 76b illustrates that syngas usage also typically results in slightly lower degrees of heat transfer except at 18.0 N-m. Here, there are two competing effects contributing to the relative availability losses through heat transfer; first, higher cylinder temperatures would (normally) result in greater degrees of heat transfer (note: in-cylinder temperatures are relatively similar except at 18.0 N-m, see Figure 19 in Chapter III). Simultaneously, the greater usage of syngas may promote increased flame quenching on the periphery of the cylinder. Thus, the conditions on the edges of the cylinder are comparatively cooler than they normally would be for more conventional combustion. At 18.0 N-m, it appears that the enhanced temperatures with *ESR* outweigh any potential flame quenching effects that can lessen heat transfer.

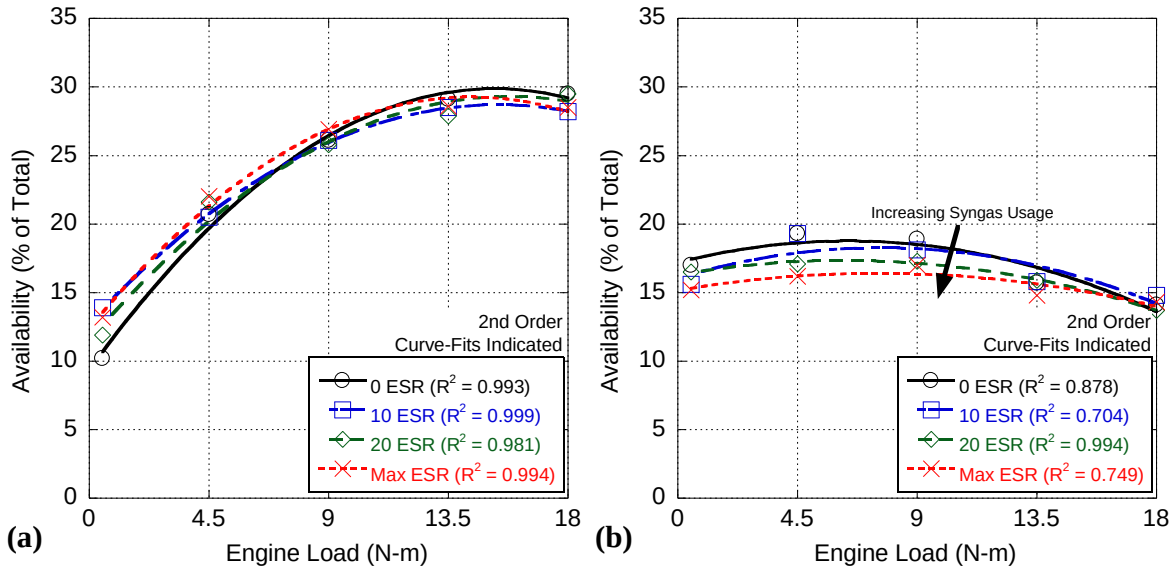

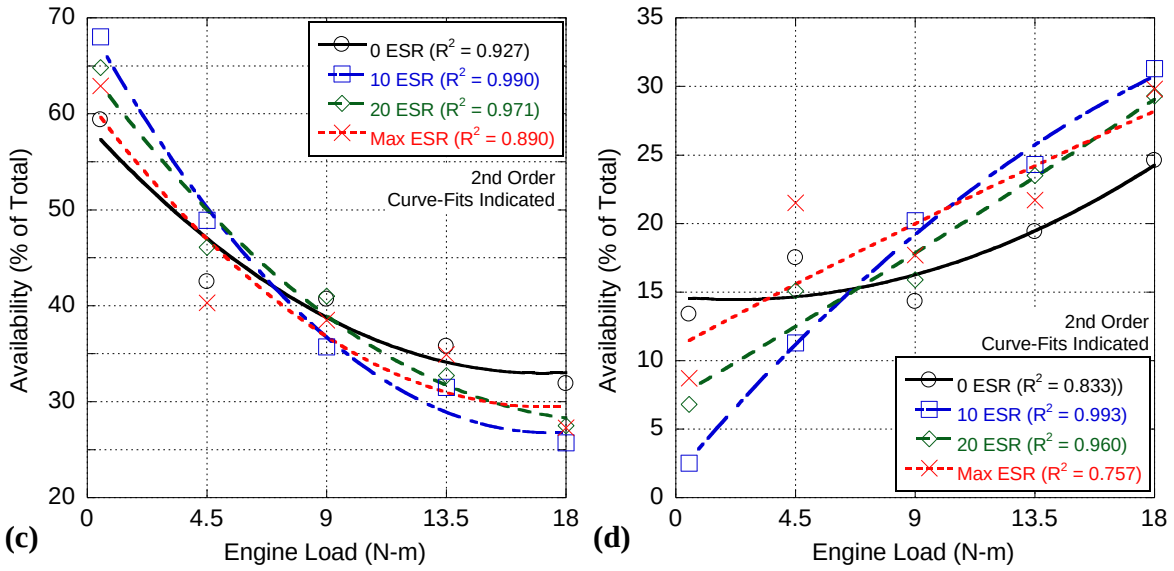

Figure 88. Percentage of Thermal Availability Transferred as Work (a), lost to Heat Transfer (b), lost to Entropy Generation (c), or retained by the Working Fluid at EVO (d) profiles for operation with biodiesel and three *ESR*s.

Entropy generation internal to the cylinder directly reflects in-cylinder temperatures. For engine loads below 9.0 N-m, adding *ESR* results in reducing in-cylinder temperatures, promoting more entropy generation. Beyond 9.0 N-m, however, the general rise in cylinder temperatures result in a decrease in entropy generation. Thus, for higher *ESR*s and high loads, this reduction in entropy generation and the relative consistency in availability flow from heat transfer and work extraction, results in a higher fraction of availability retention by the working fluid. Conversely, at low loads where temperatures drop below that of operation with ULSD, the rise in entropy generation leads to a decrease in availability retained by the exhaust gas. Of note, for high load operation, while any increase in exhaust availability is unused under normal dual-fuel operation, it presents a significant opportunity for the combination of syngas dual-fuel operation alongside waste heat recovery from the exhaust.

Overall, 2nd Law engine efficiencies are generally consistent regardless of *ESR*, or favor biodiesel usage, and can be seen in Figure 89. The 2nd Law Thermal Efficiency, in particular, is relatively steady for all *ESR*s, with a slight decrease seen at the higher engine loads where the engine is generally at its highest overall efficiency. In essence, the greater degrees of premixed combustion seen with syngas usage is offset by an increasing difficulty in maintaining constant and consistent combustion within the engine

cylinder, thanks to the high fraction of diluent gases within the syngas. On considering the 2nd Law Fuel Conversion Efficiency, it is also seen that syngas usage suffers from increasingly incomplete combustion, as numerous fuel species (particularly methane) survive the combustion process intact and are emitted in the exhaust gas.

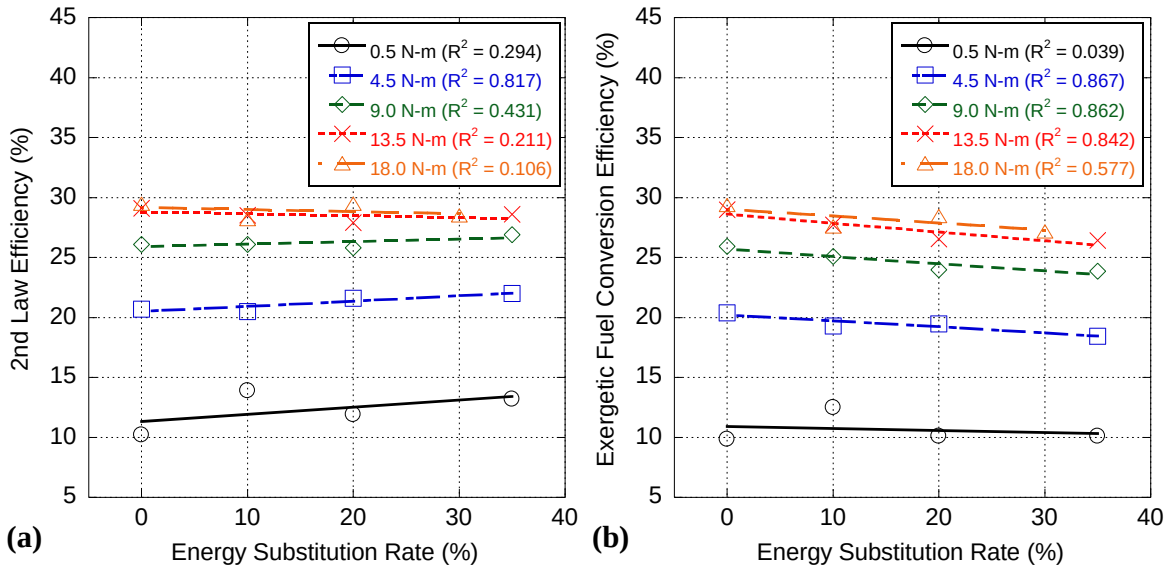

Figure 89. Exergetic Thermal (a) and Fuel Conversion (b) Efficiency for operation with biodiesel and three *ESR*s.

These efficiency changes (or lack of changes) can also be seen in the amount of fuel availability added to the engine cylinder as illustrated in Figure 90. Overall, thermal availability addition is consistent across all *ESR*s and loads tested, with a slight decrease in required thermal availability at 30% *ESR* and 18.0 N-m, thanks to the sheer difference in the degrees of premixed and diffusion-dominated combustion. When combustion inefficiencies are considered, the thermal availability is converted into total chemical availability added to the engine cylinder. Here, again, the differences in availability addition are relatively small across the various *ESR*s at each engine load. Unlike thermal availability, chemical potential availability converges at higher engine loads (where combustion is more complete), and more divergent for lower engine loads (where syngas struggles to combust in the lower-temperature environment).

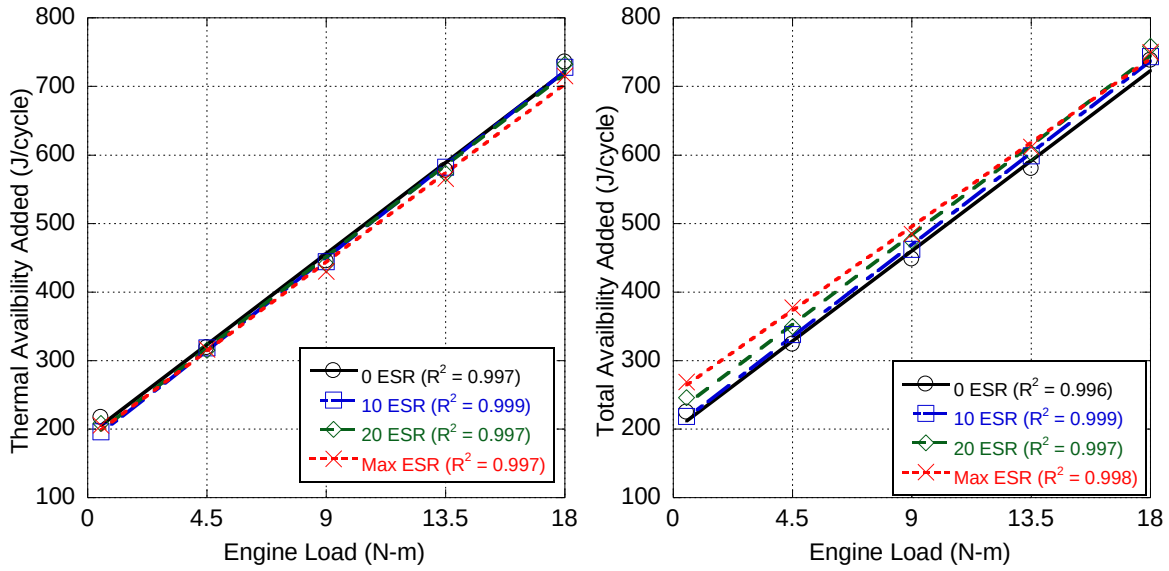

Figure 90. Thermal (a) and Total Chemical (b) Availability added to the cylinder for operation with biodiesel and three *ESR*s.

Overall, syngas-biodiesel dual fuel operation is reminiscent of and unlike dual-fuel operation with ULSD and CNG. While syngas usage displays the same (if less extreme) 1st Law behavior, the larger diluent fraction present in the syngas serves to counteract some of the behaviors (both positive and negative) seen in other dual-fuel combustion regimes. Most interestingly, syngas usage seems to be complementary to biodiesel, with increasing *ESR*s leading to relatively minor changes in engine efficiency from a 2nd Law perspective.

This is particularly useful from a control perspective; normally, dual-fuel operation above *ESR*s of 20% requires recalibration of the engine in order to maintain efficient operation, typically in the form of injection timing changes. Usage of syngas with biodiesel, however, presents only relatively small differences in operational characteristics, meaning an engine optimized to operate on biodiesel will not require significant re-optimization for dual-fuel operation with syngas. This trait may be particularly useful for biodiesel production facilities from a power production standpoint, as the facility will be able to rely on dual-fuel operation at arbitrary *ESR*s, depending on the relative availability and price of biodiesel and glycerol (or glycerol-based products). Furthermore, because the engines used in such a role would likely be optimized to operate at a single load and speed, engines employed for such power production

need not be upgraded to allow for electronic fuel injection, dramatically reducing the cost beyond an initial optimization to operate on biodiesel.

Finally, the only two significant changes with *ESR* from a 2nd Law perspective lies in the tradeoff between fuel conversion efficiency and exhaust availability. Usage of syngas will result in a lowered combustion efficiency and a higher exergetic (and energetic) consumption rate for the engine in order to offset the increasing fraction of diluent and inert species in the gaseous fuel along with the relatively high rate of survivability of some of the combustible gases (particularly, methane). For high loads, this is offset by a greater exhaust thermal availability due to lowered entropy generation within the cylinder, while at low loads it is accentuated by a loss in in-cylinder temperatures and a rise in entropy generation. This opens up syngas dual-fuel usage for waste heat recovery of the exhaust gas under high-load operation. However, this may reintroduce the need for electronic fuel injection, particularly for late fuel injection in order to keep exhaust temperatures and availability consistent across various syngas usage rates.

7.5 Conclusions

Dual-fuel combustion of biodiesel with syngas presents a novel means of providing power for a biodiesel production facility, given that syngas can be reformed directly from the glycerol byproduct of biodiesel production. From a diagnostic standpoint, syngas-biodiesel combustion is noted for its increased degree of premixed combustion at high loads, and a resulting higher peak pressure, as well as worsened performance at low load where the engine struggles to combust the syngas mixture. However, from an exergetic standpoint, syngas usage with biodiesel is difficult to discern directly from biodiesel-only usage, as both fueling modes have similar degrees of availability transfer by work extraction and heat transfer, as well as similar exergetic fuel consumption rates. This is largely due to two competing effects. First, the hydrogen- and methane-rich gas with a higher energy and exergy content is more prone to prompt, premixed, and higher-temperature combustion thanks to having sufficient time to mix prior to the initiation of combustion. However, this is offset by the high amount of diluent species present in the syngas (particularly carbon dioxide) that serve to stymie combustion, lowering efficiency overall. As with

more conventional dual-fuel combustion with ULSD and CNG, dual-fuel biodiesel-syngas combustion is marked with a decrease in exergetic fuel conversion efficiency as gaseous fuel usage rises, although this reduction is less significant than for other dual-fuel regimes. Finally, the major difference between the two modes of combustion is in the availability retention of the exhaust. At low loads, low temperatures caused by struggling combustion of syngas result in heightened entropy generation, and thus lower availability retention, whereas at higher loads the increased temperatures of syngas combustion serve to keep entropy generation within the cylinder low, and subsequently raise the ability of the exhaust gas to retain availability.

With respect to control, biodiesel-syngas combustion offers relatively small deviations in performance compared to conventional biodiesel combustion, particularly from the standpoint of the 2nd Law of Thermodynamics. This shows that biodiesel-syngas fueling modes may be receptive to arbitrary changes in syngas usage rates (which are highly dependent on the amount of available glycerol to the end user). As a result, engines optimized for biodiesel usage may require minimal (if any) reoptimization for biodiesel-syngas usage, to the point where recalibration may not be necessary. The only major exception could be if waste heat recovery systems are installed to make use of the relatively high exhaust availability, at which point late injection of biodiesel may be required to maintain consistent exhaust temperatures and availability.

Chapter VIII: An Overview of Second Law Behavior for Compression Ignition Engine Combustion

Material published as "Availability Analysis of Alternative Fuels for Compression Ignition Engine Combustion," International Congress of Automotive and Transport Engineering (AMMA 2018), September 30th, 2018

8.1 Abstract

Modeling of engine heat release from in-cylinder pressure is a common practice for characterizing engine combustion. Fuel property variation induces changes in engine performance, which can be categorized through heat release modeling. One under-utilized form includes an availability analysis that links changes in fuel properties to the amount of availability extracted as work or lost through inefficiencies. Here, a diagnostic heat release model is used to catalogue both the 1st and 2nd Law behavior of numerous alternative fuels. Conventional engine combustion using diesel, biodiesel, renewable jet fuel, and waste-plastic derived diesel are studied, alongside dual-fuel operation of compressed natural gas (with diesel) and synthesis gas (with biodiesel), allowing for the exploration of combustion with respect to changing fuel properties. In particular, more ideal fuel mixing is generally reflected directly in the 2nd Law efficiency. However, high viscosities largely result in a later availability addition that is not extracted as work. While this availability would be wasted at exhaust blowdown, deliberately increasing later temperatures may be useful if paired with exhaust heat recovery systems. Overall, the 2nd Law model presents these tradeoffs more clearly than a traditional 1st Law analysis; thus, its further use may be warranted in concert with advanced engine combustion modes.

8.2 Introduction

The effects of fuel properties on combustion are a central aspect of engine testing and a common tool for this exercise is to utilize the 1st Law of Thermodynamics to create an engine-out rate of heat release (RHR) model [13]. In particular, the 1st Law analysis is useful for identifying the relative amounts of premixed- and diffusion-dominated combustion. A lesser-utilized alternative is to employ the 2nd Law

of Thermodynamics often known as an availability analysis. This model is similar to the 1st Law analogue, but with the important addition of entropy generation [12]:

2nd Law Rate of Change of Availability	$\frac{dA_g}{d\theta} = \frac{dA_c}{d\theta} - \left(\frac{dA_w}{d\theta} + \frac{dA_{ht}}{d\theta} + \frac{dA_{ir}}{d\theta} \right)$	(48)

where dA/dθ refers to the rate of change of availability with respect to engine crank angle, and the subscripts correspond to the availability retained by the exhaust gas (g), added by combustion (c), extracted as work (w), lost by heat transfer through the cylinder walls (ht), or destroyed by internal irreversibilities (ir) by entropy generation [12].

Generally, the 2nd Law analysis is often passed over in favor of the relatively simpler 1st Law RHR analysis. For compression ignition (CI) engines, this is at least partly due to the relative consistency of engine combustion, and the degree to which conventional CI combustion is understood. However, different fuels will often result in changing performance due to dissimilar fuel properties [25]. The most common example of this is in exchanging biodiesel for ultra-low sulfur diesel (ULSD), where the increased viscosity of biodiesel generally inhibits fuel vaporization and atomization, while its higher Cetane Number (CN) and greater oxygen content results in a shortened ignition delay [13, 19]. In turn, this requires re-optimization of the engine's injection strategy to maintain peak efficiency [16]. While this recalibration was relatively difficult to achieve with older mechanical injection systems, the advent of electronic injection systems has made CI fuel-flexibility significantly more feasible [20]. Moreover, this opens up an exploration of fuels with more divergent properties. Included in this are recycled or alternative renewable fuels. For instance, the pyrolysis of waste plastic products can be used to create a liquid hydrocarbon fuel similar to petroleum diesel [21]. Furthermore, while biodiesel itself cannot generally be used in aircraft turbines, the feedstocks used to create biodiesel can alternatively be run through a hydrotreating process to generate an analogue to jet fuel [25].

Finally, electronic injection has enabled control over CI engine combustion to allow for advanced usage of gaseous fuels [6]. Normally, methane-rich fuels (e.g., compressed natural gas aka CNG) cannot be utilized as-is in a CI engine without modifications or new hazards [6]. As an alternative, gaseous fuels

can be used in a relatively unmodified CI engine through dual-fuel combustion, whereby fuel is added to the intake and ignited by a direct-injected liquid fuel, reducing efficiency but lowering fueling costs [6]. Dual-fuel combustion also presents the ability to reutilize waste products and unique feedstocks, namely synthesis gas (syngas) derived from the glycerin co-product of biodiesel production [32, 33].

Regrettably, the properties of these alternative fuels can vary widely preventing direct integration into existing systems. Specifically, fuels derived from vegetable oils generally see high amounts of variation depending on the feedstock utilized [25, 103]. Similarly, waste plastic derived diesel is prone to vary based on the methods and mixture of plastics employed in the pyrolysis process [21]. Furthermore, syngas is subject to feedstock and production differences [32], and even established products (e.g., CNG) will often deviate between regions [6]. Overall, this leads to difficulties in fuel studies, as engine researchers must utilize a model that is receptive to these changes.

As a result, this chapter explores the use of a diagnostic 2nd Law model to demonstrate the diverse effects of fuel properties on engine combustion while highlighting how it is able to identify the phenomena associated with these properties. In particular, variations in fuel density, viscosity, CN, and energy content and their relation to engine performance are observable through the lens of the 2nd Law model going beyond what is achievable with the 1st Law analysis alone.

8.3 Experimental Setup and Procedure

The investigation of these various fueling modes was accomplished on a modified naturally-aspirated Yanmar L100v air-cooled single-cylinder CI engine, with a compression ratio of 21.2 and a displacement of 435 cubic centimeters. For brevity, the information included herein is that which is most relevant to generalized operation and testing, and a thorough description (including part numbers) can be found in prior work [20]. The mechanical fuel injection system has been replaced with an electronic system, including a Bosch MS15.1 Diesel ECU, allowing injection variation at a resolution of 0.02 degrees of crank angle (DCA), and pressurized by an externally-powered Bosch CP3.2 fuel pump. The engine's built-in Exhaust Gas Recirculation system has been blocked. Speed and load control of the

engine is accomplished via a DyneSystems, Inc. Dymond Series 12 hp alternating current dynamometer, and engine torque is logged with a FUTEK torque transducer. The flowrate of intake air is measured via a Merriam laminar flow element and an Omega differential pressure transducer. Liquid fuel consumption is established by a Micro-Motion Coriolis flow meter. In-cylinder pressure is measured using a pressure transducer and crank-angle encoder at a resolution of 0.2 DCA for 60 consecutive thermodynamic cycles. The liquid fuels utilized herein are soybean biodiesel, renewable hydroprocessed jet fuel, and a fuel derived from waste plastic, along with standard ULSD. These fuels present a wide variety in fuel characteristics as illustrated in Table 1 [7, 21, 25, 32].

For dual-fuel testing, two gaseous fuels were chosen (see Table 2): a methane-rich CNG mixture relying on ULSD for a pilot ignition [6, 7] and a hydrogen-rich mixture mimicking syngas derived from glycerin with a soybean biodiesel pilot [32]. Gaseous fuel is fed into the system through a Brooks thermal mass flow controller at 50 psi_g from compressed gas cylinders [20], and is then added to the intake via a mixing box upstream of the intake to produce a relatively homogeneous fuel-air mixture [74]. Fuel flow is categorized through the relative flowrates of gaseous and liquid fuels on an energy-rate-basis, known as the Energy Substitution Rate (*ESR*) [6, 7]:

Energy Substitution Ratio	$ESR = \frac{\dot{m}_g Q_{LHV_g}}{\dot{m}_g Q_{LHV_g} + \dot{m}_p Q_{LHV_p}}$	(49)

where the term $\dot{m}$ refers to the mass flow rate, Q_{LHV} indicates the lower heating value, and g and p pertain to the gaseous and liquid (pilot) fuels, respectively. For brevity, this paper focuses on maximal gaseous fuel usage achievable in the flow controller; i.e., 85% *ESR* for CNG-ULSD operation and 30-35% *ESR* for Syngas-Biodiesel operation [6, 7, 27].

In all testing, combustion timing was normalized by shifting the liquid fuel injection timing to align the peak pressure with that of operation with ULSD [16]. All testing was accomplished under steady-state conditions at 1800 RPM. Engine performance data were logged over the course of 120 seconds at a sampling rate of 20 Hz. The engine data presented herein correspond to test results at increments of 25% of engine load, ranging from 0% (idle) to 100% of rated engine load (18.0 N-m).

However, pressure and 1st Law behavior is limited to 50% and 100% of rated load, as these loads demonstrate both premixed- and diffusion-dominated combustion, respectively [13]. Furthermore, the performance data were used to calculate time-averaged testing results, error analysis, and to generate 1st and 2nd Law Heat Release information [12, 13].

Table 35. Liquid Fuel Thermodynamic Properties [7, 21, 25, 32].

Fuel Characteristic	Ultra-Low Sulfur Diesel	Soybean Biodiesel	Renewable Jet Fuel	Waste Plastic Synthetic Diesel
Density [kg/m^3]	837.58	875.58	758.54	800.70
Kinematic Viscosity [cSt]	2.740	4.218	1.542	2.970
Cetane Number [-]	48.61	48.10	68.80	71.88
Lower Heating Value [MJ/kg]	45.60	39.88	46.25	46.29

Table 36. Gaseous Fuel Thermodynamic Properties [6, 32].

Constituent Property	Compressed Natural Gas	Hydrogen-Rich Syngas
Hydrogen [%]	-	28.70
Methane [%]	92.00	5.10
Ethylene [%]	-	4.30
Ethane [%]	3.50	2.30
Propane [%]	0.80	-
Isobutane [%]	0.15	-
Nitrogen [%]	2.85	25.90
Carbon Monoxide [%]	-	16.00
Carbon Dioxide [%]	0.70	17.70
Heating Value [MJ/kg]	51.62	10.75

8.4 Results and Discussion

The pressure traces at 50% and 100% of rated load can be seen in Figure 91. At both loads, ULSD and biodiesel produced analogous pressure behavior, thanks to their respectively similar fuel characteristics. Increasing the CN, as seen with the waste plastic and renewable jet fuels, lessened premixed combustion; hence, lower peak pressure. Finally, the dual-fueling regimes displayed similar or worsened pressure behavior at lower loads, and universally better performance at higher loads. This was due to two competing effects of the gaseous fuels; a difficulty in igniting, even in the high-temperature

environment, and a preference for large degrees of premixed combustion once ignited thanks to the more homogeneous conditions in the cylinder.

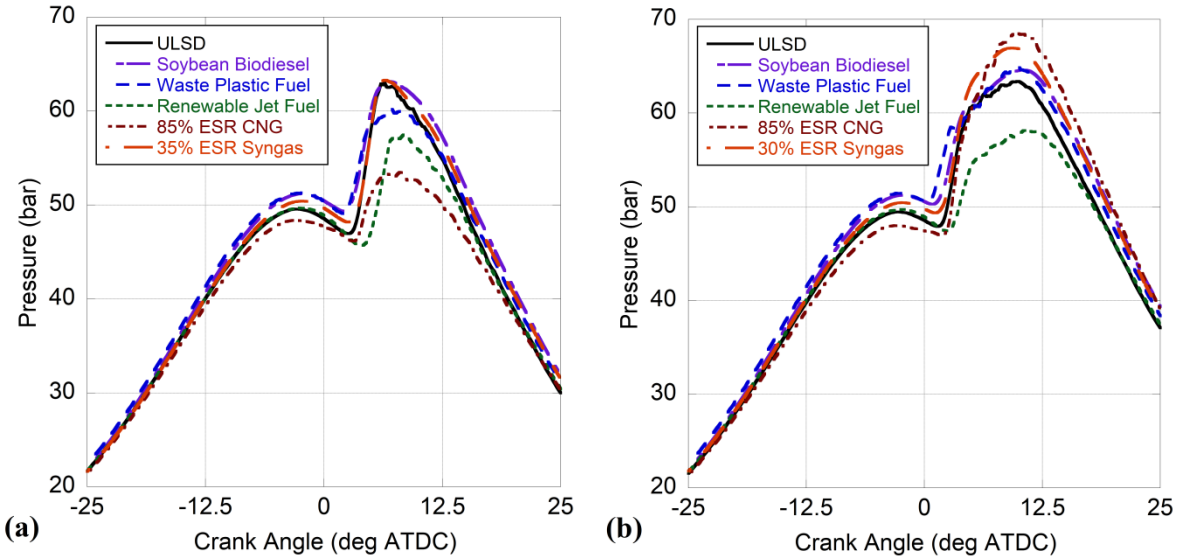

Figure 91. Measured In-Cylinder Pressure Traces for Operataion at (a) 50% and (b) 100% of rated load.

The computed RHR for operation at 50% and 100% engine load are shown in Figure 92, and largely match the behavior seen in the pressure results. Specifically, soybean biodiesel performs most similarly to ULSD, with only a slightly earlier and lower premixed spike, and somewhat worsened diffusion burn (owing to its higher viscosity inhibiting fuel breakup). Comparatively, the renewable jet and waste plastic fuels experienced lower premixed spikes. Here, the high CNs of these fuels may result in them igniting too quickly, prior to there being enough fuel in the cylinder to burn with a significant premixed spike. In the case of the renewable jet fuel, this is worsened by its respectively low viscosity that shortens the ignition delay. Finally, both dual-fuel tests produced higher premixed spikes, owing to the increased fuel-air homogeneity in-cylinder; however, the CNG-ULSD testing illustrates a growth in diffusion burn at high load as the engine struggles to combust large amounts of methane.

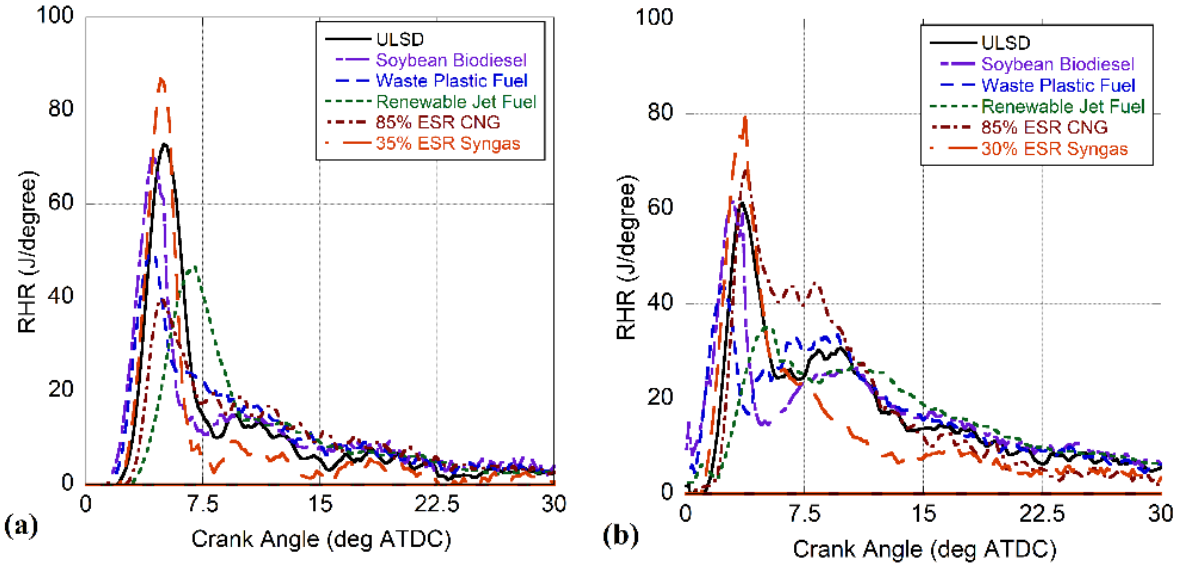

Figure 92. First Law RHR for operation at (a) 50% and (b) 100% of rated load.

With respect to the 2nd Law analysis, the efficiency (Figure 93a) primarily reflects the ease of fuel/air mixing, with the least viscous liquid fuel (renewable jet) and most homogeneous fueling mode (CNG-ULSD) providing the best operation; whereas, the reduced energy content and higher viscosity of biodiesel results in (largely) the lowest efficiency. In regards to heat transfer losses, cooler combustion leads to fewer losses as less thermal availability leeches out of the cylinder (Figure 93b). For conventional or near-conventional (i.e., low-ESR dual-fuel) combustion, the reduced temperatures principally result in more availability destruction within the cylinder (Figure 93c). Generally, the authors have found it is advisable to have hotter in-cylinder temperatures to retain availability, which will offset losses from heat transfer [12, 27, 118]. The final pathway for losses is the availability retained by the working fluid in Figure 93d. Here, higher combustion temperatures while increasing the energy produced during the expansion phase (i.e., diffusion burn) results in a greater amount of availability retention by the exhaust that is subsequently lost to the atmosphere without being utilized. However, if the engine were to be paired with an exhaust heat recovery system [180], this enhanced exhaust availability could promote a secondary work extraction.

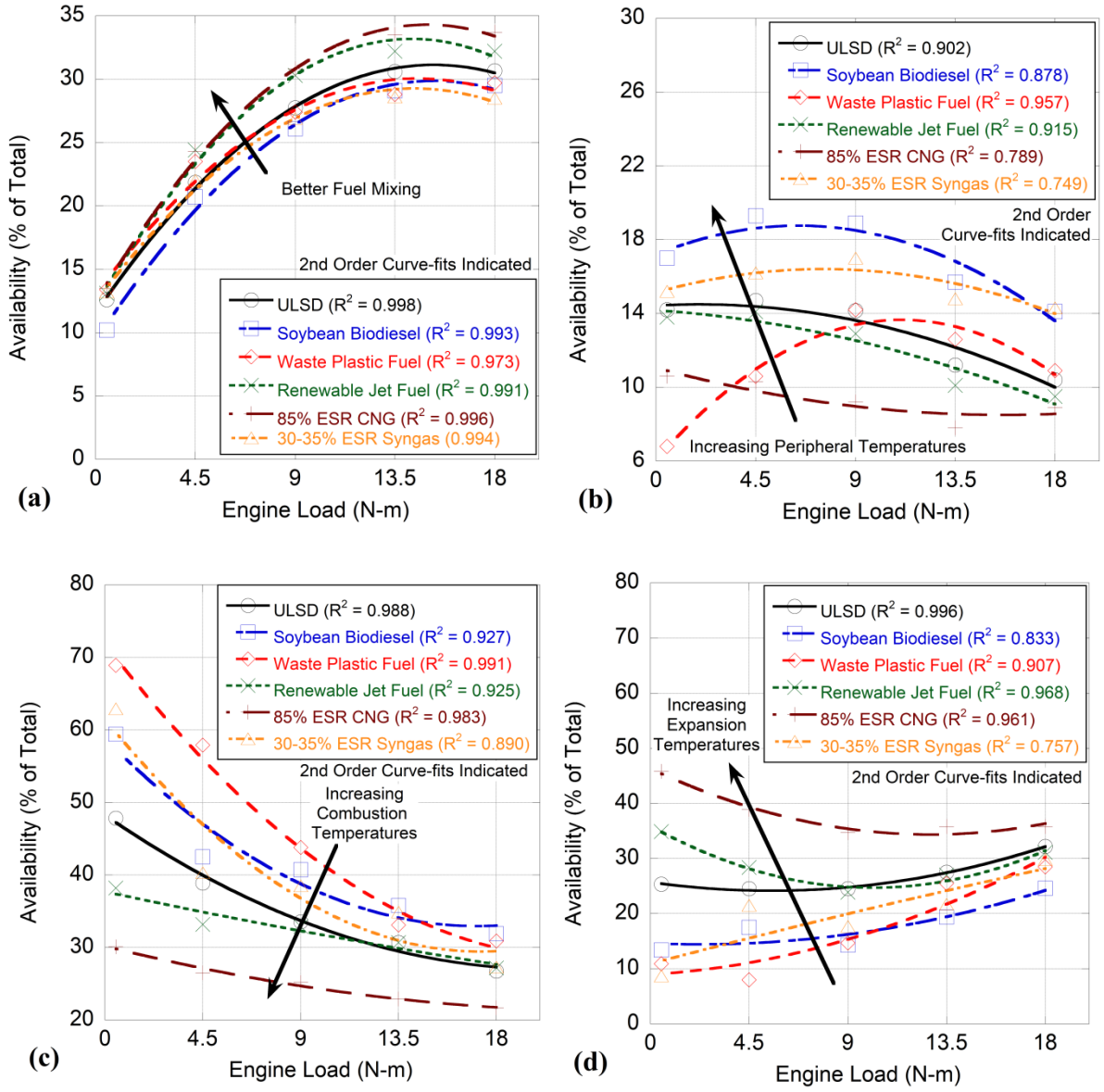

Figure 93. Percentages of Total Availability (a) Extracted as Work (2nd Law Efficiency), (b) Lost to Heat Transfer, (c) Lost to Entropy Generation, or (d) Retained by the Exhaust Gas.

Of note, high-*ESR* dual-fuel operation sees a trend that seems to contradict the prior discussion; i.e., lower entropy generation and reduced heat transfer losses. This type of operation may result in flame propagation; thus, flame quenching in the periphery of the cylinder [7, 18, 30]. This could result in relatively high local temperatures (reducing entropy generation) and low global temperatures (mitigating heat transfer losses). Furthermore, decreases in heat transfer losses have been observed in RCCI combustion as opposed to other low-temperature combustion modes, thanks to the relative inhomogeneity

of RCCI operation (particularly in comparison to HCCI) [172, 173]. This highlights the benefits of a 2nd Law analysis that is not immediately seen in a 1st Law examination. Specifically, not only do dual-fuel modes promote higher degrees of premixed combustion (1st Law), but they also may be more adept at retaining unused availability in the working fluid (2nd Law) in some cases, making them more attractive than liquid fuels if exhaust heat recovery is considered.

8.5 Conclusions

The variety of fueling modes for CI engines necessitates a broader understanding of the links between fuel properties and combustion phenomena. In particular, fuel viscosity, energy content, CN, and fuel density all impact the degree of premixed- and diffusion-dominated combustion. Furthermore, advanced operational modes (e.g., RCCI) have pushed CI engines far from their designed combustion regimes. While traditional 1st Law heat release modeling remains a vital tool, more diagnostic options are required. Hence, availability modeling provides a means to measure engine efficiency in a manner not present in the 1st Law model. Overall, 2nd Law efficiency is tied to the ability of the engine to produce a homogeneous fuel-air mixture, and this homogeneity can be increased either through lowered fuel viscosity to promote fuel breakup, or by using gaseous fuels to encourage earlier mixing. Furthermore, combustion temperature is generally reflected in two competing segments of the 2nd Law model. Specifically, higher temperatures promote heat transfer losses while also maintaining a greater temperature difference between the cylinder and the ambient; hence, limiting losses due to internal irreversibilities. Moreover, raised temperatures during expansion (from diffusion burn) can lead to higher amounts of exhaust gas availability. Finally, dual-fuel operation at high *ESR*s presents unique opportunities by enhancing premixed combustion. However, this may lead to flame propagation and quenching subsequently creating locally high temperatures (limiting entropy production and retaining availability) while also having globally low temperatures (minimizing losses to heat transfer). As a result, dual-fuel usage may promote a greater overall efficiency, particularly if paired with exhaust heat recovery. Here, this effect is only observed using 2nd Law modeling.

Chapter IX: Future Utilization of Exergy Modeling for Internal Combustion Engines

Some material published as "Availability Analysis of Alternative Fuels for Compression Ignition Engine Combustion," Fourth International Congress of Automotive and Transport Engineering, Accepted June 22nd, 2018

9.1 Introduction

The 2nd Law model described over the previous chapters presents a viable method for the analysis of combustion behavior through the measurement of an in-cylinder pressure trace. This methodology can be used in-tandem with the more traditional 1st Law model, or on its own. The 2nd Law model's inherent strength is the inclusion of the entropy generation term, which allows for combustion inefficiencies to be identified and explored, particularly when such features would normally be hidden within the 1st Law heat release analysis that only tracks the quantities of energy involved, and not the relative usefulness of this energy.

At its most basic level, the 2nd Law model is primarily useful for exploring the relationships between fuel properties and thermodynamic efficiency. The relative changes in energy density, viscosity, oxygenation, or other characteristics can have significant effects on the quality of combustion. These effects are expressed through the transformation of exergy from chemical potential to thermal availability, and then through extraction as work, loss as heat transfer, destruction due to entropy generation, or retention by the exhaust gas. The relationships discovered are summarized as follows.

9.2 Liquid Fuel Properties

Of all the various fuel properties, none is as overwhelming in terms of its importance as viscosity. Fuel viscosity is inherently related to the process of fuel breakup and atomization, and corresponds to the physical half of the greater process of ignition delay. Higher viscosities inhibit fuel breakup, and this hindering leads to decreasingly effective fuel mixing and combustion. This in turn leads to a shift in combustion away from the more efficient and energetic premixed phase into the mixing-controlled diffusion burn phase. From a 2nd Law perspective, this results in a general shift towards less efficient

combustion, and lowered exergetic thermal efficiencies since energy is released later in the expansion process where the engine struggles to extract it effectively. At the same time, a delayed heat release results in a warmer in-cylinder environment, and because the hot bulk gas cannot have its energy easily extracted, it remains relatively warm late into the cycle. As a result, entropy generation within the bulk gas falls, and heat transfer rises. Finally, while these two effects serve to counter each other, the decrease in entropy generation is generally more significant, and as a result, the exhaust gases retain a greater availability for elevated viscosity fuels. Therefore, while higher viscosity fuels are less optimal for conventional work extraction, they are (somewhat counterintuitively) useful for situations in which the exhaust gas must retain availability (i.e., exhaust gas waste heat recovery).

In contrast, lower viscosity fuels will generally perform more efficiently when operated in a conventional manner. A reduced viscosity eases fuel breakup, resulting in higher degrees of premixing, and more energetic combustion. In addition, because the period of high heat release (and larger temperatures) is relatively short, heat transfer related exergy losses are less significant. The engine also encounters a lower level of diffusion burn; thus, cooler temperatures and a higher entropy generation within the cylinder. However, because work extraction favors high pressures and temperatures near TDC, cooler temperatures later in the combustion process are less of a concern.

Energy density also influences the injection event while resulting in phenomena resembling the effects of viscosity. Because injection is done on a volumetric basis, more energy-dense fuels make it relatively easier to deliver higher amounts of chemical potential energy and exergy into the cylinder. This interacts with fuel breakup and ignition delay. Specifically, the lower a given fuel's ignition delay period, the less time the engine will have between the start of injection and the onset of combustion. Because the fuel that combusts in the premixed spike is, by definition, only fuel that is able to vaporize and mix into the bulk gas prior to combustion, late-injected fuel will combust in the diffusion phase. Thus, fuels with higher energy densities will result in lower amounts of diffusion burn, and greater amounts of premixed combustion. Hence, they will encounter enhanced exergetic efficiencies in the same way as lower-

viscosity fuels. In contrast, fuels with lower energy densities have elevated degrees of diffusion burn, lessened exergetic efficiency, and more availability retention by the exhaust gas.

Cetane Number (CN), and ignition delay in general, can produce variable outcomes. Whether or not higher CNs raise or lower efficiency is dependent on its interaction with other fuel properties. Specifically, short ignition delays can cause the fuel to begin combustion well before enough fuel can be injected to make the premixed combustion event large enough to be efficient; thus, the engine will rely mainly on diffusion burn to meet load. Similarly, longer ignition delays can alternatively lessen (by inhibiting the ignition process until too late in the expansion stroke), or raise premixed combustion (by giving the engine more time to inject and mix liquid fuel, resulting in a greater energetic ignition event). Generally, increasing premixed combustion will lead to more exergetically efficient combustion; whereas, a greater level of diffusion burn will lower efficiency, but raise retention of availability in the exhaust.

Fuel oxygenation (common in biodiesels) results in higher combustion efficiencies overall, and is advantageous to all segments of the exergy analysis. Oxygenated fuels will result in enhanced amounts of premixed combustion by growing the amount of oxygen available, even in the normally oxygen-starved core of the injection fuel spray. In addition, oxygenated fuels will result in larger late-stage temperatures in fuels with a high-degree of diffusion burn, with the oxygen content serving to aid mixing and promote consumption of fuel molecules within the cylinder. As a result, oxygenation is particularly useful for converting chemical potential availability to thermal availability, reducing entropy generation, and increasing retention of availability in the working fluid.

9.3 Dual-Fuel Combustion and Gaseous Fuels

Dual-fuel combustion results in a different set of phenomena, some of which are counterintuitive and less intuitive. However, these can be clearly exposed through the 2nd Law analysis. In general, dual-fuel combustion is dependent more on engine load than on fuel properties (including the properties of the liquid pilot fuel).

At lower loads, dual-fuel operation is noted for its significantly difficult ignition and combustion, generally due to the usage of methane or diluent species like carbon dioxide or water vapor. These species serve to soak up the thermal energy of premixed combustion (and in the case of methane, this energy absorption occurs without ignition of the fuel molecule). As a result, at low loads, the engine may struggle to maintain combustion, lowering the amount of fuel heat release and stymieing further combustion. From a 2nd Law perspective, this leads to a universal decrease in fuel conversion efficiency.

At higher loads, dual-fuel operation provides for larger degrees of premixed combustion. Here, the temperature limitations are largely overcome (at least in the premixed phase), and the high heat release of the gaseous fuels (particularly hydrogen and methane) promotes a relatively thorough burn of fuel. This higher level of premixed combustion then leads to a greater 2nd Law exergetic efficiency, in a manner similar to lowered viscosity in liquid fuels. However, high amounts of fuel-air premixing leads to a change in combustion behavior, as the engine shifts away from conventional diesel combustion and more towards potential flame propagation and flame quenching behavior. The result of this is universally improved efficiency as a function of *ESR*. Flame propagation results in an enhanced level of quenching specifically on the periphery of the cylinder, serving to insulate the warmer temperatures in the center of the cylinder from the cooler walls. This simultaneously reduces heat transfer losses, while also decreasing entropy generation losses, resulting in an increase in exhaust gas availability. As a result, dual-fuel operation presents a high potential exergetic efficiency; not only is the engine operating more efficiently thanks to the increase in premixed combustion, but much of the unused availability is retained in a form that is still usable for work extraction assuming proper systems (e.g., turbocharging, waste heat recovery) are employed.

9.4 Potential Exploration of Low Temperature Combustion

Currently, research on CI engines is increasingly focused towards Low Temperature Combustion, or LTC. This combustion regime is noted for its high thermal efficiencies, and the ability to operate without producing significant amounts of oxides of nitrogen (NO_x) or particulate matter (PM). Beating

this NO_x-PM tradeoff is of immense importance to CI engines, as it overcomes the two most prominent emissions species, which are also the most troublesome to clean from the engine exhaust. While this comes at the expense of relatively low combustion efficiencies, the resulting carbon monoxide and hydrocarbon emissions may be able to be handled more readily with existing emissions control systems. Thus, achieving and understanding LTC in CI engines is of immense interest for future research.

Two forms of LTC combustion are generally utilized in CI engines; premixed-charge compression ignition (PCCI) and reactively controlled compression ignition (RCCI). PCCI is generally achieved through the early injection of liquid fuel (often between 20 and 80 degrees of crank angle ahead of the injection timings used for conventional combustion). Given modern electronic injection systems, PCCI is (generally) more easily attempted, as it relies on the same early injection techniques already used to limit combustion noise and CI knock. However, PCCI combustion is somewhat difficult to control as the precise timing of combustion is dependent on the interplay of fuel viscosity, energy density, and ignition delay-related phenomena (as discussed earlier). Often, this results in PCCI combustion being dependent on specific ignition delays. Since ignition delay is itself a function of engine compression ratio (whereby higher compression ratios lead to shorter ignition delays), this presents a functional ceiling on engine compression ratio (and turbocharging) that can reliably achieve PCCI. At present, this compression ratio issue can only be reasonably attacked using Exhaust Gas Recirculation (EGR), which generally increases ignition delay.

The alternative of RCCI is often more appealing from a control perspective, but comes with the important caveat of how the engine is fueled, as it requires gaseous injection (typically in the intake) in conjunction with direct injection. However, this is not significantly different from more conventional dual-fuel combustion except gaseous fuel is injected early, allowed to mix properly, and then lit with a pilot injection of a conventional liquid fuel. Thus, RCCI combustion gets around the compression ratio ceiling; while it does not affect ignition delay itself, it reduces the amount of liquid fuel that is required, easing the ability of the engine to deliver and mix a sufficient amount of liquid fuel prior to ignition. This also removes the direct need for EGR, simplifying engine control.

From a 2nd Law perspective, LTC is characterized by higher exergetic efficiencies and lowered heat transfer losses, as befits highly-premixed combustion regimes. Furthermore, RCCI combustion is also characterized by increased availability retention by the exhaust gas, thanks to decreased entropy generation. This marked decrease in entropy generation can be vital for establishing if LTC combustion is occurring at all, as one of the normal markers for LTC (decreased PM emissions) is not readily apparent. Thanks to the lack of liquid fuel injection, PM production is decreased significantly regardless of the specific combustion regime; hence, a reduction in PM emissions cannot be used to infer that LTC is taking place. The result of this is that *exploration of RCCI combustion requires exergy modeling*, in addition to more conventional emissions measurements and a traditional 1st Law analysis.

Furthermore, an existing area of research is in the relatively vague boundary between conventional diesel combustion and PCCI, and also between dual-fuel combustion and RCCI. This is doubly true at higher compression ratios, due in part to the relative rarity of research engines that are simultaneously capable of high compression ratio operation and dual-fuel combustion. As the 2nd Law model is inherently required to assess LTC combustion, it is also necessary for exploring these boundary regions.

9.5 Waste Heat Recovery and Exergetic Efficiency

A final usage for 2nd Law modeling is in the integration of waste heat recovery systems alongside CI engines. As a general rule of thumb, the efficiency of all heat engines (including the Organic Rankine Cycle systems associated with heat recovery) is inherently tied to temperature difference between the exhaust gas and the environment; the higher this difference, the more energy/exergy can be extracted. In a more specific sense, however, the actual effectiveness of exhaust waste heat recovery systems is tied to the exergy content of the working fluid. Thus, while temperature differences may be sufficient for optimizing a given fuel, comparison between multiple fuels (and fueling modes) must account for numerous separate fuel properties and combustion phenomena. Therefore, exergy accounting is required to accurately compare and contrast these operational changes.

The use of exergy modeling in this manner is easiest to express with varying degrees of premixed versus diffusion combustion. Normally, premixed combustion is the most advantageous for CI engine operation, and the resulting growth in exhaust availability from diffusion burn is to be avoided, as it will normally be wasted. However, minimizing diffusion burn lowers exhaust temperatures, reducing the amount of exergy that can be extracted from waste heat recovery. As a result, for optimal exergy extraction from the combined system, it may be necessary to encourage inefficient combustion if it assists in raising the system's exergetic efficiency. Thus, exergy modeling can be utilized to maximize diffusion-dominated combustion without unnecessarily impacting premixed combustion, and can help identify characteristics in certain fuels (e.g., high viscosity and oxygenation in biodiesels) that make them more advantageous for such systems. For example, it may be useful for an engine to deliberately sacrifice efficiency and premixed combustion in order to maintain exhaust availability through a diffusion-dominated combustion, maintaining high exhaust availability as the exhaust gas passes into a turbine or heat exchanger directly coupled to the engine exhaust; the loss of engine efficiency may be a necessary sacrifice to promote the efficiency of the combined system.

9.6 Conclusions and Future Work

The 2nd Law Heat Release model, as described, is ready for more advanced analysis, and reliably and accurately describes a wide range of in-cylinder behaviors. In particular, the 2nd Law is instrumental in highlighting the efficacy of fuel breakup on combustion, and also how fuel breakup can be intentionally aided (or hindered) to promote certain emissions, combustion regimes, and pathways of availability retention or loss. Overall, the primary fuel quantities of note are viscosity and energy density, with viscosity playing a much more involved and profound role on affecting all in-cylinder behavior, from performance and emissions, and from the 1st Law to the 2nd.

With respect to future work, the most promising avenue is the potential to explore the border between conventional and low-temperature combustion, particularly with respect to PCI/PCCI combustion (with EGR usage), as well as RCCI combustion with high amounts of gaseous fuel, and

(potentially) HCCI combustion seen in spark-ignited engines (which undergoes a very similar combustion regime to dual fuel combustion). In addition, the 2nd Law model will likely be an instrumental part of any future work on exhaust waste heat recovery or Organic Rankine Cycle-based systems, due to the limitations placed on such systems based on the availability present in the engine exhaust, and not simply the temperature and thermal energy content of the exhaust.

Next, some degree of filtering of the input pressure data may be required. Generally, heat release programs encounter numerical and computational instability caused by oscillations in the pressure trace (i.e. knocking combustion), where the pressure oscillations produce large variance in the in-cylinder temperature and the 1st Law energy balance. If these oscillations are too large with respect to the resolution of the pressure trace, the instability results in the program being unable to solve the 1st Law balance, and the model fails. Thus far, the amount of knocking combustion on the Yanmar L100V has been relatively low, and the resolution is sufficiently high, thus the problem has not been significant. However, in testing with the AVL 5402 engine, and in some more recently diagnostic testing of attempted PCI combustion (not included in this work), knock has been observed to be significantly higher, which may (in some cases) warrant some degree of filtering in order for the pressure data to be acceptable for the heat release model. This filtering can be achieved using a slight variation of the knock filter discussed in Chapter 4, as the same phenomena that Chapter 4 seeks to isolate and understand are the cause of the error. Thus, applying a low-pass filter set to approximately 4 kHz should be sufficient to remove the oscillations caused by engine knock from the pressure trace.

Finally, it is a logical extension to include the effects of cylinder blow-by. Up to now, cylinder blow-by has been neglected from the model as it forms a relatively small source of error in comparison to primary measurement errors and uncertainties that have been encountered thus far. However, there exist some engines with significantly higher degrees of cylinder blow-by which can prove to be problematic to the heat release model, typically resulting in a massive underestimation of the in-cylinder temperatures; the mass in the cylinder is overstated, the pressure, volume, and speciation are all either known or easily established, and so the ideal gas law will "compensate" by reducing temperatures potentially hundreds of

Kelvin below their true values. A solution for this is more in-depth as it requires a rewriting of some of the core functions of the code (as they were all written with the core assumption that cylinder blow-by is negligible), but this rewrite should be achievable without significantly altering the core thermodynamic basis of the 1st or 2nd Law models described previously.

References

1. Heywood, J.B., *Internal combustion engine fundamentals*. Vol. 930. 1988: Mcgraw-hill New York.
2. Gatowski, J.A., et al., *Heat Release Analysis of Engine Pressure Data*, 1984, SAE International.
3. Pundir, B., *Engine emissions: pollutant formation and advances in control technology*. 2007: Alpha Science International, Limited.
4. Su, T., et al., *Experimental and numerical studies of high pressure multiple injection sprays*, 1996, SAE Technical Paper.
5. Mangus, M., et al., *Investigating the Compression Ignition Combustion of Multiple Biodiesel/ULSD Blends via Common-Rail Injection.* Energy, 2015. 89: p. 932-945.
6. Langness, C., J. Mattson, and C. Depcik, *Moderate Substitution of Varying Compressed Natural Gas Constituents for Assisted Diesel Combustion.* Combustion Science and Technology, 2017. **189**(8): p. 1354-1372.
7. Mattson, J.M.S., C. Langness, and C. Depcik, *An Analysis of Dual-Fuel Combustion of Diesel with Compressed Natural Gas in a Single-Cylinder Engine*, 2018, SAE International.
8. Langness, C.N., *Effects of Natural Gas Constituents on Engine Performance, Emissions, and COmbustion in Compressed Natural Gas-Assisted Diesel Combustion*, 2014: KU ScholarWorks.
9. Mattson, J.M.S., C. Langness, and C. Depcik, *Modified Heat Release Analysis for Diesel-Assisted CNG Combustion*, 2015, SAE International.
10. Mattson, J.M.S., M. Mangus, and C. Depcik, *Efficiency and Emissions Mapping for a Single-Cylinder, Direct Injected Compression Ignition Engine*, 2014, SAE International.
11. Mattson, J.M.S. and C. Depcik, *Emissions–calibrated equilibrium heat release model for direct injection compression ignition engines.* Fuel, 2014. **117, Part B**(0): p. 1096-1110.
12. Mattson, J., E. Reznicek, and C. Depcik. *Second Law Heat Release Modeling of a Compression Ignition Engine Fueled With Blends of Palm Biodiesel*. in *ASME 2015 International Mechanical Engineering Congress and Exposition*. 2015. American Society of Mechanical Engineers.
13. Mattson, J.M. and C. Depcik, *Emissions–calibrated equilibrium heat release model for direct injection compression ignition engines.* Fuel, 2014. **117**: p. 1096-1110.
14. Moran, M.J., et al., *Fundamentals of engineering thermodynamics*. 2010: John Wiley & Sons.
15. Moran, M.J., *Availability analysis: a guide to efficient energy use.* 1982.
16. Mattson, J.M., M. Mangus, and C. Depcik, *Efficiency and Emissions Mapping for a Single-Cylinder, Direct Injected Compression Ignition Engine*, 2014, SAE Technical Paper.
17. da Costa, Y.J.R., et al., *Energetic and exergetic analyses of a dual-fuel diesel engine.* Renewable and Sustainable Energy Reviews, 2012. **16**(7): p. 4651-4660.
18. Stelmasiak, Z., *The Impact of gas-air composition on combustion parameters of dual fuel engines fed CNG*, 2002, SAE Technical Paper.
19. Mangus, M., et al., *Comparison of neat biodiesels and ULSD in an optimized single-cylinder diesel engine with electronically-controlled fuel injection.* Energy & Fuels, 2014. **28**(6): p. 3849-3862.
20. Langness, C., M. Mangus, and C. Depcik, *Construction, instrumentation, and implementation of a low cost, single-cylinder compression ignition engine test cell*, 2014, SAE Technical Paper.
21. Churkunti, P.R., et al., *Combustion analysis of pyrolysis end of life plastic fuel blended with ultra low sulfur diesel.* Fuel Processing Technology, 2016. **142**: p. 212-218.
22. Brebu, M., et al., *Thermal degradation of PE and PS mixed with ABS-Br and debromination of pyrolysis oil by Fe-and Ca-based catalysts.* Polymer Degradation and Stability, 2004. **84**(3): p. 459-467.
23. Park, Y.-H., et al., *Pyrolysis characteristics and kinetics of oak trees using thermogravimetric analyzer and micro-tubing reactor.* Bioresource Technology, 2009. **100**(1): p. 400-405.
24. Mlynková, B., et al., *Fuels obtained by thermal cracking of individual and mixed polymers.* Chemical Papers, 2010. **64**(1): p. 15.

25. Mangus, M., J. Mattson, and C. Depcik, *Performance and Emissions Characteristics of Hydroprocessed Renewable Jet Fuel Blends in a Single-Cylinder Compression Ignition Engine with Electronically Controlled Fuel Injection*. Combustion Science and Technology, 2015. **187**(6): p. 857-873.
26. Langness, C. and C. Depcik, *Statistical analyses of CNG constituents on dual-fuel compression ignition combustion*, 2016, SAE Technical Paper.
27. Mattson, J., C. Langness, and C. Depcik, *Exergy Analysis of Dual-Fuel Operation with Diesel and Moderate Amounts of Compressed Natural Gas in a Single-Cylinder Engine*. Combustion Science and Technology, 2018. **190**(3): p. 471-489.
28. Blakey, S., L. Rye, and C.W. Wilson, *Aviation gas turbine alternative fuels: A review.* Proceedings of the combustion institute, 2011. **33**(2): p. 2863-2885.
29. Kallio, P., et al., *Renewable jet fuel.* Current opinion in biotechnology, 2014. **26**: p. 50-55.
30. Krishnan, S.R., et al., *Strategies for reduced NOx emissions in pilot-ignited natural gas engines.* Journal of Engineering for Gas Turbines and Power, 2004. **126**(3): p. 665-671.
31. Hosseini, V. and M.D. Checkel, *Using reformer gas to enhance HCCI combustion of CNG in a CFR engine*, 2006, SAE Technical Paper.
32. Mattson, J., et al., *Usage of glycerin-derived, hydrogen-rich syngas augmented by soybean biodiesel to power a biodiesel production facility.* International Journal of Hydrogen Energy, 2016. **41**(38): p. 17132-17144.
33. Pickett, D., C. Depcik, and S.M. Stagg-Williams, *Use of the Glycerin By-product from Biodiesel Production for Power Generation*. Journal of Engineering for Gas Turbines and Power, 2018.
34. Werpy, T., et al., *Top value added chemicals from biomass. Volume 1-Results of screening for potential candidates from sugars and synthesis gas*, 2004, Department of Energy Washington DC.
35. Mangus, M.D., *Implementation of Engine Control and Measurement Strategies for Biofuel Research in Compression-Ignition Engines*. 2014.
36. Van Gerpen, J. and H. Shapiro, *Second-law analysis of diesel engine combustion.* Journal of Engineering for Gas Turbines and Power, 1990. **112**(1): p. 129-137.
37. Stepanov, V., *Chemical energies and exergies of fuels.* Energy, 1995. **20**(3): p. 235-242.
38. United States Department of Energy, *21st Century Truck Partnership. Roadmap and Technical White Papers.*, 2006.
39. Mollenhauer, K., *History and Fundamental Principles of the Diesel Engine*, in *Handbook of Diesel Engines*. 2010, Springer. p. 3-30.
40. Beroun, S. and J. Martins, *The development of gas (CNG, LPG and H2) engines for buses and trucks and their emission and cycle variability characteristics*, 2001, SAE Technical Paper.
41. Konigsson, F., P. Stalhammar, and H.-E. Ångström, *Combustion modes in a diesel-CNG dual fuel engine*, 2011, SAE Technical Paper.
42. Mohammadi, A., et al., *Study on combustion control in natural-gas PCCI engines with ozone addition into intake gas*, 2006, SAE Technical Paper.
43. Langness, C. and C. Depcik, *Statistical Analyses of CNG Constituents on Dual-Fuel Compression Ignition Combustion*, 2016, SAE International.
44. Papagiannakis, R., et al., *Emission characteristics of high speed, dual fuel, compression ignition engine operating in a wide range of natural gas/diesel fuel proportions.* Fuel, 2010. **89**(7): p. 1397-1406.
45. Papagiannakis, R., D. Hountalas, and P. Kotsiopoulos, *Experimental and theoretical analysis of the combustion and pollutants formation mechanisms in dual fuel DI diesel engines*, 2005, SAE Technical Paper.
46. Demirbas, A., *Natural gas*. Methane Gas Hydrate, 2010: p. 57-76.
47. Korakianitis, T., A. Namasivayam, and R. Crookes, *Natural-gas fueled spark-ignition (SI) and compression-ignition (CI) engine performance and emissions.* Progress in Energy and Combustion science, 2011. **37**(1): p. 89-112.

48. Sudhir, C., et al., *Performance and Emission Studies on the Effect of Injection Timing and Diesel Replacement on a 4-S LPG-Diesel Dual-Fuel Engine*, 2003, SAE Technical Paper.
49. Kakaee, A.-H., P. Rahnama, and A. Paykani, *Influence of fuel composition on combustion and emissions characteristics of natural gas/diesel RCCI engine*. Journal of Natural Gas Science and Engineering, 2015. **25**: p. 58-65.
50. Wei, L. and P. Geng, *A review on natural gas/diesel dual fuel combustion, emissions and performance*. Fuel Processing Technology, 2016. **142**: p. 264-278.
51. Bilcan, A., et al., *Characterization of the LPG-diesel dual fuel combustion*, 2001, SAE Technical Paper.
52. Zuo, C. and M. Yang, *Operating characteristics and description of a dual fuel engine for diesel-natural gas heavy-duty operation*, 1999, SAE Technical Paper.
53. Karim, G.A., *Combustion in gas fueled compression: ignition engines of the dual fuel type.* Transactions - American Society of Mechanical Engineers Journal of Engineering for Gas Turbines and Power, 2003. **125**(3): p. 827-836.
54. Inagaki, K., et al., *Dual-fuel PCI combustion controlled by in-cylinder stratification of ignitability*, 2006, SAE Technical Paper.
55. Mustafi, N.N., R.R. Raine, and S. Verhelst, *Combustion and emissions characteristics of a dual fuel engine operated on alternative gaseous fuels.* Fuel, 2013. **109**: p. 669-678.
56. Sarjovaara, T. and M. Larmi, *Dual fuel diesel combustion with an E85 ethanol/gasoline blend*. Fuel, 2015. **139**: p. 704-714.
57. Singh, S., et al., *Modeling and experiments of dual-fuel engine combustion and emissions*, 2004, SAE Technical Paper.
58. Dahodwala, M., et al., *Investigation of Diesel and CNG Combustion in a Dual Fuel Regime and as an Enabler to Achieve RCCI Combustion*, 2014, SAE International.
59. Grimm, B.M. and R.T. Johnson, *Review of Simple Heat Release Computations*, 1990, SAE International.
60. Heywood, J.B., *Internal Combustion Engine Fundamentals*. 1988: McGraw-Hill, Inc. 930.
61. Foster, D.E., *An Overview of Zero-Dimensional Thermodynamic Models for IC Engine Data Analysis*, 1985, SAE International.
62. Jensen, T.K. and J. Schramm, *A Three-Zone Heat Release Model for Combustion Analysis in a Natural Gas SI Engine. -Effects of Crevices and Cyclic Variations on UHC Emissions*, 2000, SAE International.
63. Kee, R.J., et al., *CHEMKIN-III: A FORTRAN chemical kinetics package for the analysis of gas-phase chemical and plasma kinetics*.
64. Hiroyasu, H. and K. Nishida, *Simplified Three-Dimensional Modeling of Mixture Formation and Combustion in a DI Diesel Engine.* 1989.
65. Stiesch, G. and G.P. Merker, *A Phenomenological Model for Accurate and Time Efficient Prediction of Heat Release and Exhaust Emissions in Direct-Injection Diesel Engines*, 1999, SAE International.
66. Kadota, T., H. Hiroyasu, and H. Oya, *Spontaneous Ignition Delay of a Fuel Droplet in High Pressure and High Temperature Gaseous Environments.* Bulletin of JSME, 1976. **19**(130): p. 437-445.
67. Wolfer, H.H., *Ignition Lag in Diesel Engines.* VDI-Forschungsheft, 1938. **392**.
68. Spadaccini, L.J., *Autoignition Characteristics of Hydrocarbon Fuels at Elevated Temperatures and Pressures*. Journal of Engineering, 1977. **Power**(99): p. 83-87.
69. Spadaccini, L.J. and J.A. Tevelde, *Autoignition characteristics of aircraft-type fuels.* Combustion and Flame, 1982. **46**(0): p. 283-300.
70. Watson, N., A.D. Pilley, and M. Marzouk, *A Combustion Correlation for Diesel Engine Simulation*, 1980, SAE International.

71. Assanis, D.N., et al., *A Predictive Ignition Delay - Correlation Under Steady-State and Transient Operation of a Direct Injection Diesel Engine.* Journal of Engineering for Gas Turbines and Power, 2003. **125**: p. 450-457.
72. Syrimis, M., K. Shigahara, and D.N. Assanis, *Correlation Between Knock Intensity and Heat Transfer Under Light and Heavy Knocking Conditions in a Spark Ignition Engine*, 1996, SAE International.
73. Langness, C., M. Mangus, and C. Depcik, *Construction, Instrumentation, and Implementation of a Low Cost, Single-Cylinder Compression Ignition Engine Test Cell*, 2014, SAE International.
74. Bramlette, R., et al. *Employing Adaptive Mesh Refinement for Simulating the Exhaust Gas Recirculation Mixing Process*. in *ASME 2014 International Mechanical Engineering Congress and Exposition*. 2014. American Society of Mechanical Engineers.
75. Kinder, J.D., *Evaulation of Bio-Derived Synthetic Paraffinic Kerosenes (Bio-SPKs)*, 2010, Boeing Commercial Airplanes, UOP, United States Air Force Research Laboratory.
76. Ciaravino, C., et al., *The Key Role of the Closed-loop Combustion Control for Exploiting the Potential of Biodiesel in a Modern Diesel Engine for Passenger Car Applications.* SAE Int. J. Engines, 2011. **4**(2): p. 2576-2589.
77. Zhou, D., et al., *Dual-fuel RCCI engine combustion modeling with detailed chemistry considering flame propagation in partially premixed combustion.* Applied Energy, 2017. **203**: p. 164-176.
78. Singh, S., et al., *Development of a flame propagation model for dual-fuel partially premixed compression ignition engines.* International Journal of Engine Research, 2006. **7**(1): p. 65-75.
79. Königsson, F., *Advancing the limits of dual fuel combustion*, 2012, KTH Royal Institute of Technology.
80. Mangus, M., et al., *Ozone-Assisted Combustion: Experimental Assessment of the Influence of Ozone in a Single-Cylinder Diesel Engine*, 2015, SAE Technical Paper.
81. Greene, D.L., J.L. Hopson, and J. Li, *Have we run out of oil yet? Oil peaking analysis from an optimist's perspective.* Energy Policy, 2006. **34**(5): p. 515-531.
82. Pickett, D.K., *Design and Operation of the Synthesis Gas Geneartor System for Reformed Propane and Glycerin*, 2013: KU ScholarWorks.
83. Stelmachowski, M., *Utilization of glycerol, a by-product of the transestrification process of vegetable oils: a review.* Ecological Chemistry and Engineering. S, 2011. **18**(1): p. 9-30.
84. Gui, M.M., K. Lee, and S. Bhatia, *Feasibility of edible oil vs. non-edible oil vs. waste edible oil as biodiesel feedstock.* Energy, 2008. **33**(11): p. 1646-1653.
85. Chiu, C.-W., et al., *Removal of residual catalyst from simulated biodiesel's crude glycerol for glycerol hydrogenolysis to propylene glycol.* Industrial & engineering chemistry research, 2006. **45**(2): p. 791-795.
86. Pandey, R.K., A. Rehman, and R. Sarviya, *Impact of alternative fuel properties on fuel spray behavior and atomization.* Renewable and Sustainable Energy Reviews, 2012. **16**(3): p. 1762-1778.
87. Kinoshita, E., et al., *Combustion characteristics for diesel engines with emulsified biodiesel without adding emulsifier*, 2004, SAE Technical Paper.
88. Zhang, Y., et al., *Biodiesel production from waste cooking oil: 1. Process design and technological assessment.* Bioresource technology, 2003. **89**(1): p. 1-16.
89. Carraretto, C., et al., *Biodiesel as alternative fuel: experimental analysis and energetic evaluations.* Energy, 2004. **29**(12): p. 2195-2211.
90. Cecrle, E., et al., *Analysis of the effects of reformate (hydrogen/carbon monoxide) as an assistive fuel on the performance and emissions of used canola-oil biodiesel.* International Journal of Hydrogen Energy, 2012. **37**(4): p. 3510-3527.
91. Jamal, Y. and M. Wyszynski, *On-board generation of hydrogen-rich gaseous fuels—a review.* International Journal of Hydrogen Energy, 1994. **19**(7): p. 557-572.
92. Lilik, G.K., et al., *Hydrogen assisted diesel combustion.* International Journal of Hydrogen Energy, 2010. **35**(9): p. 4382-4398.

93. Zhou, J., C. Cheung, and C. Leung, *Combustion, performance, regulated and unregulated emissions of a diesel engine with hydrogen addition.* Applied Energy, 2014. **126**: p. 1-12.
94. Zhou, J., C. Cheung, and C. Leung, *Combustion, performance and emissions of ULSD, PME and B50 fueled multi-cylinder diesel engine with naturally aspirated hydrogen.* International Journal of Hydrogen Energy, 2013. **38**(34): p. 14837-14848.
95. Zhou, J., C. Cheung, and C. Leung, *Combustion, performance and emissions of a diesel engine with H 2, CH 4 and H 2–CH 4 addition.* International Journal of Hydrogen Energy, 2014. **39**(9): p. 4611-4621.
96. Miyamoto, T., et al., *Effects of Hydrogen Addition to Intake Mixture on Cyclic Variation of Diesel Engine*, 2011, SAE International.
97. Bika, A.S., L. Franklin, and D. Kittelson, *Cycle Efficiency and Gaseous Emissions from a Diesel Engine Assisted with Varying Proportions of Hydrogen and Carbon Monoxide (Synthesis Gas)*, 2011, SAE International.
98. Birtas, A., et al., *Effects of Air-Hydrogen Induction on Performance and Combustion of a Diesel Engine*, 2011, SAE International.
99. Wagemakers, A.M.L.M. and C.A.J. Leermakers, *Review on the Effects of Dual-Fuel Operation, Using Diesel and Gaseous Fuels, on Emissions and Performance*, 2012, SAE International.
100. Gatts, T., et al., *An experimental investigation of incomplete combustion of gaseous fuels of a heavy-duty diesel engine supplemented with hydrogen and natural gas.* International Journal of Hydrogen Energy, 2012. **37**(9): p. 7848-7859.
101. Czernichowski, A. *Conversion of waste Glycerol into Synthesis Gas*. in *19th Int. Symp. on Plasma Chem.(ISPC-19), Bochum, Germany, July 26*. 2009.
102. Mattson, J.M.S., *Power, Efficiency and Emissions Optimization of a Single Cylinder Direct-Injected Diesel Engine for Testing of Alternative Fuels through Heat Release Modeling*, in *Department of Mechanical Engineering, School of Engineering*2013, University of Kansas: Lawrence, KS.
103. Mangus, M. and C. Depcik, *Comparison of ULSD, Used Cooking Oil Biodiesel, and JP-8 Performance and Emissions in a Single-Cylinder Compression-Ignition Engine.* SAE International Journal of Fuels and Lubricants, 2012. **5**(3): p. 1382-1394.
104. Maji, S., A. Pal, and B. Arora, *Use of CNG and diesel in CI engines in dual fuel mode*, 2008, SAE Technical Paper.
105. Carlucci, A., et al., *Experimental investigation and combustion analysis of a direct injection dual-fuel diesel–natural gas engine.* Energy, 2008. **33**(2): p. 256-263.
106. Papagiannakis, R.G., et al., *Combustion and performance characteristics of a DI diesel engine operating from low to high natural gas supplement ratios at various operating conditions*, 2008, SAE Technical Paper.
107. Jacobs, T., D.N. Assanis, and Z. Filipi, *The Impact of Exhaust Gas Recirculation on Performance and Emissions of a Heavy-Duty Diesel Engine*, 2003, SAE International.
108. Karim, G.A., *A review of combustion processes in the dual fuel engine—the gas diesel engine.* Progress in energy and combustion science, 1980. **6**(3): p. 277-285.
109. Yoshimoto, Y., *Combustion Characteristics of a Dual Fuel Diesel Engine with Natural Gas (Study with Fatty Acid Methyl Esters Used as Ignition Fuels)*, 2010, SAE International.
110. Syrimis, M. and D.N. Assanis, *Knocking Cylinder Pressure Data Characteristics in a Spark-Ignition Engine.* Journal of Engineering for Gas Turbines and Power, 2003. **125**(2): p. 494-499.
111. Rusly, A., et al., *High-Speed Imaging of Soot Luminosity and Spectral Analysis of In-Cylinder Pressure Trace during Diesel Knock*, 2014, SAE International.
112. Park, S.S., Y. Jung, and C. Bae, *Diesel Knock Visualization and Frequency Analysis of Premixed Charge Compression Ignition Combustion with a Narrow Injection Angle*, 2013, SAE International.
113. Mitchell, R.H. and D.B. Olsen, *Extending Substitution Limits of a Diesel–Natural Gas Dual Fuel Engine.* Journal of Energy Resources Technology, 2017. **140**(5): p. 052202-052202-12.

114. Kirsten, M., et al., *Advanced Knock Detection for Diesel/Natural Gas Engine Operation.* SAE Int. J. Engines, 2016. **9**(3).
115. Lowe, D.P., et al., *Diesel knock combustion and its detection using acoustic emission.*
116. Ren, Y., R. Randall, and B. Milton, *Influence of the resonant frequency on the control of knock in diesel engines.* Proceedings of the Institution of Mechanical Engineers, Part D: Journal of Automobile Engineering, 1999. **213**(2): p. 127-133.
117. Hickling, R., D. Feldmaier, and S. Sung, *Knock- induced cavity resonances in open chamber diesel engines.* The Journal of the Acoustical Society of America, 1979. **65**(6): p. 1474-1479.
118. Mattson, J.M. and C. Depcik, *First and Second Law Heat Release Analysis in a Single Cylinder Engine.* SAE International Journal of Engines, 2016. **9**(2016-01-0559): p. 536-545.
119. Ragone, C., *Emission reduction and assisted combustion strategies for compression ignition engines with subsequent testing on a single-cylinder engine*, 2012, University of Kansas.
120. Shahlari, A.J., et al., *Correlation of cylinder pressure–based engine noise metrics to measured microphone data*. International Journal of Engine Research, 2014: p. 1468087414552831.
121. Churkunti, P., J.M.S. Mattson, and C. Depcik, *Influence of Fuel Injection Pressure and Biodiesel upon NOx Emissions*, 2016, SAE International.
122. Brunt, M.F.J., H. Rai, and A.L. Emtage, *The Calculation of Heat Release Energy from Engine Cylinder Pressure Data*, 1998, SAE International.
123. Lapuerta, M., O. Armas, and J. Hernández, *Diagnosis of DI Diesel combustion from in-cylinder pressure signal by estimation of mean thermodynamic properties of the gas.* Applied Thermal Engineering, 1999. **19**(5): p. 513-529.
124. Van Gerpen, J.H. and H.N. Shapiro, *Second-Law Analysis of Diesel Engine Combustion.* Journal of Engineering for Gas Turbines and Power, 1990. **112**(1): p. 129-137.
125. Rakopoulos, C.D. and E.G. Giakoumis, *Second-law analyses applied to internal combustion engines operation.* Progress in Energy and Combustion Science, 2006. **32**(1): p. 2-47.
126. Jafarmadar, S., *Three-dimensional modeling and exergy analysis in Combustion Chambers of an indirect injection diesel engine.* Fuel, 2013. **107**(0): p. 439-447.
127. Jafarmadar, S., *Exergy analysis of hydrogen/diesel combustion in a dual fuel engine using three-dimensional model.* International Journal of Hydrogen Energy, 2014. **39**(17): p. 9505-9514.
128. Taghavifar, H., et al., *Numerical energetic and exergetic analysis of CI diesel engine performance for different fuels of hydrogen, dimethyl ether, and diesel under various engine speeds.* International Journal of Hydrogen Energy, 2014. **39**(17): p. 9515-9526.
129. Ramos da Costa, Y.J., et al., *Energetic and exergetic analyses of a dual-fuel diesel engine.* Renewable and Sustainable Energy Reviews, 2012. **16**(7): p. 4651-4660.
130. Bueno, A.V., J.A. Velásquez, and L.F. Milanez, *Heat release and engine performance effects of soybean oil ethyl ester blending into diesel fuel.* Energy, 2011. **36**(6): p. 3907-3916.
131. Rakopoulos, C.D. and D.C. Kyritsis, *Comparative second-law analysis of internal combustion engine operation for methane, methanol, and dodecane fuels.* Energy, 2001. **26**(7): p. 705-722.
132. Alkidas, A., *The use of availability and energy balances in diesel engines*, 1989, SAE Technical Paper.
133. Brzustowski, T. and A. Brena, *Second-law analysis of energy processes. IV- The exergy of hydrocarbon fuels.* Canadian Society for Mechanical Engineering, Transactions, 1986. **10**(3): p. 121-128.
134. Abusoglu, A. and M. Kanoglu, *First and second law analysis of diesel engine powered cogeneration systems.* Energy Conversion and Management, 2008. **49**(8): p. 2026-2031.
135. Stepanov, V.S., *Chemical energies and exergies of fuels.* Energy, 1995. **20**(3): p. 235-242.
136. Tat, M.E., *Cetane number effect on the energetic and exergetic efficiency of a diesel engine fuelled with biodiesel.* Fuel Processing Technology, 2011. **92**(7): p. 1311-1321.
137. Kotas, T.J., *The exergy method of thermal plant analysis*. 2013: Elsevier.

138. Mattson, J.M.S., *Power, Efficiency, and Emissions Optimization of a Single Cylinder Direct-Injected Diesel Engine for Testing of Alternative Fuels through Heat Release Modeling*, 2013, University of Kansas.
139. Woschni, G., *A Universally Applicable Equation for the Instantaneous Heat Transfer Coefficient in the Internal Combustion Engine*, 1967, SAE International.
140. Hohenberg, G.F., *Advanced Approaches for Heat Transfer Calculations*, 1979, SAE International.
141. Bahadori, A. and H.B. Vuthaluru, *Predicting Emissivities of Combustion Gases.* Chemical engineering progress, 2009. **105**(6): p. 38-41.
142. Rajasekar, E. and S. Selvi, *Review of combustion characteristics of CI engines fueled with biodiesel.* Renewable and Sustainable Energy Reviews, 2014. **35**(0): p. 390-399.
143. Tazerout, M., O. Le Corre, and S. Rousseau, *TDC determination in IC engines based on the thermodynamic analysis of the temperature-entropy diagram*, 1999, SAE technical paper.
144. Szybist, J.P., et al., *Biodiesel combustion, emissions and emission control.* Fuel Processing Technology, 2007. **88**(7): p. 679-691.
145. de Oliveira Costa, L. and R.S. Santos, *Impacts on the Emissions Monitoring System (OBD) Due to the Use of Biodiesel and Higher NOx Emissions*, 2011, SAE International.
146. Cecrle, E., et al., *An Investigation of the Effects of Biodiesel Feedstock on the Performance and Emissions of a Single-Cylinder Diesel Engine*. Energy and Fuels, 2012.
147. Reddy, A., et al., *Effect of Compression Ratio on the Performance of Diesel Engine at Different Loads.* International Journal of Engineering Research and Applications, 2015. **5**(10): p. 62-68.
148. Mattson, J., et al., *Second law analysis of waste cooking oil biodiesel versus ULSD during operation of a CI engine.* Fuel, 2019. **255**: p. 115753.
149. Union, E., *Directive 2009/28/EC of the European Parliament and of the Council of 23 April 2009 on the promotion of the use of energy from renewable sources and amending and subsequently repealing Directives 2001/77/EC and 2003/30/EC.* Official Journal of the European Union, 2009. **5**: p. 2009.
150. Tat, M.E. and J.H. Van Gerpen, *Measurement of Biodiesel Speed of Sound and Its Impact on Injection Timing: Final Report; Report 4 in a Series of 6*, 2003, National Renewable Energy Lab., Golden, CO.(US).
151. Boehman, A.L., et al., *The impact of the bulk modulus of diesel fuels on fuel injection timing.* Energy & Fuels, 2004. **18**(6): p. 1877-1882.
152. Hwang, J., C. Bae, and T. Gupta, *Application of waste cooking oil (WCO) biodiesel in a compression ignition engine.* Fuel, 2016. **176**: p. 20-31.
153. Hwang, J., et al., *Effect of injection parameters on the combustion and emission characteristics in a common-rail direct injection diesel engine fueled with waste cooking oil biodiesel.* Renewable Energy, 2014. **63**: p. 9-17.
154. Mohan, B., et al., *Experimental study of spray characteristics of biodiesel derived from waste cooking oil.* Energy Conversion and Management, 2014. **88**: p. 622-632.
155. Montefrio, M.J., T. Xinwen, and J.P. Obbard, *Recovery and pre-treatment of fats, oil and grease from grease interceptors for biodiesel production.* Applied Energy, 2010. **87**(10): p. 3155-3161.
156. Hendricks, T. and M. O'Keefe, *Heavy vehicle auxiliary load electrification for the essential power system program: Benefits, tradeoffs, and remaining challenges*, 2002, SAE Technical Paper.
157. Reiter, A.J. and S.-C. Kong, *Combustion and emissions characteristics of compression-ignition engine using dual ammonia-diesel fuel.* Fuel, 2011. **90**(1): p. 87-97.
158. Sahoo, B., N. Sahoo, and U. Saha, *Effect of engine parameters and type of gaseous fuel on the performance of dual-fuel gas diesel engines—A critical review.* Renewable and Sustainable Energy Reviews, 2009. **13**(6): p. 1151-1184.
159. Li, W., Z. Liu, and Z. Wang, *Experimental and theoretical analysis of the combustion process at low loads of a diesel natural gas dual-fuel engine*. Energy, 2016. **94**: p. 728-741.

160. Vaja, I. and A. Gambarotta, *Internal combustion engine (ICE) bottoming with organic Rankine cycles (ORCs).* Energy, 2010. **35**(2): p. 1084-1093.
161. Srinivasan, K.K., P.J. Mago, and S.R. Krishnan, *Analysis of exhaust waste heat recovery from a dual fuel low temperature combustion engine using an Organic Rankine Cycle.* Energy, 2010. **35**(6): p. 2387-2399.
162. Sprouse III, C.E., *Combined Diesel Particulate Filter/Heat Exchanger for Engine Exhaust Waste Heat Recovery with Organic Rankine Cycle*, 2016, University of Kansas.
163. Abusoglu, A. and M. Kanoglu, *Exergetic and thermoeconomic analyses of diesel engine powered cogeneration: Part 1–Formulations.* Applied Thermal Engineering, 2009. **29**(2): p. 234-241.
164. Wang, Z., et al., *Impact of pilot diesel ignition mode on combustion and emissions characteristics of a diesel/natural gas dual fuel heavy-duty engine.* Fuel, 2016. **167**: p. 248-256.
165. Srivatsa, C., J. Mattson, and C. Depcik, *Investigating Pre-Mixed Charge Compression Ignition Combustion in a High Compression Ratio Engine*, 2018, SAE Technical Paper.
166. Srivatsa, C.V., J. Mattson, and C. Depcik, *Performance and Emission Analysis of Partially Premixed Charge Compression Ignition Combustion.* Journal of Engineering for Gas Turbines and Power, 2019. **141**(6): p. 061004.
167. Srivatsa, C.V.C., *Performance and Emissions Analysis of Pre-mixed and Partially Pre-mixed Charge Compression Ignition Combustion*, 2017, University of Kansas.
168. Rakopoulos, C. and E. Giakoumis, *Second-law analyses applied to internal combustion engines operation.* Progress in Energy and Combustion science, 2006. **32**(1): p. 2-47.
169. Rakopoulos, C., et al., *Availability analysis of hydrogen/natural gas blends combustion in internal combustion engines.* Energy, 2008. **33**(2): p. 248-255.
170. Kyritsis, D.C. and C.D. Rakopoulos, *Parametric study of the availability balance in an internal combustion engine cylinder*, 2001, SAE Technical Paper.
171. Som, S. and A. Datta, *Thermodynamic irreversibilities and exergy balance in combustion processes.* Progress in Energy and Combustion science, 2008. **34**(3): p. 351-376.
172. Li, Y., et al., *Thermodynamic energy and exergy analysis of three different engine combustion regimes.* Applied Energy, 2016. **180**: p. 849-858.
173. Verma, S., et al., *An experimental investigation of exergetic performance and emission characteristics of hydrogen supplemented biogas-diesel dual fuel engine.* International Journal of Hydrogen Energy, 2018. **43**(4): p. 2452-2468.
174. Kimura, S., et al., *Ultra-clean combustion technology combining a low-temperature and premixed combustion concept for meeting future emission standards*, 2001, SAE Technical Paper.
175. Kimura, S., et al., *New combustion concept for ultra-clean and high-efficiency small DI diesel engines*, 1999, SAE Technical Paper.
176. Kawano, D., et al., *Ignition and combustion control of diesel HCCI*, 2005, SAE Technical Paper.
177. Sudhir, C.V., et al., *Performance and Emission Studies on the Effect of Injection Timing and Diesel Replacement on a 4-S LPG-Diesel Dual-Fuel Engine*, 2003, SAE International.
178. Sahoo, B.B., U.K. Saha, and N. Sahoo, *Theoretical performance limits of a syngas–diesel fueled compression ignition engine from second law analysis.* Energy, 2011. **36**(2): p. 760-769.
179. Mangus, M.D., *Design, construction, and validation of an in-cylinder pressure recording system for internal combustion engine analysis*, 2012, University of Kansas.
180. Sprouse III, C. and C. Depcik, *Review of organic Rankine cycles for internal combustion engine exhaust waste heat recovery.* Applied Thermal Engineering, 2013. **51**(1-2): p. 711-722.

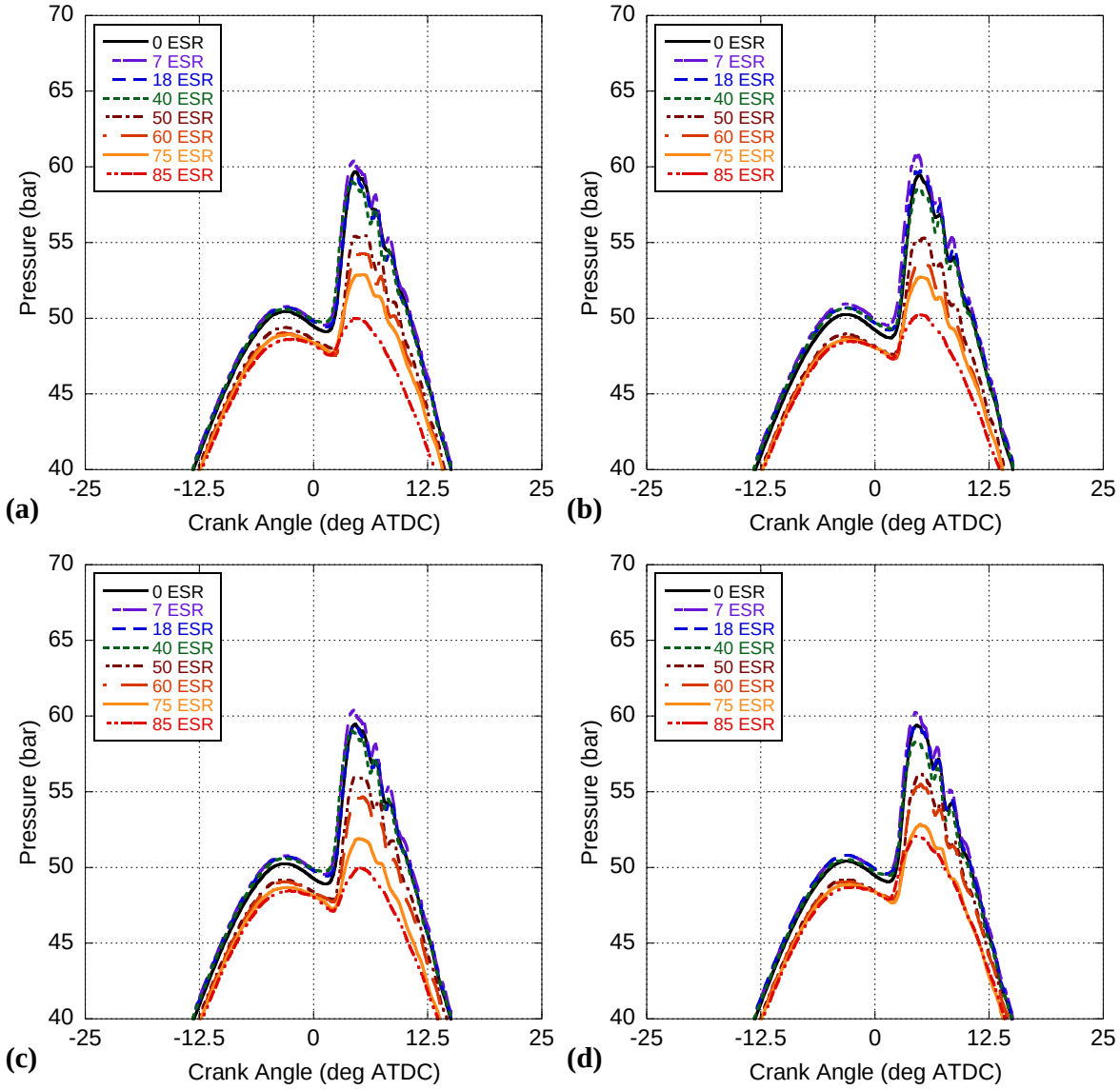

Figure A1: Measured In-Cylinder pressure for ULSD 0.5 N-m with M87 (a), M91 (b), M92 (c), M96 (d).

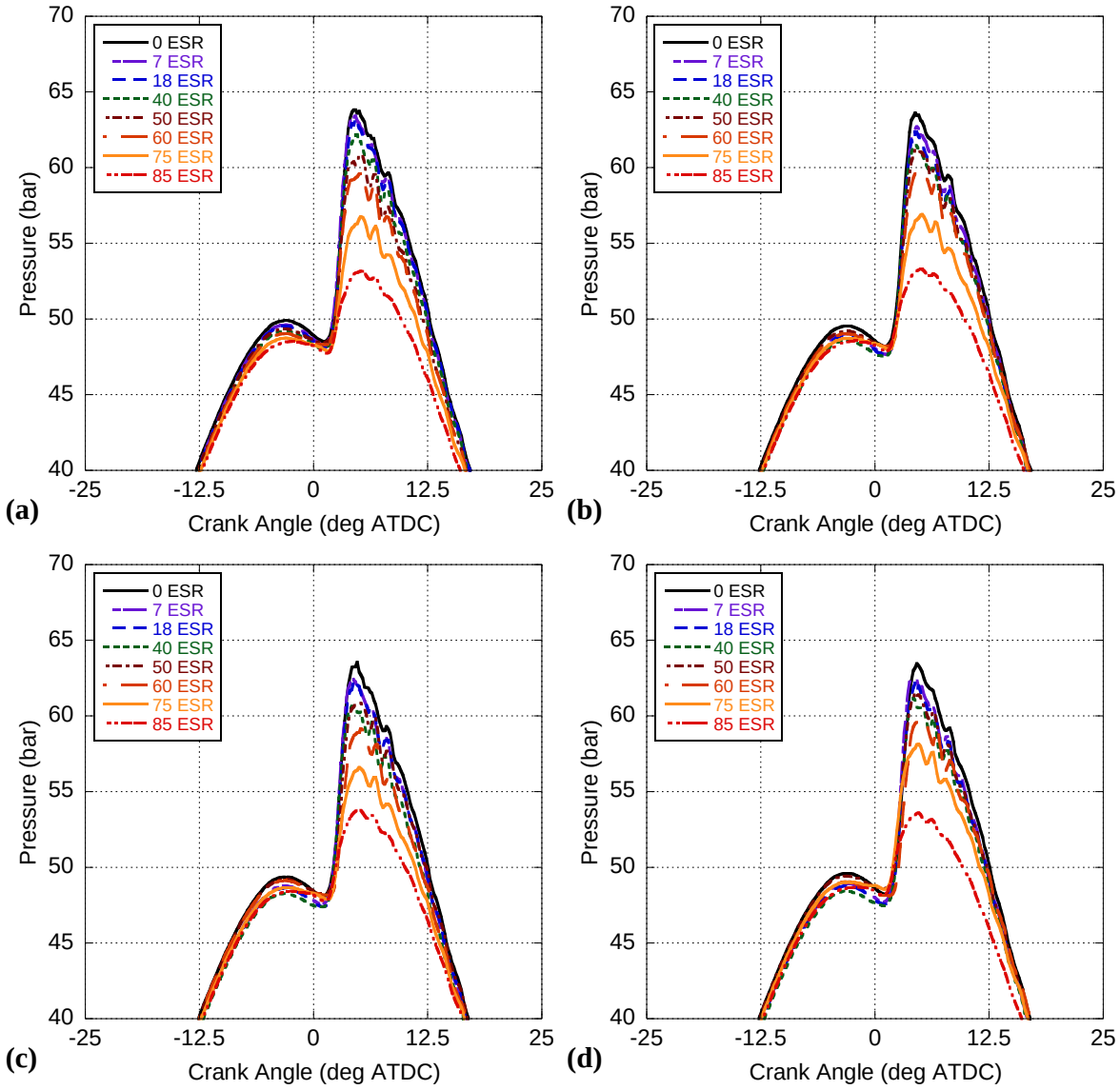

Figure A2: Measured In-Cylinder pressure for ULSD 4.5 N-m with M87 (a), M91 (b), M92 (c), M96 (d).

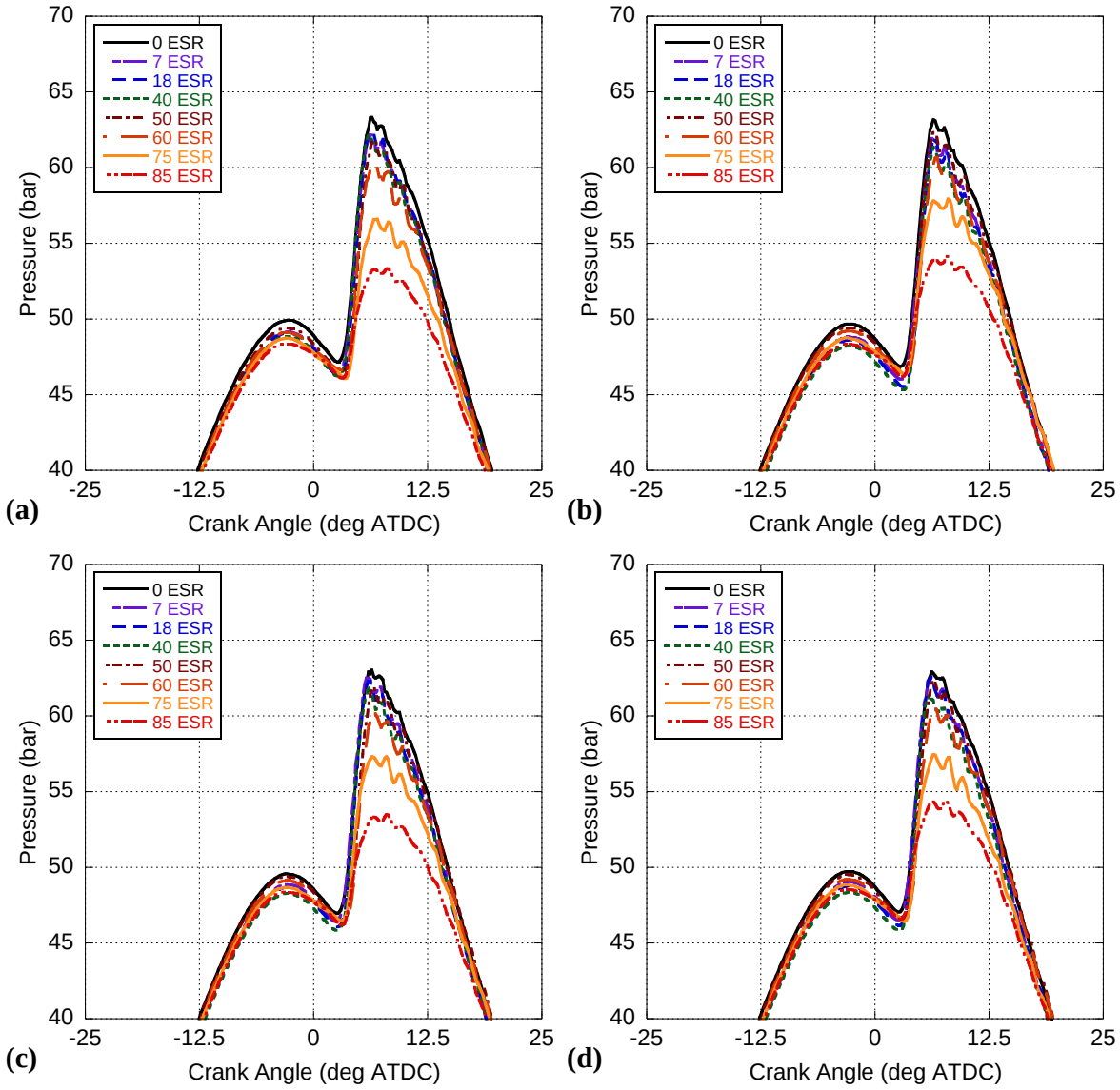

Figure A3: Measured In-Cylinder pressure for ULSD 9.0 N-m with M87 (a), M91 (b), M92 (c), M96 (d).

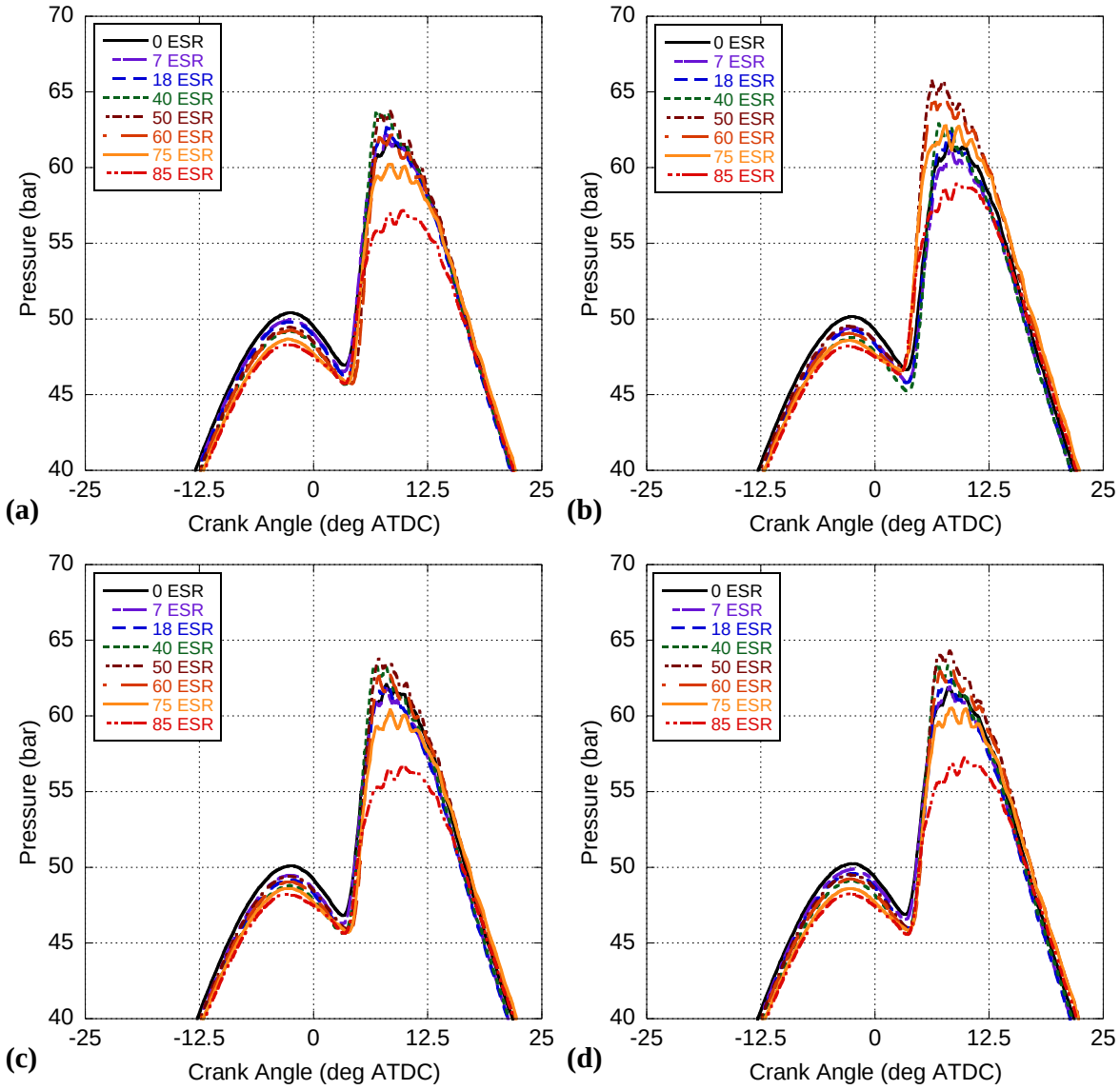

Figure A4: Measured In-Cylinder pressure for ULSD 13.5 N-m with M87 (a), M91 (b), M92 (c), M96 (d).

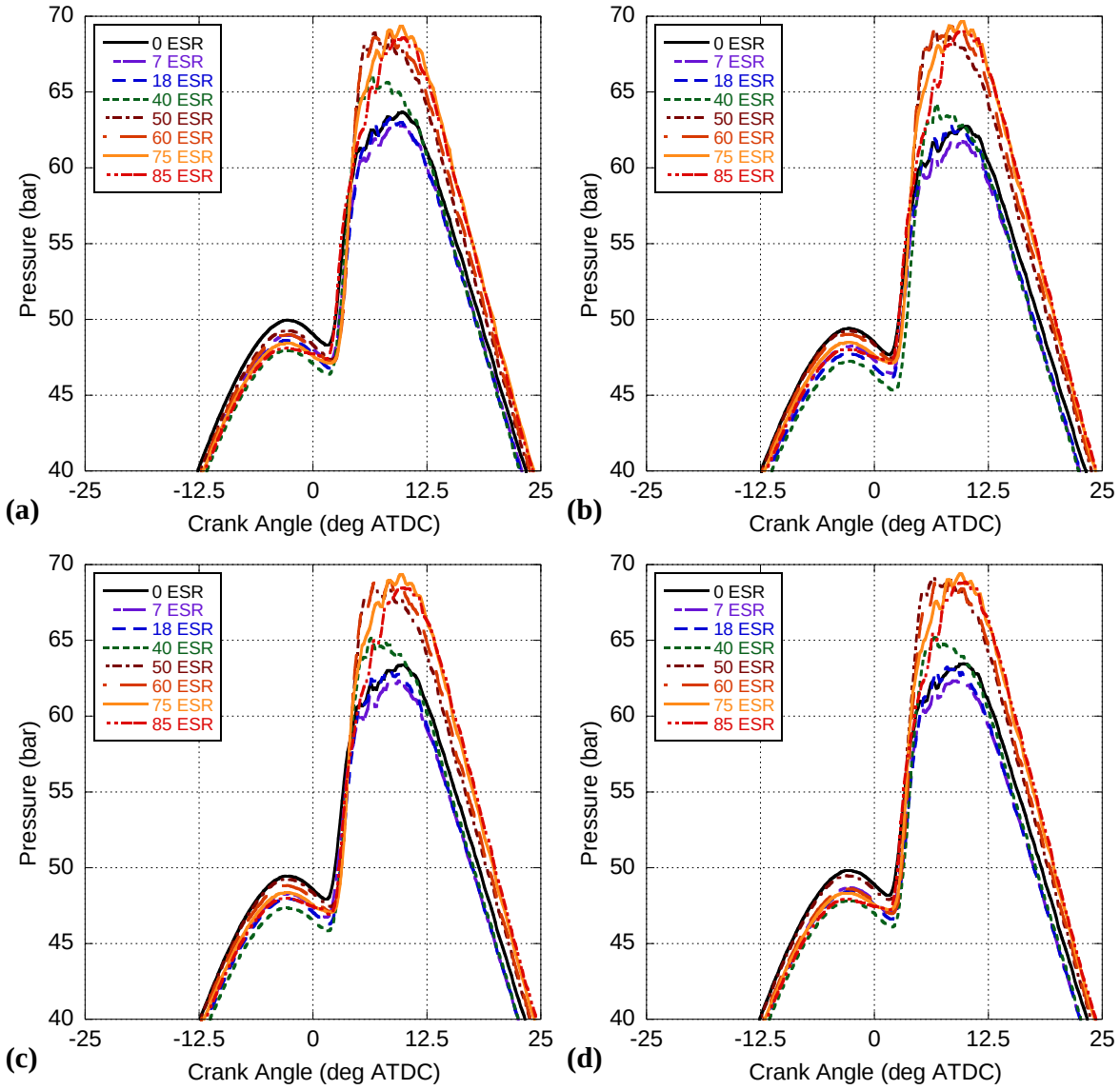

Figure A5: Measured In-Cylinder pressure for ULSD 18.0 N-m with M87 (a), M91 (b), M92 (c), M96 (d).

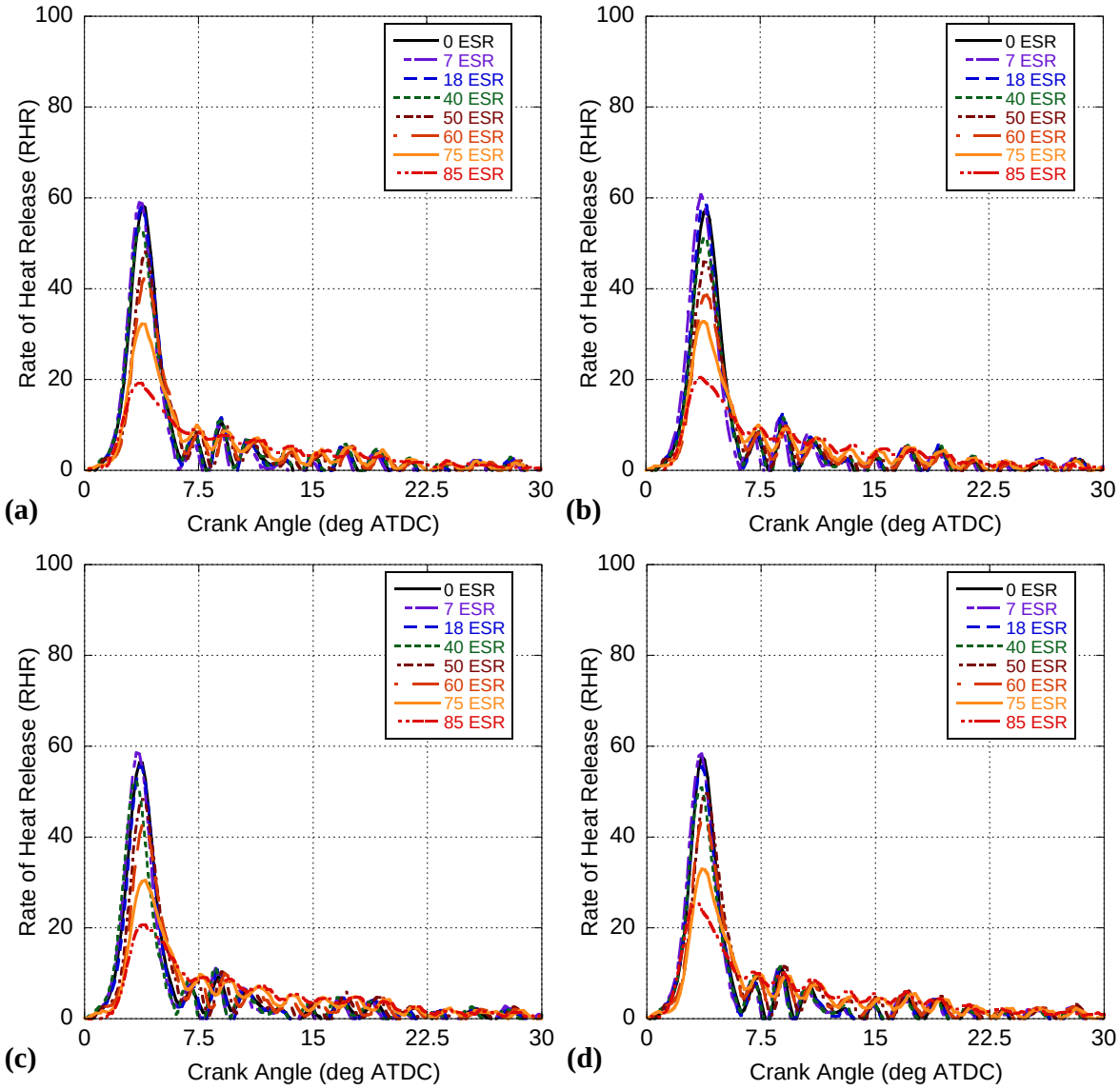

Figure A6: Rates of Heat Release for ULSD 0.5 N-m with M87 (a), M91 (b), M92 (c), M96 (d).

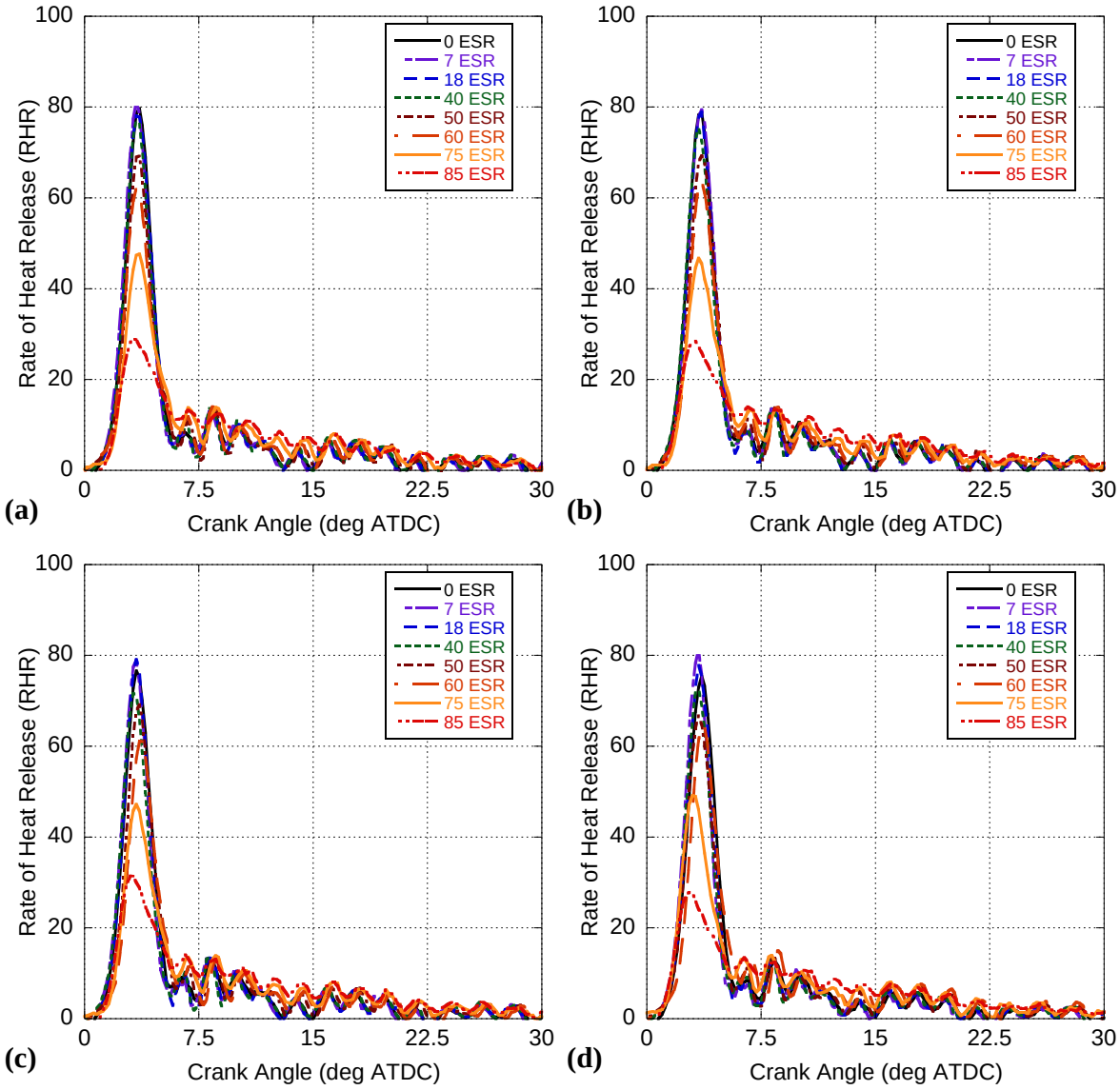

Figure A7: Rates of Heat Release for ULSD 4.5 N-m with M87 (a), M91 (b), M92 (c), M96 (d).

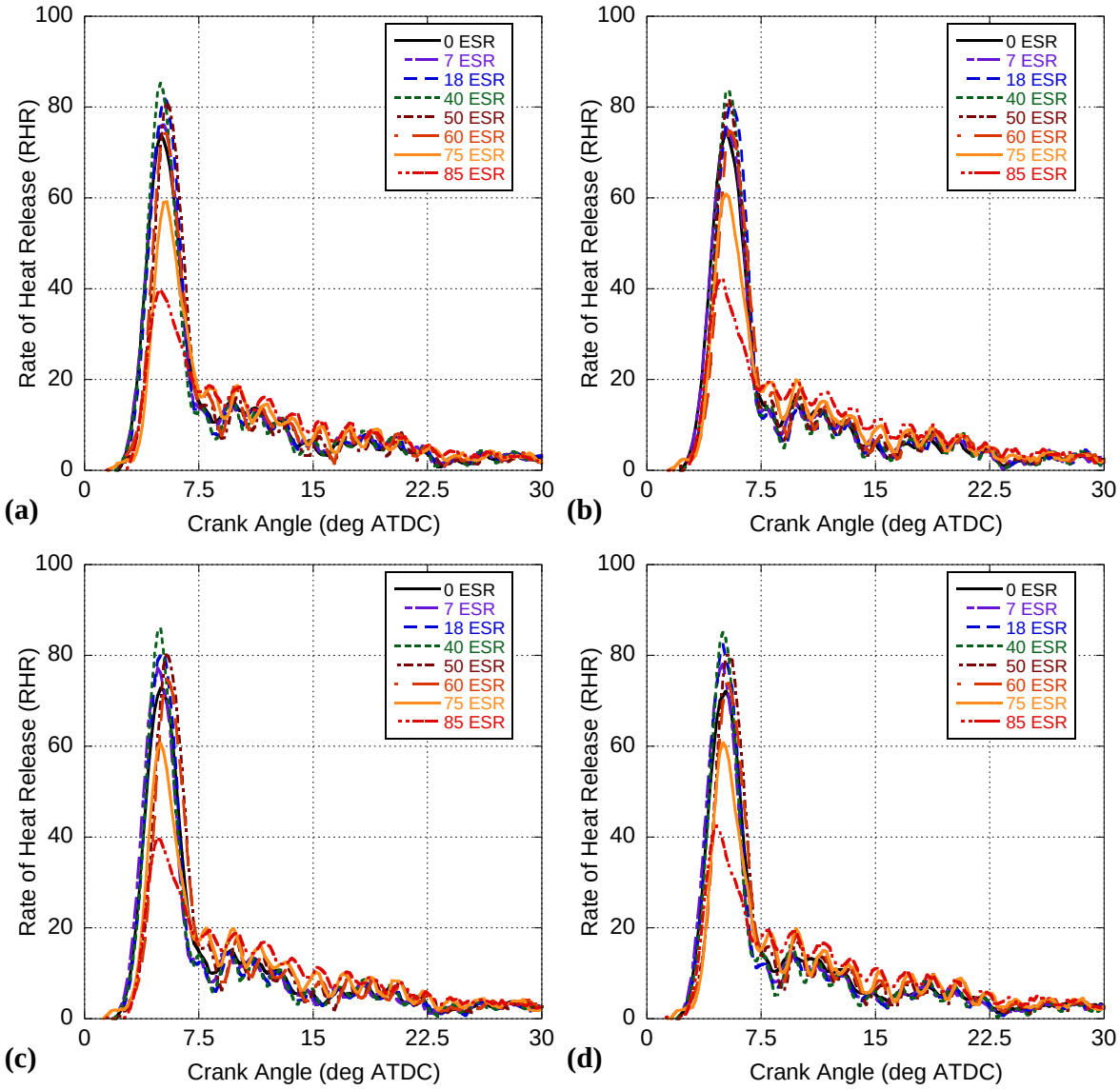

Figure A8: Rates of Heat Release for ULSD 9.0 N-m with M87 (a), M91 (b), M92 (c), M96 (d).

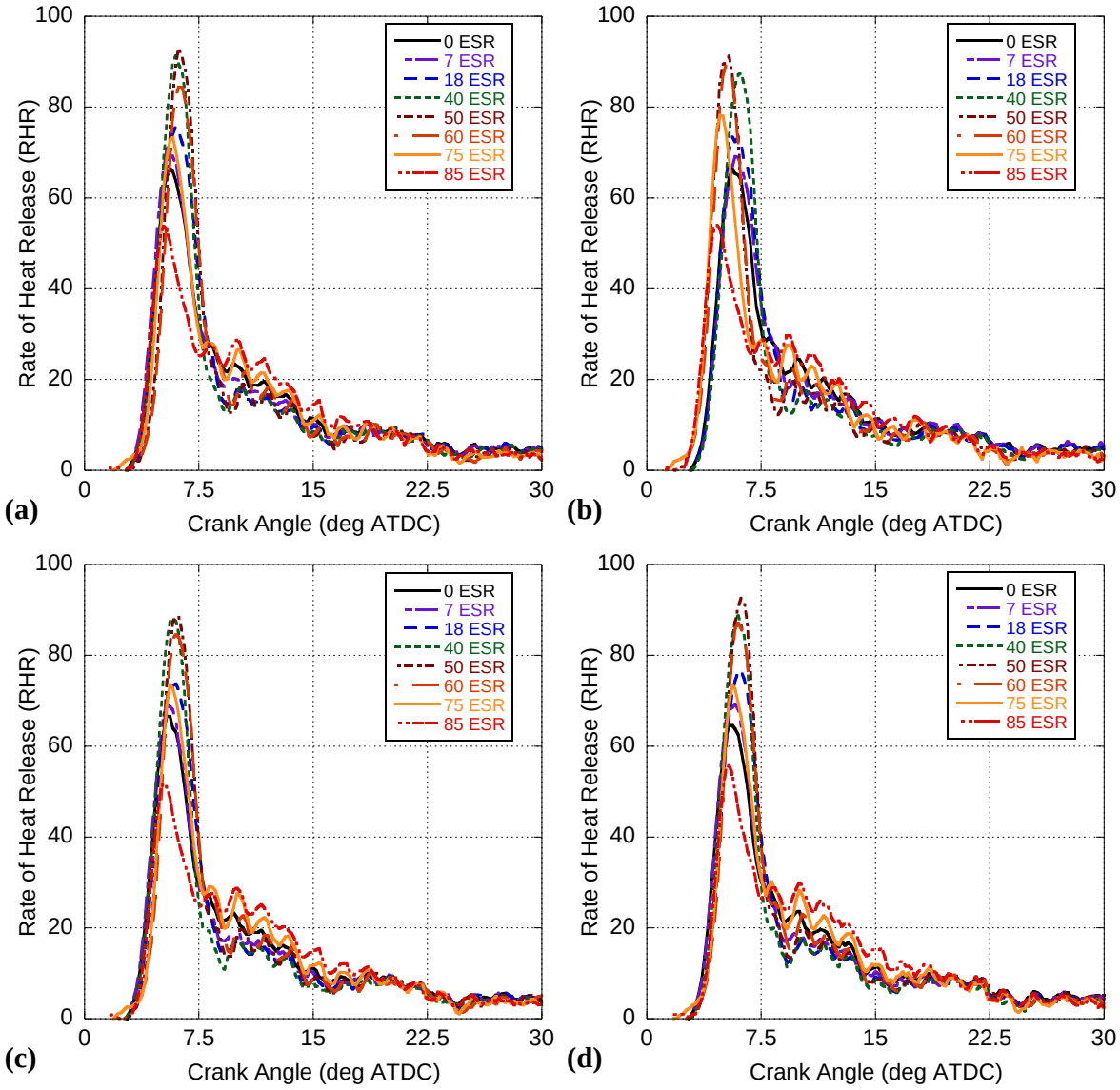

Figure A9: Rates of Heat Release for ULSD 13.5 N-m with M87 (a), M91 (b), M92 (c), M96 (d).

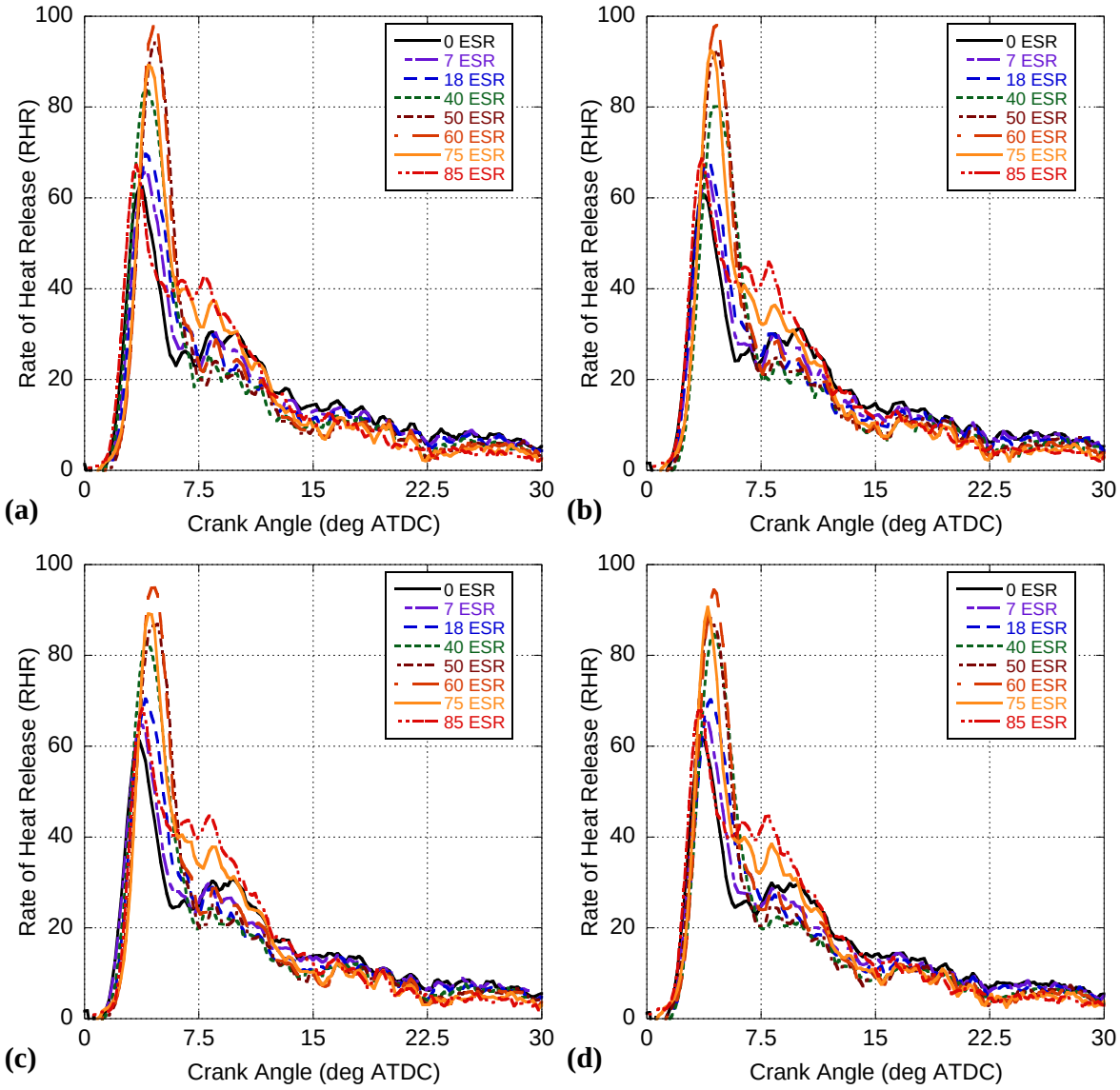

Figure A10: Rates of Heat Release for ULSD 18.0 N-m with M87 (a), M91 (b), M92 (c), M96 (d).

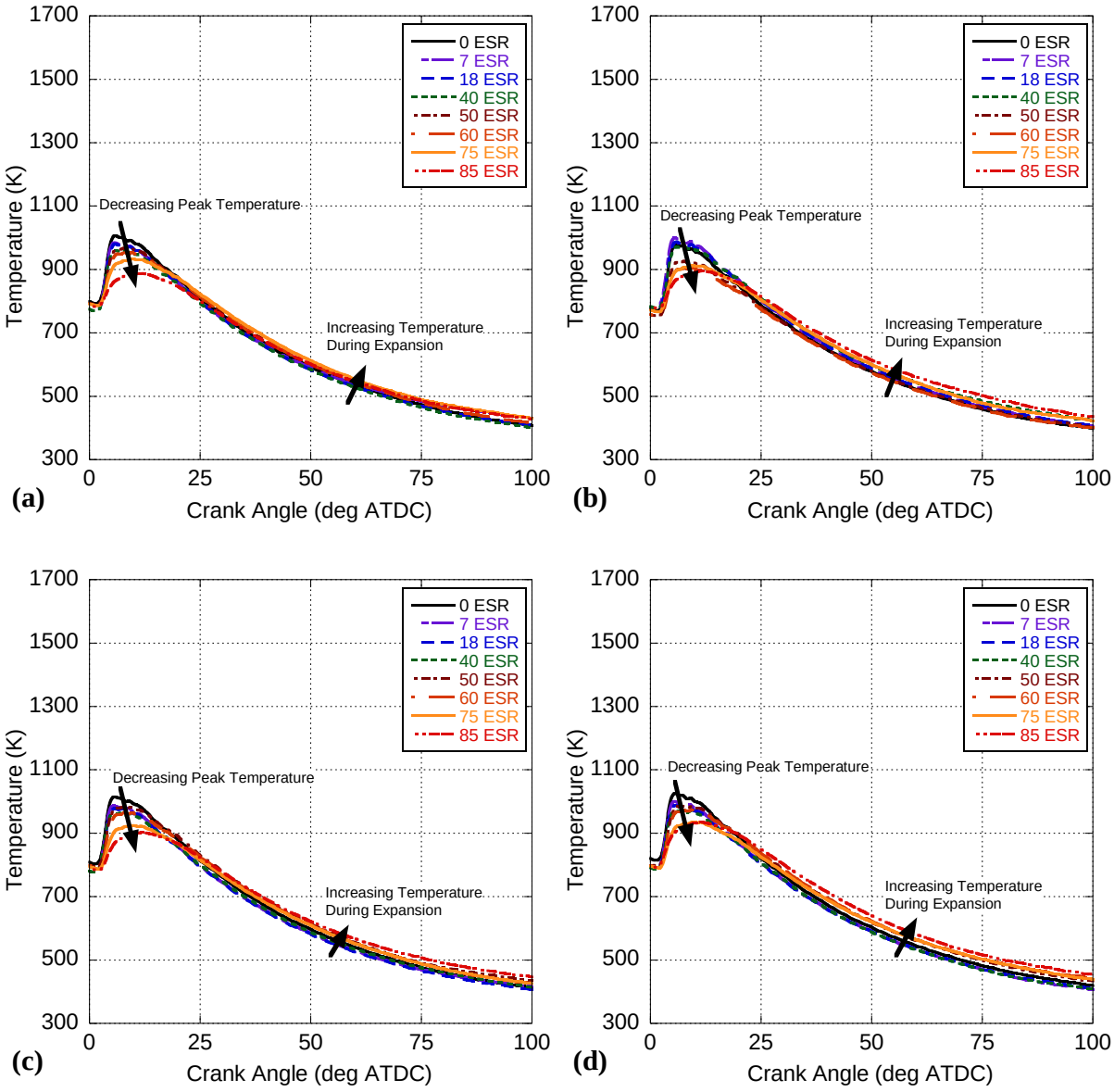

Figure A11: In-Cylinder Temperature for ULSD 0.5 N-m with M87 (a), M91 (b), M92 (c), M96 (d).

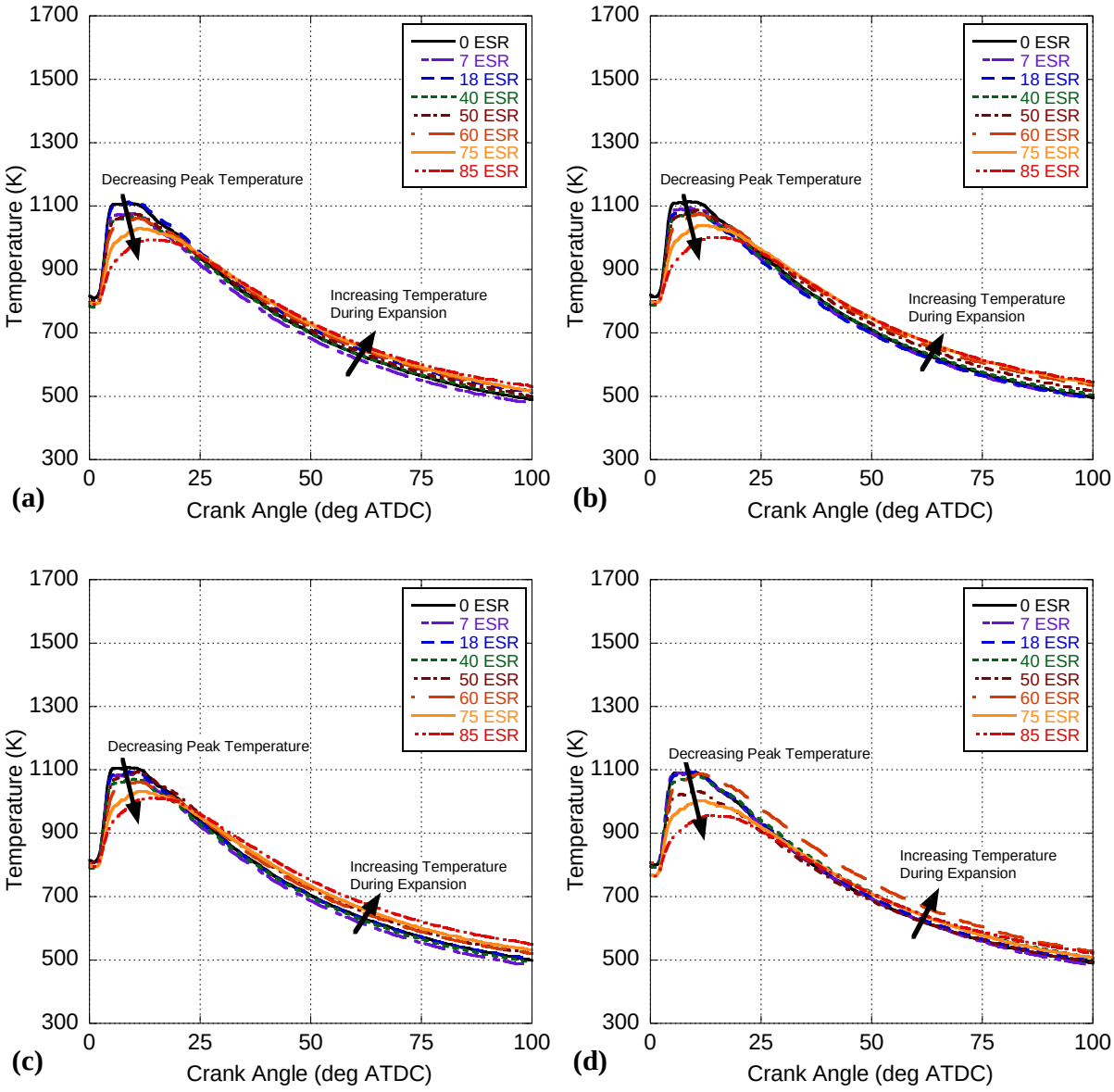

Figure A12: In-Cylinder Temperature for ULSD 4.5 N-m with M87 (a), M91 (b), M92 (c), M96 (d).

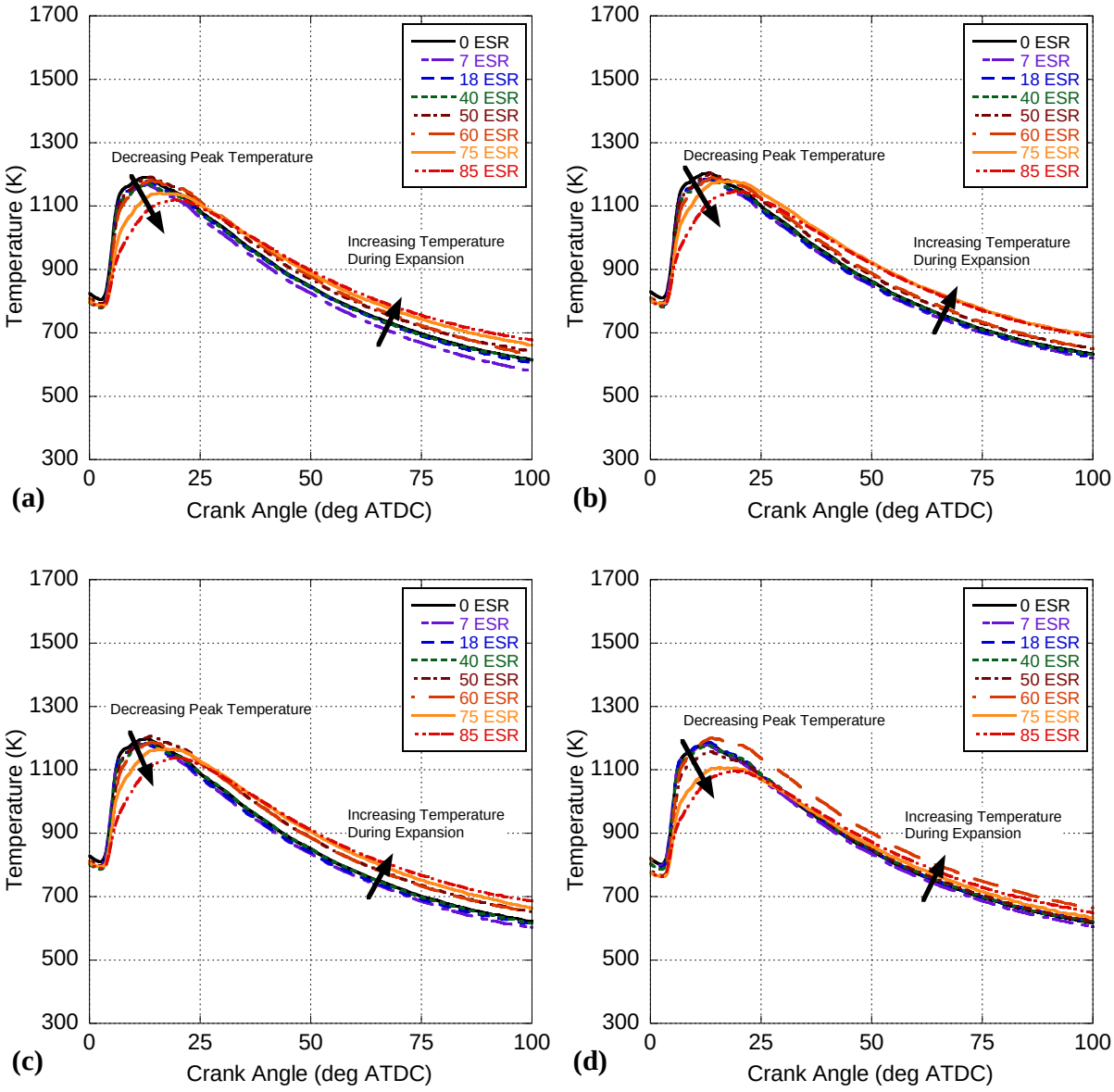

Figure A13: In-Cylinder Temperature for ULSD 9.0 N-m with M87 (a), M91 (b), M92 (c), M96 (d).

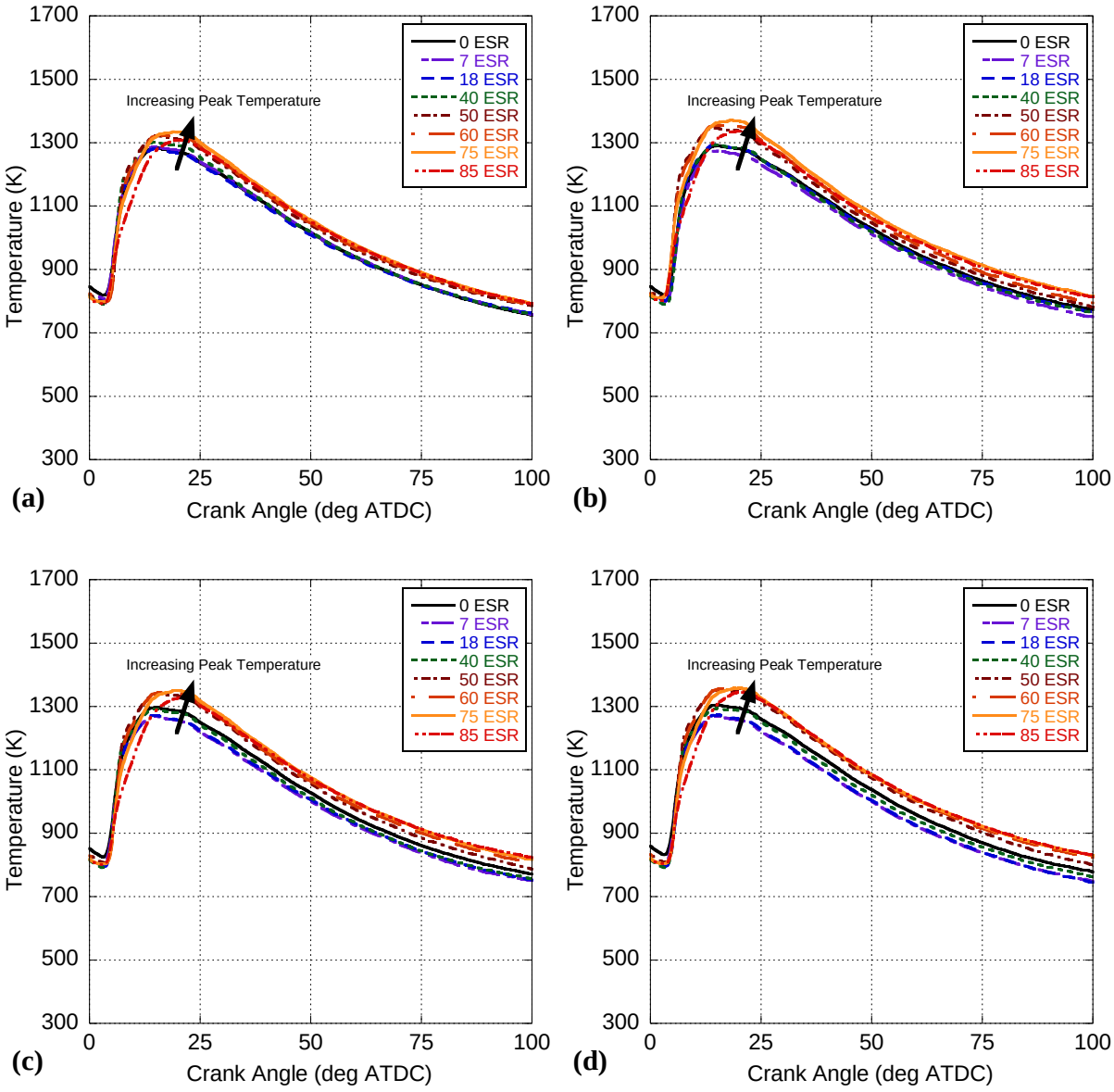

Figure A14: In-Cylinder Temperature for ULSD 13.5 N-m with M87 (a), M91 (b), M92 (c), M96 (d).

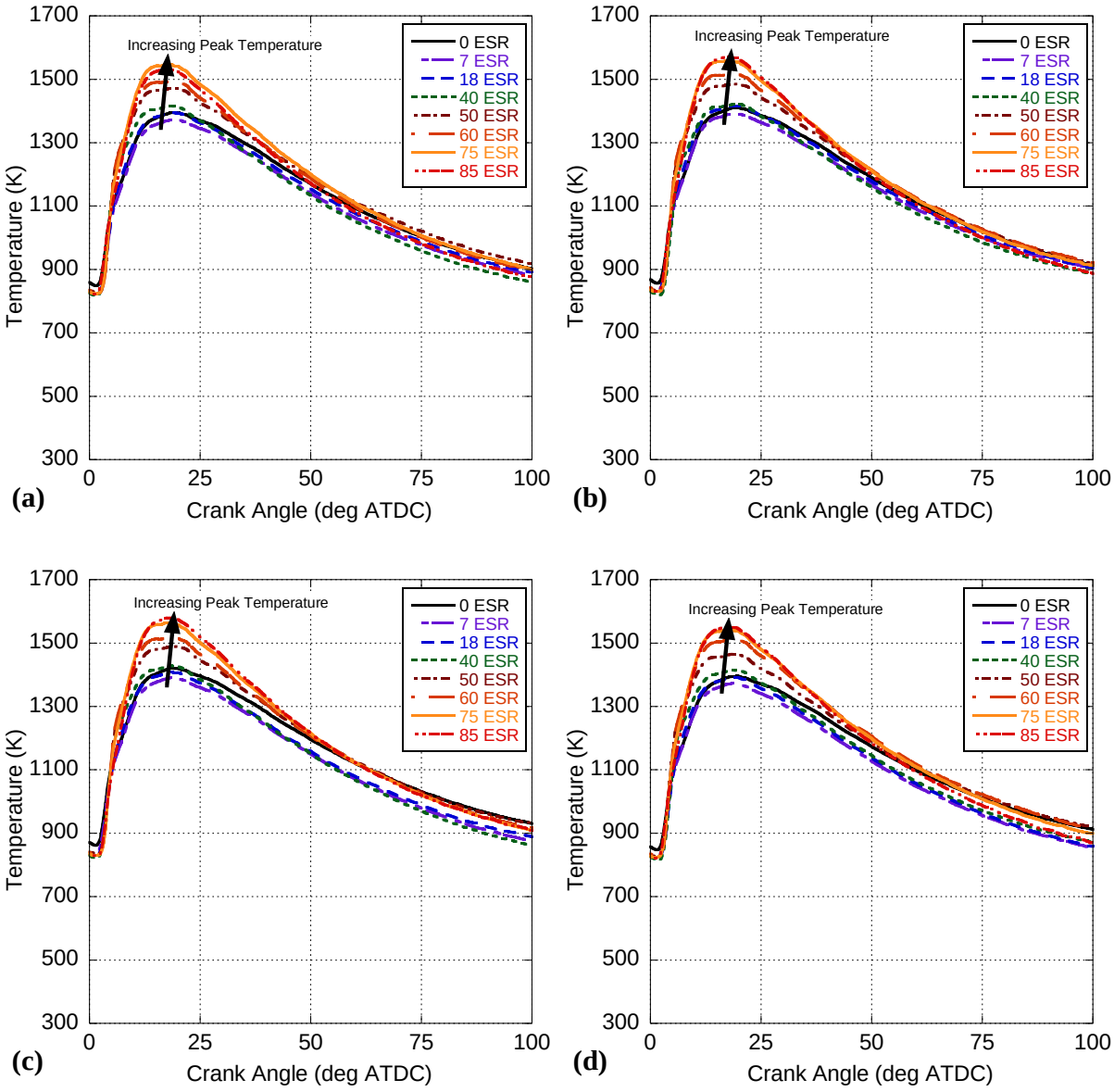

Figure A15: In-Cylinder Temperature for ULSD 18.0 N-m with M87 (a), M91 (b), M92 (c), M96 (d).

Appendix B: Compressed Natural Gas Behavior for Varying Mixtures, 2nd Law Analysis

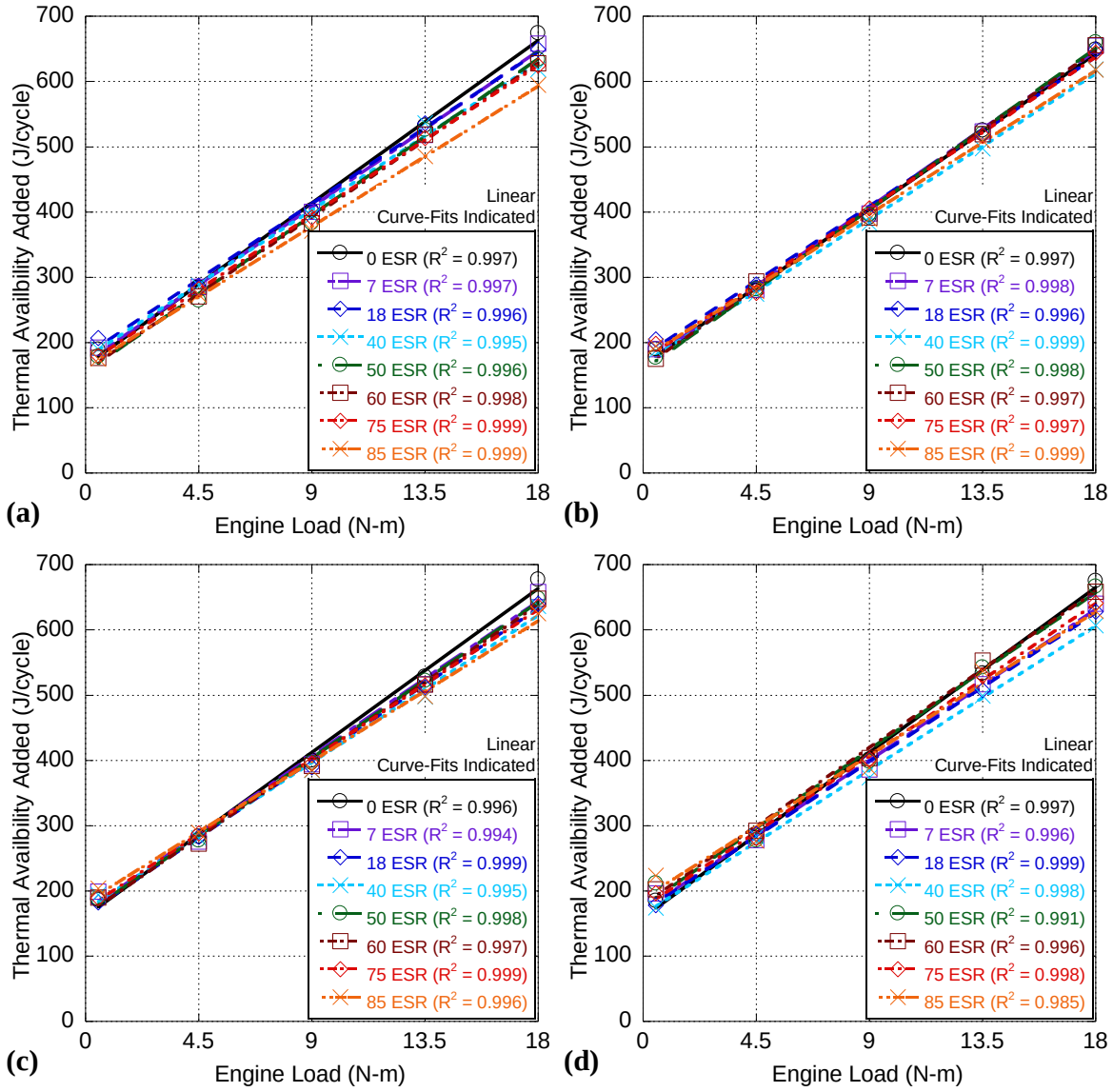

Figure B1: Thermal Availability Added to the Cylinder for M87 (a), M91 (b), M92 (c), and M96 (d) Gas Mixtures for all *ESR*s and engine loads.

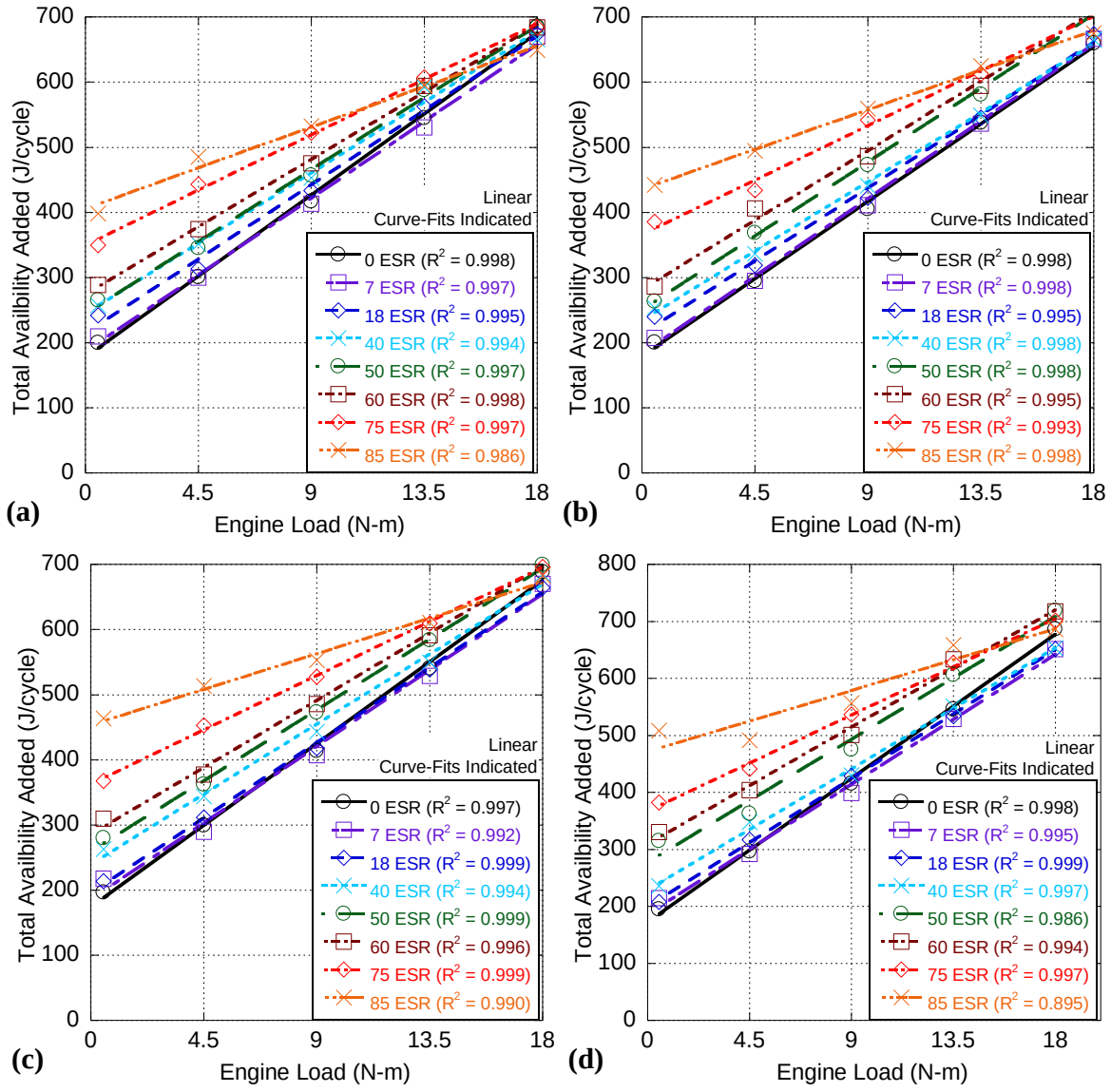

Figure B2: Chemical Potential Availability Added to the Cylinder for M87 (a), M91 (b), M92 (c), and M96 (d) Gas Mixtures for all *ESR*s and engine loads.

Appendix C: Design and Construction of Multi-Cylinder Test Cell

C.1 Introduction

While the single-cylinder engine test cell is extremely useful in terms of functionality and adaptability to a wide variety of testing regimes, there is a potential shortcoming in terms of applying results from that experimental setup to the real world, mainly because the single-cylinder engine itself is not precisely representative of CI engines in use today. This is primarily reflected in its relatively high compression ratio of 21.2, its usage of natural aspiration as opposed to turbocharging, and its intended use as a generator (meant to only operate at a single speed and a small variety of loads). To counter this, part of this work will be concerned with the construction, instrumentation, and initial bench testing of an engine significantly more representative of the existing market of CI engines.

The engine chosen for this is a turbocharged and intercooled eight-cylinder Duramax LBZ engine, made by General Motors (GM), and commonly utilized for the diesel-engined Chevy Silverado (see Figure C1). This specific iteration of the Duramax engine is a 6.6 liter engine from the 2006-2007 era vehicles, but is still representative of the modern iteration of the same class of engine (which features the same displacement and general construction, but better overall control systems). The Duramax LBZ itself was only offered for two years before being replaced by the LMM engines, and was largely phased out due to tightening emissions control standards. Mechanically, however, the LBZ if functionally identical to the LMM that replaced it, with the only substantive differences being general updates to the engine software, and a more effective diesel particulate filtering system (not included with the engine present at KU).

Figure C1. Duramax LBZ original (left) and current (right) states.

The general characteristics of the engine are shown in Table C1. Overall, the engine features a geometric compression ratio of 16.8:1, as well as common-rail direct injection, with a peak power of 360 hp (268.5 kW) at 3200 RPM, and a peak torque of 650 ft-lbs (881.3 N-m) at 1600 RPM.

Table C1. Duramax LBZ Engine Parameters.

Type	90° V8 Direct Injected
Intake	Turbocharged and Intercooled
Cooling	Liquid-Cooled
Cycle	4-Stroke
Displacement [cc]	6600
Number of Valves	4 (2 intake, 2 exhaust)
Bore [cm]	10.3
Stroke [cm]	9.9
Connecting Rod Length [mm]	188.0
Crank Radius [mm]	38.0
Clearance Volume [cm^3]	21.611
Piston Area [cm^2]	83.322
Continuous Rate Output [hp] (SAE)]	360
Rated Speed [RPM]	3250
Engine Oil Used	Shell 15W-40
Dynamometer Manufacturer/Model	DyneSystems, Inc. Dymond Series 12
Continuous Rated Torque [N-m]	1248.7
Continuous Power [hp (SAE)]	351.0
Maximum Speed [RPM]	7500
Voltage [VAC]	480
Frequency and Phase	60 Hz Three-Phase
Controller	DyneSystems, Inter-Loc V OCS

For speed and load control of the engine, the LBZ is connected to an air-cooled three-phase AC regenerative dynamometer, capable of operation from 0-7500 RPM, and able to safely control engine operation up to 351 hp (261.5 kW) and 921 ft-lbs (1248.7 N-m) of torque below 2000 RPM (see Figure C2). Control of the dynamometer is achieved through an attached Inter-Loc V Operational Control Station (OCS) controller, functionally identical to the control setup utilized for the single-cylinder test cell, albeit with an added power amplifier unit (PAU) and cell interface assistant (CIA-III) to provide additional stability and monitoring of the dynamometer and test cell (see Figure C3).

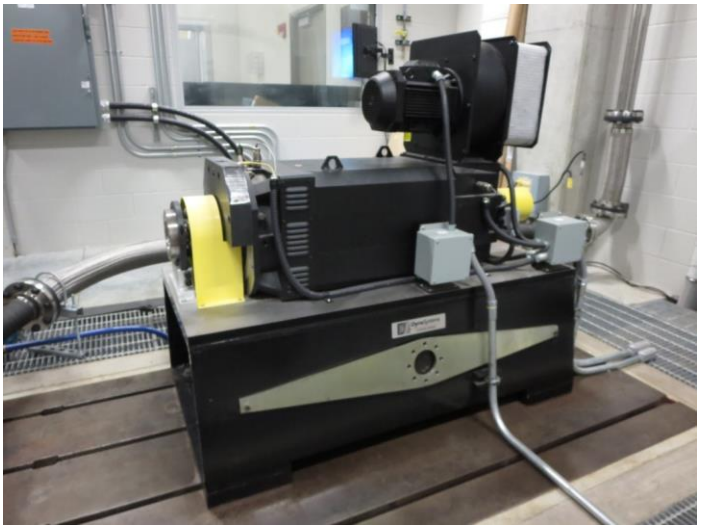

Figure C2. Dyne Systems 351 hp 3-phase AC dynamometer.

Figure C3. Dyne Inter-Loc V OCS, PAU, and CIA-III control and monitoring equipment.

As a result, despite the massive difference in size and power between the single-cylinder and multi-cylinder dynamometers, their control architecture is absolutely identical. The result of this is that the engine experimental procedures are also very similar, which (when combined with the electronic injection systems of the engine) mean the engine can be brought up to speed and forcibly motored by the dynamometer, and then fuel injection can be triggered by the test cell operator, with the dynamometer either supplying or absorbing whatever torque is required to keep the engine operating at a constant speed. The OCS accomplishes this via proportional-integral-derivative (PID) control systems that can be specifically tuned to the Duramax LBZ engine over time and successive operation, with minimal variation in engine speed even as torque is increased or decreased.

Other than the obvious size difference, the Duramax features only one significant uncontrolled departure from the single-cylinder engine, in the form of an integrated mechanical fuel pump to pressurize the common rail system. In the case of the single-cylinder engine, the power needed to run the fuel pump would be a significant drain on the total power being provided by the engine itself; thus, it is powered separately. In the case of the multi-cylinder engine, however, the engine's power vastly dwarfs that required by the fuel pump, and removing the fuel pump would needlessly complicate the setup of the multi-cylinder engine. This will result in a discrepancy between the amount of work indicated by the in-cylinder pressure trace and the work absorbed (and displayed) by the dynamometer (with the difference being the work required by the pump), but this can be experimentally ascertained during the initial bench testing of the multi-cylinder engine.

C.2 Room, Air, and Fuel Control Systems

To facilitate full operational control, a unique test cell environment is required. To this end, during the construction of the KU Engineering M2SEC facility, a specialized area was built to allow for safe engine operation in the form of a test cell and an attached control room, along with necessary safety and environmental control systems (see Figure C4).

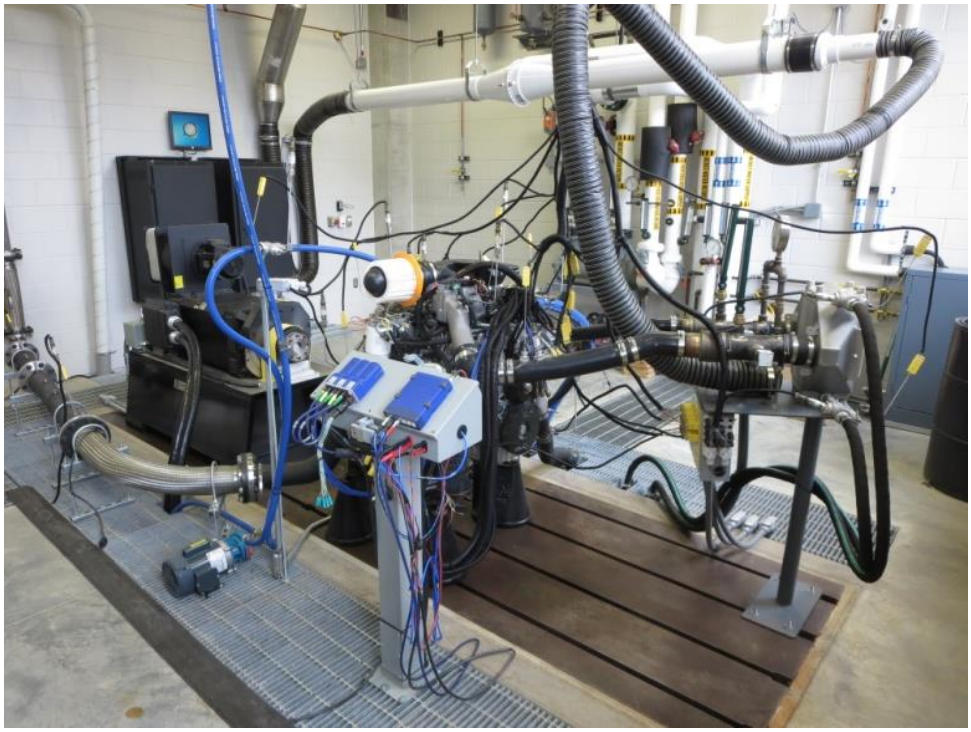

Figure C4. Multi-cylinder engine test cell, engine, and equipment.

Developed alongside the engine test cell itself was a specialized system built by Max Palmer of Bachelor Controls (BC) in LabVIEW, featuring systems to control the temperature of both the intake air and fuel charges flowing into the engine, the flow of separate coolants through both the engine and intercooler, the ambient temperature and humidity of the room, and emergency systems necessary to clear the room of exhaust gases in the case of a failure. This system operates separately from those used for engine control and data acquisition, and is accessed via a computer in the neighboring control room. In addition to the building air charge controls provided by BC, the intake air flow rate will be measured via a laminar volumetric flow element, which is simply an upsized variant of the laminar flow element used on the single-cylinder engine. Note that the following sections will provide a snapshot of the BC control systems; for a more thorough description, consult the separate manual provided for operation of the system [1].

While the fuel flow rate is controlled by the ECU directly, the BC LabVIEW system deployed allows for temperature control and monitoring of the fuel charge. This allows for an extreme amount of control and normalization in fuel testing. In addition, this can be utilized as a means to undergo engine

testing with fuels at various temperatures, generally changing the viscosity and density of the consumed fuel, which in turn affects the efficacy of the in-cylinder injection event.

Coolant is supplied to the intake intercooler in the form of water directly from the building water supply. This jacket water cooling system is controlled via the BC LabVIEW system, through a heat exchanger used to control the precise temperature of the water flowing through the intercooler (see Figure C5). In this way, the operator will have direct control over the temperature of the turbocharged air after it passes through the intercooler and into the engine itself.

Figure C5. Liquid-cooled Duramax LBZ intercooler.

Engine coolant is supplied in the form of a 50-50 mixture of water and ethylene glycol. This coolant mixture is in a self-contained loop, with pressure controlled by a mechanical pump built into the engine. A secondary boost/utility pump is also included, in order to provide additional pressure needed to

return the coolant to the raised reservoir, or to fill the system without motoring the engine. This engine coolant system passes through a heat exchanger in the room, with heat passing into a secondary coolant loop composed of pure ethylene glycol. The flow rate of this secondary system is controlled entirely by the BC LabVIEW program, and moves the engine heat into an industrial heat exchanger elsewhere in M2SEC, meant to supplement the thermal energy needed to provide hot water to the building (see Figure C6).

Figure C6. Fuel and coolant hardware interfacing with M2SEC building (left) and Duramax LBZ (right). The two segments interface with each other beneath the floor grates.

Room air systems are also controlled via the BC LabVIEW system, through a secondary pair of air handling unit from the engine intake controls. Of these two systems, one controls the flow of air into the room, and the second actively removes air from the room, allowing the facility to cycle fresh air into and out of the test cell. In addition, there is a separate small fan system attached to this system, which serves to keep the test cell at a lower pressure than the neighboring control room and the ambient conditions. This pressure differential will keep any buildup of gases or fumes contained to the test cell and exhaust systems, keeping the neighboring control room clear. This room air system is also tied to the emergency systems in the room. In the event of an emergency (triggered through a number of various alarms), the second section of the air handling unit ramps up to an emergency mode to evacuate any hazardous gases within the room.

The alarms built into this system are three-fold, and will monitor for the most apparent symptoms of an imminent or actual engine failure. First, the built-in temperature monitoring system actively displays and communicates the current status of the dynamometer; here, any spike in operating temperatures signify that the dynamometer is operating beyond its own limits, or is suffering from some form of malfunction, and a buildup of temperatures would lead to an inevitable catastrophic failure of the dynamometer used to control the engine. Thus, any spike in temperatures must trigger an alarm, prompting the operator to reduce fuel flow rate and stop both the engine and dynamometer (including triggering the emergency stop contingency, discussed below).

The second set of alarms is built into the test cell itself, tied to abnormal heat and emissions within the room. Three separate emissions sensors (one each for carbon monoxide, methane, and oxides of nitrogen) are in place at the door that leads from the control room to the test cell proper (see Figure C7). In addition, separate heat- and flame-sensitive sensors placed around the engine monitor for sudden rises in temperature. Should any of these alarms be triggered (signifying a fire, or a buildup of toxic or flammable gases within the test cell), the fuel flow rate to the engine will automatically be cut, the dynamometer will coast the engine down to a stop, and the exhaust air systems will be triggered to quickly vent any gases built up in the room. In addition, these alarms are integrated into the M2SEC safety systems, such that any alarm is communicated directly to the rest of M2SEC, likely leading to a triggering of the building alarm system (essentially, a fire alarm).

Figure C7. Multi-cylinder test cell gas and fire monitoring, emergency stop, and alarm systems.

The final set of alarms are the emergency stop buttons placed throughout the interior of the test cell, and linked to the dynamometer control system. Should any of these buttons be pressed, the dynamometer enters a locked state, forcibly arresting the engine and halting any further operation. These buttons are built into the same alarm system as the gaseous and thermal sensors, and so will trigger the exhaust air handling system to vent the room, but will not trigger the building alarm systems unless the secondary alarm button is triggered at the door between the control room and the test cell (see Figure C7).

C.3 ECU Development

Key to the development and operation of the multi-cylinder test cell are the control systems for the engine itself, most notably the ECU. For this application, a Bosch FlexECU (model F-00K-107-106) specifically meant for research applications is to be used. Connectivity and control to the FlexECU is achieved through a number of ETAS interface modules (ES 592, ES410, ES420, and ES430, see Figure C8) via ETK connection to the FlexECU, and via a direct ethernet connection to the high-speed computer

and server cabinets (discussed later). Of note, the FlexECU and ETAS modules require an outside source of power. As a result, in an emergency, power can be cut either remotely, or manually, between the cabinet and the FlexECU. This represents a final failsafe to halt runaway engine operation by interrupting the connection to the fuel injection system, entirely preventing injection from occurring and instantly unloading the engine. With the engine unloaded, the dynamometer can then be used to immediately bring the engine down to halt.

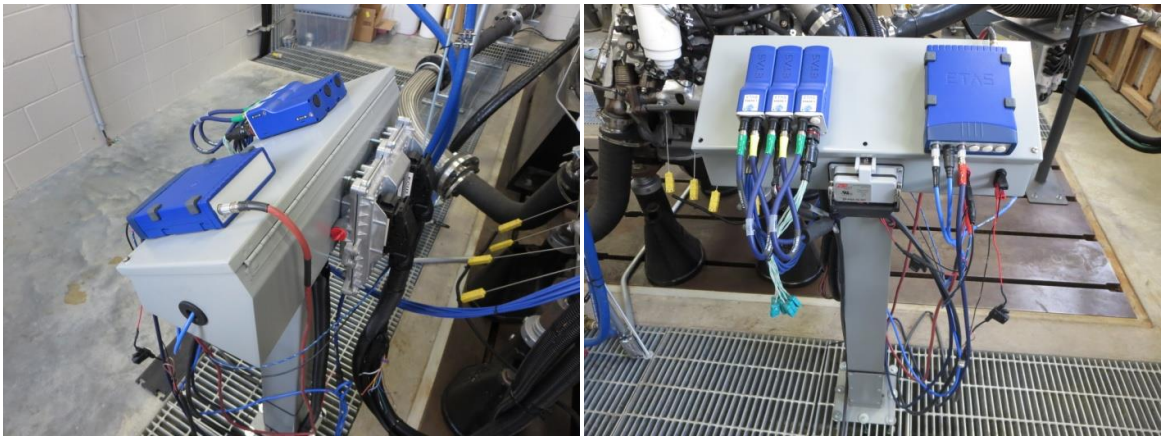

Figure C8. Bosch FlexECU and ETAS interface modules.

Programming and software-based control of the FlexECU and engine will be achieved through ETAS INCA, with development and calibration provided by ETAS EHOOKS-CAL and EHOOKS-BYP software. Through INCA, the engine operator will be able to update and change engine operation on the fly, particularly in the case of increasing or decreasing engine load through the fuel injection timing and pressure, through the FlexECU and interface modules (see Figure C9). Altogether this will allow for precision control, measurement, and monitoring of engine operating characteristics by the ECU through the engine's own sensor suite. This system is also in addition to the plethora of other sensors added to the test cell and engine in order to monitor engine operation in excess of the existing sensors built into the engine by GM. Note that the specifics of both the hardware and software of the ECU and control systems are provided in the literature provided by Bosch and ETAS [2, 3].

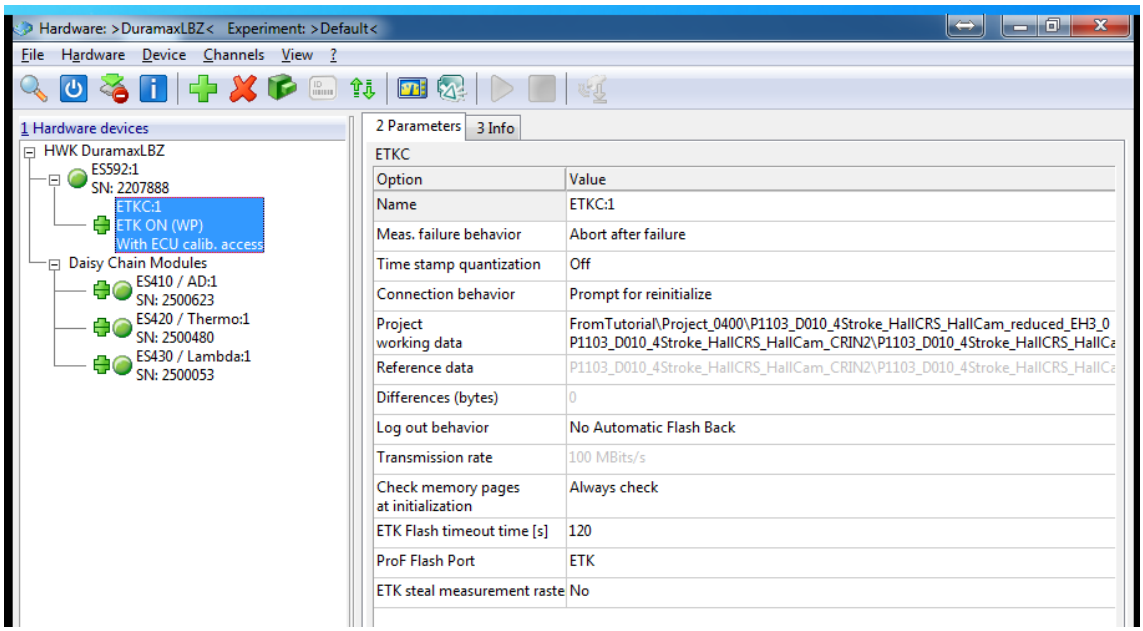

Figure C9. ETAS INCA Engine Control Unit Interface, showing connection to the ECU via ETK connection.

C.4 Engine Performance Sensors

The multi-cylinder test cell is to be constructed using subsystems and architecture reminiscent of that of the existing single-cylinder test cell [4-6]. This is most apparent in the usage of the Dyne Systems dynamometer controller technology, meaning the core control technology between the two cells is identical. In the same fashion, the core systems used to monitor and collect data on the engine during operation will be fundamentally based off of those of the single-cylinder test cell.

In-cylinder pressure trace analysis is to be achieved with a Kistler 6056A piezoelectric pressure transducer, capable of reading from 0 to 250 bar (with an error of no more than ±0.5%) and a Kistler Crank Angle Encoder and Pulse Multiplier, capable of 0.1 to 6 degrees of crank angle resolution, depending on the engine speed [4-6]. Using these, initial benchmarking of the multi-cylinder engine will be achieved at a resolution of 0.2 degrees of crank angle over 60 consecutive cycles, identical to the single-cylinder setup. At 1800 RPM (likely at the high end of operational speeds for the test cell), this will yield in-cylinder pressure data at a rate of 54 kHz, more than enough to register the high-frequency pressure oscillations associated with knock (which generally exist between 8 and 20 kHz), as well as

increasing the number of discretizations within the pressure trace, and thus improve the stability of the RHR models [7]. This has also necessitated a purpose-built high-speed computer that can capture the sheer volume of data of the pressure trace, as well as allowing communication with the ECU. The high-speed LabVIEW program utilized on the single-cylinder will again be used on the multi-cylinder with minimal changes, as the overall system architecture will be virtually identical [4-6].

Like the single-cylinder engine, the multi-cylinder setup will also contain additional thermocouples and pressure transducers to monitor and record the temperature and pressure of engine and intercooler coolant, and fuel (prior to mechanical fuel pump), as well as intake air temperature (before and after the turbocharger, after the intercooler, after the EGR outlet, and at each cylinders' intake valve), and exhaust gas temperature (at each cylinders' exhaust valve, before and after the EGR inlet, and at varying points in the exhaust pipe). In all, the test cell will have the capability to measure up to 60 separate thermocouple measurements, and 16 pressure measurements, split between two junction boxes (see Figure C10). The second junction box is intended to be largely vacant for the immediate future, as they are intended to offer auxiliary measurements for any additional instruments added to the engine exhaust systems.

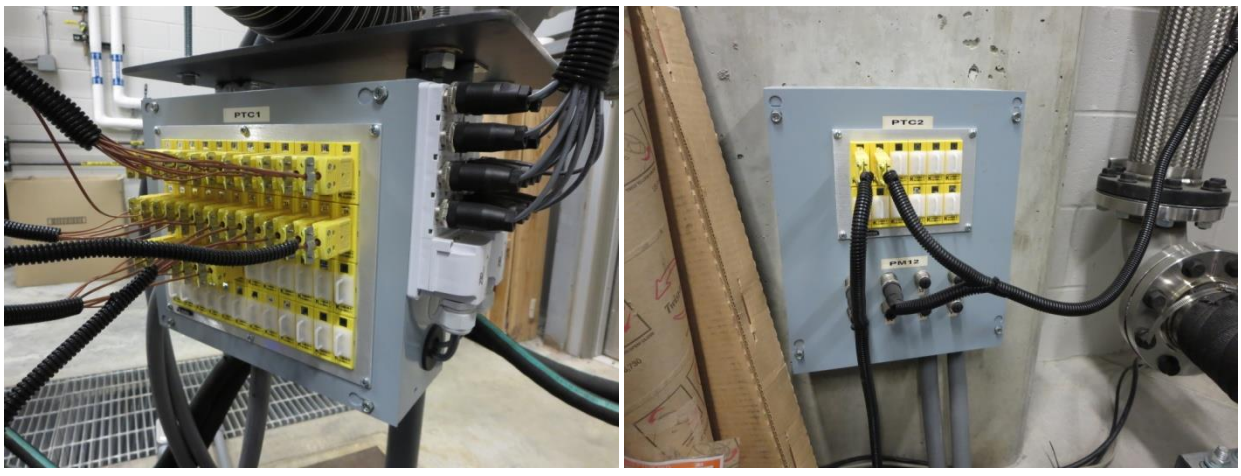

Figure C10. Thermocouple and pressure transducer junction boxes, featuring additional ports for later expansion of measurement capabilities.

From the junction boxes, the thermocouple and pressure transducer connections (as well as connections required for some of the rooms other systems) are bundled together and run under the room

grates to a pair of server cabinets mounted on the wall behind the dynamometer that will serve as the general hub for data collection and communication with the engine (see Figure C11). As such, the data hub and cabinets will contain the compact-reconfigurable input/output (cRIO) used for collecting performance data, the high-speed computer, wiring terminals for the pressure transducer an thermocouple connections, and power terminals for systems not linked to BC systems (e.g. ECU, fuel and engine coolant boost pumps). The cRIO-9024 utilized for this application is the more robust successor to the cRIO-9014 utilized on the single-cylinder engine, and features virtually identical hardware and features.

Figure C11. Multi-cylinder test cell control cabinets, featuring power terminals and high speed computer (left) and cRIO-9024 and measurement terminals (right).

The advantages of these development choices are threefold. First, this allows for mutual development of engine data acquisition programs between the single-cylinder and multi-cylinder engines, as fixes and updates in one system can be easily transferred to the other. Second, this also makes it significantly easier for new operators to become familiar with the multi-cylinder setup, assuming they

have spent time training on with the single-cylinder engine. Third, the LabVIEW system utilized in the single-cylinder setup has already proven itself very adaptable, and allowing for plug-and-play development of both software and hardware, meaning future operators will find it relatively easy to adapt the LabVIEW setup to accommodate new equipment [4-6].

This performance data collection will be communicated from the cRIO-9024 via ethernet directly to a second computer system in the neighboring control room, which will be utilized for acquisition of all engine data other than the in-cylinder pressure trace itself (see Figure C12). From the control room, the operator will be able to monitor engine performance on one computer system, the in-cylinder pressure trace and FlexECU communications via a second (the high-speed computer system), the BC control system from a third computer, the dynamometer controls and monitoring system mounted on the wall, and the room emergency shutdown and alarm systems, allowing a single operator complete control of all of the necessary systems to ensure safe and reliable operation of the multi-cylinder engine.

Figure C12. Multi-cylinder control room, adjacent the test cell.

C.5 Bench Testing Guidelines

For eventually multi-cylinder engine testing, the engine must first be calibrated in order to establish the key operational setpoints used for standard engine testing. In particular, there are three primary engine parameters that must be understood, at assumed operation between 1500 and 2400 RPM, and operating with standard #2 ultra-low sulfur diesel (ULSD). The first two are the injection timing and injection pressure setpoints, which the multi-cylinder engine shares with the smaller Yanmar. For these setpoints, the injection pressure should be set somewhere in excess of the reported idling fuel pressure of the Duramax LBZ, approximately 35 MPa, but generally should be held constant inasmuch as possible. The choice of a value in excess of 35 MPa is to allow for injection pressure optimization, particularly for fuels that require injection pressures below that of standard operation. The target injection pressure should be 65 MPa. However, it may be useful for a secondary set of operational setpoints to be acquired with injection pressures of 45-50 MPa, in order to provide a direct comparison between the Yanmar and Duramax engines in a way that controls for injection pressures. Next, injection timing should be varied at each engine load tested so as to ascertain the timing of Maximum Brake Torque (MBT), or (more accurately) the specific injection timing that achieves a given engine load that also minimizes the fuel consumption of the engine.

Third, the engine's turbocharger vane controls must be set to a given optimal boost rating for testing. This boost pressure must also not be maximized for any given speed and load, particularly if the vanes must be changed with respect to different fuel testing at a given load depending on the amount of energy recovered by the turbocharger. For example, a given fuel may generate alternatively more or less boost at a given speed, load, and turbocharger vane position than ULSD (likely because of altered degrees of premixed vs. diffusion-dominated combustion). As a result, it may be necessary to alter the turbocharger vane positions so as to maintain a constant amount of boost, ensuring that in-cylinder conditions are maintained.

It may also be useful to establish a baseline of engine operation with ULSD but with the turbocharger vanes opened such that the turbocharger provides little to no boosting of the engine. In doing

so, the performance of the engine and fuel themselves can be ascertained, without any additional effects from boosting. In combination with a lowered injection pressures, this minimizes the operational differences between the Duramax and the Yanmar, allowing for the most direct comparison between the two engines (i.e. the most major differences are due to speed differences and the difference in compression ratios). Finally, while the engine's exhaust gas recirculation (EGR) percentage can also be adjusted, the EGR flowrate should be minimized for general testing, so as to minimize its effect on calibration and general operation of the engine and reduce the number of variables that must be tracked and controlled during engine testing.

In order to establish these setpoints, the Duramax must be tested using the same procedures done to optimize the Yanmar, as described previously [8, 9]. For a given mapping, the general procedure should go as follows;

1. A given operational speed and injection pressure setpoint must be chosen.
2. For each given fraction of the rated engine load at the chosen speed, a specific amount of turbocharger boost must be chosen.
3. At each engine loading, the injection timing must be varied in increments of 0.5-1.0 degrees of crank angle, with the turbocharger vanes adjusted to maintain constant boost. The range of injection timings to be tested such that the engine achieves a timing of peak (fired) pressure between 5-20 degrees after top-dead center (ATDC). Testing should begin at earlier injection timings and proceed towards later timings.
4. After completing testing at all loads, engine data can be analyzed to establish which particular injection timing results in the lowest brake-specific fuel consumption. These injection timings (and turbocharger vane setpoints) are thereafter the MBT timings used for all future testing.

Of note, the range of injection timings tested can be abridged based on emissions of hydrocarbons, particulate matter, or carbon monoxide, or based off of the observed fuel demand of the engine needed to maintain a given engine load. If any of these readings significantly increase as injection timing is further

retarded, it indicates that the engine has exited its envelope of ideal combustion, and already passed the timing of MBT for that particular setpoint.

In order to utilize the MBT setpoints in future tests (particularly with novel fuels, fueling modes, or alternative operational modes e.g. increase EGR), the engine must first be operated with ULSD at the standardized MBT setpoints, and the precise timing and magnitude of peak pressure should be logged. Next, when the engine's operation is changed (e.g. the ULSD is exchanged for another fuel), operation must be adjusted so as to realign the timing of peak pressure to match that of operation with ULSD. For general testing (particularly with alternative liquid fuels and blends), realigning the timing of injection is sufficient. However, for some testing it may be necessary to reshape the in-cylinder pressure trace so as to match both the timing of peak pressure, but the shape of the pressure trace. To accomplish this, injection pressure can be adjusted, which generally adjusts the precise efficacy of fuel mixing (e.g. higher pressures offer better mixing, lower pressures offer poorer mixing). Note that adjusting injection pressures can also change peak pressure timings, but the effect is generally small and controllable through additional changes in injection timing to counteract the effect. Thus, when adjusting both injection timing and injection pressure for combustion shaping studies, first the injection timing should be broadly adjusted to the approximately correct timing, and then the injection pressure and injection timing should be alternatively adjusted until the fired pressure trace approximates the original [10].

C.6 Appendix C References

1. Palmer, Max. *KU M2SEC Project –BCI: Engine Test Cell (ETC) Controller Operation Manual (Rev. 4)*, Bachelor Controls, May 7, 2012.
2. Hamatschek, Mark. *Diesel FlexECU TCI Electrical Characteristic Data 0281 B10 1XF*, Bosch Engineering North America.
3. *FlexECU-D1, D010 Low Level Software Interface Definition Description*, ETAS.
4. Mangus, M.D., *Design, construction, and validation of an in-cylinder pressure recording system for internal combustion engine analysis*, 2012, University of Kansas.

5. Mangus, M.D., *Implementation of Engine Control and Measurement Strategies for Biofuel Research in Compression-Ignition Engines*, 2014, University of Kansas.
6. Langness, C., M. Magnus, and C. Depcik, *Construction, Instrumentation, and Implementation of a Low Cost, Single-Cylinder Compression Ignition Engine Test Cell*, 2014, SAE Technical Paper #2014-01-0817.
7. Heywood, J.B., *Internal Combustion Engine Fundamentals*, Vol. 930. 1988: McGraw-Hill, New York.
8. Mattson, J.M.S., *Power, Efficiency, and Emissions Optimization of a Single Cylinder Direct-Injected Diesel Engine for Testing of Alternative Fuels through Heat Release Modeling*, 2013, University of Kansas.
9. Mattson, J.M.S., M. Mangus, and C. Depcik, *Efficiency and Emissions Mapping for a Single Cylinder, Direct-Injected Compression Ignition Engine*, 2014, SAE Technical Paper #2014-01-1242.
10. Churkunti, P., J. Mattson, and C. Depcik, *Influence of Fuel Injection Pressure and Biodiesel upon NO_x Emissions*, 2016, SAE Technical Paper #2016-01-0877.